New Technologies Driving Decade-Bandwidth Radio Astronomy:

Quad-Ridged Flared Horn
&
Compound-Semiconductor LNAs

Thesis by

Ahmed Halid Akgiray

In Partial Fulfillment of the Requirements
for the Degree of
Doctor of Philosophy

California Institute of Technology
Pasadena, California

2013
(Defended April 19, 2013)

Acknowledgments

For the last three and one half years, I have had the privilege and honor of working with Dr. Sander Weinreb, my research advisor. I have learned so much from his unparalleled technical knowledge, his research philosophy, and his incredible humility, generosity, and kindness. I thank him for patiently listening to me—whether the subject matter was technical or not—and sharing his insight. I consider myself extremely lucky to have known such a technical pioneer and a wonderful person, yet at the same time I am saddened to be closing this chapter of my life. I am forever indebted to Dr. Sander Weinreb, a one-of-a-kind advisor, mentor, and confidant.

To Dr. William Imbriale: I thank him for his invaluable help and useful feedback throughout my PhD research and also for finding the time to serve on my thesis committee. I would also like to express my gratitude to the other members of my thesis committee, Prof. Ali Hajimiri, Prof. David Rutledge, and Prof. Jonas Zmuidzinas, who found the time in their busy schedules to review my work and provide valuable feedback. I extend a special note of appreciation to Prof. Ali Hajimiri for allowing me to borrow test equipment from his laboratory. I would also like to thank Prof. Anthony Readhead for serving as my academic advisor.

To Stephen Smith, I am especially grateful for the daily discussions and his invaluable feedback on both topics of my research, his patience in listening to me on everything related to microwave engineering and beyond, and his willingness to share his in-depth technical knowledge and insight on technical and non-technical topics alike. His friendship will be dearly missed.

I would like to thank Hector Navarette for assembly of the low-noise amplifiers and discrete transistors described in the second part of this thesis. I also appreciate the expert machining work of Mike Martin-Vegue, who fabricated all of the quad-ridged flared horns presented herein.

To Christopher Beaudoin, I thank him very much for carrying out the first on-telescope tests of the quad-ridged horn on a very long baseline interferometry antenna and demonstrating to the wider radio astronomy community its potential. He is not only our most loyal customer of the quad-ridged flared horns, but also a close collaborator with whom I enjoyed working.

A large portion of the second part of this thesis would not have been possible without the generosity of Dr. M. Rocchi of OMMIC. I am grateful to him for letting us evaluate our low-noise amplifier designs and discrete transistors on OMMIC's process. I also thank R. Leblanc of OMMIC

for patiently answering my questions, providing documentation and helping with layouts of our amplifiers.

To Dr. Daniel Hoppe: I am grateful for his support both before and during my PhD tenure at Caltech. I have benefited much from his deep technical expertise and his personal advice.

I have sincerely enjoyed being the teaching assistant of the Caltech microwave class for two years and I thank Dr. Dimitrios Antsos for the opportunity, as well as the useful discussions we had on my PhD research. The students, who took the class in these two years, are also much appreciated for what I hope were mutually beneficial discussions and office hour sessions.

I would like to thank my peers at Caltech (and some who have since left) from whom I learned much, namely G. Jones (Columbia University), Prof. J. Bardin (University of Massachusetts Amherst), R. Reeves, K. Cleary, R. Gawande, A. Pai, K. Dasgupta, Prof. K. Sengupta (Princeton University), S. Bowers, J. Schleeh (Chalmers University of Technology), S. Romanenko, A. Safaripour, B. Abiri, F. Aflatouni, and P. Pal.

A special thank you to the administrative assistants who helped me so much throughout my time at Caltech: T. Owen, L. Acosta, S. Slattery.

For financial support, I thank the California Institute of Technology. The quad-ridged horn research was funded in part by the National Science Foundation.

My dream of obtaining a PhD would be so much harder if it were not for the constant support I received from my parents. I cannot thank them enough for all they have given me. I am also deeply indebted to my parents-in-law who have always supported us, this would all be much more difficult without their help.

Last but certainly not the least, I would like to thank my precious family. To Ayşe Zeynep and Ömer Taha, thank you for somehow managing to brighten every day of my life. And to my wonderful wife Banu, I thank her for the encouragement and sacrifice during the last few years. Many people questioned my wisdom in pursuing a PhD with two children; she deserves much of the credit. I hope to return the favor in the following years.

Abstract

Among the branches of astronomy, radio astronomy is unique in that it spans the largest portion of the electromagnetic spectrum, e.g., from about 10 MHz to 300 GHz. On the other hand, due to scientific priorities as well as technological limitations, radio astronomy receivers have traditionally covered only about an octave bandwidth. This approach of “one specialized receiver for one primary science goal” is, however, not only becoming too expensive for next-generation radio telescopes comprising thousands of small antennas, but also is inadequate to answer some of the scientific questions of today which require simultaneous coverage of very large bandwidths.

This thesis presents significant improvements on the state of the art of two key receiver components in pursuit of decade-bandwidth radio astronomy: 1) reflector feed antennas; 2) low-noise amplifiers on compound-semiconductor technologies.

The first part of this thesis introduces the quadruple-ridged flared horn, a flexible, dual linear-polarization reflector feed antenna that achieves 5:1–7:1 frequency bandwidths while maintaining near-constant beamwidth. The horn is unique in that it is the only wideband feed antenna suitable for radio astronomy that: 1) can be designed to have nominal 10 dB beamwidth between 30 and 150 degrees; 2) requires one single-ended 50 Ω low-noise amplifier per polarization. Design, analysis, and measurements of several quad-ridged horns are presented to demonstrate its feasibility and flexibility.

The second part of the thesis focuses on modeling and measurements of discrete high-electron mobility transistors (HEMTs) and their applications in wideband, extremely low-noise amplifiers. The transistors and microwave monolithic integrated circuit low-noise amplifiers described herein have been fabricated on two state-of-the-art HEMT processes: 1) 35 nm indium phosphide; 2) 70 nm gallium arsenide. DC and microwave performance of transistors from both processes at room and cryogenic temperatures are included, as well as first-reported measurements of detailed noise characterization of the sub-micron HEMTs at both temperatures. Design and measurements of two low-noise amplifiers covering 1–20 and 8–50 GHz fabricated on both processes are also provided, which show that the 1–20 GHz amplifier improves the state of the art in cryogenic noise and bandwidth, while the 8–50 GHz amplifier achieves noise performance only slightly worse than the best published results but does so with nearly a decade bandwidth.

Contents

I The Quad-Ridged Flared Horn 9

List of Figures

List of Tables

Chapter 1

Introduction and Background

Radio astronomy instrumentation has consistently been at the forefront of microwave electronics from feed antennas, through low-noise amplifiers (LNAs) and to back-end electronics. Since Karl Jansky first discovered the radio emission from the Milky Way in 1932, each of these components has undergone tremendous development resulting in orders of magnitude improvement in sensitivity and bandwidth of receivers. Today, the key components of a typical radio astronomy receiver that primarily determine sensitivity and bandwidth are:

1. Corrugated horn feed antenna with about octave bandwidth;
2. Silicon germanium (SiGe), indium phosphide (InP), or gallium arsenide (GaAs) low-noise amplifier with at least octave bandwidth;
3. Digital back-end electronics, such as correlators, spectrometers, etc., capable of processing multi-GHz bandwidths simultaneously.

This dissertation is about pushing the *simultaneous* bandwidth of the first two components in pursuit of decade-bandwidth radio astronomy receivers.

In addition to system versatility, motivations for decade-bandwidth radio astronomy are two-fold. First, simultaneous frequency coverage enables exploration of new scientific questions. In particular, transient and continuum radio astronomy would benefit the most from decade or near-decade bandwidths. Some scientific applications are the following:

1. Observations of pulsed (pulsars) and transient radiation which occur in limited time periods but over many octaves of frequency (0.6 to 3 GHz and 2 to 12 GHz are desired bands). The detection sensitivity and timing accuracy can be enhanced by receiving systems matched to this wide spectrum and the pulsar timing observations are of great interest for the detection of gravitational waves [1];
2. For very long baseline interferometry (VLBI) observations where large bandwidth (2 to 14 GHz) increases sensitivity and removes fringe ambiguity [2, 3];

Figure 1.1: Receiver room of the Green Bank Telescope

3. For measuring the spectral shape (spectral index) of continuum radio sources (such as supernova remnants and quasars) which helps to determine the emission mechanism [4, 5];
4. While spectral line observations typically require the highest sensitivity and may thus not be the first candidate for decade-bandwidth systems, such systems could still prove valuable to search for radio spectral lines with large unknown red-shifts (8 to 50 GHz would be useful).

The second, and arguably more practical, motivation for decade-bandwidth radio astronomy instrumentation is cost. Recent trends in radio astronomy are in the direction of increased number of elements, be it dishes or focal plane elements, simultaneously covering decade bandwidths. For example, the Square Kilometer Array (SKA) is currently the biggest radio telescope project and when completed, it will consist of roughly 3000 dishes and possibly many more dipole elements which, in aggregate, will amount to a square kilometer collecting area [6, 7].

Realizing telescopes such as the SKA using today's octave-bandwidth receivers could be so costly to the point of being impossible. As an example, Figure 1.1 shows the receiver room of the Green Bank Telescope (GBT) operated by the National Radio Astronomy Observatory in Green Bank, West Virginia which covers 100 MHz to 100 GHz with more than 10 front-end receivers. Each front-end involves a feed antenna, an LNA, and associated cryogenics. Suppose the cost of each receiver is \$100,000 and the target frequency range is much smaller than the GBT, e.g., 1 GHz to 10 GHz as is suggested for initial phase of the SKA. This frequency range can be covered with a single decade-bandwidth receiver instead of four octave-bandwidth ones. The total savings in receiver electronics costs is \$300,000 per antenna or \$900 million for 3000 dishes. Even with a more conservative approach which assumes two near-decade-bandwidth receivers, the cost savings is \$600 million. And this does not even include savings in power and maintenance bills!

This thesis is divided into two parts:

1. **The quadruple-ridged flared horn (Chapters 2–4):** The first part begins with an overview of radio telescope reflector antennas and the common metrics used to evaluate their performance. The requirements of radio telescope feed antennas are discussed in length. In Chapter 3, the quadruple-ridged flared horn (QRFH)—a near-constant-beamwidth reflector antenna feed capable of achieving 7:1 frequency bandwidths—is introduced and its design and analysis are detailed. This discussion is followed by five example QRFH designs demonstrating suitability of the quad-ridged horn in wide range of radio telescopes.

2. **Compound-Semiconductor LNAs (Chapters 5–7):** The topic of the second part of the thesis is design, analysis and measurements of wideband LNAs on two state-of-the-art high electron mobility transistor (HEMT) processes which are introduced in Chapter 5. The results of extensive dc, small-signal and noise characterization of discrete transistors from both processes are described in Chapter 6. In the last chapter of this part, design and measurements of LNAs fabricated on these processes achieving decade bandwidth and more are detailed.

1.1 State of the art in Wideband Feeds

As alluded to earlier, corrugated horns are the standard bearer in terms of reflector antenna feeds for applications above 0.5 GHz requiring the highest sensitivity such as radio astronomy. They meet or exceed all the performance requirements of a radio telescope feed antenna, namely they achieve:

1. almost Gaussian, circularly symmetric radiation pattern with a prescribed nominal beamwidth;

2. little to no change in radiation patterns with frequency;

3. very low sidelobes;

4. excellent cross-polarization;

5. constant or near-constant phase center with frequency.

However, these desirable characteristics can only be realized over a 2:1 frequency bandwidth at most. The bandwidth limitation arises from two factors: 1) depth of corrugations in the horn are proportional to quarter wavelength; 2) ortho-mode transducers used to obtain dual linear polarization.

Due to increasing interest in decade-bandwidth radio astronomy, there has been much emphasis in feed antennas achieving such large bandwidths in the last couple years. As a result, number of ultra-wideband feed antennas with dual linear polarization have emerged. For instance, the four feed antennas under consideration for the SKA project are:

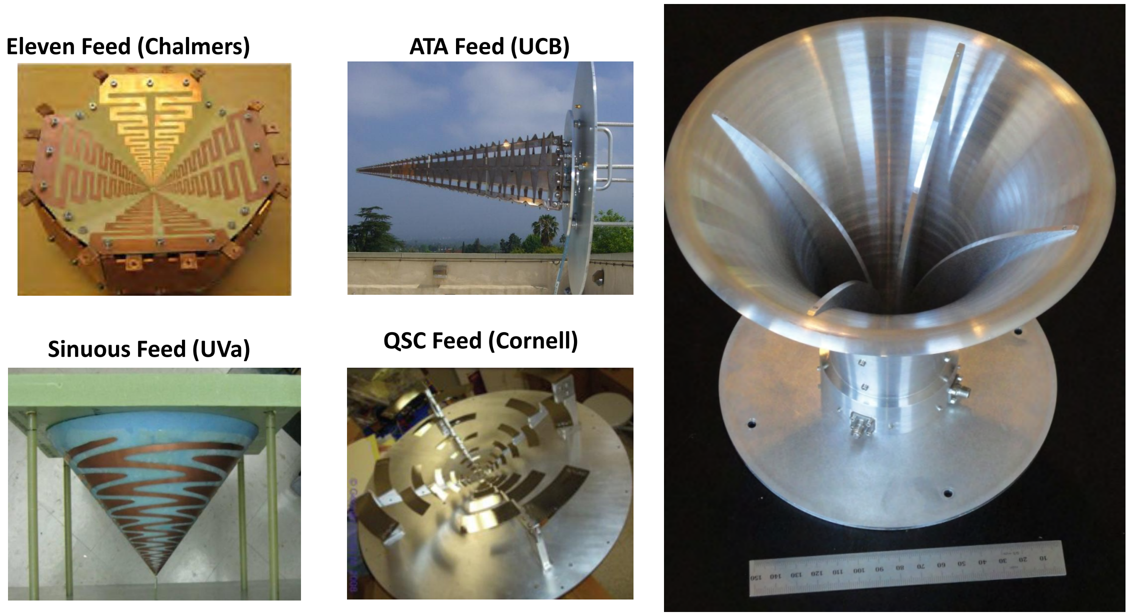

(a) (b)

Figure 1.2: Photographs of the (a) “log-periodic” type wideband feeds, (b) quad-ridged flared horn, all of which are currently under consideration for the SKA project.

1. Eleven feed from Chalmers University of Technology [8];
2. Allen Telescope Array (ATA) feed from University of California Berkeley [9];
3. Quasi self-complementary feed from Cornell University;
4. Sinuous feed from University of Virginia [10]

whose photographs are shown in Figure 1.2(a). It is seen that all are of the “log-periodic” type. As a result, they possess a lot of similar features. Table 1.1 summarizes key features of all of these feed antennas in addition to the quad-ridged flared horn.

Because log-periodic antennas are frequency independent, they maintain constant beamwidth with frequency [11]. This is the case for the three of the four wideband feeds listed above where the exception is the sinuous feed which exhibits more beamwidth variation resulting in somewhat elliptical radiation patterns. On the other hand, the first three feeds, especially the Eleven and the ATA feeds, achieve constant beamwidth over $\geq$ 7:1 frequency bandwidths with fairly good circular symmetry of radiation patterns. Another similarity between these feeds is that they all have differential inputs with 200-260 Ω nominal input impedance. All but the Eleven feed require either two differential LNAs or four single-ended LNAs which need to be gain and phase matched. The Eleven feed employs eight single-ended, matched LNAs or four differential LNAs where each pair of differential LNAs also have to be matched. The ATA feed exhibits significant phase center

	Radiation Pattern Features	Input Imp.	Bandwidth	Cost Est.
Corr. horn	Almost Gaussian beam, constant with freq; low sidelobes, excellent x-pol; const phase center can be designed for different beamwidths	50 Ω	2:1	Low
Eleven feed	Const beamwidth with circular beam; mediocre x-pol; const phase center; tough to change beamwidth	200 Ω diff	7:1	High
ATA feed	Const beamwidth with circular beam; mediocre to poor x-pol; large phase center variation; tough to change beamwidth	200 Ω diff	10:1	Med. to high
QSC feed	Const beamwidth with circular beam; mediocre-poor x-pol; tough to change beamwidth	200 Ω diff	10:1	N/A
Sinuous feed	Mediocre beamwidth stability w/ elliptical beam; mediocre x-pol; const phase center; tough to change beamwidth	200 Ω diff	4:1	Medium
QRFH	**Good beamwidth stability in E & D-planes; mediocre x-pol; small phase center variation; can be designed for different beamwidths**	**50 Ω**	**5:1 – 7:1**	**Low**

Table 1.1: Summary of key features of the five ultra-wideband feeds under consideration for the SKA project

variation with frequency while the others have constant or near-constant phase centers. Finally, nominal beamwidths of these antennas cannot easily be changed to accommodate different reflector antenna optics.

On the other hand, the quadruple-ridged flared horn described in the first part of this thesis possesses two unique capabilities when compared to the other wideband feeds. Its most distinct feature is the ability to design the horn to have a nearly constant beamwidth over a $\geq$ 5:1 frequency band for nominal 10 dB beamwidths between 30 and 140 degrees. Similar to corrugated horns, this flexibility is a result of the horn radiation patterns being primarily determined by the so-called flare angle, defined and explained in Chapter 3. Therefore, this horn could enable broadband frequency coverage on radio telescopes of different optical configurations. The second unique feature of this horn is that its input impedance could be designed to have a nominal value between 50 and 100 Ω while requiring only one single-ended LNA per polarization. This further reduces costs of the next generation telescope systems. Presently, the only disadvantage of the QRFH is the poor beamwidth stability in $\phi = 90°$ plane, while it exhibits good beamwidth stability in $\phi = 0°$, 45° planes. Phase center variation of the horn is small enough that its impact on aperture efficiency over the desired frequency range is very small.

1.2 State of the art in Wideband LNAs

Compound semiconductor low-noise amplifiers (LNAs) have long been the leading front-end receiver component in applications requiring state-of-the-art performance such as defense, remote sensing, and radio astronomy. Among these, radio astronomy systems require the lowest noise temperature and very high gain stability under cryogenic operation. Today, III-V semiconductor amplifiers dominate radio astronomy receivers due to the pioneering work of Weinreb in 1980 [12] demonstrating the superior performance of these technologies.

Increasing number of elements simultaneously covering decade bandwidths in next generation radio telescopes necessitate very large number of ultra-widebandwidth LNAs with low power consumption. Traditionally, InP has been the semiconductor of choice in radio astronomy microwave and millimeter-wave LNAs due to its superior noise and gain performance up through 150 GHz [13, 14, 15, 16, 17, 18] beyond which super-conducting mixers have been employed. However, due to its niche market, InP has seen the slowest development pace compared to GaAs and silicon. Moreover, centimeter-wave LNAs designed at Caltech and fabricated by Northrop Grumman Corporation have exhibited no improvement in cryogenic noise in addition to roughly 50% yield after pre-selecting MMICs at room temperature based on gate leakage and pinch-off characteristics [19]. This is primarily due to the fact that NGC's InP process is research-oriented rather than a commercial process and is primarily aimed for millimeter-wave electronics as evidenced by record-breaking results produced by NGC InP amplifiers operating above 75 GHz up to 0.5 THz (see [20, 21] as well as some of the references earlier in this paragraph).

As radio astronomy receivers get more complex and require many more elements, there is renewed emphasis on cost, yield and process stability. This leads to reconsideration of GaAs which is commercially more attractive and thus, has enjoyed more investment in process development in recent years [22, 23, 24]. In the second part of this dissertation, room temperature and cryogenic performance of discrete transistors and MMIC LNAs achieving very low noise over decade bandwidths from two state-of-the-art HEMT processes: 35 nm InP pHEMT and 70 nm GaAs mHEMT are investigated. The two LNA designs presented herein cover the following frequency ranges: 1) 1–20 GHz; 2) 8–50 GHz.

In cm-wave astronomy, typical frequency bands of interest for MMIC LNAs have been: 1–12, 4–8, 4–12, 2–14, 3–18 GHz[1]. Another motivation for the 1–20 GHz LNAs designed in this research is the possibility of covering all of these frequency bands in one MMIC. While the packaged amplifier could be optimized for specific frequency bands by specialized input matching networks, a versatile MMIC covering 1-20 GHz could prove very useful and convenient. Additionally, such an LNA with good low-power performance would be very attractive as IF amplifier following SIS mixers whose IF

---

[1] These are in addition to more traditional hybrid LNAs usually covering octave bandwidths.

	Technology	BW [GHz]	Gain [dB]	NF [dB]	$\lvert S_{11}\rvert$ [dB]	Power [mW]
Caltech WBA13	0.1 μm InP	1–12	38	1 @ 300 K 0.08 @ 20 K	-15	15-20
Caltech 6-18	0.1 μm InP	6–18	35	0.09 @ 20 K	-15	12
LNF (Chalmers)	0.13 μm InP	1–12	38	0.9 @ 300 K 0.08 @ 12 K	-12	15-20
LNF (Chalmers)	0.15 μm GaAs	6–20	31	1 @ 300 K 0.15 @ 10 K	-10	22

Table 1.2: Key performance specifications of four cryogenic LNAs covering 1–20 GHz

bandwidths reach 15 GHz. Table 1.2 lists key performance metrics of four state-of-the-art cryogenic MMIC LNAs covering subsets of this frequency range.

A cryogenic low-noise amplifier covering 8–50 GHz is not currently available for radio astronomy applications. Instead, typical LNAs in radio astronomy usually only cover a waveguide band, e.g., 26–40 GHz. For instance, a 30–43 GHz amplifier designed at Caltech and fabricated on NGC 0.1 μm InP process achieves 30 dB gain and noise figure of 2 dB at 300 K and 0.36 dB at 20 K with 15–20 mW DC power consumption. Wider bandwidth LNAs with similar or somewhat higher noise performance is of interest as IF amplifier following hot-electron-bolometer (HEB) super-conducting mixers. Another motivation for this LNA in this research has been integration of such a MMIC into a future 8–50 GHz quad-ridged flared horn.

1.3 Publications

Parts of this research has been published as listed below:

- **A. Akgiray** and S. Weinreb, "Noise Measurements of Discrete HEMT Transistors and Application to Wideband, Very Low Noise Amplifiers," submitted to *IEEE Trans. Microwave Theory Tech.*, Jan 2013.
- R. Keller, C. Kasemann, S. Weinreb, **A. Akgiray**, U. Bach, P. Freire, K. Grypstra, R. Karuppusamy, M. Kramer, P. Müller, F. Schäfer and B. Winkel, "An Ultra Broad Band Radiometer Receiver for the Effelsberg 100m Telescope," in press, *Advances in Radio Science*, Jan 2013.
- **A. Akgiray**, S. Weinreb and W. A. Imbriale, "Circular Quadruple-Ridged Flared Horn Achieving Near-Constant Beamwidth Over Multi-Octave Bandwidth: Design and Measurements," *IEEE Trans. Antennas Propag.*, vol. 61, no. 3, 2013.
- W. A. Imbriale, S. Weinreb, G. Jones, H. Mani, and **A. Akgiray**, "The Design and Performance

of a Wideband Radio Telescope for the GAVRT Program," *IEEE Trans. Antennas Propag.*, vol. 59, no. 6, pp. 1954-1962, 2011.

- **A. Akgiray** and S. Weinreb, "The quadruple-ridged flared horn: A flexible, multi-octave reflector feed spanning $f/0.3$ to $f/2.5$," ***invited paper***, *the 7th European Conference on Antennas and Propagation,* Gothenburg, Sweden, April 2013.
- M. Varonen, R. Reeves, P. Kangaslahti, L. Samoska, **A. Akgiray**, K. Cleary, R. Gawande, A. Fung, T. Gaier, S. Weinreb, A. C. S. Readhead, C. Lawrence, S. Sarkozy, and R. Lai, "A 75-116-GHz with 23-K noise temperature at 108 GHz," to be presented at the *2013 IEEE International Microwave Symposium,* Seattle, WA, USA, June 2013.
- **A. Akgiray** and S. Weinreb, "Ultrawideband Square and Circular Quad-Ridge Horns With Near-Constant Beamwidth," presented at *2012 IEEE International Conference on Ultra-Wideband,* Syracuse, NY, USA, September 2012.
- S. Weinreb, **A. Akgiray** and D. Russell, "Wideband Feeds and Low Noise Amplifiers for Large Arrays," presented at *XXX URSI General Assembly and Scientific Symposium of International Union of Radio Science,* Istanbul, Turkey, August 2011.
- **A. Akgiray**, W. A. Imbriale and S. Weinreb, "Design and Measurements of Dual-Polarized Wideband Constant-Beamwidth Quadruple-Ridged Flared Horn," *2011 IEEE Int. Symposium on Antennas and Propag. and USNC/URSI National Radio Science Meeting,* Spokane, WA, USA, July 2011. ***Student Paper Competition Honorable Mention***
- W. A. Imbriale and **A. Akgiray**, "Performance of a Quad-Ridged Feed in a Wideband Radio Telescope," *5th European Conference on Antennas and Propag.,* Rome, Italy, April 2011.
- **A. Akgiray** and S. Weinreb, "Wideband Near-Constant Beamwidth Flared Quad-Ridge Horn Feed for Reflector Antennas in Radio Astronomy," *2011 USNC-URSI National Radio Science Meeting*, Boulder, CO, USA, January 2011.

Part I

The Quad-Ridged Flared Horn

Chapter 2

Key Requirements of Radio Telescope Feeds

Almost all of today's radio telescopes operating above 0.5 GHz use reflector antennas consisting of one or more mirror(s), where the primary mirror is very large in terms of wavelength because astronomical signals are extremely weak and a large antenna collecting area (equivalently, large antenna gain) is needed to detect them. This chapter begins with a brief overview of radio telescope reflector antennas followed by a discussion of the metrics used to quantify a reflector antenna's performance, namely aperture efficiency and system noise temperature. The figure of merit most commonly used in radio astronomy is then discussed. The chapter concludes with an explanation of the key requirements of radio telescope feed antennas.

2.1 Reflector Antenna Optics

Reflector antennas come in variety of configurations depending on mirror type, number of mirrors, optical geometry, etc. The most common mirror types are planar, spherical, conical, paraboloid, hyperboloid and ellipsoid with the last three being the dominant types in very high gain applications. Further, reflectors can be symmetric or offset; shaped or unshaped; can have one, two or more mirrors which may be arranged in Gregorian, Cassegrain, ring-focus, beam-waveguide, etc., configurations. In shaped systems, there are at least two mirrors whose surfaces are synthesized to achieve particular amplitude and phase distributions on the reflector aperture. The design of reflector antennas is usually performed first using geometrical optics (GO) and refined through physical optics (PO), physical theory of diffraction (PTD) or geometrical theory of diffraction (GTD) [25].

The most common reflector antenna configurations in radio astronomy are symmetric and offset dual-reflector antennas in Cassegrain or Gregorian geometries which are depicted in Figure 2.1. The front-fed reflector is also sometimes used, especially for low-frequency radio astronomy and is shown in the same figure as well. In all of these configurations, the primary mirror is a paraboloid and

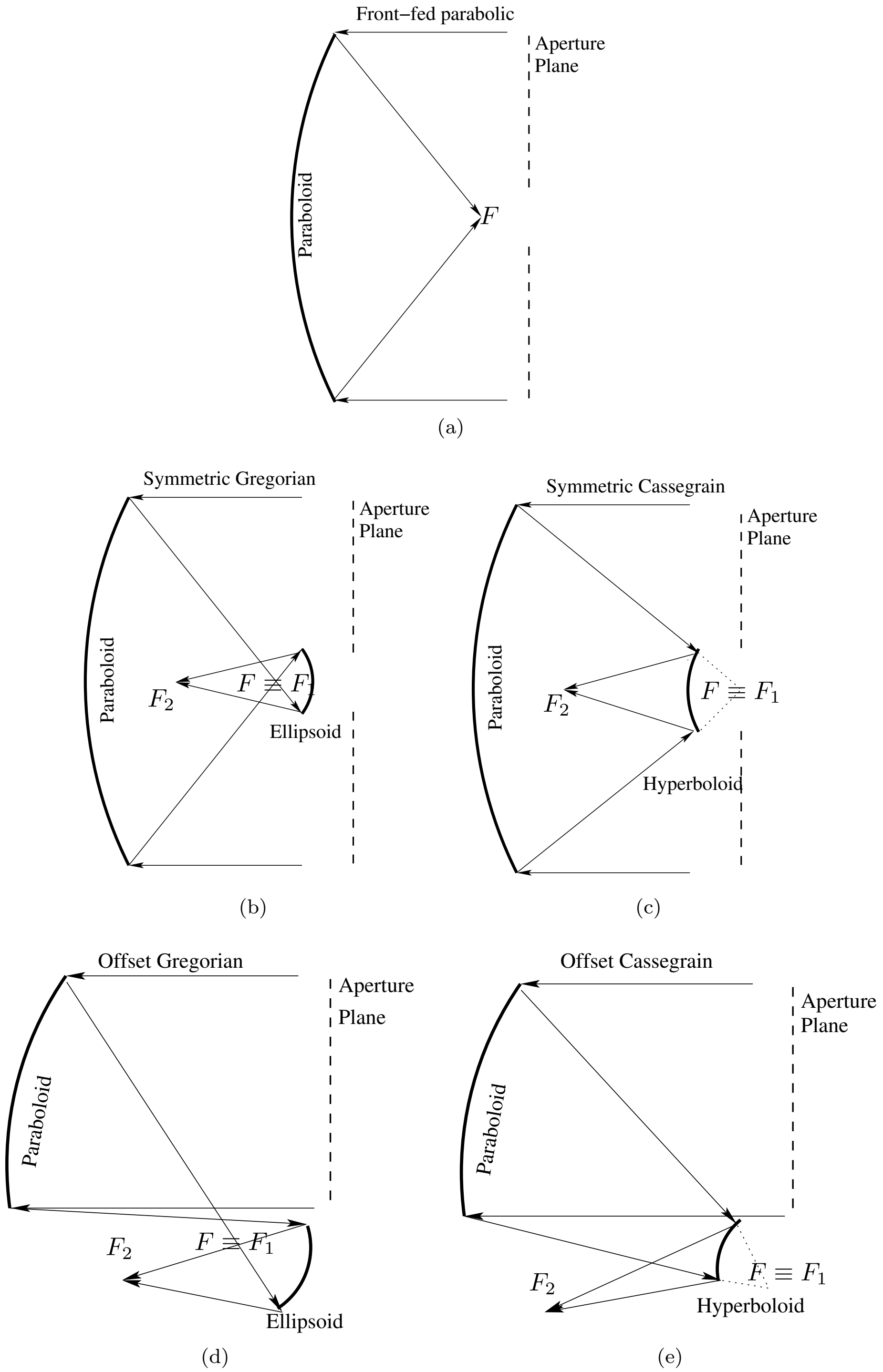

Figure 2.1: The most common reflector antenna optical configurations in radio astronomy

focuses plane waves from distant sources onto a single focal point F.

The Gregorian configuration comprises an ellipsoidal secondary mirror in addition to the parabolic primary. The focal point of the parabola, F, is collocated with one of the foci of the ellipsoid F_1; the feed antenna is located at the other focal point of the ellipsoid, F_2. The Cassegrain reflector antenna uses a hyperboloidal secondary mirror instead of an ellipsoid. The focal point of the primary is collocated with the hyperboloid's focal point behind the secondary mirror F_1 and the feed antenna is located at the other focal point F_2. An important disadvantage of the symmetric configurations as compared to their offset counterparts of Figure 2.1 is the aperture blockage due to the secondary mirror (or the feed in the case of the front-fed parabola) which reduces the aperture efficiency as explained in the next section.

Some of the parameters of interest in the design of a reflector antenna include gain, spillover, first and far-out sidelobe levels, cross-polarization level. All of these are strongly dependent on the feed antenna performance and are most commonly quantified via aperture efficiency discussed in detail next.

2.2 Aperture Efficiency

Reflector antennas, just like horn and lens antennas, are aperture antennas which are characterized by a planar aperture, perpendicular to the direction of maximum radiation, through which the majority of the radiation passes [25]. Apertures of the typical reflector configurations are depicted in Figure 2.1. In all of these cases, the aperture is circular, and reflector analysis using GO reduces to tracing rays from the feed antenna to the aperture and taking the Fourier transform of aperture fields to obtain far-field radiation patterns [11].

One of the canonical examples of an aperture antenna (and one that is relevant to reflector antennas) is a circular aperture of radius a in an infinite ground plane which can be analyzed in closed form under uniform illumination and yields the well-known Airy disc far-field pattern[1] [26]

$$\frac{J_1\left(ka\sin\theta\right)}{ka\sin\theta} \tag{2.1}$$

where k is the wavenumber and J_1 is the first-order Bessel function of the first kind. Figure 2.2(a) displays the aperture field distributions with uniform and tapered illuminations, and the resultant far-fields are plotted in part (b) for $a = 3\lambda$. The tapered illumination is designed with an edge taper of -15 dB which represents a reasonable approximation of realistic aperture distributions on radio telescopes.

The first observation from these plots is the small but significant difference in gains between the

---

[1] Note that the aperture area is assumed to be much larger than λ^2.

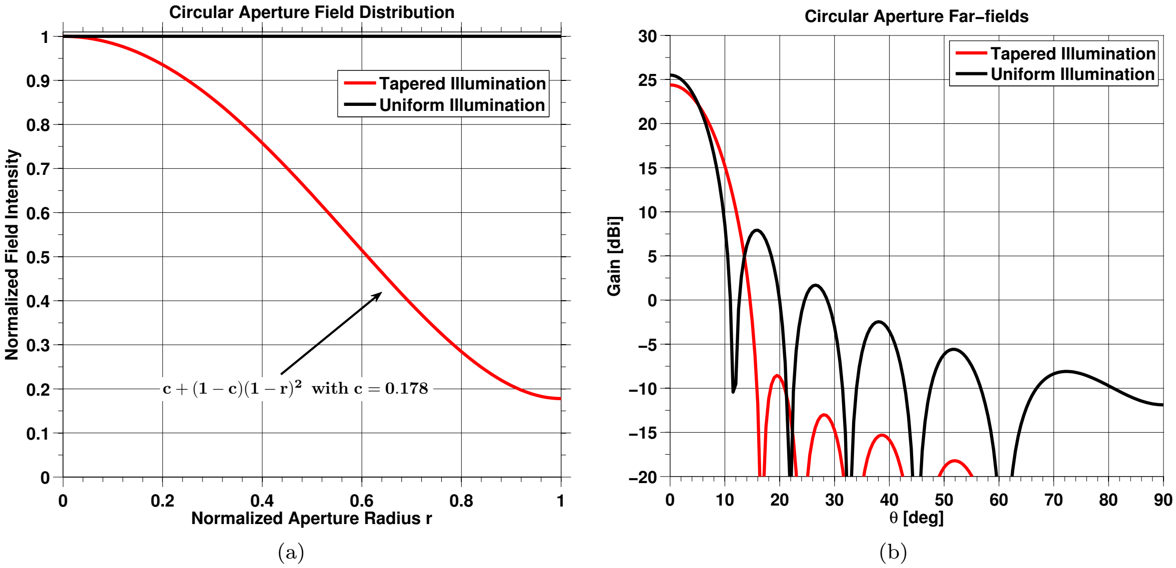

Figure 2.2: (a) Field distribution (with uniform phase), (b) the resultant far-field patterns of a circular aperture in an infinite ground plane under uniform and tapered illuminations. The far-field pattern of the tapered distribution is calculated using the results in [27].

two cases. In fact, it can be shown that uniform illumination always yields the maximum gain[2] for any aperture shape, and in the case of a circular aperture, the maximum gain is [26]

$$G_{max,circ} = \frac{4\pi}{\lambda^2}\left(\pi a^2\right)$$

or more generally, the maximum gain for an arbitrary aperture shape is

$$G_{max} = \frac{4\pi}{\lambda^2} A_{phys}$$

where A_{phys} is the physical area of the aperture. The tapered illumination, on the other hand, yields slightly lower gain and larger beamwidth with the same aperture size. This directly leads to the definition of *effective* aperture area or *effective* area of an antenna: it is the area of a uniformly illuminated aperture that yields the same gain G, namely [25],

$$A_{eff} \equiv \frac{\lambda^2}{4\pi} G \tag{2.2}$$

The aperture efficiency, also known as antenna efficiency, is then defined as the ratio of an

---

[2] Technically, directivity is the correct term to use here; however, the two are equal for an antenna with no ohmic losses which is the underlying assumption.

antenna's effective area to its physical area [25]

$$\eta \equiv \frac{A_{eff}}{A_{phys}} = \frac{G}{G_{max}} \tag{2.3}$$

which is valid for $A_{phys} \gg \lambda^2$. Under tapered illumination, for instance, the aperture efficiency is approximately 78% because gain is about 1.1 dB lower than that for uniform illumination.

Aperture efficiency of a reflector antenna is determined not only by the aperture field taper. In fact, any power loss in the on-axis direction (i.e., $\theta = 0$) results in lower efficiency. Such loss factors include phase errors in aperture fields, spillover energy, cross-polarization, aperture blockage, scattering from support structures, surface errors, etc. In the design of feed antennas for reflectors, it is common to approximate the aperture efficiency by neglecting losses due to blockage, support structure scattering, and surface errors. This approximate efficiency is then primarily a function of feed antenna performance, and is sometimes called the antenna feed efficiency [28]. Henceforth, the term aperture efficiency is used to refer to this approximate efficiency.

Obtaining a general, closed-form expression for aperture efficiency of a reflector antenna is not possible as it depends on the particular reflector optics and feed antenna radiation pattern. The efficiency can be calculated numerically using GO, PO, GTD or PTD; however, these are computationally expensive severely limiting their use in feed antenna design. Thus, an approximate closed-form expression is sought. To that end, the following radiation pattern is frequently assumed for the feed antenna (x-polarization):

$$E_f \equiv V_\theta(\theta)\cos\phi\hat{\theta} - V_\phi(\theta)\sin\phi\hat{\phi} \tag{2.4}$$

because: 1) ϕ integration can be performed analytically due to circular symmetry; 2) far-field patterns first-order azimuthal terms maximize gain of a paraboloidal reflector antenna [29] (also see Section 3.5). Then, the approximate aperture efficiency of a symmetric prime-focus or Cassegrain reflector is given by [30]

$$\eta = 2\cot^2\frac{\theta_s}{2}\,\frac{\left|\int_0^{\theta_s} V_{co45}(\theta)\tan\frac{\theta}{2}\,d\theta\right|^2}{\int_0^{\pi}\left[\left|V_{co45}(\theta)\right|^2 + \left|V_{xp45}(\theta)\right|^2\right]\sin\theta\,d\theta} \tag{2.5}$$

where

$$V_{co45}(\theta) \equiv \frac{1}{2}\left[V_\theta(\theta) - V_\phi(\theta)\right] \tag{2.6}$$

$$V_{xp45}(\theta) \equiv \frac{1}{2}\left[V_\theta(\theta) + V_\phi(\theta)\right] \tag{2.7}$$

and θ_s is one half of the subtended angle to the edge of the primary (or secondary) reflector.

In order to further evaluate sources of efficiency loss during feed antenna design, the aperture efficiency expression is frequently factored into “sub-efficiency” terms η_i such that

$$\eta = \prod_i \eta_i. \tag{2.8}$$

Many factorization has been proposed in the literature [28, 31, 32]. In this research, a slightly modified version of the factorization in [30, 32] is used. In particular, the aperture efficiency is factored as,

$$\eta = \eta_{ill}\ \eta_{sp}\ \eta_{\phi}\ \eta_{xp}\ \eta_{BOR1} \tag{2.9}$$

which, from left to right, are illumination, spillover, phase, cross-polarization, and Body-of-Revolution-1 (BOR1) sub-efficiencies. The expressions for these terms are available in [30, 32] and are not reproduced; however, a brief explanation of each follows.

Illumination: Measures how close the realized aperture distribution is to uniform illumination. This is what was referred to as “aperture efficiency” above for the non-uniformly illuminated circular aperture, because all other “sub-efficiency” terms are equal to one in that case. This term is sometimes called taper efficiency.

Spillover: Ratio of power captured by the reflector to total radiated power. Conversely, $(1 - \eta_{sp}) \times 100$ represents the percentage power lost to energy spilling past the reflector. In the circular aperture example above, the assumption was that the aperture fields abruptly fall to zero right at the aperture rim which is impossible to realize. This is a very important term, as explained in the next section, because spillover energy increases antenna noise temperature.

Phase: Measures how uniform the phase distribution is in the reflector aperture. It is the only sub-efficiency that depends on the physical location of the feed with respect to the focal point of the reflector. Linear phase in the aperture would steer the reflector beam and any other phase perturbation results in far-field pattern degradation such as increased sidelobe level and shallow nulls [11]. Feed antennas with significant phase center variation in terms of wavelength in the frequency band of interest yield poor phase efficiency. Conversely, constant phase center implies constant phase efficiency that is approximately equal to one.

Polarization: Measures the peak cross-polarization level in the $\phi = 45°$ plane, namely $\max_\theta |V_{xp45}(\theta)|$. Most reflector antennas contribute little to no cross-polarization, and the feed cross-polarization performance predominantly determines the overall performance. This efficiency is called the polarization sidelobe efficiency in [30]. (Note that the definition of V_{xp45} in (2.7) is same as Ludwig’s 3rd definition [33] only for the so-called Body-of-Revolution-1 antennas)

BOR1: The feed radiation pattern definition in (2.4) only has first-order azimuthal terms, because,

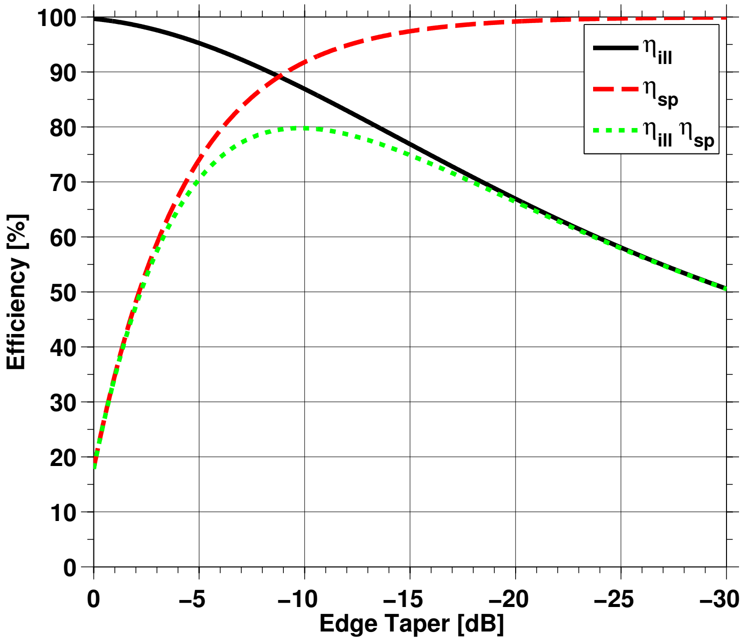

Figure 2.3: Illumination efficiency η_{ill} (black solid), spillover efficiency η_{sp} (red dashed) and $\eta_{ill} \times \eta_{sp}$ (green dotted) calculated using equations in [30]

> as alluded to earlier, such far-field patterns give the maximum secondary gain. In other words, higher-order azimuthal terms do not contribute to on-axis gain of the reflector antenna, and thus represent a power loss [29]. BOR1 efficiency quantifies this power loss and is defined as the ratio of power in first-order azimuthal modes to total radiated power. This efficiency is sometimes called azimuth mode efficiency [31].

The illumination and spillover efficiencies calculated using the results in [30] are plotted in Figure 2.3 as a function of feed edge taper[3] which, in combination with Figure 2.2, reveals some key points regarding aperture illumination and spillover. In particular, tapered aperture illumination results in

1. Broader beamwidth;
2. Reduced gain ⇒ reduced aperture efficiency;
3. Greatly reduced first sidelobe level;
4. Much reduced spillover energy.

These figures also show the well-known trade-off between illumination and spillover, and demonstrate the theoretical maximum aperture efficiency of a symmetric paraboloidal reflector antenna, 80%, attained at approximately -10 dB feed edge taper. The realized aperture efficiency will necessarily be lower due both to aforementioned losses in the reflector and the feed.

---

[3] Due to path loss, edge taper at the reflector rim would be slightly less

The approximate aperture efficiency and the sub-efficiencies mentioned above are only used in this research in comparing one quad-ridged horn to another during the design process. When a promising quad-ridged horn design is identified, PO calculations are carried out to evaluate its performance on the telescope.

2.3 Figure of Merit for a Radio Telescope

The primary goal in the design of radio telescopes and deep-space communication reflector antennas is to maximize the gain and minimize system noise temperature, both of which increase telescope's sensitivity. Therefore, the most widely used figure of merit in radio telescope design is given as

$$FoM \equiv \frac{A_{eff}}{T_{sys}} = \eta \frac{A_{phys}}{T_{sys}} \tag{2.10}$$

where T_{sys} is the system noise temperature and the other parameters are defined in the previous section. The system noise temperature is given by[4]

$$T_{sys} \equiv T_{Ant} + T_{LNA} = (1 - \eta_{spill})\, T_n + T_{sky} + T_{LNA} \tag{2.11}$$

where T_{LNA} is the effective input noise temperature of the low-noise amplifier proceeding the feed antenna; T_{sky} represents noise pick-up from the sky; T_n is the effective temperature seen by the spillover energy (e.g., if all spillover energy hit the ground, T_n would be 300K). It is seen from (2.10) that maximizing aperture efficiency is critical, but minimizing spillover is perhaps even more important because both the numerator and the denominator depend on it. For instance, assuming $T_n = 150$ K, $\eta = 0.6$, $\eta_{spill} = 0.9$, and $T_{sky} + T_{LNA} = 10$ K, a 2% increase in spillover efficiency (increases from 90 to 92%) yields more than 14% increase in the figure of merit.

2.4 Requirements of Radio Telescope Feed Antennas

The discussions in the previous two sections bring out the most important requirements of feed antennas to be used in radio astronomy:

1. Constant beamwidth
2. Circularly symmetric radiation pattern (first-order azimuthal terms only)
3. Small, preferably no, phase center variation
4. Low cross-polarization

---

[4] Assuming gain of the LNA is large enough so that input noise contribution of components following the LNA is negligible

5. Good input return loss to reduce impact on T_{sys}

and these need to be achieved over an octave or larger bandwidth. In addition, the feed should be easily integrable into a cryogenic dewar. Presently, the only antennas that meet and exceed all of these requirements are Pickett-Potter type [34, 35] and corrugated horns, which can achieve an octave bandwidth at most.

Chapter 3

Design, Analysis, and Fabrication of Quad-Ridged Horns

This chapter focuses on design and analysis of quad-ridged horns achieving near-constant beamwidth over multi-octave bandwidths. In the first section, a brief overview of the literature on dual- and quad-ridged structures is provided. The initial approach of and the software tools developed for quad-ridged horn design are detailed in the second section of the chapter. Key features of the quad-ridged horn and its design are discussed in detail. In addition, quad-ridged horn fabrication details are briefly reviewed. The chapter concludes with an outline of the method used to compute aperture mode content of the QRFH.

3.1 Historical Overview

Dual-ridged waveguides have been identified for their ultra-wideband capabilities as early as the 1940s [36, 37]. Most of the initial analyses relied on transverse-resonance methods and on deriving equivalent circuits for the ridged waveguide to calculate cutoff frequencies. Hopfer [38] expanded upon the existing literature by providing parametric studies of cutoff frequencies, attenuation, etc. Montgomery [39] generalized the analysis to include the complete eigenvalue spectrum of these structures. These studies all showed that the dual-ridged waveguide exhibits significantly larger bandwidth compared with hollow waveguides due to the ridges lowering the dominant mode cutoff frequency by nearly a factor of four. The term "bandwidth" is defined here as the ratio of cutoff frequency of the dominant mode to that of the next higher-order mode, i.e., single-mode bandwidth. The major practical limitation of dual-ridged waveguides and horns is the fact that they can only support single linear polarization; hence, quad-ridged structures, initially thought to also support similarly large bandwidths, gained prominence where dual linear polarization was required.

Quad-ridged waveguides have been analyzed using the finite-element method [40] and magnetic field integral equations [41, 42] for cutoff frequencies and mode fields of the first few modes as a function of ridge-to-ridge gap and ridge thickness. These analyses show that while the dominant mode cutoff frequency in quad-ridged structures is also decreased by nearly factor of four, the single-mode bandwidth of such waveguides is not as large as their dual-ridged counterparts. This is due to mode splitting of the TE_{21} and TE_{20} modes of circular and square waveguides, respectively, whereby cutoff frequency of one of the split modes is significantly loaded by the ridges causing it to decrease along with the dominant mode. Despite having reduced single-mode bandwidth, quad-ridged structures are still widely used in many microwave applications requiring octave to multi-octave bandwidths, e.g., wideband ortho-mode transducers (OMTs) [43, 44], quad-ridged horns [45, 46, 47]. This is due to two reasons: 1) many applications do not require single mode propagation; 2) if structure has both x- and y- symmetry (two-fold symmetry), the TE_{21} (TE_{20}) mode will not be excited.

Design of quad-ridged waveguide structures—especially ones with flared cross sections in the direction of propagation—still suffer from lack of a theoretical or empirical analysis. The aforementioned papers on quad-ridged waveguides only address the first few eigenmodes whereas more knowledge on the eigenvalue spectrum of the structure and the coupling between eigenmodes via tapered ridges/walls are needed to efficiently design components such as the horns presented herein. In the absence of such relationships, design and development of these components have traditionally been based on numerical analysis.

3.2 Numerical Design Approach

While desired aperture mode coefficients can be computed in a relatively straight-forward fashion as explained in the previous chapter, finding the geometry to realize the necessary aperture modes is difficult and can only be done by trial and error numerical design. Numerical electromagnetic analysis of antennas spanning multi-octave bandwidths, on the other hand, usually requires long simulation times. In order to accelerate this process and facilitate unattended operation, an extensive software setup was established early in this research. A number of scripts were written in MATLAB to communicate with the electromagnetic solver CST Microwave Studio (MWS) [48] via Matlab's COM and CST's Visual Basic interfaces, in addition to performing computations such as those in Chapter 2. Figure 3.1 shows a flow diagram of the optimization algorithm.

The quad-ridged horn geometry is represented in MATLAB by approximately 15 parameters, the most important of which are shown in Figure 3.2. The first step in the optimization is to provide the initial set of parameters defining the QRFH geometry, the frequency range of interest, and the subtended angle to the primary (secondary) reflector. While not shown in the flow chart of Figure 3.1, the user also selects at this point the subset of parameters to be used in the optimization routine and defines a range for each such that the optimization is carried out within this range.

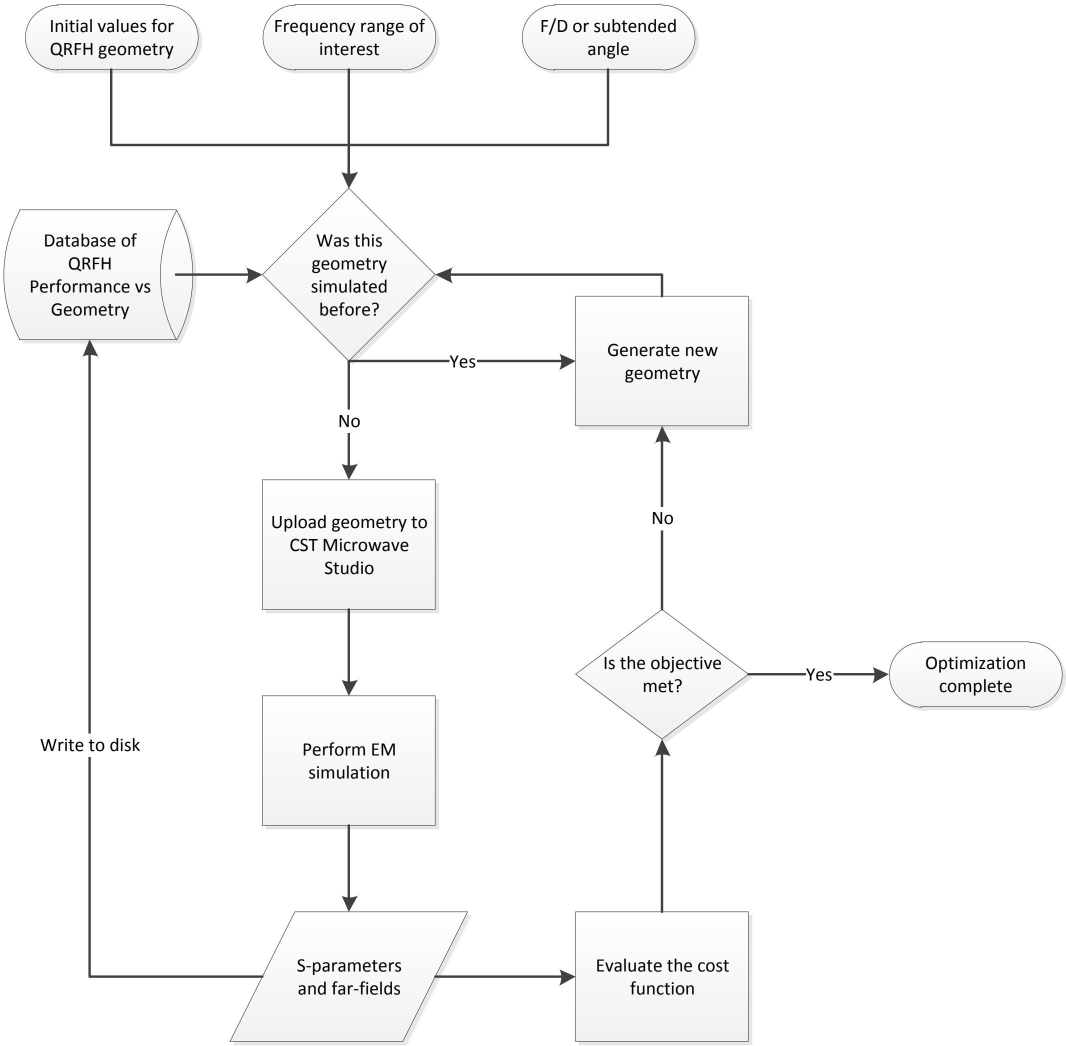

Figure 3.1: The optimization algorithm used for QRFH design. All the steps except "Perform EM simulation" are executed in MATLAB.

The software then checks the existing database to ensure the initial QRFH geometry input by the user has not been simulated previously. If the geometry has been simulated previously, a new set of parameters are generated so that each simulated geometry is unique. Once a unique parameter set is found, the geometry is uploaded to CST MWS and the EM simulation is started. Upon completion of the simulation, MATLAB commands CST to write scattering parameters and far-field patterns to disk for archiving.

The data set is also simultaneously read into MATLAB to calculate the optimization cost function. The cost function involves the input reflection coefficient, aperture efficiency, and ratio of power in the main beam of a $\cos^q$ pattern of a given edge taper to that of the simulated patterns. The input reflection coefficient error is represented by three terms. First, define the return loss and standing-wave ratio errors as, respectively,

$$\Gamma_{err}\left(f_i\right) = 20\log_{10}\left|\Gamma_{sim}\left(f_i\right)\right| + 10 \tag{3.1}$$

$$SWR_{err}\left(f_i\right) = SWR_{sim}\left(f_i\right) - 2 \tag{3.2}$$

where $\Gamma_{sim}\left(f_i\right)$ and $SWR_{sim}\left(f_i\right)$ are, respectively, the simulated reflection coefficient and standing-wave ratio as a function of discrete frequency f_i; and the +10 and -2 terms on the right-hand sides are because the return loss optimization goal is ≥ 10 dB (equivalent to $SWR \approx 2$). These errors are stored in vector format in MATLAB and all the negative error terms are discarded. Then, the three terms in the cost function proportional to the reflection coefficient are

$$\begin{aligned}
\Gamma_{err-mean} &= \frac{1}{N}\sum_{i=1}^{N}\Gamma_{err}\left(f_i\right) && (3.3)\\
\Gamma_{err-max} &= \max\left[\Gamma_{err}\left(f_i\right)\right] && (3.4)\\
\mathbf{SWR_{err}} &= SWR_{err}\left(f_i\right)\ \text{for } i = 1, \ldots, M && (3.5)
\end{aligned}$$

where the index M is usually much less than N, the total number of frequency points at which the scattering parameters are calculated. The point of this last term is to increase error weights at the low-frequency end of the QRFH band, which is where the QRFH becomes close to cutoff and return loss rapidly approaches 0 dB ($\Rightarrow SWR \to \infty$). The aperture efficiency is calculated per the equations in Section 2.2 and the aperture efficiency error is given as

$$\boldsymbol{\eta}_{\mathbf{err}}\left(f_i\right) = 55\% - 100 \times \eta_{sim}\left(f_i\right) \tag{3.6}$$

where η_{sim} is calculated as described in Section 2.2 and discrete frequency f_i represents the frequencies at which the radiation patterns are calculated (usually much fewer than number of frequency points used in scattering parameter simulation). The final error term in the cost function compares the simulated radiation patterns to the ideal $\cos^q$ pattern in the E- and H-planes. The user defines the desired edge taper, ET, at the half subtended angle θ_s and from this, the $\cos^q$ pattern is easily obtained

$$g\left(\theta\right) = \cos^q\theta \text{ with } q = \frac{ET}{20\log_{10}\left(\cos\theta_s\right)}. \tag{3.7}$$

This pattern is then integrated to get the "total power" and compared with the integral of the simulated patterns in the E- and H-planes, namely

$$\mathbf{PWR_{err-E}} = \frac{\int_0^{\frac{\pi}{2}} E_{sim}\left(\theta\right)|_{\phi=0^\circ}\sin\theta d\theta}{\int_0^{\frac{\pi}{2}} g\left(\theta\right)\sin\theta d\theta} \tag{3.8}$$

$$\mathbf{PWR_{err-H}} = \frac{\int_0^{\frac{\pi}{2}} E_{sim}\left(\theta\right)|_{\phi=90^\circ}\sin\theta d\theta}{\int_0^{\frac{\pi}{2}} g\left(\theta\right)\sin\theta d\theta} \tag{3.9}$$

The purpose of these terms is to ensure that not only the simulated edge taper approaches the desired value, but also to avoid nulls and large ripples in the main beam. The final cost vector is then given by

$$C = \begin{bmatrix} \Gamma_{err-mean} \\ \Gamma_{err-max} \\ \mathbf{SWR_{err}} \\ \boldsymbol{\eta}_{\mathbf{err}} \\ \mathbf{PWR_{err-E}} \\ \mathbf{PWR_{err-H}} \end{bmatrix}$$

where bold-face indicates vector quantities dependent on frequency. Once the cost function is evaluated, MATLAB resumes the optimization until design objectives are met.

Three built-in MATLAB optimization routines have been used in this research, namely `lsqnonlin`, `GlobalSearch`, `simulannealbnd`. The first is the default non-linear least-squares optimizer in MATLAB. It has the advantage of estimating Jacobian of the cost function with respect to the optimization variables thereby learning to predict how a given change in one parameter will affect the cost function. Its biggest disadvantage, however, is that it can easily converge to and get stuck in a local minima, which severely limited its use in this research. The last two routines are part of Matlab's global optimization toolbox. The most time was spent using the simulated annealing algorithm. Its rate of convergence is very slow; however, it automatically restarts the optimizer with a randomly generated parameter set after a prescribed number of iterations. This results in better coverage of the parameter space and has yielded the most number of useful QRFH geometries.

This automated software configuration, combined with a dedicated workstation with a graphics processing unit (GPU), has enabled tremendous decrease in simulation times and facilitated compilation of an extensive database of quad-ridged horn performance as a function of geometric parameters

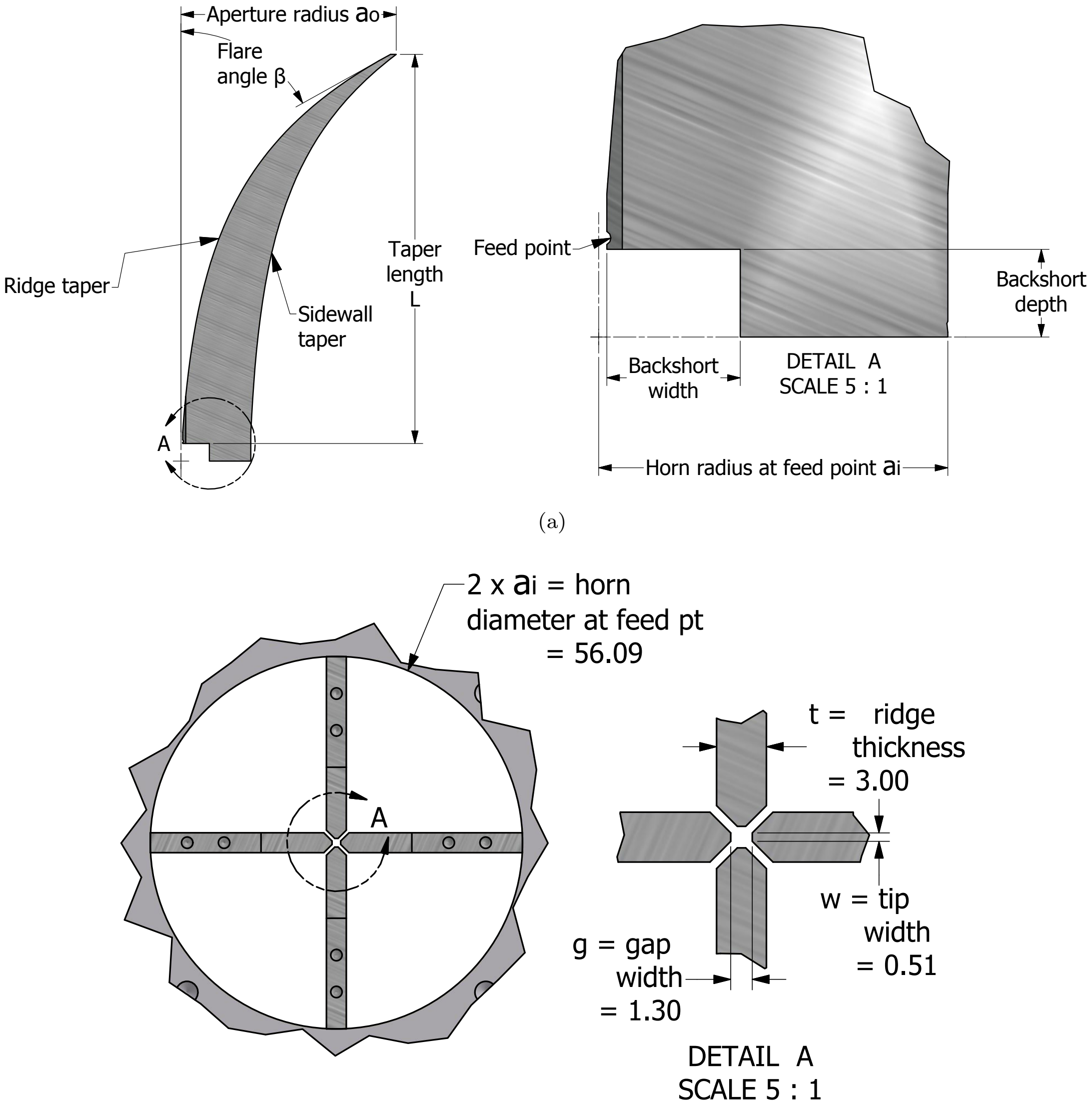

(a)

(b)

Figure 3.2: (a) Ridge side view, (b) view from the bottom looking up. Dimensions in (b) are in millimeters and are the actual dimensions of the first QRFH built. Coordinates of the ridge and horn profiles of this QRFH (the medium gain QRFH) are provided in Appendix A

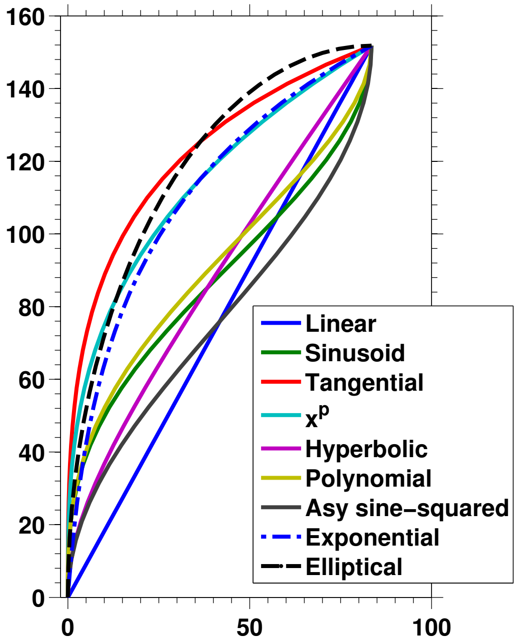

Figure 3.3: Plots of the profiles listed in Table 3.1.

(with more than 15000 different geometrical configurations and counting). While such an extensive database is costly in terms of storage space, the archived results are frequently re-evaluated using different criteria, cost functions, etc., serving as excellent baselines for new QRFH designs.

3.3 The QRFH Design: A Qualitative Look

While there are many parameters defining the quadruple-ridge horn geometry, designing a quad-ridge horn with a prescribed beamwidth reduces to proper selection of the ridge and sidewall profiles. The optimal ridge/wall profile combination is the one that achieves:

1. Circular radiation pattern with the desired 10 dB beamwidth over the frequency range of interest, and

2. Smooth impedance transformation between 50 Ohm and free-space impedance.

While majority of the prior work on double- and quadruple-ridged horns focuses on exponential and elliptical profiles for both ridges and sidewall, we have investigated many other profiles in this research, most of which are from corrugated and smooth-wall horn literature [49]. Expressions for all the profiles used in this work and their plots for a typical QRFH geometry are presented in Table 3.1 and Figure 3.3, respectively.

As explained in Section 3.5, obtaining constant beamwidth from a circular aperture necessitates an aperture field distribution that shrinks in area as frequency is increased (see Figure 3.7(a))

Profile name	Expression
Linear	$a\left(z\right)=a_i+\left(a_o-a_i\right)\frac{z}{L}$
Sinusoid	$a\left(z\right)=a_i+\left(a_o-a_i\right)\left[\left(1-A\right)\frac{z}{L}+A\sin^p\left(\frac{\pi z}{2L}\right)\right]$
Tangential	$a\left(z\right)=a_i+\left(a_o-a_i\right)\left[\left(1-A\right)\frac{z}{L}+A\tan^p\left(\frac{\pi z}{4L}\right)\right]$
x^p	$a\left(z\right)=a_i+\left(a_o-a_i\right)\left[\left(1-A\right)\frac{z}{L}+A\left(\frac{z}{L}\right)^p\right]$
Hyperbolic	$a\left(z\right)=\sqrt{a_i^2+\frac{z^2\left(a_o^2-a_i^2\right)}{L^2}}$
Polynomial	$a\left(z\right)=a_i+\left(p+1\right)\left(a_o-a_i\right)\left(1-\frac{pz}{(p+1)L}\right)\left(\frac{z}{L}\right)^p$
Asymmetric sine-squared	$a\left(z\right)=\begin{cases}a_i+\frac{2(a_o-a_i)}{1+\gamma}\sin^2\left(\frac{\pi z}{4L_1}\right) & 0\leq z\leq L_1\\ a_i+\frac{2(a_o-a_i)}{1+\gamma}\left[\gamma\sin^2\left(\frac{\pi(z+L_2-L_1)}{4L_2}\right)+\frac{1-\gamma}{2}\right] & L_1\leq z\leq L\end{cases}$ where $L=L_1+L_2$ and $\gamma=\frac{L_2}{L_1}$
Exponential	$a\left(z\right)=\left(1-A\right)\left[a_i+\left(a_o-a_i\right)\frac{z}{L}\right]+A\left(c_1e^{Rz}+c_2\right)$ where $c_1=\frac{a_o-a_i}{e^{RL}-1},\ c_2=\frac{a_ie^{RL}-a_o}{e^{RL}-1}.$
Elliptical	$x = a_o+r_1\cos\theta\cos\phi-r_2\sin\theta\sin\phi$ $z = r_1\cos\theta\sin\phi+r_2\sin\theta\sin\phi$ where $r_1=\max\left(a_o,\,L\right),\ r_2=\min\left(a_o,\,L\right),\ \phi=\begin{cases}0, & a_o>L\\ \pi/2, & \text{else}\end{cases}$

Table 3.1: Profile options considered in this work. All profiles except the exponential and elliptical are from [49]; the exponential profile is a modified version of the one in [50]. a_i and a_o are the radii at the feed point and horn aperture, respectively; L is the taper length; R is the exponential opening rate; p is the exponent of sinusoid, polynomial, x^p, and $\tan^p$ profiles and can take on values in the range $\left[0,\infty\right]$; A is a parameter between $\left[0,1\right]$ that determines how much linear taper is added.

assuming uniform phase at the aperture. Figure 3.4(a) presents $|E_x|$ (left) and $\angle E_x$ (right) at the aperture of the first QRFH at 1, 2, 3.5, 5, and 6 f_{lo}. It is immediately observed that the aperture field magnitude distribution in the horizontal plane (plane of the excited polarization) is quite constant over the 6:1 frequency range (field distribution in the vertical plane shows more variability). In contrast, $|E_x|$ and $\angle E_x$ of an identical horn but without the ridges display significant variability both in terms of amplitude and phase distributions as shown in Figure 3.4(b).

Figure 3.4(a) reveals that in the case of the quad-ridge horn, it is the aperture area with uniform phase that is shrinking as frequency is increased. This is attained predominantly by the ridge profile. Specifically, difference in path lengths along the horn's longitudinal axis and along the ridge profile introduces additional phase to fields near the aperture rim. The additional phase accrued increases as frequency is increased which results in the reduced aperture area with uniform phase. This is very similar to smooth-wall and corrugated horns which are sometimes referred to as flare-angle limited horns. The flare angle for the QRFH geometry is defined in Figure 3.2(a) and primarily determines the beamwidth of the horn in $\phi = 0^\circ$ and 45° planes. To illustrate this point, two sets of simulations are carried out which use the design of the first built QRFH (see Section 4.4) as baseline. This quad-ridge horn employs exponential ridge and sidewall tapers with the functional form given in Table 3.1.

In the first case, the exponential opening rate, R of Table 3.1, is varied $\pm 40\%$ with respect to the as-built value of R_0, thereby changing the flare angle. Fig. 3.5(a) shows the simulated ridge profiles with all other parameters fixed. 10 dB beamwidths in $\phi = 0$, 45, 90 degree planes at a constant frequency of 5 GHz are plotted in Fig. 3.5(c). Strong dependence of beamwidth on flare angle is noted in the $\phi = 0$, 45 degree planes. H-plane beamwidth shows markedly weaker dependence.

For the second set of simulations, aperture diameter of the quad-ridge horn is swept from -20% to $+40\%$ of the as-built value, D_0, while maintaining identical flare angles, which requires scaling of horn's taper length. Resulting profiles are depicted in Fig. 3.5(b) and Fig. 3.5(d) plots 10 dB beamwidths and lowest useable frequency which show that aperture size has only a secondary effect on both.

While the flare angle—or more generally, the ridge profile—determines the nominal beamwidth of the horn, the ridges serve another important purpose. Namely, they enable multi-octave-bandwidth operation by lowering cutoff frequency of the dominant waveguide mode. The parameters defining the geometry near the bottom of the horn, shown in 3.2(b), are critical for achieving such wideband operation, and are:

1. horn radius at the throat;
2. ridge-to-ridge gap width g;
3. ridge thickness t;

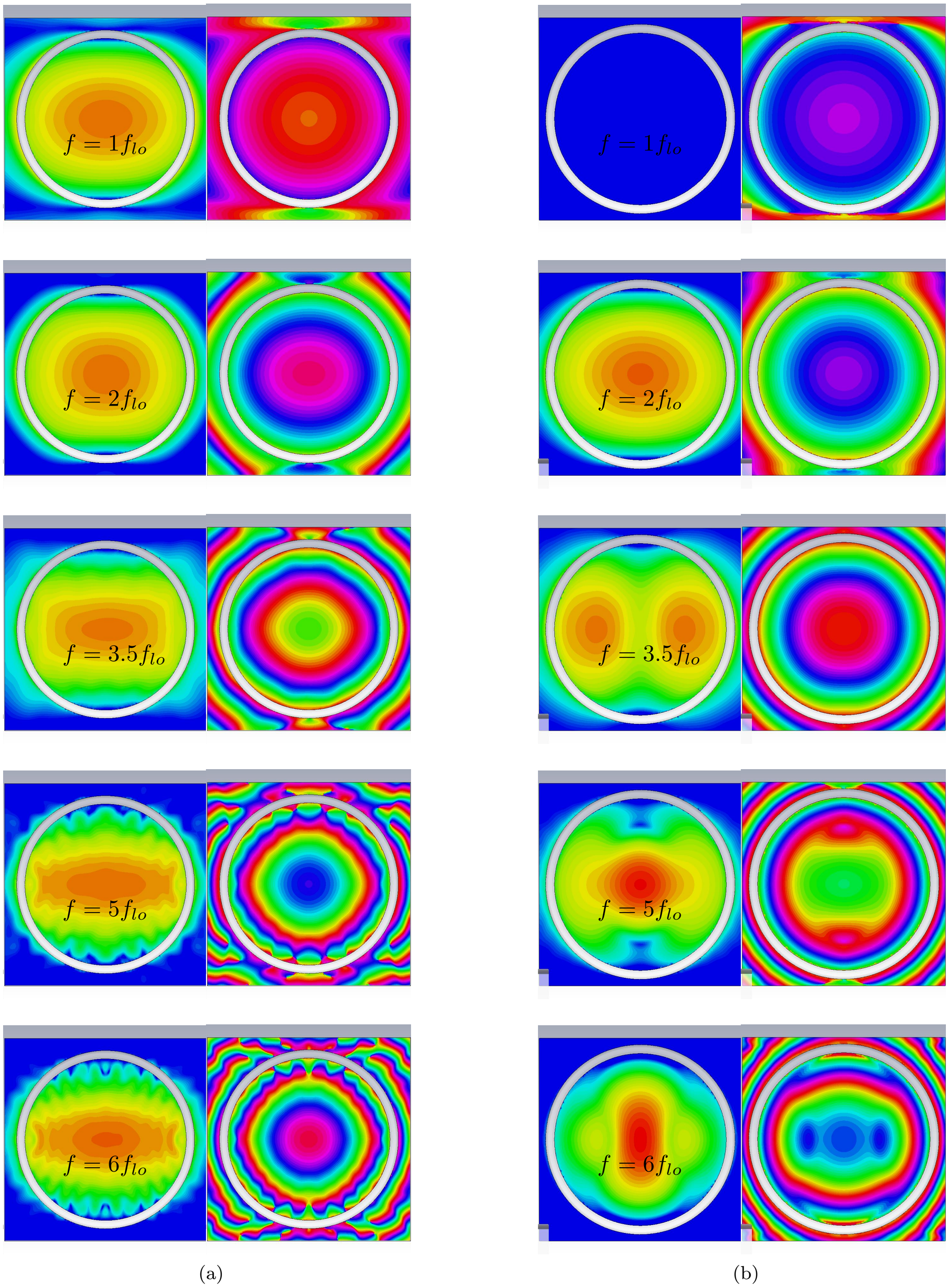

Figure 3.4: x-directed aperture fields of (a) the medium gain QRFH of Section 4.4, (b) identical horn but without the ridges. Magnitude is plotted on the left and phase on the right for both (a) and (b). All plots are on the same scale.

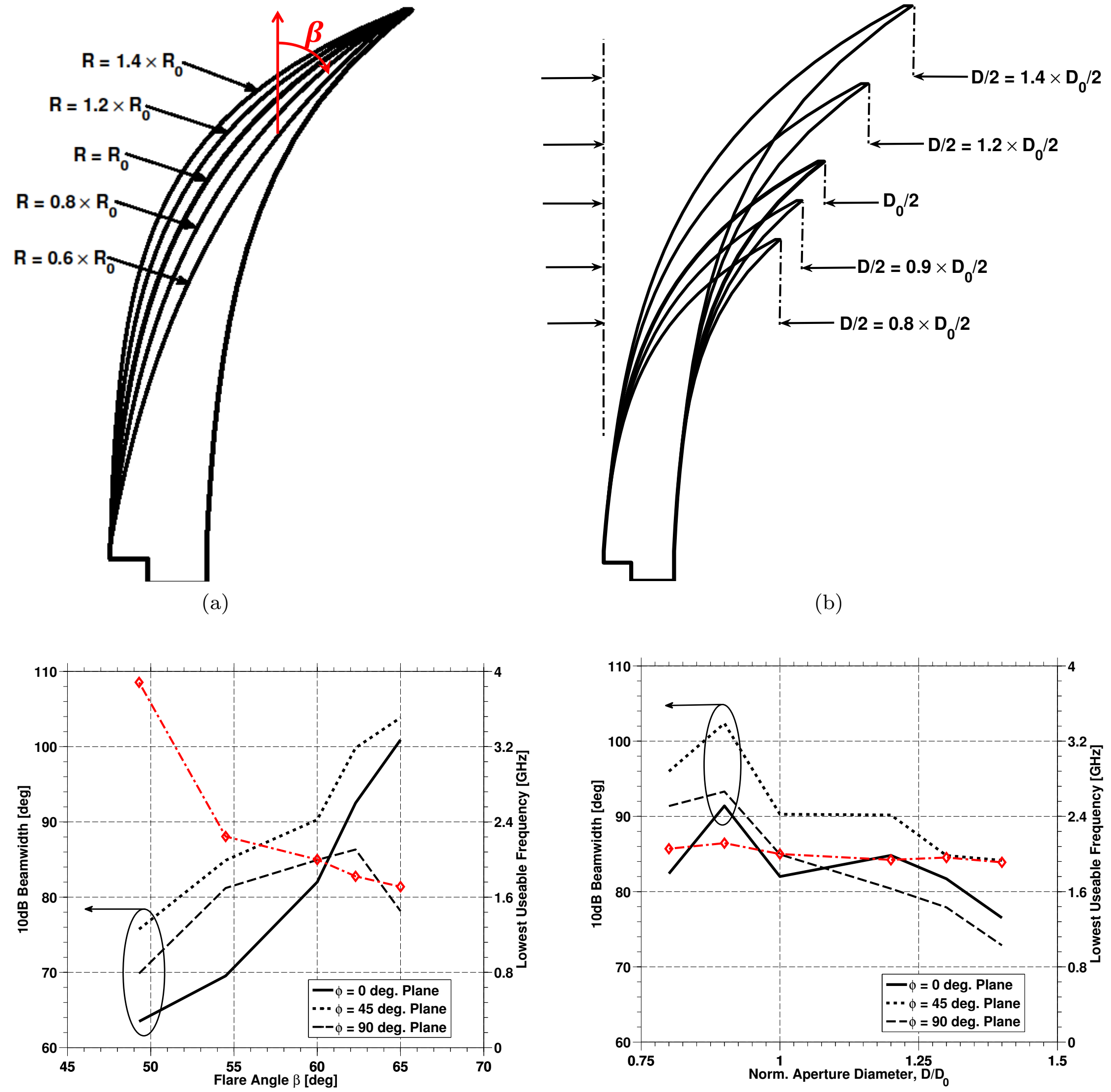

(a) (b)

(c) (d)

Figure 3.5: Side view of the ridge as: (a) exponential opening rate is swept from -40% to +40% of the baseline value R_0, (b) aperture diameter is swept from -20% to +40% of the baseline value D_0; 10 dB beamwidth in $\phi = 0$, 45, 90 degree planes (at a constant frequency of 5 GHz) and lowest useable frequency as a function of: (c) the exponential opening rate of the ridge, (d) the aperture diameter. $\phi = 0$, 45, 90 curves are plotted using, respectively, solid, dash-dotted and dashed lines. Dash-dotted curve with diamond markers is lowest useable frequency below which the quad-ridge horn is cutoff. The flare angle β is shown in part (a).

4. ridge tip width w

where the last three are not independent. As shown in [42], heavily loaded ridges, namely $g \rightarrow 0$, lower cutoff frequency of the dominant mode by as much as factor of four. For example, cutoff frequency of the dominant mode in a circular waveguide of radius 27.395 millimeters (as-built radius of the medium gain QRFH of Section 4.4) is 3.21 GHz whereas the cutoff frequency of the dominant mode in the same waveguide but with heavily loaded ridges is computed numerically to be 0.85 GHz. Comparing the top plots in Figure 3.4(a) and (b) also underline this fact, which show that in the absence of the ridges, the horn is below cutoff at 2 GHz. Increasing ridge thickness also reduces the dominant mode cutoff frequency, but its impact is much less pronounced.

Another consideration in selecting the ridge and sidewall profiles is that the ridge-to-ridge gap must be small enough at any cross section along the horn's longitudinal axis to ensure propagation of the dominant mode in the desired frequency range. The dominant mode cutoff frequency is a strong function of gap width implying the cutoff frequency increase due to a small increase in the gap width can only be offset by a larger change in the sidewall radius. This, in turn, makes the horn prone to unwanted higher-order mode excitation. For example, the lowest useable frequency of Figure 3.5(c) does not approach the cutoff frequency in the throat, namely 0.85 GHz, because the dominant mode is below cutoff further up in the horn due to ridge-to-ridge gap increasing rapidly. In summary, horn radius at the throat, gap width g and the ridge profile are critical in determining the lowest useable frequency of the horn.

The gap width, in conjunction with the ridge thickness, also establishes the nominal input impedance of the horn. Smaller gap width translates to lower input impedance and vice versa. Same effect can also be obtained by increasing the ridge thickness. This suggests that not only tip-to-tip gap width is critical but also the gap between adjacent ridges (along the chamfered edges) which, to a large extent, is controlled by the gap width. This is because thicker ridges—or smaller gap width—implies larger shunt capacitance.

3.4 Fabrication Considerations

The quad-ridge horns built to date have been built in pieces using a numerically controlled milling machine. The base of the horn (i.e. around the feed point) is the most critical part in terms of tolerances on dimensions, locations and orientations of the ridges. The gap width and ridge-to-ridge distance along the chamfered edges (see Figure 3.2(b)) are the primary factors determining input impedance, and proper location and orientation of ridges are of utmost importance to avoid unwanted higher-order mode excitations due to asymmetry.

The feed point of the QRFH is inherently asymmetric due to different diameter holes in two opposing ridges; however, this asymmetry is very minor and does not excite higher-order modes.

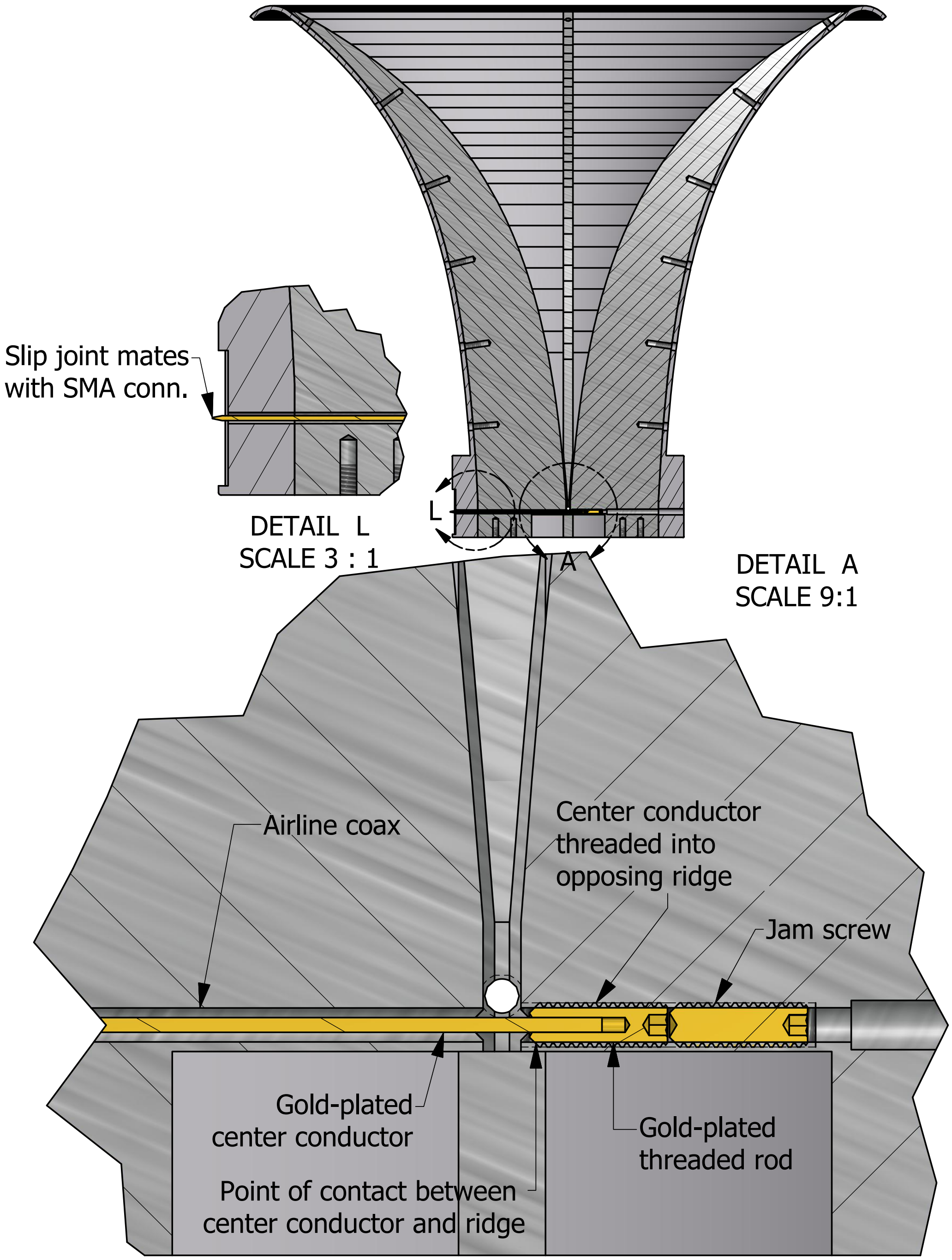

Figure 3.6: Detailed view of input coax center conductor connection with opposing ridge. The other two ridges and sidewall are not shown in Detail A for clarity.

If, on the other hand, the ridge location and orientation is not properly set, it would have a direct impact on the mode content due to the changing boundary conditions in the horn.

While numerically controlled parts facilitate keeping of tolerances, the fact that ridges are bolted onto the sidewall and difficulty of drilling ridge mounting holes at precise locations suggest that another method be used to constrain the ridge orientation and location. Two mounting holes per ridge on the flat bottom plate and guiding pins are used to keep the ridges at the proper locations. Ridge-to-sidewall as well as ridge-to-backplate mounting holes are shown in Figure 3.6.

A low-loss coaxial air line through one ridge with center conductor connected to the opposite ridge is used to form a balun and excite the ridge waveguide at the base of the horn. The connection of the center conductor of this air line to the opposite ridge is quite critical. This could be accomplished with a pin socket for the center conductor but a more positive contact was selected which also allows some adjustment of the contact point. An accurate 0.508 mm diameter gold-plated gage pin is press-fit into a short 0-80 threaded stud which screws into a threaded hole through the opposite ridge. A set screw from the back of the ridge is then utilized to lock the thread of the center conductor. The input end of the center conductor plugs into a well-formed socket of a commercial SMA connector with a slip joint to accommodate tolerances and differential thermal expansion of center conductor and horn body. A small degree of tuning of the feed return loss is accomplished by turning the threaded rod to adjust the contact point in the opposite ridge. These details are provided in the bottom half of Figure 3.6. It is also worth noting that because coaxial line of the second polarization is physically above the first one, there is inherently a slight performance difference between two ports.

3.5 Aperture Mode Content

Before proceeding to example QRFH designs of the next chapter, a method for calculating TE and TM mode coefficients required at a circular aperture to achieve given radiation patterns is presented. This procedure is based on [29] and is used in the next chapter to evaluate aperture mode content of the quad-ridged horns.

The approach relies on the fact that far-field patterns of all hollow circular waveguide modes are expressed in closed form [29, 51]. Neglecting reflections at the aperture, the far-field patterns of transverse-electric mode TE_{mn} are

$$E_{\theta,mn}^{TE} = -a_{mn}\, j^m m J_m\left(X'_{mn}\right)\frac{J_m\left(ka\sin\theta\right)}{ka\sin\theta}\cos m\phi\;\Psi\left(\theta\right) \tag{3.10}$$

$$E_{\phi,mn}^{TE} = a_{mn}\, j^m X'^2_{mn} J_m\left(X'_{mn}\right)\frac{J'_m\left(ka\sin\theta\right)}{X'^2_{mn}-\left(ka\sin\theta\right)^2}\sin m\phi\;\Psi\left(\theta\right) \tag{3.11}$$

and those of the transverse-magnetic mode TM_{mn} are

$$E_{\theta,mn}^{TM} = b_{mn}\, j^m X_{mn} J_m' \left(X_{mn}\right) \frac{ka \sin\theta J_m \left(ka \sin\theta\right)}{X_{mn}^2 - \left(ka \sin\theta\right)^2} \cos m\phi \; \Psi\left(\theta\right) \tag{3.12}$$

where

$$\begin{aligned}
\Psi\left(\theta\right) &= \frac{ka^2}{2}\left(1+\cos\theta\right)\frac{e^{-jkR}}{R} \\
k &= \frac{2\pi}{\lambda} \\
\lambda &= \text{Wavelength} \\
a &= \text{Waveguide aperture radius} \\
R &= \text{Far-field radius} \\
X_{mn} &= n\text{th zero of } J_m\left(x\right) \\
X_{mn}' &= n\text{th zero of } J_m'\left(x\right),
\end{aligned}$$

$m \in [0,\infty]$, $n \in [1,\infty]$; a_{mn} and b_{mn} are complex amplitude coefficients of the TE and TM modes, respectively. These equations underline an important feature. Specifically, ϕ-directed far-fields are determined only by the TE modes, and the shape of the θ-directed far-fields of the TE modes depend on m but not on n. This implies that, for a given m, the ϕ-component of the radiation patterns can be synthesized entirely from TE modes, and then the θ-component may be synthesized from TM modes without affecting the former.

Consequently, an arbitrary radiation pattern $f\left(\theta,\phi\right)$ can be written as a sum of patterns of each mode, i.e.,

$$\begin{aligned}
f\left(u,\phi\right) = \frac{1+\sqrt{1-\left(\frac{u}{ka}\right)^2}}{2} & \left\{ \sum_{\substack{m=0\\n=1}}^{M,N} \left[A_{mn}\frac{mJ_m\left(u\right)}{X_{mn}'^2 u} - B_{mn}\frac{uJ_m\left(u\right)}{u^2-X_{mn}^2}\right]\cos m\phi\;\hat{\theta} \right. \\
& \left. + \left[A_{mn}\frac{J_m'\left(u\right)}{u^2-X_{mn}'^2}\right]\sin m\phi\;\hat{\phi}\right\}
\end{aligned} \tag{3.13}$$

where

$$\begin{aligned}
A_{mn} &= -a_{mn} j^m k J_m\left(X_{mn}'\right) X_{mn}'^2 a^2 \\
B_{mn} &= b_{mn} j^m k J_m'\left(X_{mn}\right) X_{mn} a^2 \\
u &= ka\sin\theta
\end{aligned} \tag{3.14}$$

After some algebra and using orthogonality of sine and cosine, the final expressions for the complex

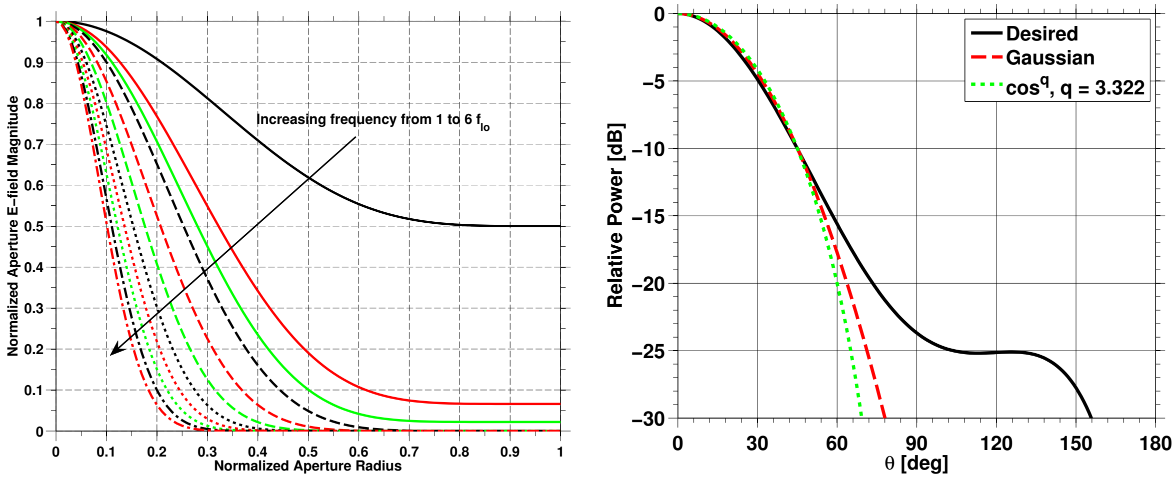

(a) (b)

Figure 3.7: (a) Aperture distributions as a function of frequency and (b) the resultant far-field patterns (black) in addition to Gaussian (red dashed) and $\cos^q$ (green dotted) radiation patterns. 10 dB beamwidth is 90 degrees.

mode coefficients are found to be [29]

$$A_{pq} = \frac{2}{1+\sqrt{1-\left(\frac{X'_{pq}}{ka}\right)^2}} \frac{2X'_{pq}}{\pi J''_p\left(X'_{pq}\right)} \int_0^{2\pi} f_\phi\left(X'_{pq},\phi\right)\sin p\phi d\phi. \tag{3.15}$$

$$B_{pq} = \frac{2}{1+\sqrt{1-\left(\frac{X_{pq}}{ka}\right)^2}} \frac{2}{\pi J_{p+1}\left(X_{pq}\right)} \int_0^{2\pi} f_\theta\left(X_{pq},\phi\right)\cos p\phi d\phi \tag{3.16}$$

which demonstrates that the TE and TM coefficients are in fact independent, as alluded to earlier.

Before proceeding into calculation of mode coefficients of an "ideal" radiation pattern, it is worthwhile to make a few observations. First, the summation in (3.13) is finite so long as the aperture is of finite extent and wavelength is greater than zero, because only modes above cutoff at the aperture can contribute to far-field radiation patterns, and for a given aperture size, number of such modes is always finite. Secondly, fits to the desired radiation pattern obtained through this approach are necessarily approximate, because the fitting is performed at a set of discrete points, namely $u = X_{pq}$ for the θ-component and $u = X'_{pq}$ for the ϕ-component.

Another important observation from these equations is that the radiation patterns of individual modes reach their maxima near the points $u = X_{mn}$ and $u = X'_{mn}$ for TM_{mn} and TE_{mn} modes, respectively. This implies that for a fixed aperture size, adding more modes broadens the radiation pattern. Conversely, using more modes necessitates a larger aperture to maintain constant beamwidth [29]. However, phase errors in the horn aperture can significantly degrade performance

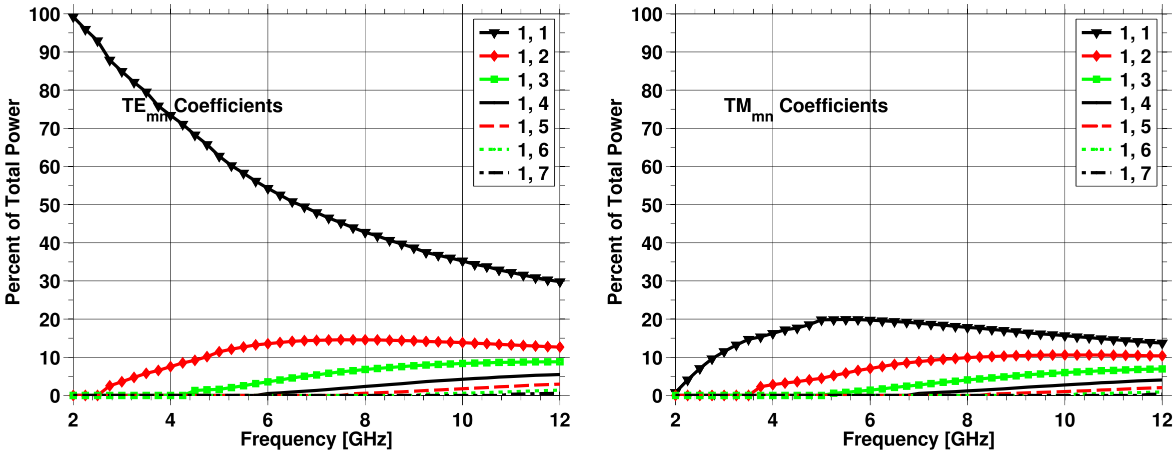

(a) (b)

Figure 3.8: (a) TE and (b) TM modes required at a circular aperture of radius $a = 0.6\lambda_{lo}$ to achieve the desired far-field pattern of Figure 3.7 from 1 to 6 f_{lo}. Mode coefficients are normalized such that total power in all modes at a given frequency sums to 1.

for large apertures. This is the reason it is more difficult to design octave-band corrugated horns with wide beamwidths. The same holds for quadruple-ridged horns as demonstrated in Chapter 4.

Equations (3.15) and (3.16) are now used to calculate the necessary modes at an aperture with radius $0.6\lambda_{lo}$ to achieve circularly symmetric radiation pattern with 10 dB beamwidth of 90 degrees. Figure 3.7(a) shows the aperture distributions required to achieve far-field patterns with 90 degree beamwidth over 6:1 frequency band which are calculated using the results in [27, 52]. The far-field pattern obtained from these distributions are plotted in part (b) of the same figure in black along with Gaussian and $\cos^q$ patterns yielding the same beamwidth.

The mode coefficient computations are performed in MATLAB [53] and the results are provided graphically in Figure 3.8. A subset of the results are also listed in Table 3.2. As expected, the TE_{11} mode is the dominant mode throughout the frequency range; however, its relative power decreases monotonically with frequency. The next three most significant modes are TM_{11}, TE_{12}, and TM_{12}. This observation, as well as the relative power content in each mode, is in good agreement with the power distribution in an optimum four-mode horn [29].

The requirement of circular symmetry in the radiation patterns necessitates far-field patterns exhibiting the following azimuthal dependence[1]

$$f(u,\phi) \propto V_\theta(u)\cos\phi\hat{\theta} + V_\phi(u)\sin\phi\hat{\phi}. \tag{3.17}$$

As observed from (3.13), such patterns are attained with only $m = 1$ modes at the aperture. The results of Figure 3.8, where only $m = 1$ modes are present, confirm this point. Lack of even-order

---

[1] This is the "optimum" far-field pattern of Ludwig [29].

Mode	Frequency			
	$1f_{lo}$	$3f_{lo}$	$4.5f_{lo}$	$6f_{lo}$
TE_{11}	1.0000	1.0000	1.0000	1.0000
TM_{11}	0.0878	0.6027	0.6580	0.6789
TE_{12}	0	0.4996	0.6079	0.6517
TM_{12}	0	0.3605	0.5190	0.5897
TE_{13}	0	0.2556	0.4480	0.5440
TM_{13}	0	0.1595	0.3645	0.4828
TE_{14}	0	0.0949	0.2941	0.4289
TM_{14}	0	0	0.2248	0.3687
TE_{15}	0	0	0.1693	0.3155
TM_{15}	0	0	0.1209	0.2619
TE_{16}	0	0	0	0.2159
TM_{16}	0	0	0	0.1728
TE_{17}	0	0	0	0.1372
TM_{17}	0	0	0	0.1058

Table 3.2: Amplitudes of TE and TM modes, normalized to that of TE_{11}, required to realize the desired radiation pattern of Figure 3.7 with a circular aperture of radius $a = 0.6\lambda_{lo}$. All modes are in phase with TE_{11}.

modes, e.g. $m = 0, 2, 4, \cdots$, is due to perfect two-fold symmetry of the aperture field distribution. Moreover, the curves in this figure reinforce the earlier point on the need to have more modes at the aperture to maintain large beamwidth and circular beam as aperture size grows in terms of wavelength.

We conclude this section by highlighting the inherent assumptions in the above development. One of these assumptions, neglecting reflections at the aperture, has already been mentioned. More importantly, this development also approximates the guide wavelength at the aperture with the free-space wavelength. This is certainly not true for the example calculation presented in Figure 3.8 at the low end of the frequency band where, for instance, the aperture diameter is only $1.2\lambda_{lo}$. On the other hand, it is a fairly good assumption in the upper half of the frequency band for the first three or four modes. It is possible to address both of these assumptions by modifying equations (3.10-3.12) as outlined in [51]. This, however, is not pursued, because the increase in accuracy gained from such an exercise is thought to be small, especially when the aperture mode calculation is applied to circular quadruple-ridged horns as is done in Chapter 4.

Chapter 4

Example Designs

The flexibility to design the QRFH for varying nominal 10 dB beamwidths through proper choice of ridge/wall profiles has made it a very attractive radio telescope feed antenna in the two years since the first QRFH was built. Its appeal is further increased because it is:

1. currently the only ultra-wideband feed that requires one single-ended 50 Ohm LNA per polarization;
2. the easiest to scale for operation in different frequency bands;
3. very stable and repeatable structurally. It can be accurately and cheaply machined from aluminum;
4. inherently low loss because of no dielectrics and relatively low current density with no thin metal surfaces.

As a result, there has been ample interest in quad-ridge horns designed at Caltech. Table 4.1 lists status of all the QRFH designs built to date in addition to those that are currently in discussion. Figure 4.1 displays this list in a more visual format.

Majority of today's cm-wave radio telescopes have f-numbers (f/D ratios) between 0.3 and 0.5 at primary, because low f-numbers yield more compact telescope designs. On the other hand, there are some notable secondary focus antennas with high f/D such as the Green Bank Telescope, the 65 meter antenna at Shanghai Astronomical Observatory, and NASA's Deep Space Network antennas[1].

In this chapter, simulated—and, where available, measured—performance of five QRFH antennas are presented. The designs are selected to demonstrate the suitability of the quad-ridge horn in telescopes with f-numbers from 0.3 to 2.5. Measured system performance of a radio telescope with one of the quad-ridge designs presented herein is also provided while predicted system performance curves are included for the remaining designs. A square QRFH design is demonstrated which is very

---

[1] Deep Space Network antennas are technically not radio telescopes, but they are sometimes used for radio astronomy.

Table 4.1: List of QRFH antennas delivered to telescopes around the world as well as those currently in discussion. The designs that are in bold print are presented herein.

Telescope	Primary Diam. [m]	QRFH 10 dB beamwidth [deg]	Frequency range [GHz]	Feed Diam & Length [cm]	Operated by	Status	See Section
NASA Goddard	**12**	**90**	**2-12**	**18 x 16.4**	**MIT Haystack Observatory**	**On telescope**	**4.4**
Westford	**18.3**	**140**	**2.3-14**	**14.3 x 11.9**	**MIT Haystack Observatory**	**On telescope**	**4.6**
Effelsberg	100	140	0.6-2.5	74.6 x 35	Max Planck Institute for Radio Astronomy	On telescope	
Caltech	6	150	0.6-3	72.6 x 32	Caltech	On telescope	
Japanese VLBI	**13.2**	**120**	**2.3-14**	**20 x 13.4**	**Geospatial Information Authority of Japan**	**Shipped**	**4.5**
Caltech OVRO	27	120	1-6 and 3-18	12.4 x 5.7 (3-18)	Caltech OVRO	In fabrication	
Haystack VLBI	N/A	120	2.3-14	20 x 13.4	MIT Haystack Observatory	Under test	
Shanghai VLBI	N/A	120	2.3-14	20 x 13.4	Shanghai Astronomical Observatory	Under test	
Deep Space Network	**70**	**30**	**0.5-3.5**	**230 x 401**	**NASA/JPL**	**In discussion**	**4.2**
Shanghai	65	30	4-28?	TBD	Shanghai Astronomical Observatory	In discussion	
Australian VLBI	N/A	90	2.3-14	TBD	CSIRO	In discussion	
GAVRT	**34**	**65**	**0.7-4.9**	**82 x 73.2**	**Lewis Center for Educational Research/Caltech**	**On hold**	**4.3**

Map data ©2013 MapLink, Tele Atlas -

Figure 4.1: A world map showing locations of the quad-ridge flared horns delivered to date (red place marks) and those that are in discussion phase (yellow place marks). The map was generated using Google Maps.

attractive for low-frequency operation due to relative ease of fabrication. Additionally, TE and TM mode coefficients at the aperture of the first three quad-ridge horns are presented.

The first section describes the antenna far-field measurement setup used for the QRFH measurements. The subsequent sections detail the five QRFH designs and are arranged in ascending order of nominal beamwidth. Target applications for these horns can be found in Table 4.1. Figure 4.2 compares profiles of the five horns which underscores the relationship between flare angle and nominal beamwidth. All results of this chapter, except measured and predicted system performance curves, are scaled such that the lowest frequency of operation, f_{lo}, of all quad-ridge horns is identical and relative bandwidths are used instead of absolute ones.

4.1 Pattern Measurement Setup

The radiation patterns of the quad-ridge horns were measured using a far-field pattern measurement setup on the roof of the electrical engineering building at California Institute of Technology. Figure 4.3 displays a photo and the block diagram of the far-field range. Obstacles on the roof limit the accuracy of the patterns to the -25 dB level; however, this is sufficient to determine the main beam, the first side lobes and performance in a reflector system.

Both co- and cross-polarized radiation patterns are measured in three azimuthal planes, namely ϕ = 0, 45, and 90 degrees, for θ = [-180, 180] degrees with one degree steps in the main beam.

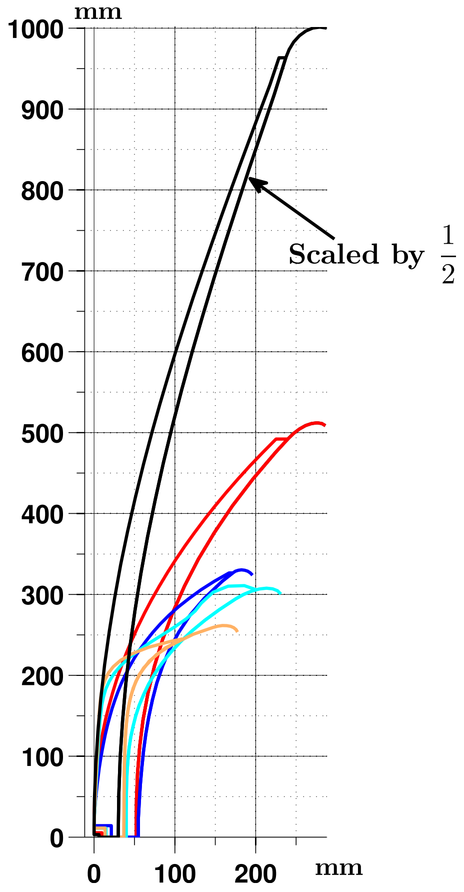

Figure 4.2: Profiles of the very high (black), high (red), medium (blue), low (cyan), and very low (orange) gain quad-ridge designs. All profiles are scaled such that their lowest frequency of operation f_{lo} is 1 GHz. Dimensions are in millimeters

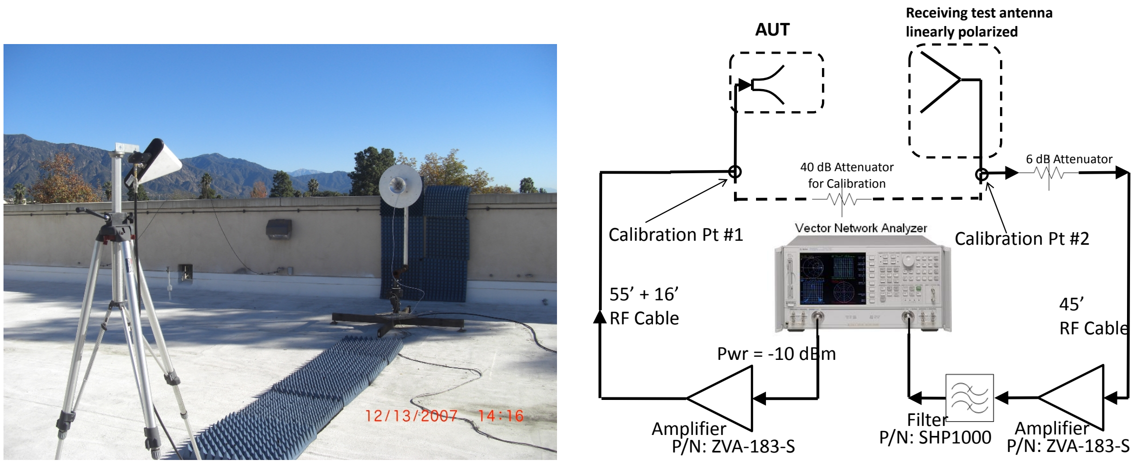

(a) (b)

Figure 4.3: (a) Photo and (b) block diagram of the pattern measurement setup on the roof of Moore Laboratory at California Institute of Technology.

The far-field range is designed to work between 1 and 18 GHz. It is limited at the low end by very strong RFI as a result of which a high-pass filter with 1 GHz cutoff frequency is used for most of the measurements presented here. Maximum frequency of the receiving antenna, a broadband log-periodic dipole, is 18 GHz and determines the upper frequency of the pattern range.

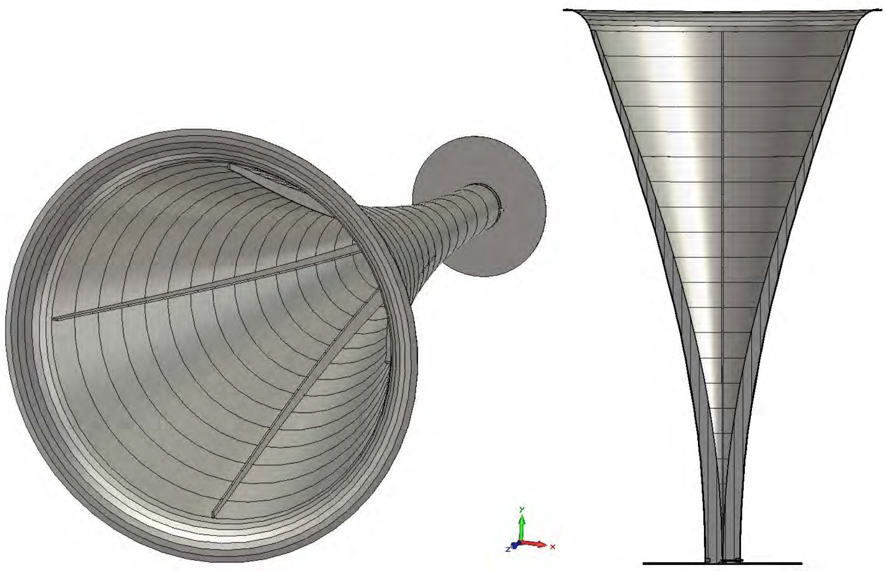

Figure 4.4: Three-dimensional CAD drawings of the very high gain quad-ridge horn. Feed diameter is 230 cm ($3.83\lambda_{lo}$) and length is 400.5 cm ($6.68\lambda_{lo}$) with $f_{lo} = 0.5$ GHz

4.2 Very-High Gain QRFH

Of the quad-ridge horns presented herein, this QRFH has undergone the least amount of optimization mainly because the interest in such high gain, wideband horns has been considerably less in the radio astronomy community. However, as this design and the next show, the high-gain quad-ridge designs achieve 7:1 bandwidths and perform as well as, if not better than, the lower gain designs.

4.2.1 Application

The intended application of the very high gain quad-ridge horn is as a low-frequency feed, primarily for pulsar timing experiments, on the 70 meter DSS-14 antenna located at the Goldstone Deep Space Communication Complex near Barstow, California. DSS-14 comprises of two mirrors in Cassegrain configuration and the feed antennas are located at the vertex of the primary mirror. The full subtended angle to the secondary reflector is 32 degrees ($f/D = 1.78$).

4.2.2 Simulations

The nominal 10 dB beamwidth of this feed is 30-32 degrees which yields somewhat high edge taper; however, the horn size becomes prohibitively large for narrower beamwidths. The ridge and sidewall tapers use the asymmetric sine-squared profile of Table 3.1. This is the largest quad-ridge horn designed as part of this research with an aperture diameter of approximately $3.3\lambda_{lo}$ and length of around $6.4\lambda_{lo}$. The flare angle is 19 degrees.

The simulated reflection coefficients of both polarizations are plotted in Figure 4.5 along with

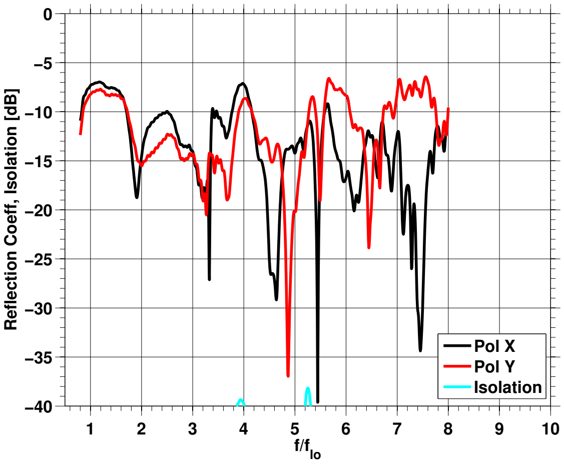

Figure 4.5: Simulated scattering parameters of the very high gain QRFH

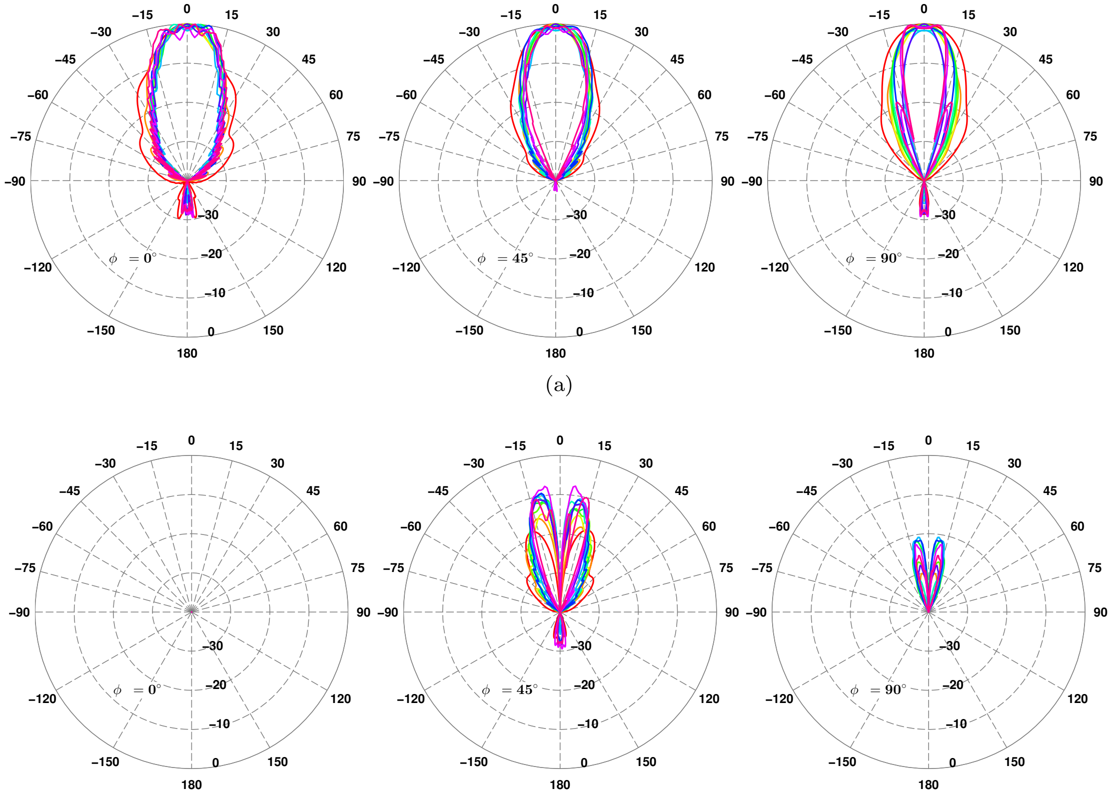

(a)

(b)

Figure 4.6: Simulated (a) co-polarized, (b) cross-polarized (Ludwig 3rd definition) radiation patterns of the very high gain QRFH in $\phi = 0°$, 45°, 90° azimuthal planes over the frequency range $f/f_{lo} =$ [1, 7]

isolation between the two polarizations. The match needs improvement; it is the worst among the QRFH designs presented herein which is mainly due to insufficient optimization.

Figure 4.6 presents polar plots of the co- and cross-polarized radiation patterns (Ludwig's 3rd definition [33]) in the $\phi = 0^\circ\,(E)$, $45^\circ\,(D)$, $90^\circ\,(H)$ planes. The three-dimensional, total far-field patterns are displayed in Figure 4.7. The 10 dB beamwidths in the E- and D-planes are approximately 30 degrees, while the H-plane beamwidth varies between 40 and 20 degrees. There are no visible sidelobes, backlobes are at least 30 dB down from boresight, and the beam is well-formed and shows no splitting over 7:1 frequency range. The cross-polarization in the diagonal plane is better than -10 dB over most of the band, and peaks to about -9 dB over very narrow frequency range.

Intensity plots (function of both phase and magnitude) of x-directed electric field, E_x, in the horn as a function of frequency are presented in Figure 4.8. They reveal that the electric field is more tightly coupled to the ridges all the way up to the aperture for lower frequencies. On the other hand, this coupling becomes looser at higher frequencies. Qualitatively, this could be thought of as radiation beginning further in the horn at higher frequencies. The fields seem to "break up" around 6-7 f_{lo} showing considerable intensity near the ridges, which may be because of reflections due to unwanted mode coupling.

4.2.3 Aperture mode content

The mode coefficients at the aperture of the very high gain QRFH are calculated using the method described in Appendix 3.5. The modes required to generate the desired radiation patterns are also calculated using the same approach. Figure 4.9 presents these normalized mode coefficients where only the first four modes needed for the desired radiation patterns are plotted.

These curves show that the simulated mode content at the aperture comes fairly close to the desired mode distribution; however, better mode control is needed, especially for TM modes. Furthermore, there is fine structure in the simulated coefficients in the middle as well as the upper end of the frequency range. This is believed to be in part due to the limited optimization this design has undergone. The field "break up" around 6–7 f_{lo}, mentioned in the previous subsection, seems to be correlated strongly with decrease in TE_{11} and TM_{11} coefficients while TE_{12} and TE_{13} coefficients become more prominent.

Another observation from these plots is the absence of even-order azimuthal modes, which is an important result that suggests that ridges do not significantly alter the mode conversion expected from a smooth-walled horn with the identical profile. In particular, it was shown in [54] that horn diameter variations can only cause coupling between modes of same azimuthal order.

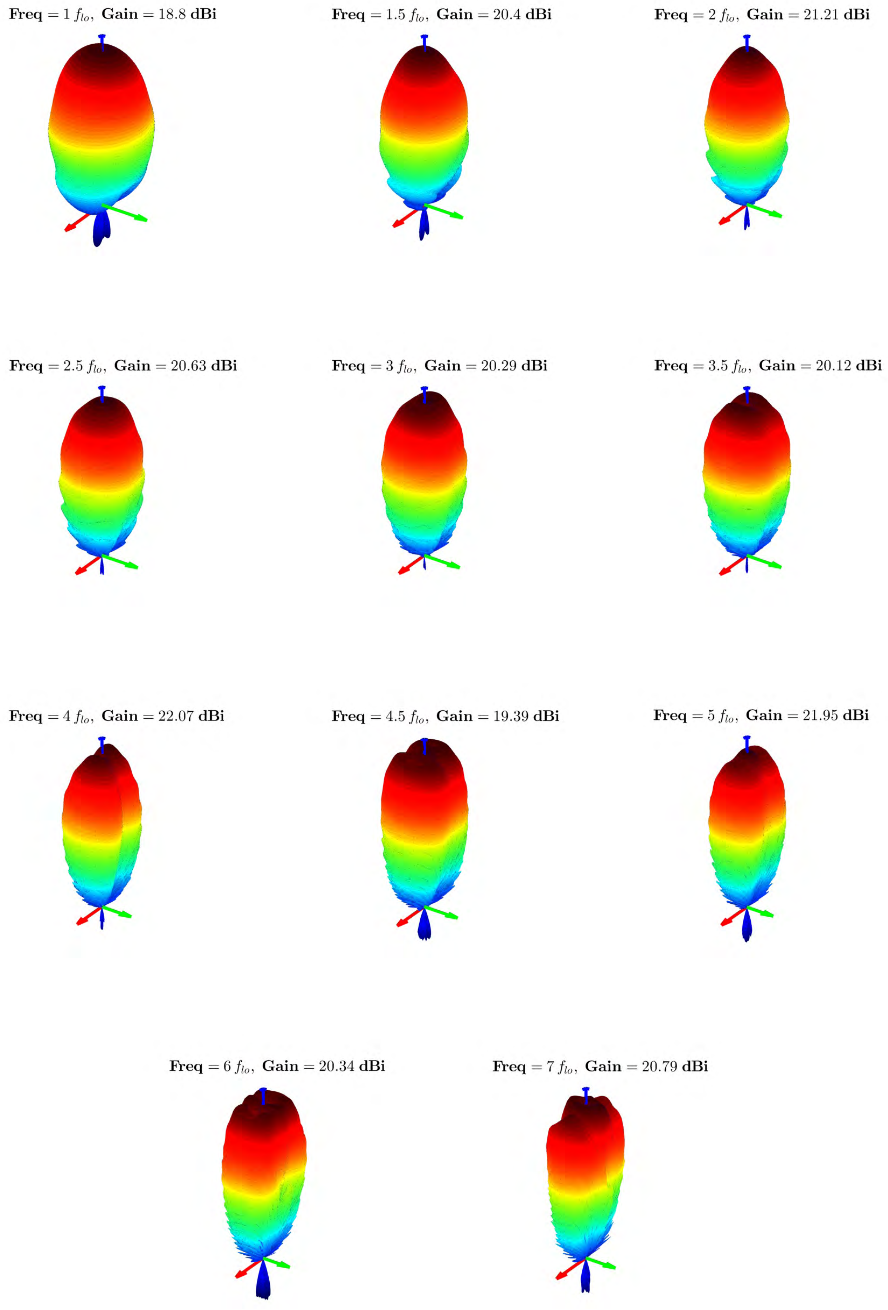

Freq = 1 f_{lo}, **Gain** = 18.8 **dBi**

Freq = 1.5 f_{lo}, **Gain** = 20.4 **dBi**

Freq = 2 f_{lo}, **Gain** = 21.21 **dBi**

Freq = 2.5 f_{lo}, **Gain** = 20.63 **dBi**

Freq = 3 f_{lo}, **Gain** = 20.29 **dBi**

Freq = 3.5 f_{lo}, **Gain** = 20.12 **dBi**

Freq = 4 f_{lo}, **Gain** = 22.07 **dBi**

Freq = 4.5 f_{lo}, **Gain** = 19.39 **dBi**

Freq = 5 f_{lo}, **Gain** = 21.95 **dBi**

Freq = 6 f_{lo}, **Gain** = 20.34 **dBi**

Freq = 7 f_{lo}, **Gain** = 20.79 **dBi**

Figure 4.7: Three dimensional radiation patterns of the very high gain QRFH.

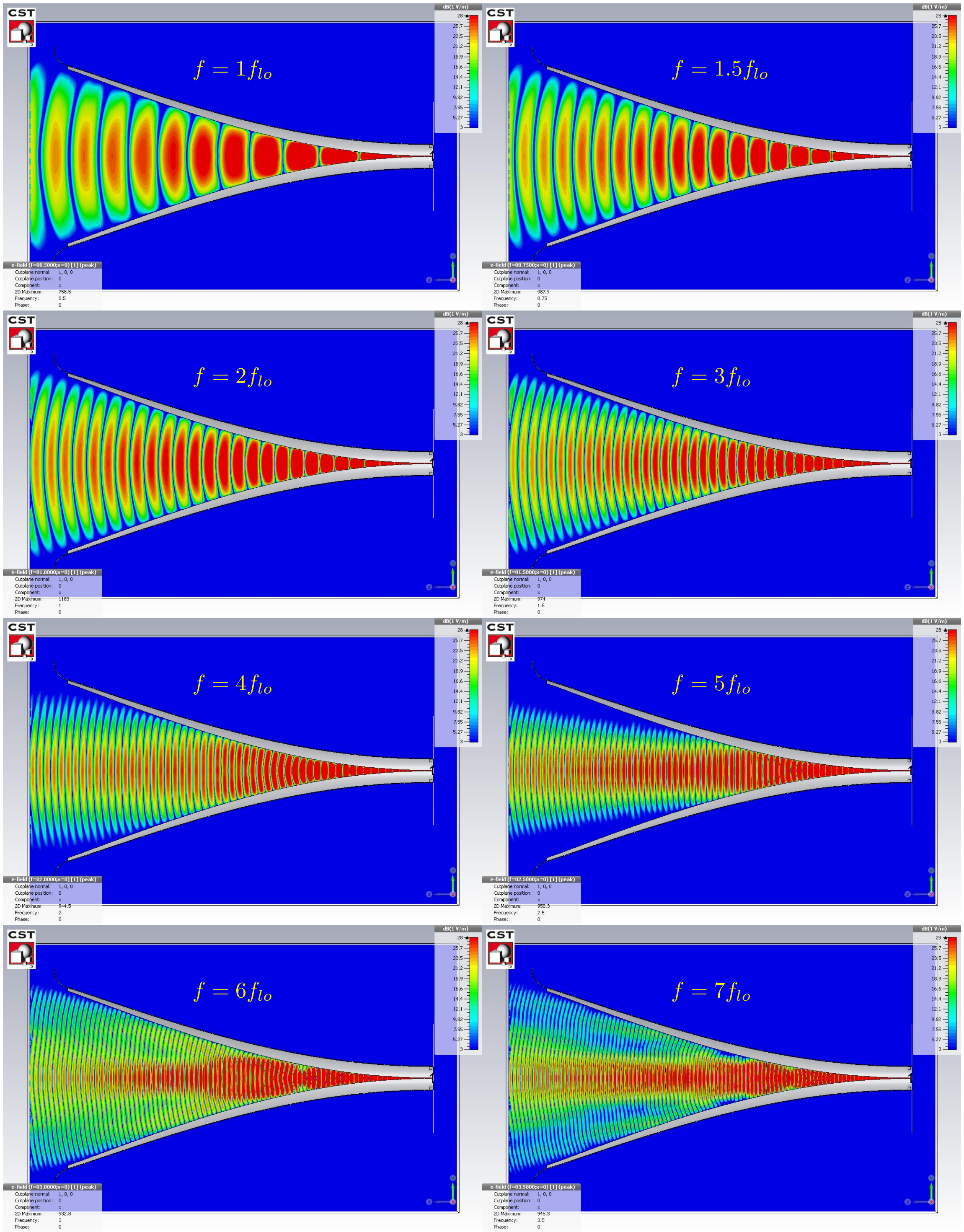

Figure 4.8: Intensity plots of E_x on the $x = 0$ plane in the very high gain quad-ridge horn which is excited in the x-polarization.

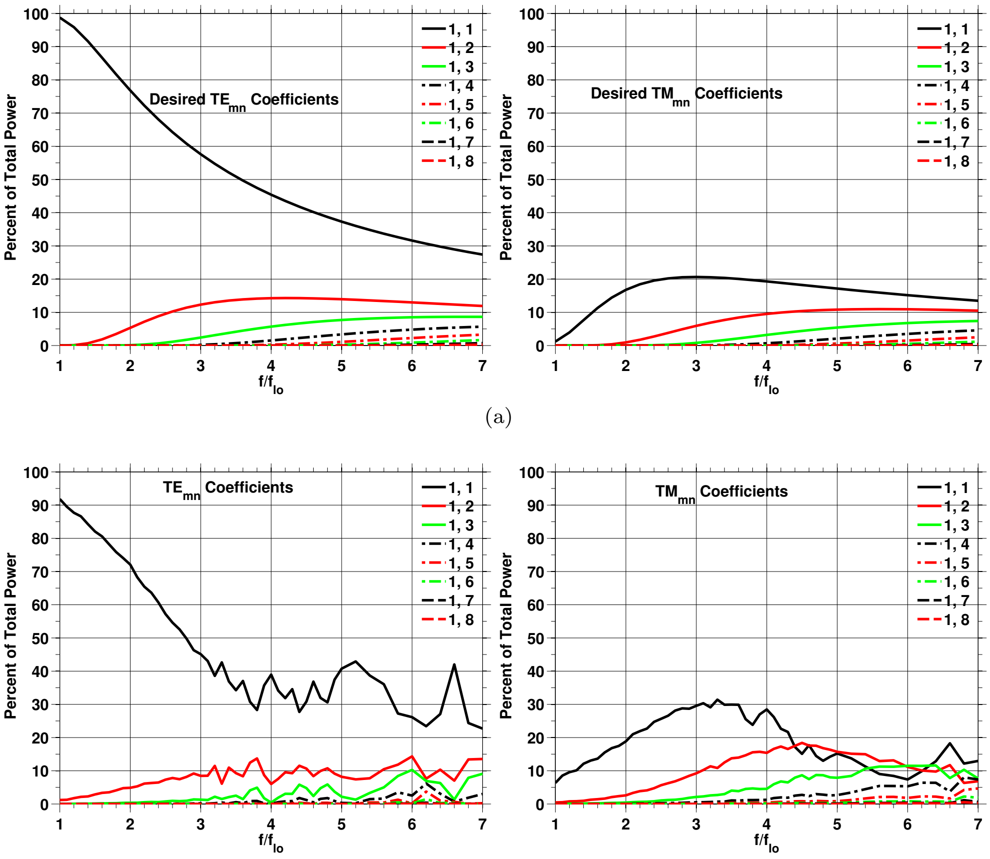

(a)

(b)

Figure 4.9: Normalized mode coefficients (a) required to achieve the desired radiation pattern, (b) at the aperture of the very high gain QRFH calculated using the simulated patterns. While all the modes present in the horn are not plotted, the modes plotted account for well more than 99% of the total power.

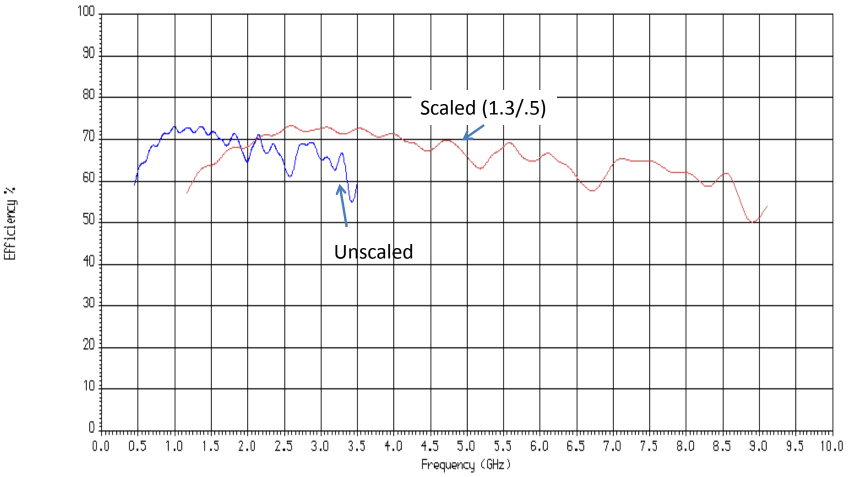

Figure 4.10: Predicted aperture efficiency of the DSS-14 70-meter antenna with the very high gain QRFH as the feed antenna. The efficiency is calculated using physical optics and losses due to RMS surface error, blockage, struts, etc., are ignored.

4.2.4 Predicted system performance

This QRFH was initially designed to cover 0.5 to 3.5 GHz. The PO aperture efficiency of the DSS-14 over this frequency range with the QRFH at the secondary focus appears in Figure 4.10 in blue which is computed with simulated patterns. It is seen that the average efficiency is $> 65\%$ and the efficiency stays above 55% throughout the band. Recently, there has also been interest at a higher frequency version of this horn on the DSS-14, namely f_{lo} of 1.3 GHz. The predicted aperture efficiency of this version is also plotted in the same figure and is slightly lower, but still maintains an average of $\sim$65%. These results suggest that both horns attain 7:1 frequency bandwidth, at least according to simulations.

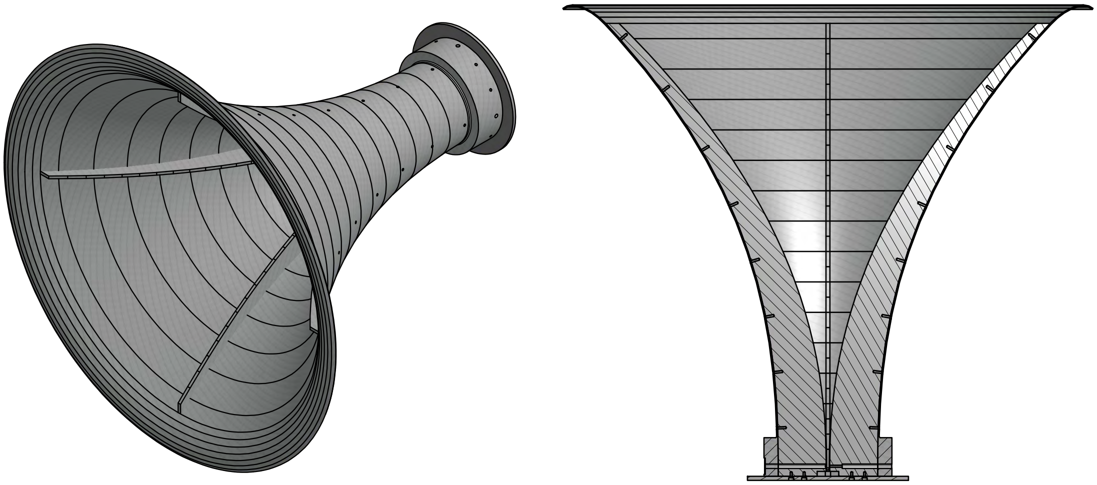

Figure 4.11: Three-dimensional CAD drawings of the high-gain quad-ridge horn. Feed diameter is 82 cm ($1.9\lambda_{lo}$) and length is 73.2 cm ($1.7\lambda_{lo}$) with $f_{lo} = 0.7$ GHz

4.3 High-Gain QRFH

4.3.1 Application

This QRFH was designed to be used as the low-frequency feed of the Goldstone Apple Valley Radio Telescope (GAVRT) [5] for wide bandwidth pulsar timing experiments. The reflector antenna of this telescope is the 34 meter DSS-28 located at the Goldstone Deep Space Communication Complex near Barstow, California. DSS-28 was initially designed for high-power transmission employing two mirrors in Cassegrain configuration and a beam-waveguide feed system [55]. The antenna was then retrofitted with a tertiary paraboloid mirror at the vertex of the dish which enabled focusing of the beam onto a feed mounted on the surface and near the vertex of the dish antenna. The full subtended angle to the tertiary mirror is 81.2 degrees, but due to the unusual optics the telescope aperture efficiency increases with increased edge taper at the tertiary reflector.

4.3.2 Simulations

The nominal 10 dB beamwidth of the quad-ridge horn is selected 65 degrees due to size restrictions near the vertex of the reflector as narrower beamwidths necessitate longer horns with wider apertures (see Figure 4.2). Both the ridge and sidewall tapers of the final design, shown in Figure 4.11, employ the x^p profile. The aperture diameter is $1.69\lambda_{lo}$ and the ridge profile length is $1.64\lambda_{lo}$. The flare angle is approximately 45 degrees.

Figure 4.12 presents the simulated S-parameters of this quad-ridge horn. The simulated reflection coefficient is better than 10 dB across the 7:1 frequency band and better than 15 dB over much of this range. Figure 4.13 displays two-dimensional cuts of the co- and cross-polarized (Ludwig's 3rd

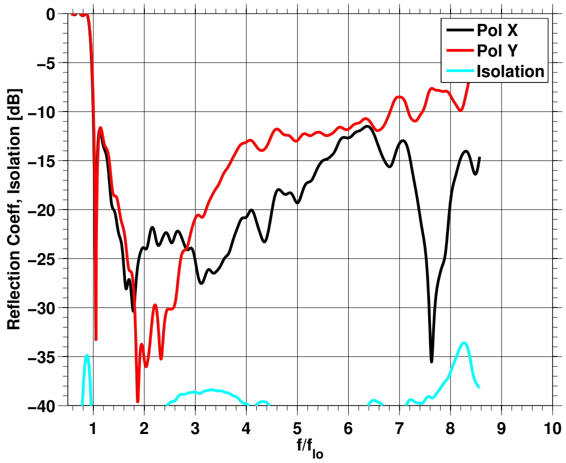

Figure 4.12: Simulated scattering parameters of the high-gain QRFH

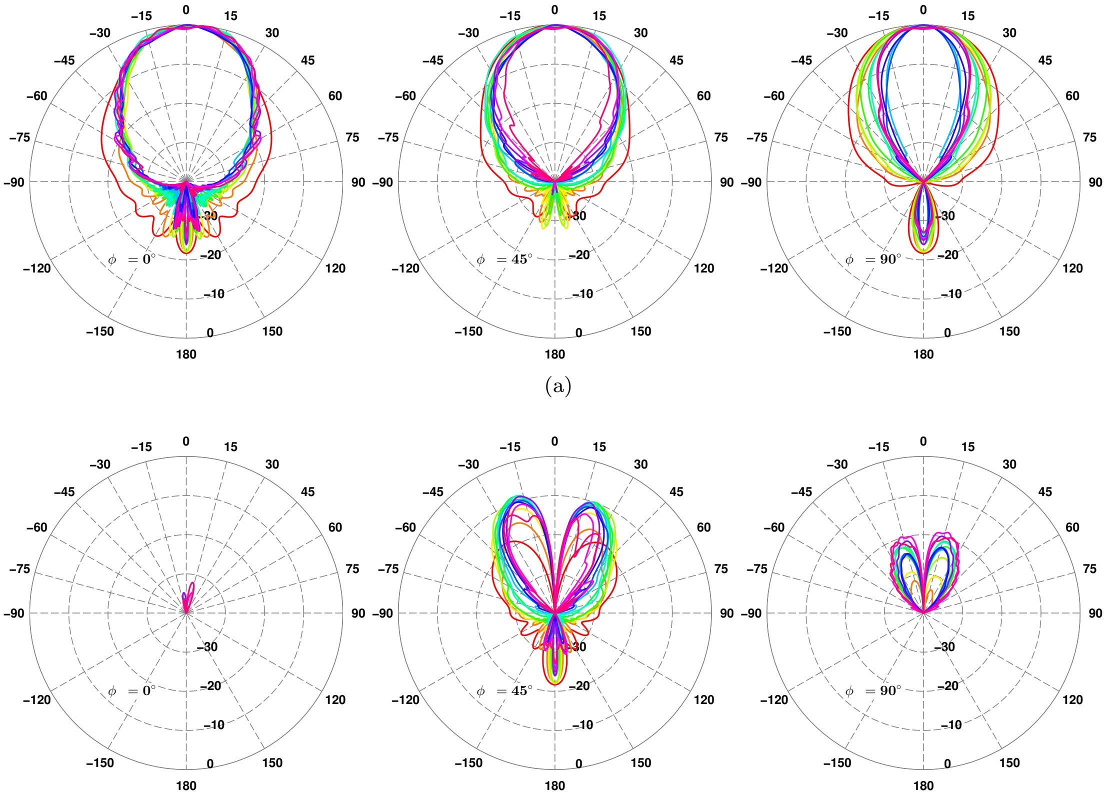

(a)

(b)

Figure 4.13: Simulated (a) co-polarized, (b) cross-polarized (Ludwig 3rd definition) radiation patterns of the high-gain QRFH in $\phi = 0°, 45°, 90°$ azimuthal planes over the frequency range $f/f_{lo} = [1,\ 7]$

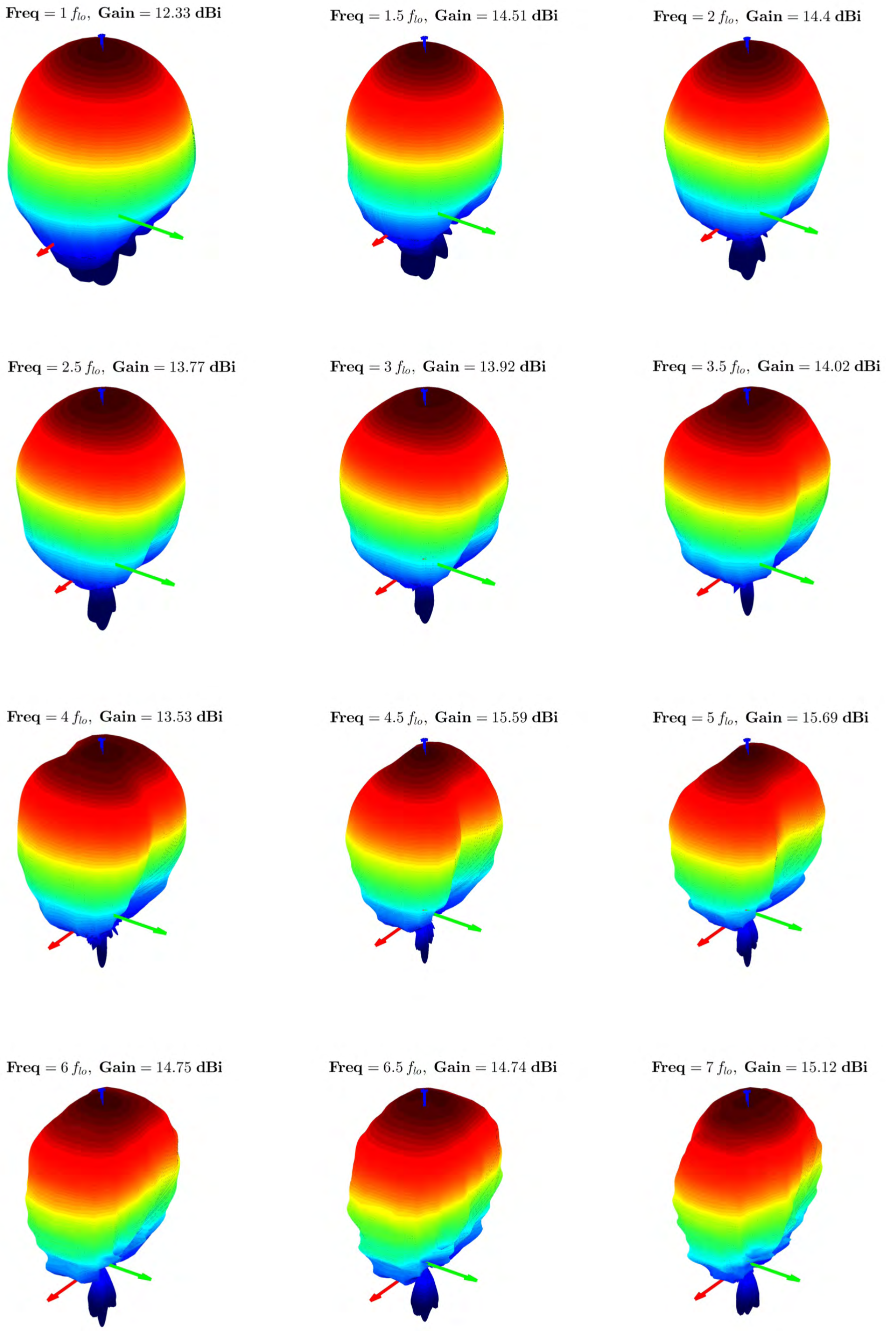

Freq $= 1\ f_{lo}$, **Gain** $= 12.33$ **dBi**

Freq $= 1.5\ f_{lo}$, **Gain** $= 14.51$ **dBi**

Freq $= 2\ f_{lo}$, **Gain** $= 14.4$ **dBi**

Freq $= 2.5\ f_{lo}$, **Gain** $= 13.77$ **dBi**

Freq $= 3\ f_{lo}$, **Gain** $= 13.92$ **dBi**

Freq $= 3.5\ f_{lo}$, **Gain** $= 14.02$ **dBi**

Freq $= 4\ f_{lo}$, **Gain** $= 13.53$ **dBi**

Freq $= 4.5\ f_{lo}$, **Gain** $= 15.59$ **dBi**

Freq $= 5\ f_{lo}$, **Gain** $= 15.69$ **dBi**

Freq $= 6\ f_{lo}$, **Gain** $= 14.75$ **dBi**

Freq $= 6.5\ f_{lo}$, **Gain** $= 14.74$ **dBi**

Freq $= 7\ f_{lo}$, **Gain** $= 15.12$ **dBi**

Figure 4.14: Three-dimensional radiation patterns of the high-gain QRFH

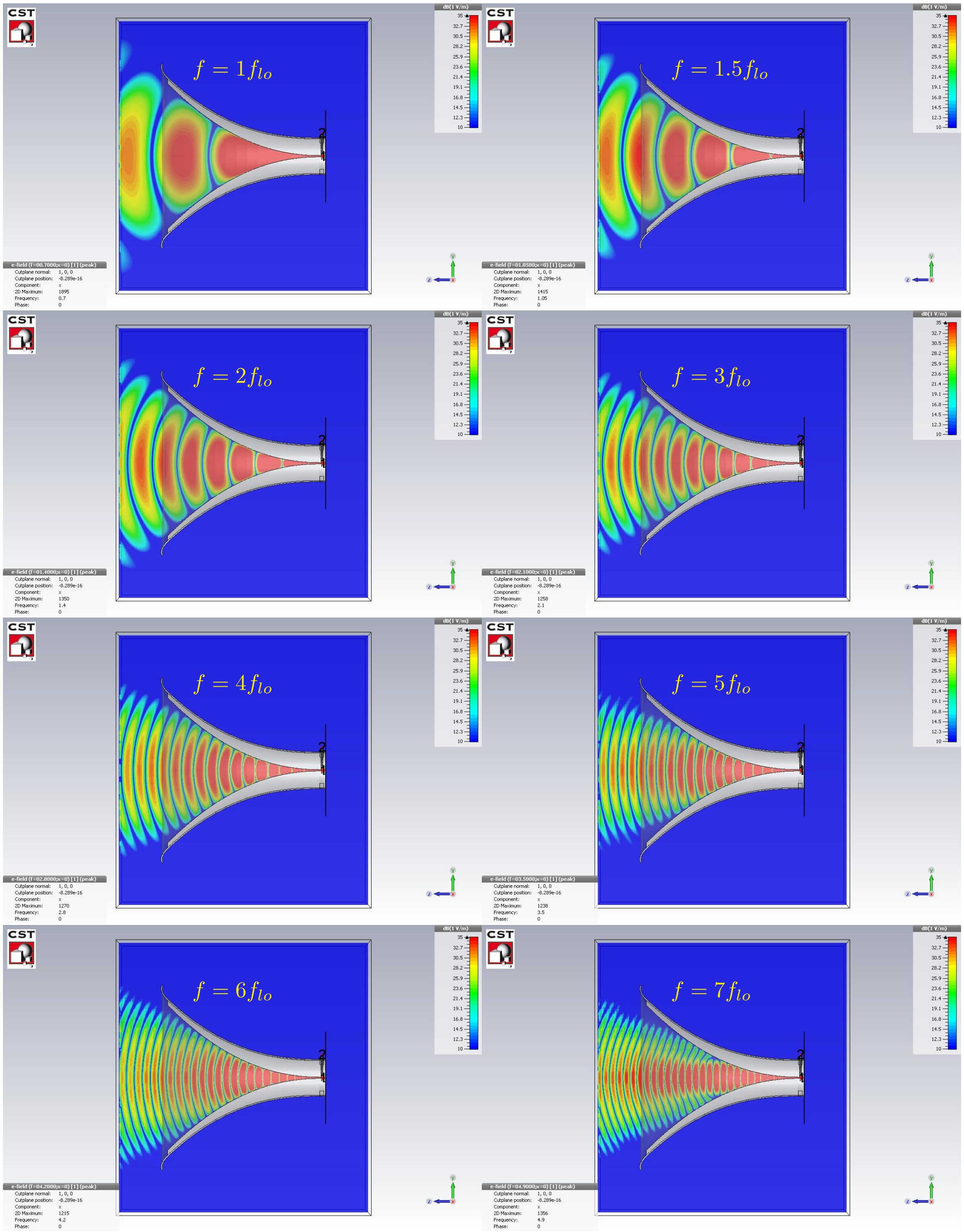

Figure 4.15: Intensity plots of E_x on the $x = 0$ plane in the high-gain quad-ridge horn which is excited in the x-polarization

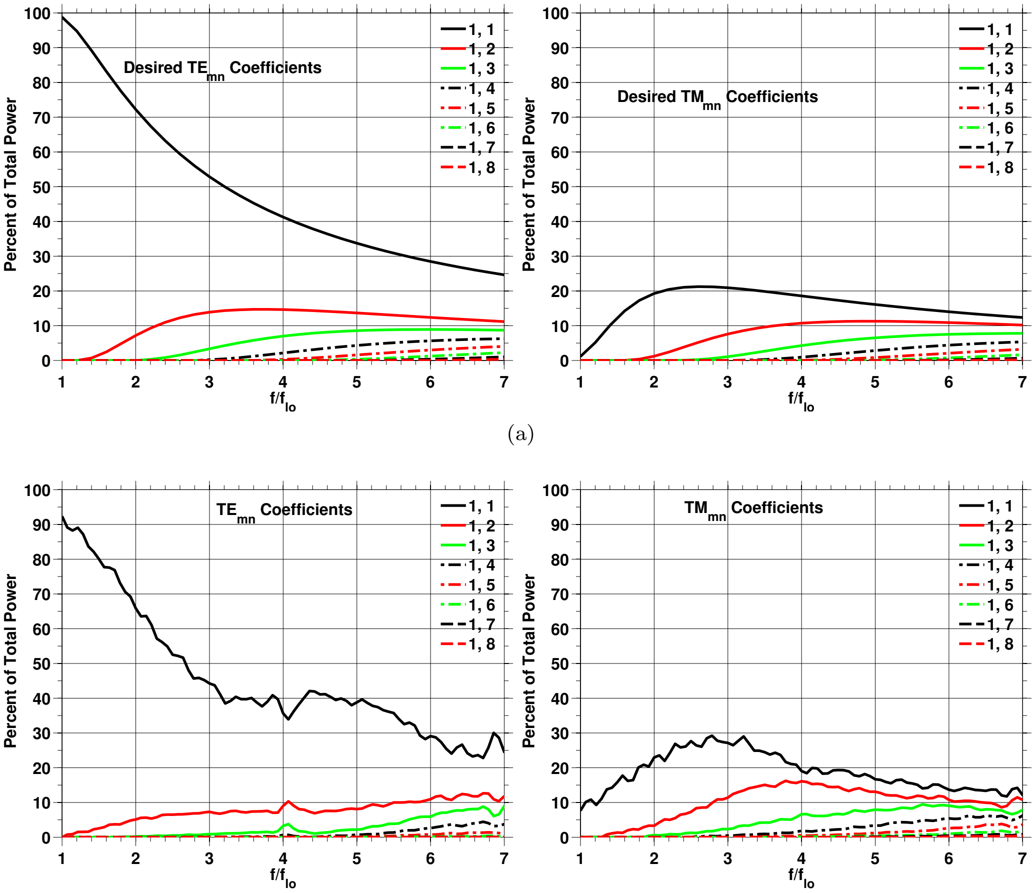

(a)

(b)

Figure 4.16: Normalized mode coefficients (a) required to achieve the desired radiation pattern, (b) at the aperture of the high-gain QRFH calculated using the simulated patterns. While all the modes present in the horn are not plotted, the modes plotted account for well more than 99% of the total power.

definition [33]) far-field patterns in $\phi = 0^\circ$, 45°, 90° planes and the three-dimensional, total radiation patterns are provided in Figure 4.14. The 10 dB beamwidths in E- and D-planes—and the azimuthal planes in between—are on average 65 degrees and the beamwidth stability is good. On the other hand, the H-plane beamwidth decreases from 80 to 40 degrees with increasing frequency resulting in a more elliptical beam at the upper end of the band. The cross-polarization in the D-plane peaks to -9 dB over narrow frequency ranges, and is below -10 dB over much of the band.

The intensity plots of E_x shown in Figure 4.15 once again shows tighter coupling to the ridges at the low end of the frequency band. There is discernible disruption of the fields at $7f_{lo}$ near the middle of the horn that could be due to undesired mode coupling. This could also be correlated with the decreasing return loss predicted by the simulations.

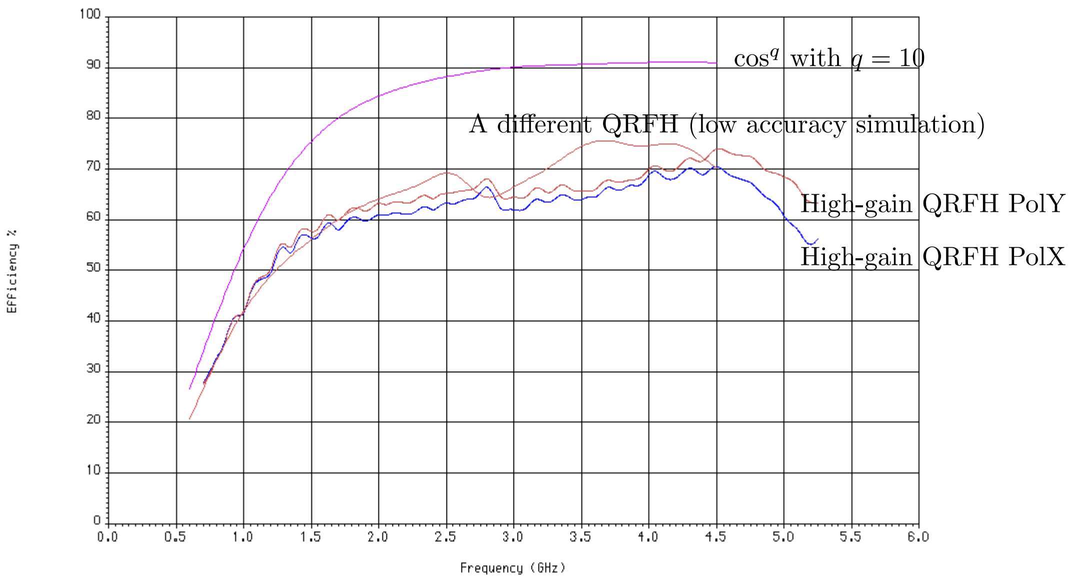

Figure 4.17: Predicted aperture efficiency of GAVRT with the high-gain QRFH as the feed antenna. The efficiency is calculated using physical optics and losses due to RMS surface error, blockage, struts, etc., are ignored.

4.3.3 Aperture mode content

Figure 4.16(a) and (b) plot, respectively, the calculated aperture mode coefficients of the high-gain QRFH and the mode coefficients required to achieve the desired radiation pattern, circularly symmetric far-fields with 10 dB beamwidth of 65 degrees. This design performs better compared to the very high gain QRFH with regards to achieving a mode distribution as close as possible to the desired one, the TM coefficient amplitudes showing especially significant improvement. Once again, the lack of even-order azimuthal modes is noted. Moreover, the mode coefficients exhibit smoother variation with frequency. The dip in TE_{11} amplitude—and the increase in TE_{12} and TE_{13} amplitudes—near $4f_{lo}$ corresponds to a similar drop in aperture efficiency presented in the next subsection.

4.3.4 Predicted system performance

Aperture efficiency of the Goldstone Apple Valley Radio Telescope with the high-gain quad-ridge as the feed antenna has been calculated from 0.7 to 5.2 GHz using physical optics. The calculations use simulated patterns and neglect losses due to RMS surface errors, blockage, struts, etc.

Figure 4.17 presents the aperture efficiency of both polarizations in addition to the maximum attainable aperture efficiency which is realized by $\cos^q$ feed pattern with $q = 10$. Also plotted in the same figure is aperture efficiency of the telescope with an earlier QRFH design that works at lower frequencies than the high-gain horn presented herein. The modeled efficiency is between 60 to 70%

from about 1.5 to 5 GHz on both polarizations. The efficiency roll-off at the low end of the band is due to the tertiary mirror being too small in terms of wavelength and not due to the horn. While the antenna noise temperature has not been calculated in this case, it is reasonable to expect very low spillover pick-up due to two reasons: 1) the quad-ridge horn under-illuminates the tertiary for most of the band; 2) spillover energy does not see the earth, but instead gets reflected from the primary mirror and radiates into space. Therefore, for most elevation angles the antenna noise temperature is expected to be less than 10 K.

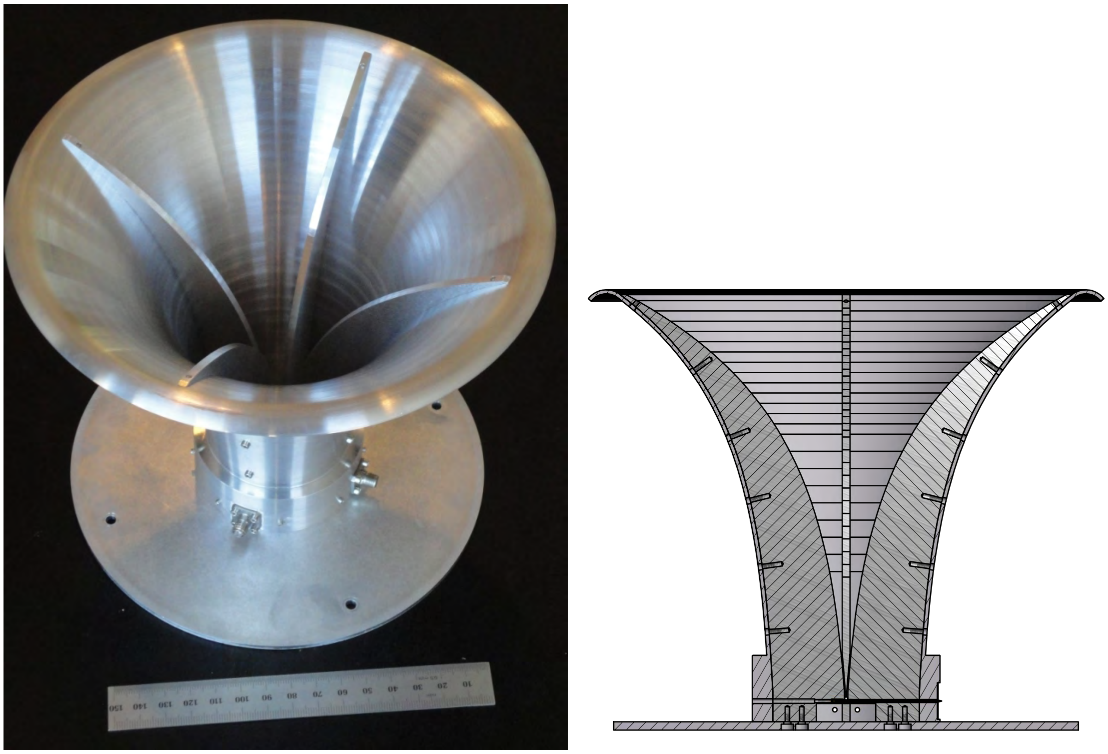

Figure 4.18: A photo and three-dimensional CAD drawing of the medium-gain quad-ridge horn. Feed diameter is 18 cm ($1.2\lambda_{lo}$) and length is 16.4 cm ($1.1\lambda_{lo}$) with $f_{lo} = 2$ GHz.

4.4 Medium-Gain QRFH

4.4.1 Application

The shaped dual-reflector radio telescope, for which the medium-gain QRFH is designed, was built with optics designed at the Jet Propulsion Laboratory [56] and mechanical design and construction by Patriot/Cobham. The primary reflector has a diameter of 12 meters and the full subtended angle to the secondary reflector is 100 degrees. It is located at the Goddard Geophysical and Astronomical Observatory (GGAO), where it serves as a radio telescope for a geodetic VLBI application requiring 50% aperture efficiency and 50 Kelvin system noise temperature.

4.4.2 Stand-alone measurements

The quad-ridge horn is designed with nominal 10 dB beamwidth of 90 degrees and the target frequency band is 6:1. Both the ridge and sidewall tapers use the exponential profile with an aperture diameter of $1.18\lambda_{lo}$ and the horn length of $1.09\lambda_{lo}$. The measured reflection coefficients and isolation are plotted in Figure 4.19. The measured isolation is better than 30 dB up to $10f_{lo}$, which is higher than the simulated isolation (not plotted for clarity) of 40 dB up to $7.5f_{lo}$. The return loss is better than 10 dB up to almost $10f_{lo}$ for both ports and significantly better than 15 dB over

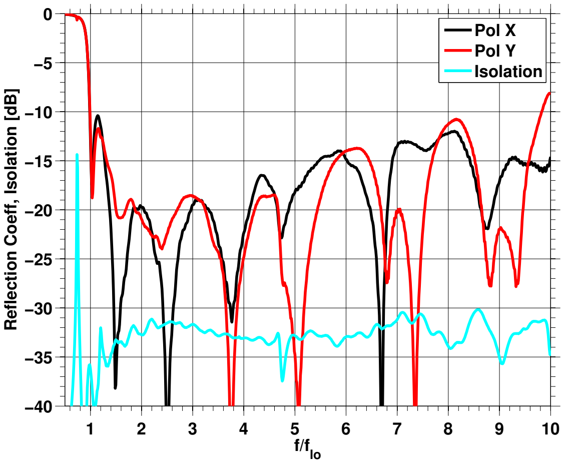

Figure 4.19: Measured scattering parameters of the medium-gain QRFH

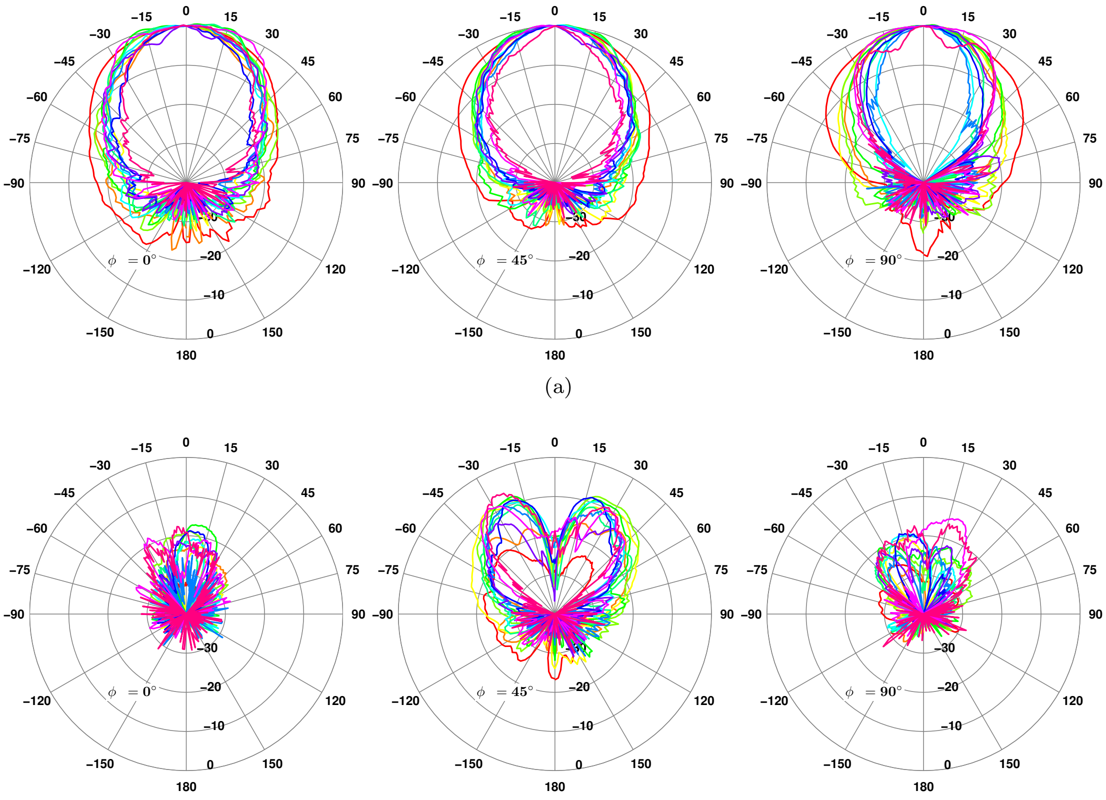

(a)

(b)

Figure 4.20: Measured (a) co-polarized, (b) cross-polarized (Ludwig 3rd definition) radiation patterns of the medium-gain QRFH in $\phi = 0°, 45°, 90°$ azimuthal planes over the frequency range $f/f_{lo} = [1,\ 6]$

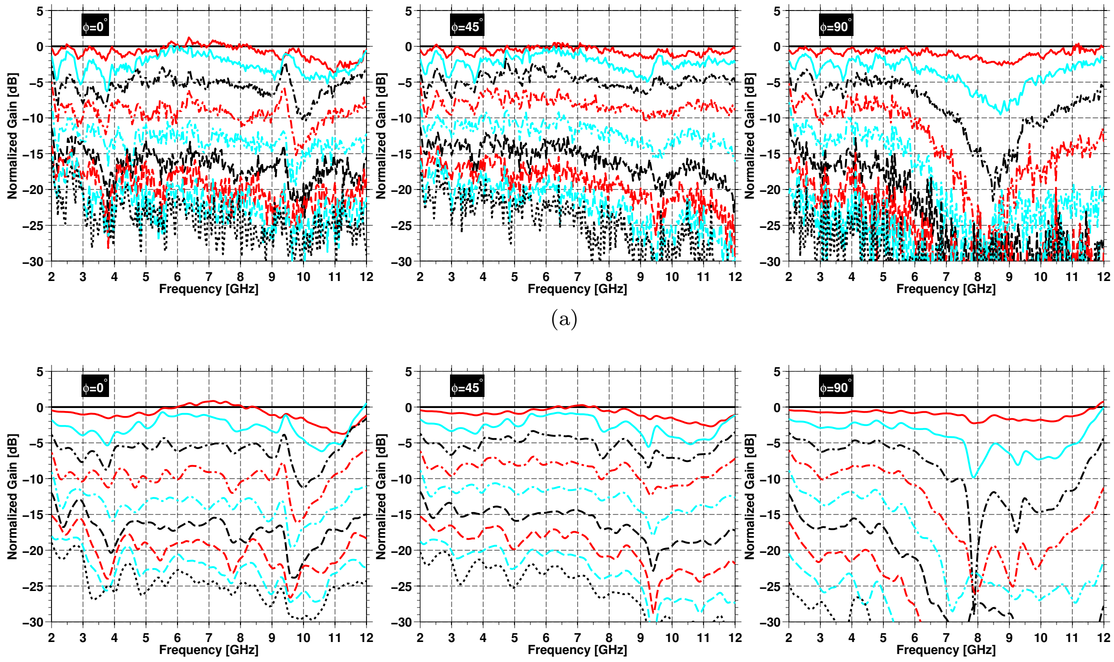

(a)

(b)

Figure 4.21: Comparison of (a) measured and (b) simulated co-polarized radiation patterns of the medium-gain QRFH in $\phi = 0°$, $45°$, $90°$ azimuthal planes over the frequency range $f/f_{lo} = [1, 6]$. The curves are at θ angles from 0 to 90 degrees in steps of 10 degrees and are normalized to $\theta = 0°$.

majority of the band.

The normalized radiation patterns of the QRFH are plotted in Figure 4.20 up to $6f_{lo}$ in the E-, D- and H-planes and the simulated three-dimensional patterns are presented in Figure 4.22. Good beamwidth stability is noted in both E- and D-planes. Like the other quad-ridge horns, H-plane beamwidth shows more variability because of the different boundary condition on the magnetic fields in the horn. The peak cross-polarization, similar to the horns described previously, is around -10 dB.

Figure 4.21 compares measured and simulated patterns in the three azimuthal planes which demonstrates that the CST MWS does an excellent job estimating the far-zone radiation patterns of the QRFH. Most of the fine features in the measurements are captured by the simulations. This figure also indicates that high-frequency ripple in measured patterns is an artifact of the far-field range and not due to the horn.

Simulated intensity plots of E_x in Figure 4.23 highlight the fact that both the aperture diameter and the horn length are small in terms of wavelength at the low end of the band. Energy leaking in the back direction around $2f_{lo}$ results in increased backlobes, approximately 18 dB below boresight according to the simulations; however, this is not observed in the measured patterns which could be due to the mounting plate used during tests. There is also some minor field disruption at $6f_{lo}$, which may be correlated with the beam widening observed in the three-dimensional patterns.

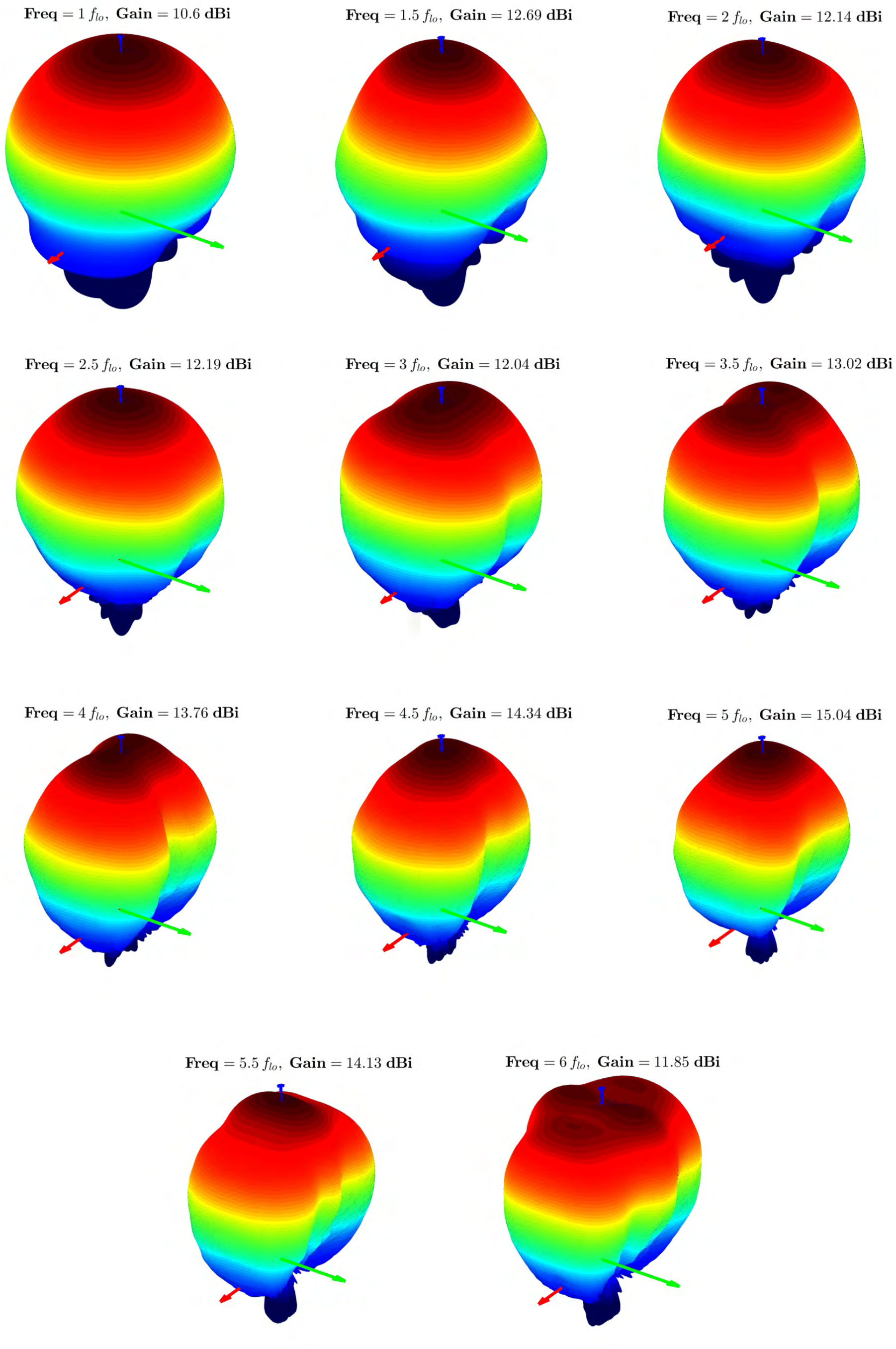

Figure 4.22: Three-dimensional simulated far-field patterns of the medium-gain QRFH.

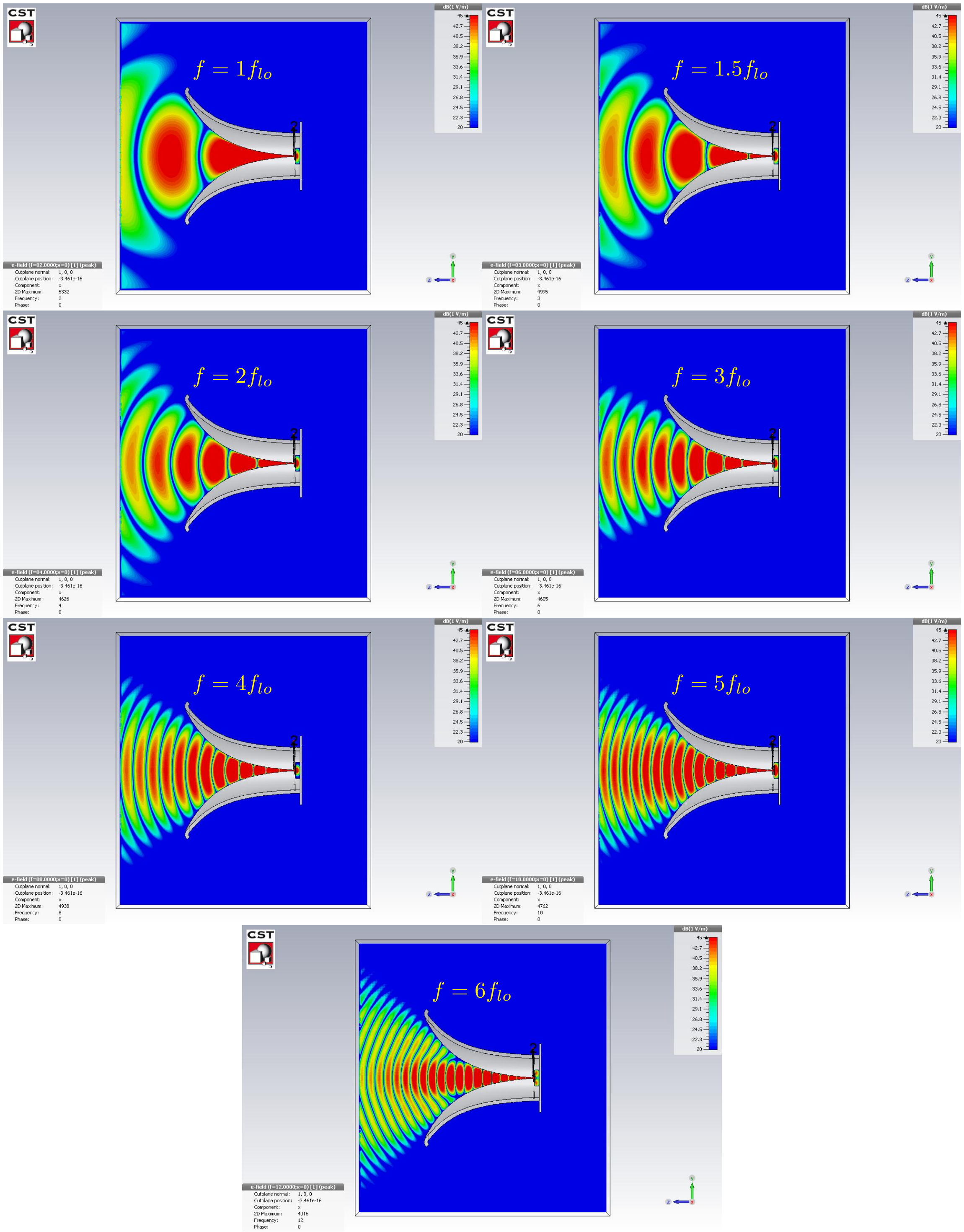

Figure 4.23: Intensity plots of E_x on the $x = 0$ plane in the medium-gain quad-ridge horn which is excited in the x-polarization.

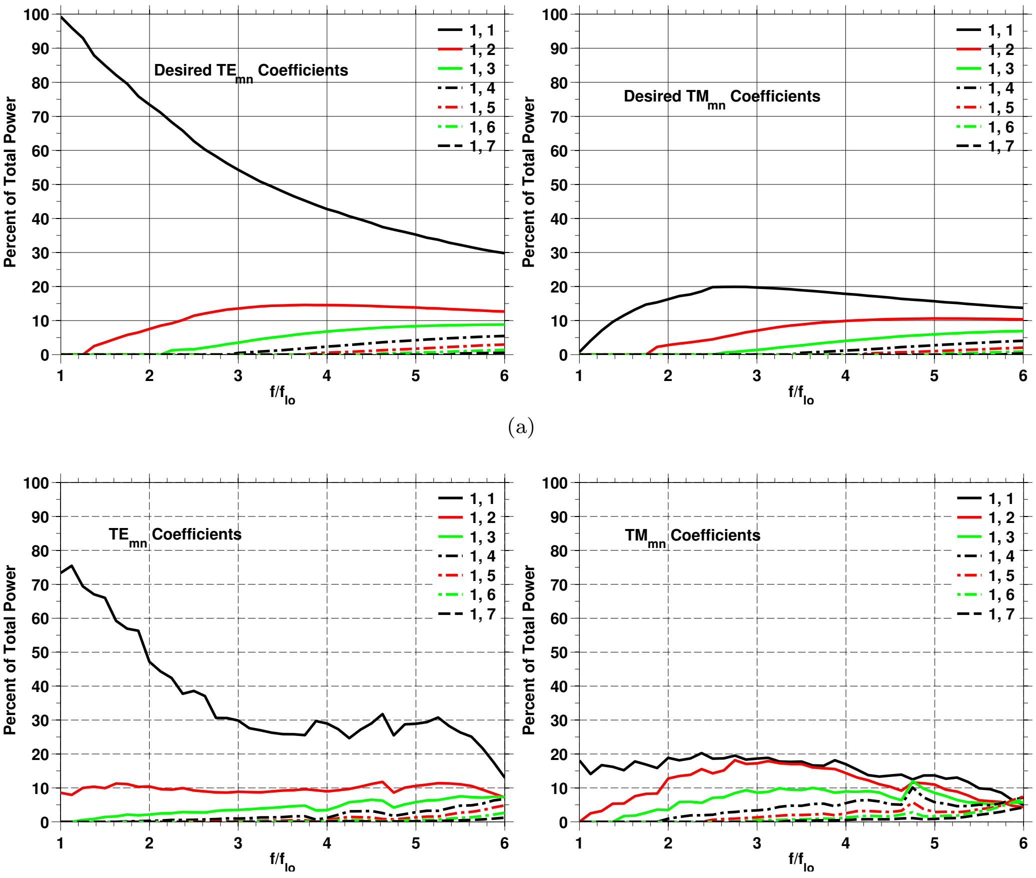

(a)

(b)

Figure 4.24: Normalized mode coefficients (a) required to achieve the desired radiation pattern, (b) at the aperture of the medium-gain QRFH calculated using the simulated patterns. The first 7 TE and 7 TM modes are plotted, which carry the vast majority of the power in the aperture. The simulated patterns are used, instead of measurements, because of higher azimuthal resolution.

4.4.3 Aperture mode content

Figure 4.24 presents the aperture mode analysis results in part (a) and the necessary mode amplitudes in part (b). The achieved TE_{11} amplitude is considerably lower than the desired amplitude at the low end of the band with the TE_{12} and TM_{11} modes mostly carrying the power difference. This disparity is likely due in part to the aperture being too small in terms of wavelength at these frequencies and the error due to assumptions in the mode calculation (see Appendix 3.5) could be significant. Another interesting observation not seen on the previous two horn designs is that the TE_{12} mode carries roughly the same fraction of the total power regardless of frequency. It is below cutoff at the feed point of the horn all the way up to approximately 8 GHz which suggests that it is generated by curvature of ridges and sidewall and is not excited significantly at the feed point.

4.4.4 System measurements

The block diagram of the 2-14 GHz broadband receiver installed on the 12m telescope is shown in Figure 4.25(b). The QRFH is followed by two broadband stripline couplers and two cryogenic low-noise amplifiers (also developed at Caltech) which are all located inside the cryogenic dewar (see right half of Figure 4.25(a)) and are cooled to 20 Kelvin physical temperature during telescope operation. The couplers, despite being cooled, increase overall system noise temperature by a small amount and are necessary to calibrate the system gain and phase.

The microwave outputs of the LNAs are then passed through two power dividers in order to split the low-frequency and high-frequency bands due to strong S-band radio frequency interference and thereby increase dynamic range beyond 4 GHz. The system results presented here are from the high-frequency band which, as shown in the block diagram, employs 4 GHz high-pass filters. Due to the total RF bandwidth available from the front-end, the sheer volume of back-end electronics makes it prohibitive to collocate them with the RF front-end near the apex of the primary reflector. Instead, a microwave-over-fiber link, which provides fairly uniform insertion loss up through 14 GHz, is employed to bring the microwave signals down to the electronics room housing the down-converter and subsequent digital electronics.

To assess the sensitivity of the GGAO 12m radio telescope, a broadband system equivalent flux density, $SEFD\left(f\right)$, was measured. It is the source flux which will produce a receiver power output equal to that produced by the system noise and is measured by moving the telescope on and off a source of known flux as described as follows:

$$SEFD\left(f\right) = \frac{P_{off}\left(f\right)}{P_{on}\left(f\right) - P_{off}\left(f\right)} \frac{S_{src}\left(f\right)}{\Delta\left(f\right)} \tag{4.1}$$

where f is frequency. In this technique, the telescope observes a radio source of known broadband flux $S_{src}\left(f\right)$ in units of Jansky and the on-source power spectrum, $P_{on}\left(f\right)$, is measured by the broadband radio receiver. Then, the off-source power spectrum, $P_{off}\left(f\right)$, is measured with the antenna pointed off source azimuthally (to maintain constant atmospheric noise) by 3 beamwidths at the lowest observation frequency. The source size correction factor, $\Delta\left(f\right)$, compensates for the fact that the antenna beam is not large enough to collect all the flux from the target radio source.

The SEFD estimates of the GGAO 12m telescope were obtained using Cassiopeia A (Cas A) as the radio source calibrator. The frequency dependent source flux of Cas A is given by [57, 58]:

$$\log_{10}\left[S_{src}\left(f\right)\right] = 5.745 - 0.770 \log_{10} f \tag{4.2}$$

with frequency f in MHz. The source flux density also needs to be corrected for the secular decrease

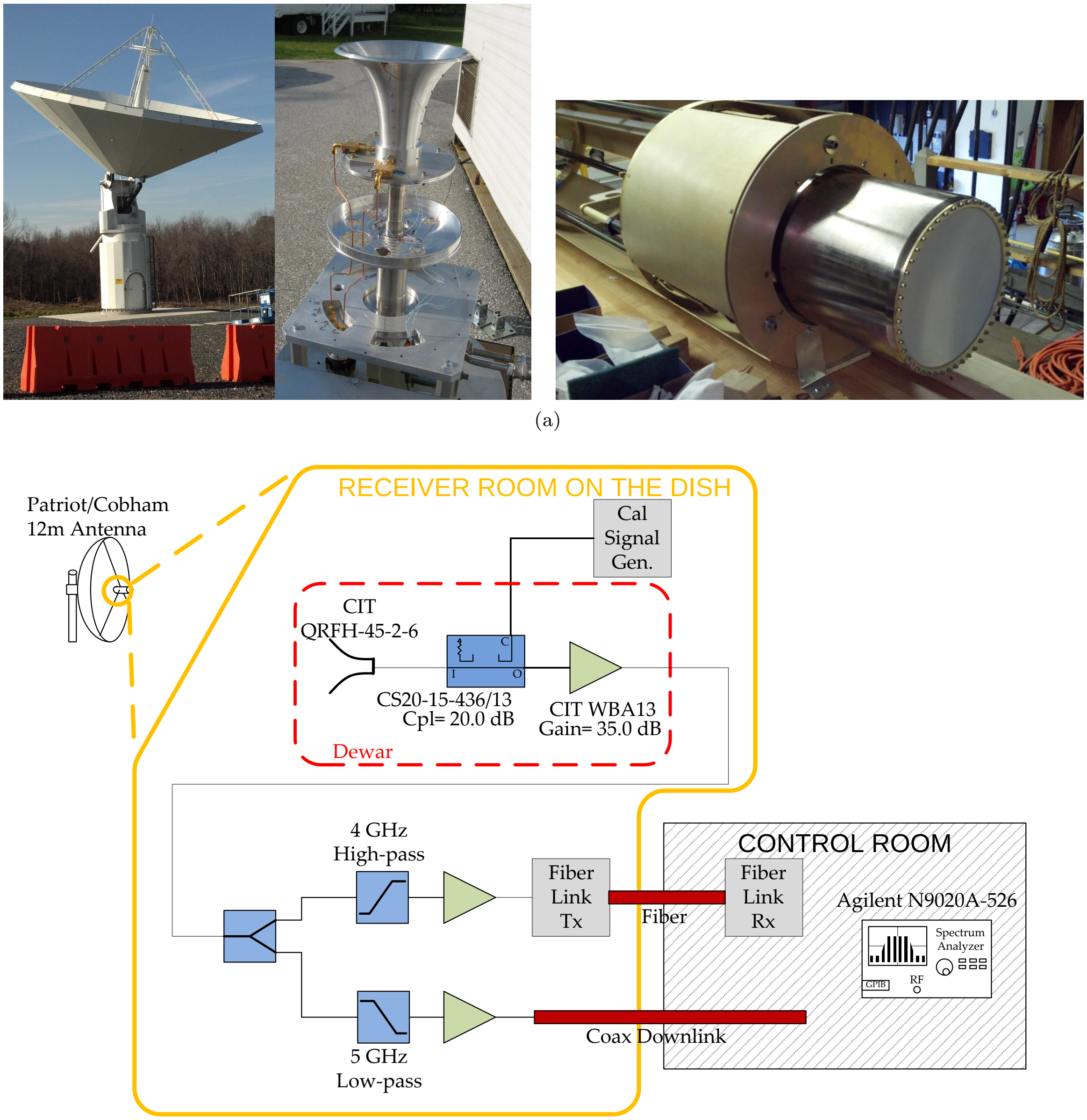

(a)

(b)

Figure 4.25: (a) 12 meter Patriot antenna at GGAO (left) and integration of the circular QRFH into the dewar (calibration couplers not shown; right), (b) block diagram of the 12 meter radio telescope front-end showing RF electronics for one linear polarization only.

in flux density of Cas A whose percentage value per year is given by [58]

$$d\left(f\right) = 0.97 - 0.3 \log_{10} f - 3 \tag{4.3}$$

with f in MHz again. The radio source structure of Cas A is modeled with a disk source distribution, the form of the source size correction factor for such a model is given by [57, 59]:

$$\Delta\left(f\right) = \frac{x^2}{1 - e^{-x^2}} \text{ with } x = \sqrt{4 \ln 2} \times \frac{R}{\theta_{HPBW}} \tag{4.4}$$

where R is the angular radius of the disk and is 2.15 arcminutes [57], and θ_{HPBW} is the half-power beamwidth of the telescope.

An Agilent N9020A-526 signal analyzer was used as the broadband radio receiver for the sensitivity evaluation. In these experiments, the signal analyzer was configured to collect power spectrum measurements from 2-14 GHz with a 3 MHz resolution bandwidth. Power spectrum measurements were collected with the telescope both on and off the radio source and stored on hard disk for subsequent data processing. In order to reduce trace noise in the measurements and in turn enhance the precision in the SEFD estimate, a sliding window filter of length of approximately 100 MHz was applied to both on- and off-source data sets in post processing.

The broadband source equivalent flux density measurements with Cas A were conducted and equations (4.1)-(4.4) were used to compute the SEFD to estimate the telescope sensitivity. Converting the SEFD estimate to more familiar aperture efficiency requires knowledge of system noise temperature T_{sys} and is accomplished via:

$$A_{eff} = \frac{2kT_{sys}}{SEFD\left(f\right) \cdot \pi r^2} \times 10^{26} \tag{4.5}$$

where k is Boltzmann's constant and r is radius of primary reflector. The system noise temperature is defined as

$$T_{sys} \equiv T_{Rx} + \underbrace{T_{sky} + T_{spillover}}_{T_{antenna}} \tag{4.6}$$

where the terms on the right-hand side are, in order from left to right, receiver, sky, and spillover noise temperatures. The T_{sys} is calculated using the Y-factor method with hot/cold loads and is given by

$$T_{sys} = \frac{T_{hot} - YT_{cold}}{Y - 1}. \tag{4.7}$$

The hot load used for these tests is an ambient temperature RF absorber with measured physical temperature T_{hot}, of the order of 295 K, and the Y-factor is given by the ratio of receiver output power with hot load to that with cold load, i.e., P_{hot}/P_{cold}. The cold load measurements is performed

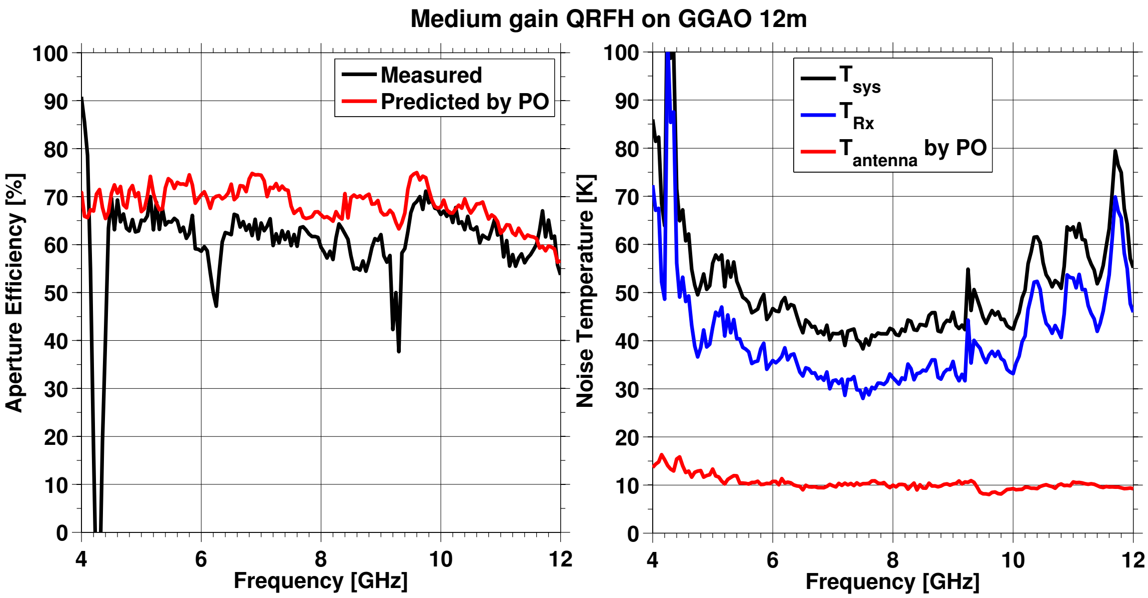

Figure 4.26: The measured system noise temperature and aperture efficiency of the circular QRFH installed on the GGAO 12 m telescope. The predicted aperture efficiency and antenna noise temperature—both based upon QRFH far-field pattern integration—are also plotted. The sky noise temperature is calculated per the method outlined in [60], and is 5.5K at 4 GHz and 6.5K at 10 GHz.

by pointing the telescope off the radio source instead of using an actual liquid nitrogen termination. As such, $T_{cold} = T_{sys}$ which gives

$$T_{sys} = \frac{295 - T_{sky} - T_{spillover}}{Y - 1} \tag{4.8}$$

Without the knowledge of T_{sky} and $T_{spillover}$, this equation cannot be solved to obtain T_{sys}. Consequently, the sky and spillover noise temperatures are estimated by using predicted values from physical optics calculations as explained below. The system noise temperature measurements are carried out in the same configuration as SEFD observations, namely with feed, couplers and LNAs in the dewar on the telescope followed by the fiber link and the associated back-end electronics.

Using (4.5), the measured broadband aperture efficiency of the GGAO 12m antenna with the QRFH feed is plotted in Figure 4.26. Also plotted in the same figure are predicted aperture efficiency and spillover and sky noise temperatures curves based upon the QRFH pattern measurements. A custom physical optics program, which takes into account shaping of both reflectors, was used to compute all three quantities with the spillover and sky noise temperatures computed at 48 degree elevation angle. On the other hand, the Cas A SEFD measurements were performed at an elevation angle of 60 degrees; however, because spillover and sky temperatures do not usually change rapidly with elevation angle, the predicted spillover and sky temperatures at 48 degree elevation are used to estimate the receiver noise contribution.

The measured aperture efficiency is better than 60% up to 8 GHz and stays above 54% up to 12 GHz. Aperture efficiency averaged over the entire band is 60%. The dips in efficiency near 4, 6 and 9 GHz are not due to the horn, but rather are likely artifacts of interference. This is the first demonstration of a quad-ridge horn achieving such good performance on a radio telescope. The measured efficiency is in very good agreement with the efficiency calculated by physical optics using the measured antenna patterns. The fairly small difference between the predictions from physical optics and the measurements is most likely due to blockage by the subreflector and its struts.

The measured system noise temperature is better than 50 K from 5 to 10 GHz and is mostly dominated by the receiver temperature. The Caltech LNAs achieve between 5-20 K noise in this band where the noise degradation is due to protection diodes. There is an estimated 1 dB loss preceding the LNA in addition to 3 K additional noise through the coupled arm of the directional coupler due to finite directivity. Taking all of this into account, there remains about $\geq$ 10 K discrepancy between estimated T_{Rx} and that suggested by measurements. At this point, the source of this discrepancy is unclear, but is thought to be one or more of the following:

1. increased $T_{antenna}$ due to scattering off of struts and other supporting structures of the reflector. It is very unlikely the additional noise is due to feed loss because the theoretical loss of the feed, mostly in the internal coaxial lines, is of the order of 0.1dB, and this would contribute only 0.5K with the feed at 20K.

2. Cryogenic losses, especially preceding the LNAs, unaccounted for in the existing analysis.

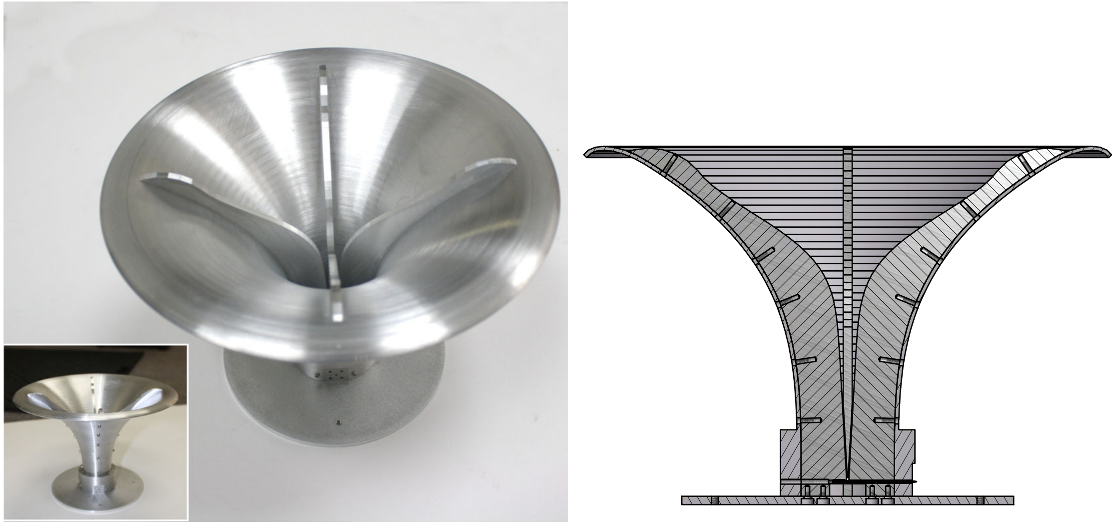

Figure 4.27: Photo and three-dimensional CAD drawing of the low-gain QRFH. Feed diameter is 20 cm ($1.5\lambda_{lo}$) and length is 13.4 cm ($1.03\lambda_{lo}$) with $f_{lo} = 2.3$ GHz.

4.5 Low-Gain QRFH

4.5.1 Application

This QRFH is intended for telescopes with $f/D \approx 0.4$. The first of this design has been built and tested and is in the process of being integrated into a VLBI2010 [2] front-end in Japan. Two more identical horns are being built, one for MIT Haystack Observatory and the other for Shanghai Astronomical Observatory.

The telescope in Japan, on which this QRFH will be installed, is a copy of the so-called Twin-Telescope Wettzell, designed and fabricated in Germany [61]. It has a ring-focus secondary mirror with a primary mirror diameter of 13.2 meters and an effective f/D of approximately 0.4.

4.5.2 Stand-alone measurements

The quad-ridge horn ridge taper uses the sinusoidal profile while the sidewall taper follows the x^p functional form. The nominal 10 dB beamwidth is 120 degrees and the desired bandwidth is 6:1. The horn length is about $1\lambda_{lo}$ and the aperture diameter is $1.12\lambda_{lo}$ with a flare angle of 55 degrees.

The measured reflection coefficients of both polarizations are plotted in Figure 4.28 along with the isolation. Except between 1.2 and $1.6f_{lo}$, the return loss is 15 dB or better across most of the band for both polarizations, and the isolation is better than 25 dB. The increase in return loss between 1.2 and $1.6f_{lo}$ was predicted by simulations and was a conscious design choice.

Figure 4.29 presents the measured patterns in polar format for the E-, D-, and H-planes. The three-dimensional patterns are plotted in Figure 4.30. One of the first observations is that the beamwidth in D-plane is not as constant as the higher gain QRFHs presented herein and it is

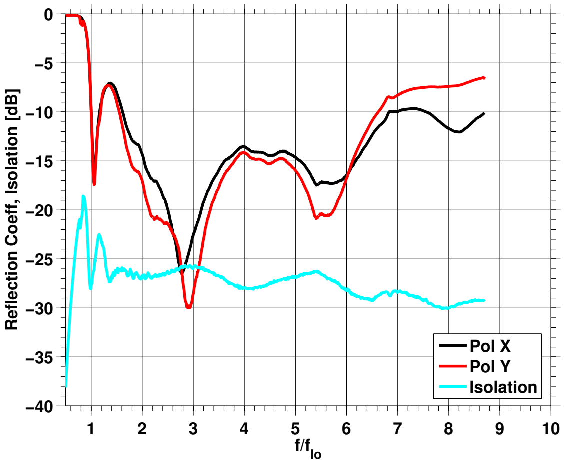

Figure 4.28: Measured scattering parameters of the low-gain QRFH

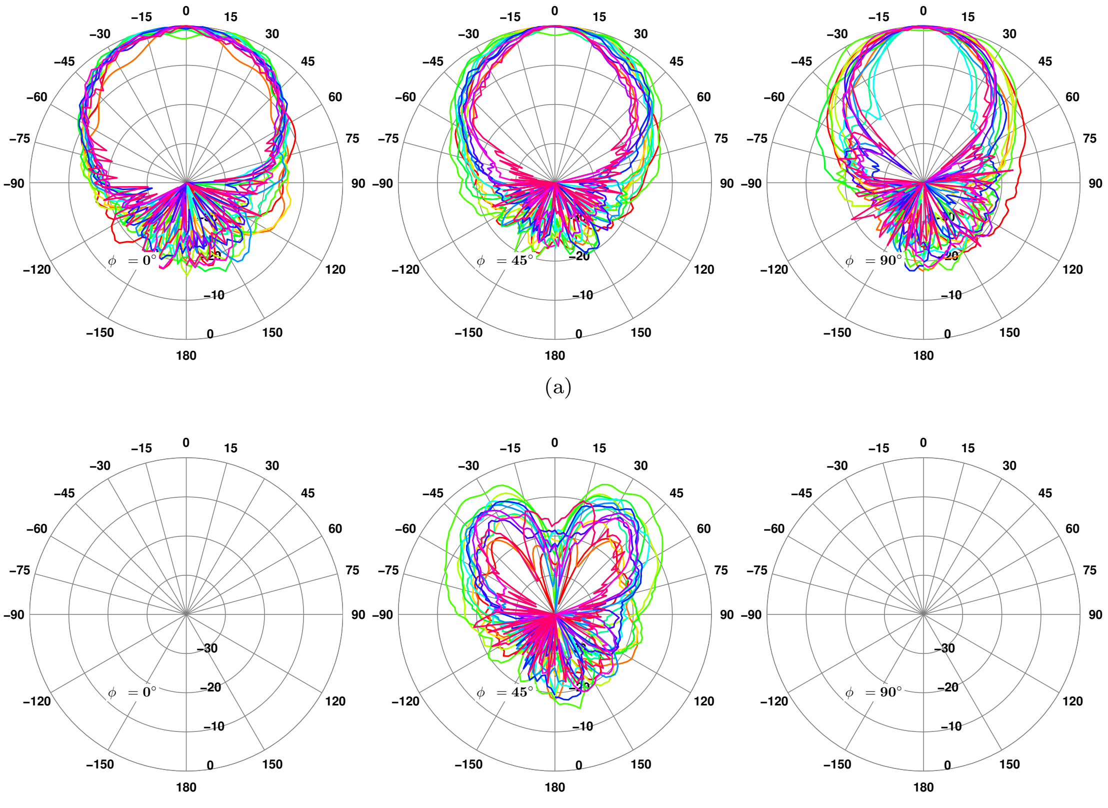

(a)

(b)

Figure 4.29: Measured (a) co-polarized, (b) cross-polarized (Ludwig 3rd definition) radiation patterns of the low-gain QRFH in $\phi = 0°, 45°, 90°$ azimuthal planes over the frequency range $f/f_{lo} = [1,\, 6]$

on average narrower than the beamwidth in the E-plane which is 120 degrees. Like the other quad-ridge horns, the H-plane shows significantly more variation. The asymmetry in the radiation patterns between θ around -90 degrees and 90 degrees is due to the pattern measurement setup. The roof wall is at $\theta = 90$ degrees causing this beam widening artifact in the measurements. The cross-polarization level of this horn peaks to -5 dB over very narrow frequency range with a nominal level of -8 to -9 dB which is higher than previous designs.

The intensity plots of E_x in Figure 4.31 show similar features as the other horns. Comparing the intensity plots of the higher gain horns to those of the lower gain ones, one observes significant difference between curvatures of the wave fronts in the two cases. The lower gain horns exhibit more curvature and the fields are coupled fairly strongly to the ridges even near the aperture. These are most easily noticed at mid to upper end of the frequency band. On the other hand, the higher gain horns usually have more planar wave fronts and the fields are loosely coupled to the ridges near the aperture.

4.5.3 Predicted system performance

Aperture efficiency of the 13.2 meter ring-focus telescope is computed using physical optics ignoring losses due to blockage, struts, rms surface errors, etc. The simulated patterns are used in the calculations, which is justified by the close agreement between modeling and measurements of this horn. Antenna noise temperature is also computed, using the method described in [60, 62], for the telescope pointing near zenith. Both efficiency and noise temperature are calculated from 2 to 15 GHz as the frequency band of interest in VLBI2010 applications is 2.3 to 14 GHz.

Figure 4.32 presents the computed aperture efficiency and the antenna noise temperature in parts (a) and (b), respectively. Also plotted in this figure are the efficiency and antenna noise temperature of the telescope with the medium-gain QRFH presented herein as the feed antenna. The efficiency with the low-gain QRFH is better than 50% all the way up to 15 GHz and the average efficiency in the frequency range of interest is $> 55\%$. The antenna noise temperature is also very good, less than 10 K from 2.5 to 15 GHz.

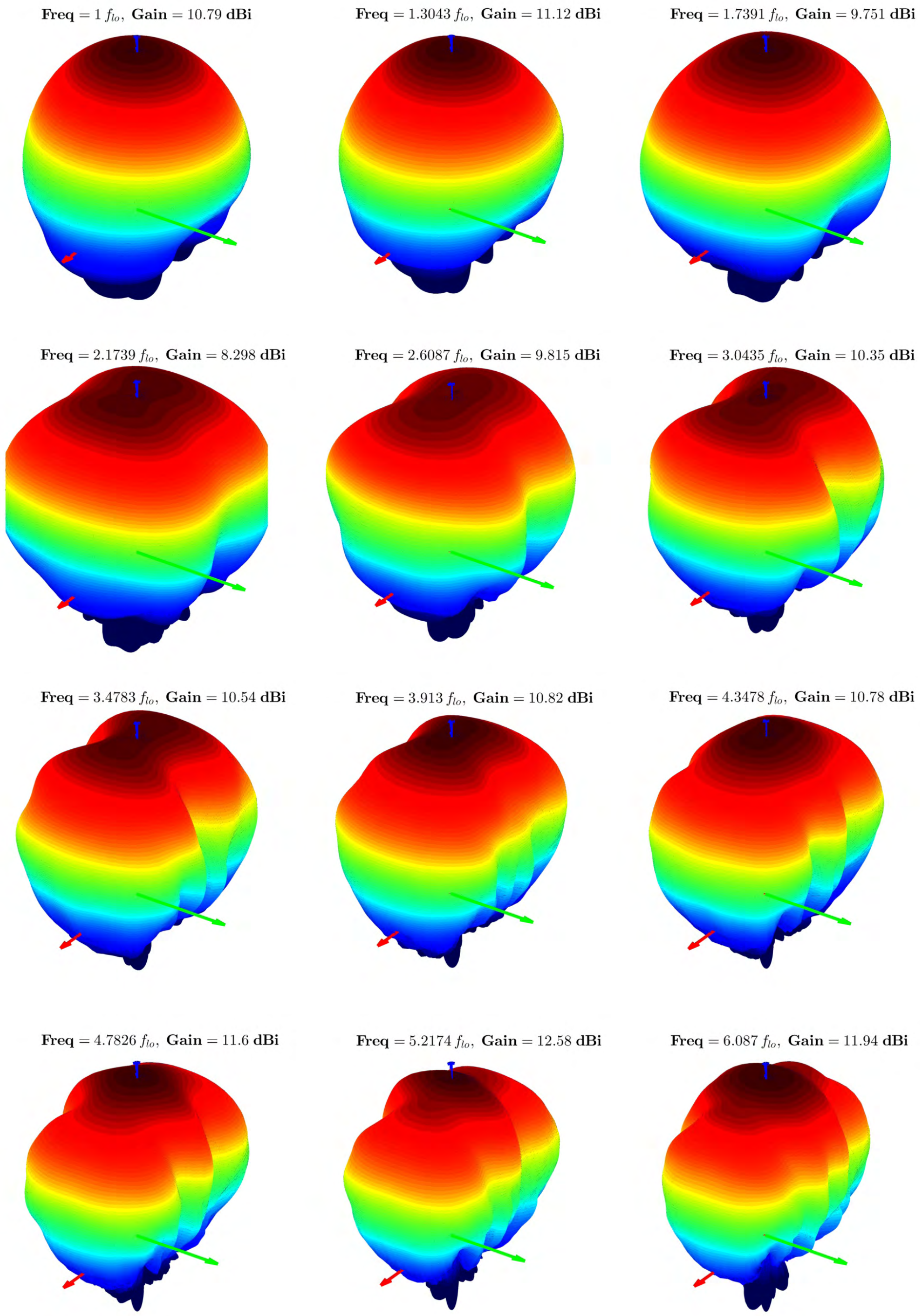

Figure 4.30: Three-dimensional simulated far-field patterns of the low-gain QRFH

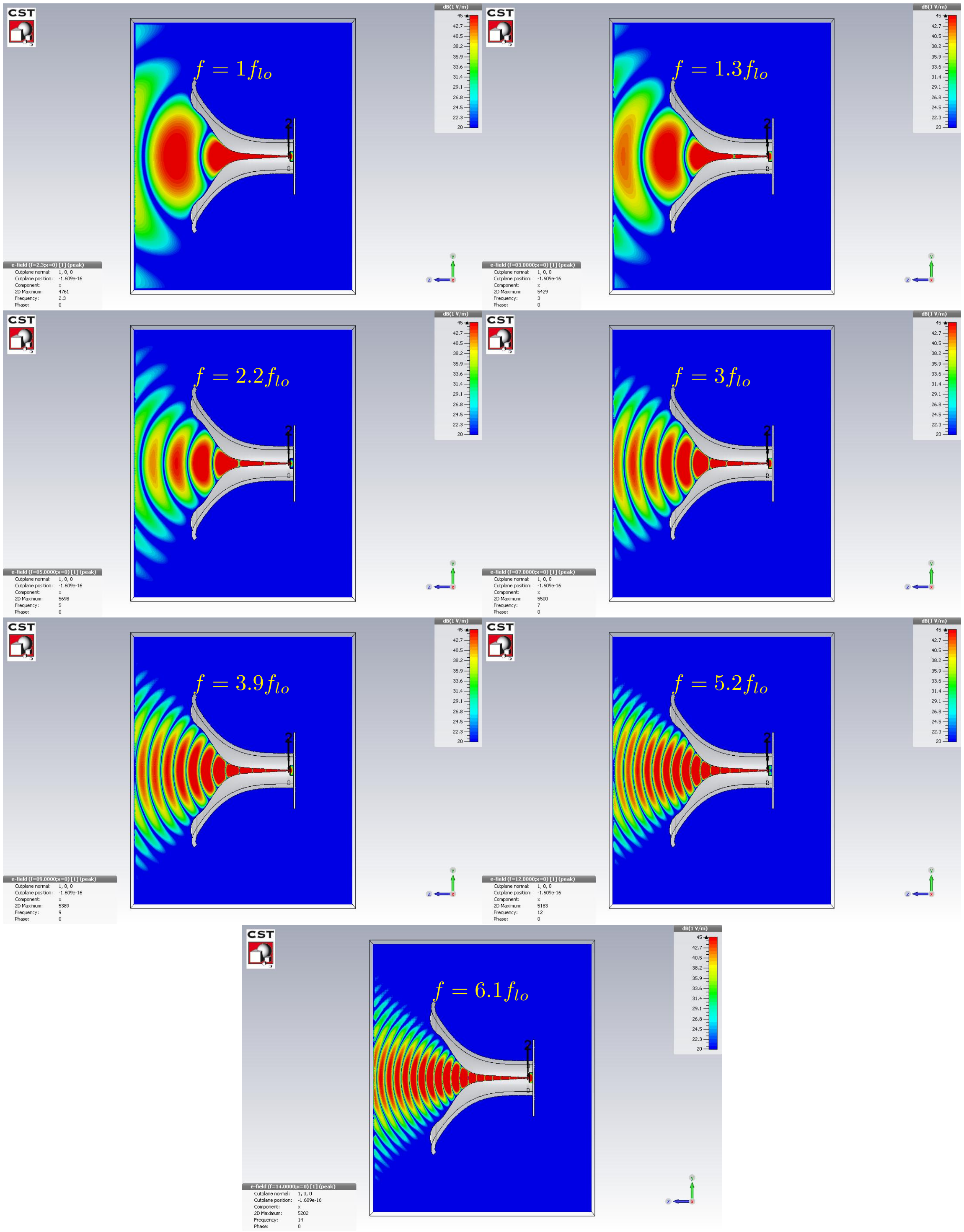

Figure 4.31: Intensity plots of E_x on the $x = 0$ plane in the low-gain quad-ridge horn which is excited in the x-polarization

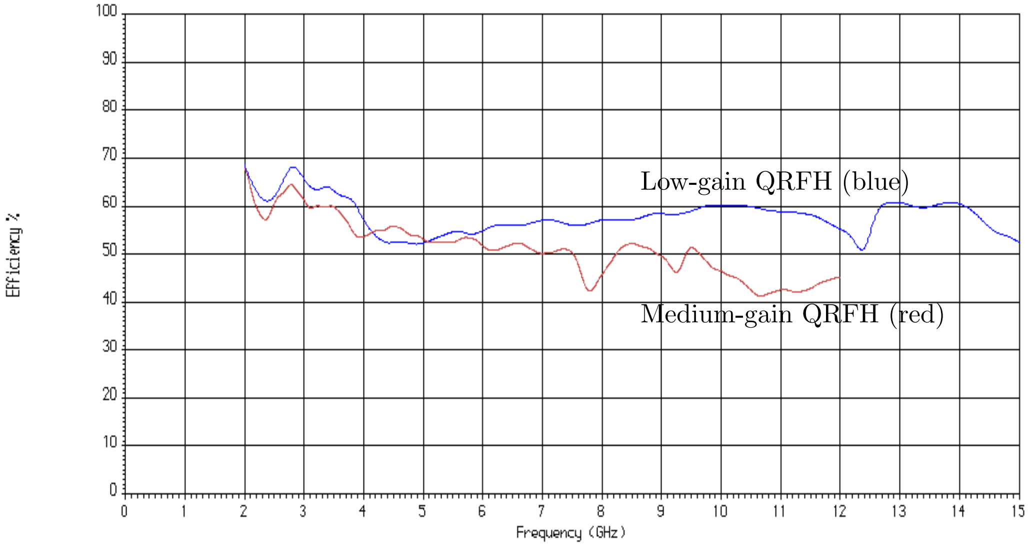

(a)

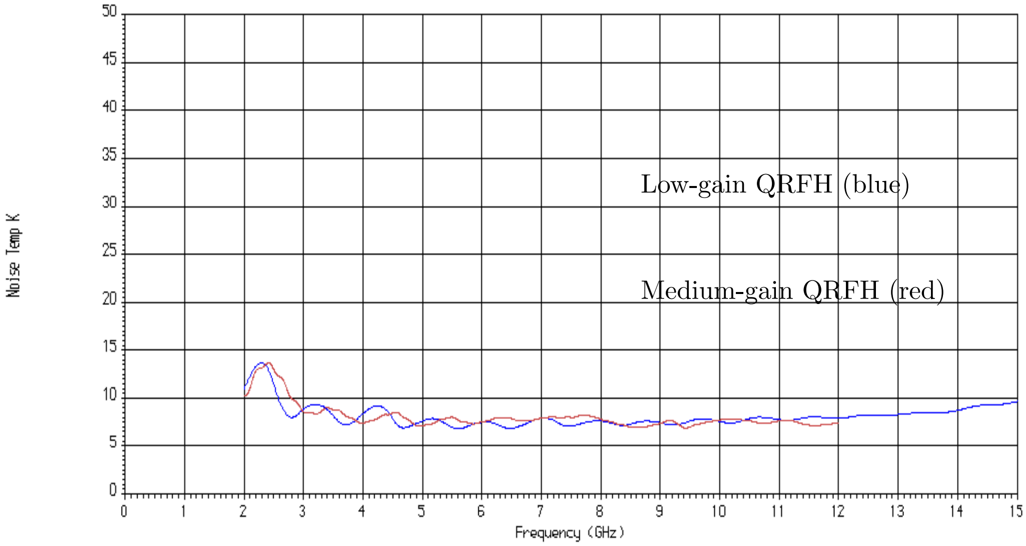

(b)

Figure 4.32: Predicted (a) aperture efficiency, (b) antenna noise temperature of the 13.2 meter ring-focus telescope with the low-gain (blue) and medium-gain (red) QRFH as the feed antenna. The efficiencies are calculated using physical optics and losses due to RMS surface error, blockage, struts, etc., are ignored. Telescope is assumed to point near zenith for noise temperature calculations.

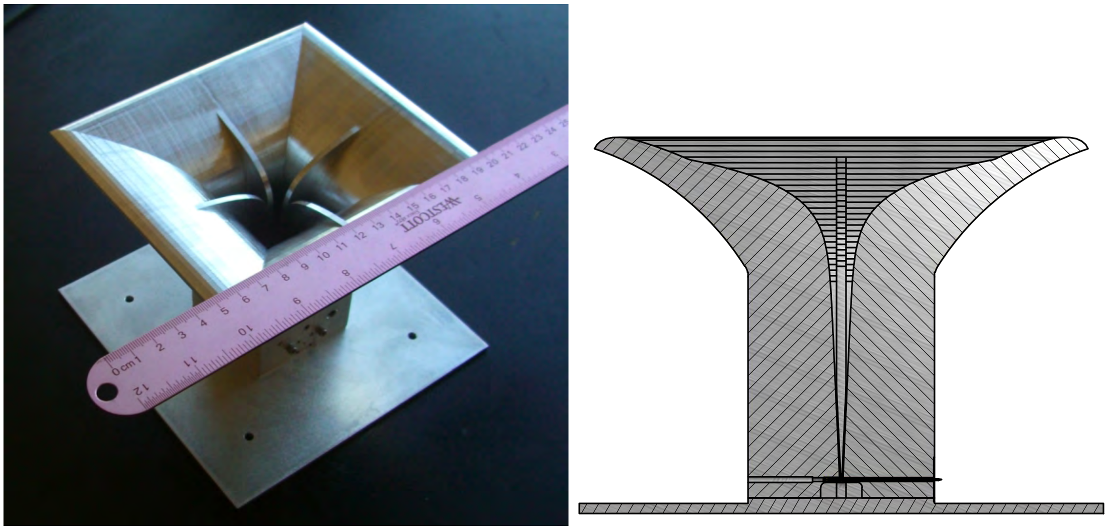

Figure 4.33: Photo and three-dimensional CAD drawing of the very low gain quad-ridge horn. Feed diameter is 14.3 cm ($1.1\lambda_{lo}$) and length is 11.9 cm ($0.91\lambda_{lo}$) with $f_{lo} = 2.3$ GHz.

4.6 Very-Low Gain QRFH

4.6.1 Application

The quad-ridge horn with the widest beamwidth is designed for the Westford Radio Telescope at MIT Haystack Observatory. It is a dual reflector system in Cassegrain configuration with a symmetric paraboloid primary mirror (diameter of 18.3 meters) and $f/D = 0.3$ [63]. The horn is currently integrated into a VLBI2010 receiver at MIT Haystack Observatory.

4.6.2 Stand-alone measurements

The unique aspect of this horn is that it is square instead of circular, see Figure 4.33 for a photo. Square horns are more favorable for low-frequency designs because they are only curved in one plane and thus, could be made out of sheet metal much more easily than circular horns. However, their disadvantage is the increased size at the aperture along the diagonal. The design uses exponential sidewall taper and x^p profile for the ridge taper. The nominal beamwidth is 140 degrees. The aperture side length is $1.05\lambda_{lo}$ and the horn length is $0.87\lambda_{lo}$. The flare angle is approximately 74 degrees. This is the smallest horn in terms of wavelength designed as part of this research.

The measured return loss of both polarizations and the simulated isolation (due to lack of measurement) are provided in Figure 4.34. The match is poor below $2f_{lo}$. This is similar to (and worse than) the low-gain design of the previous section in that only the low-frequency input match deteriorates. The reason low-frequency match degrades with increasing beamwidth is the reduction in aperture size and horn length. In other words, the horn is becoming too small in terms of wavelength which implies reflections from the aperture which, in turn, degrade input match.

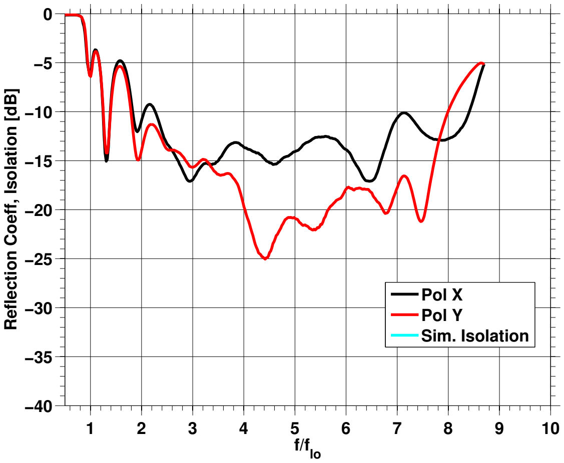

Figure 4.34: Measured scattering parameters of the very low gain QRFH

The patterns of this horn are measured and are presented in polar format in Figure 4.35. However, the measurements were incorrectly performed with the two antennas in the near-fields of each other. This invalidates the phase measurements, but its impact on magnitude measurements is thought to be less pronounced. Further, high-frequency harmonics at the output of wideband amplifiers in the pattern measurement setup due to very strong low-frequency RFI have plagued these measurements. Nevertheless, the measurements are presented here along with the simulated three-dimensional patterns in Figure 4.36.

Both the measured and the simulated far-fields underline the difficulty in designing such wide-beamwidth quad-ridge horns. Beamwidth control becomes more difficult and unlike higher gain designs, there is a serious trade-off between low-frequency input match and high-frequency radiation pattern performance. This is in line with the discussion in Section 3.5 where it is stated that for a given aperture size, wider beamwidths require many more modes. Generating and controlling these become very challenging over such large bandwidths. The intensity plots of E_x also show that near operating frequency of f_{lo}, the horn is too small and there is much energy “leaking” outside the aperture towards the back and sides.

4.6.3 Predicted system performance

Just as is done for the other quad-ridge horns presented herein, aperture efficiency of the Westford radio telescope when illuminated by the very low gain QRFH is calculated using physical optics and losses due to blockage, struts, surface errors are neglected. Because the primary mirror is a symmetric paraboloid, the physical optics calculations reduce to that of an 18.3 meter parabola with the QRFH at prime focus.

Figure 4.38 presents the predicted efficiency using both the simulated and measured patterns. The efficiency using measured patterns falls rapidly with frequency which is completely due to the

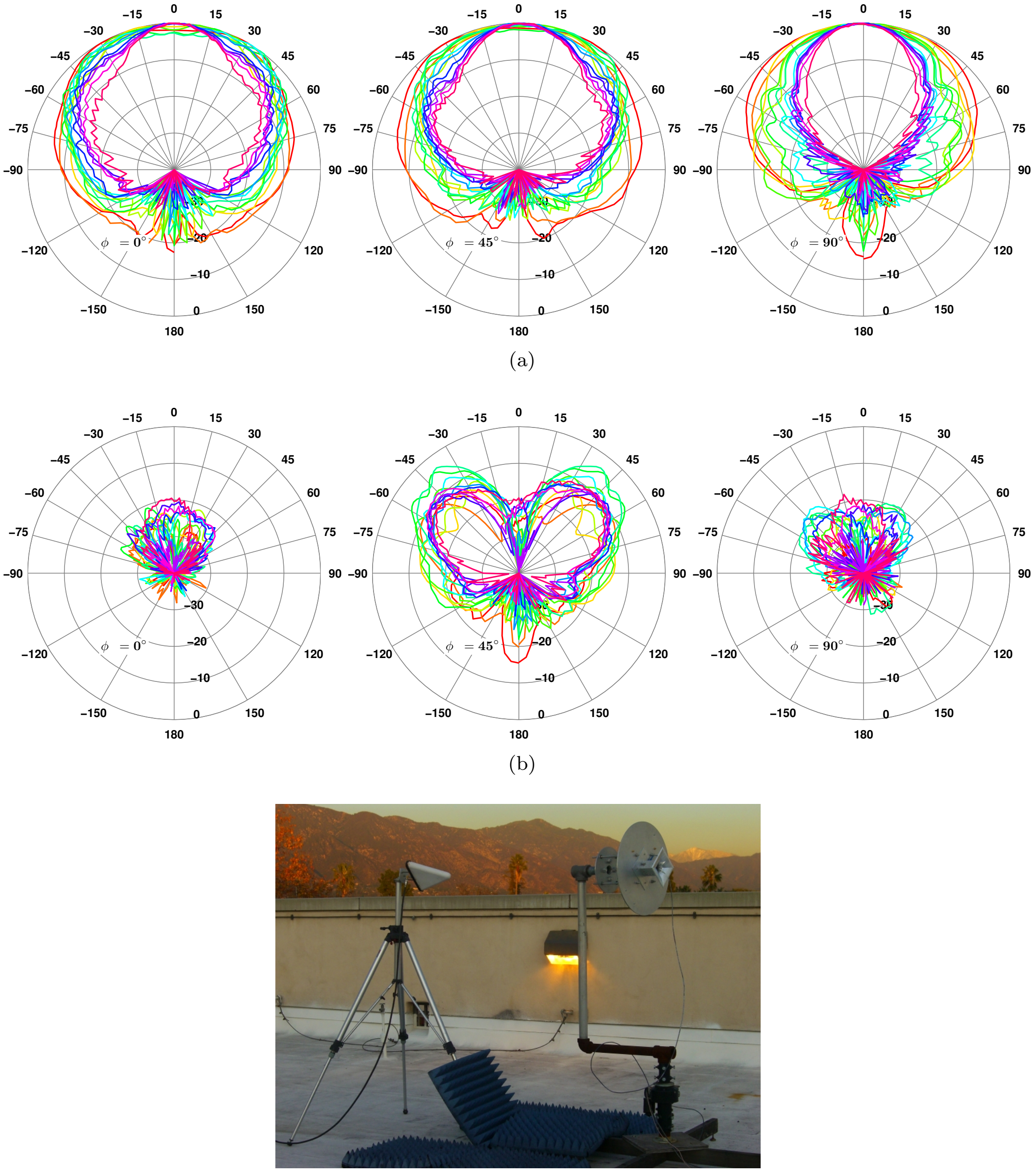

(a)

(b)

(c)

Figure 4.35: Measured (a) co-polarized, (b) cross-polarized (Ludwig 3rd definition) radiation patterns of the very low gain QRFH in $\phi = 0°$, $45°$, $90°$ azimuthal planes over the frequency range $f/f_{lo} = [1, 6]$. Part (c) shows photo of the horn during pattern measurements where the two antennas were incorrectly placed in each other's near-field regions.

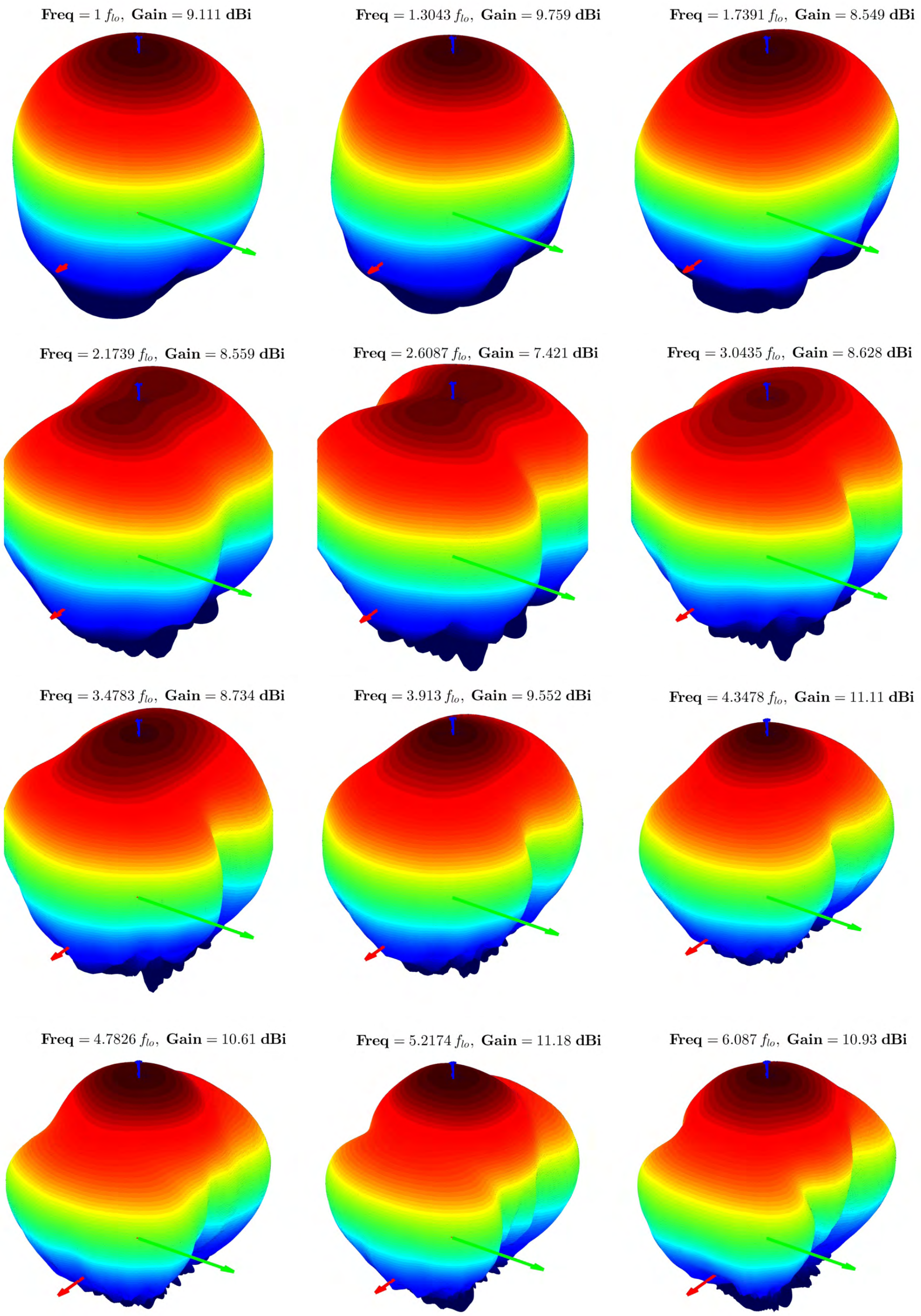

Figure 4.36: Three-dimensional simulated far-field patterns of the very low gain QRFH

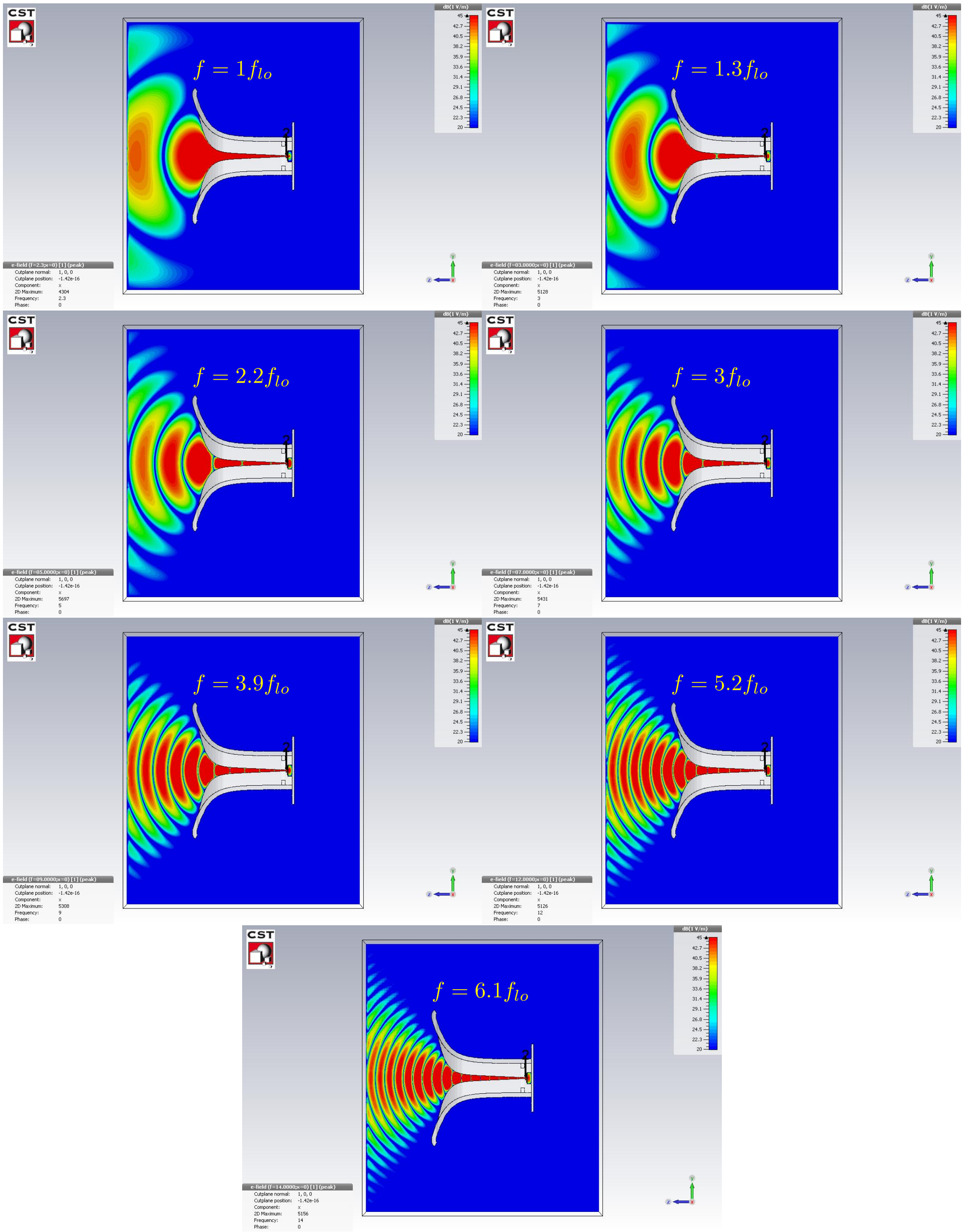

e-field (f=2.3;x=0) [1] (peak)
Cutplane normal: 1, 0, 0
Cutplane position: -1.42e-16
Component: x
2D Maximum: 4304
Frequency: 2.3
Phase: 0

e-field (f=03.0000;x=0) [1] (peak)
Cutplane normal: 1, 0, 0
Cutplane position: -1.42e-16
Component: x
2D Maximum: 5128
Frequency: 3
Phase: 0

e-field (f=05.0000;x=0) [1] (peak)
Cutplane normal: 1, 0, 0
Cutplane position: -1.42e-16
Component: x
2D Maximum: 5697
Frequency: 5
Phase: 0

e-field (f=07.0000;x=0) [1] (peak)
Cutplane normal: 1, 0, 0
Cutplane position: -1.42e-16
Component: x
2D Maximum: 5431
Frequency: 7
Phase: 0

e-field (f=09.0000;x=0) [1] (peak)
Cutplane normal: 1, 0, 0
Cutplane position: -1.42e-16
Component: x
2D Maximum: 5308
Frequency: 9
Phase: 0

e-field (f=12.0000;x=0) [1] (peak)
Cutplane normal: 1, 0, 0
Cutplane position: -1.42e-16
Component: x
2D Maximum: 5126
Frequency: 12
Phase: 0

e-field (f=14.0000;x=0) [1] (peak)
Cutplane normal: 1, 0, 0
Cutplane position: -1.42e-16
Component: x
2D Maximum: 5156
Frequency: 14
Phase: 0

Figure 4.37: Intensity plots of E_x on the $x = 0$ plane in the very low gain quad-ridge horn which is excited in the x-polarization

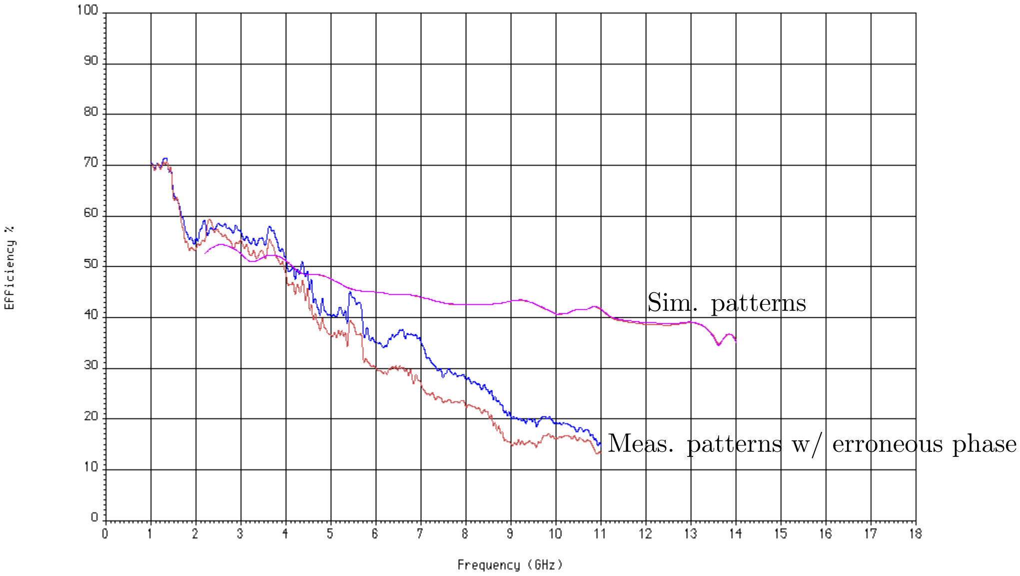

Figure 4.38: Predicted aperture efficiency of an 18.3 meter prime-focus telescope with $f/D = 0.3$ with the very low gain QRFH as the feed antenna. The efficiencies using both simulated and measured patterns are plotted where the latter is significantly lower due to phase error in measurements. The efficiencies are calculated using physical optics and losses due to RMS surface error, blockage, struts, etc., are ignored. Telescope is assumed to point near zenith for noise temperature calculations.

aforementioned error in pattern measurements resulting in erroneous phase data. This was verified by computing the efficiency using the combination of measured far-field magnitude and simulated far-field phase (not shown for clarity) which yielded results very similar to the efficiency using simulated patterns only.

The predicted aperture efficiency is the lowest among all the quad-ridge horns presented, > 40 % over much of the frequency range of interest 2.3 to 14 GHz but falling as low as 35% above 13.5 GHz. A circular quad-ridge horn covering 0.6–2.5 GHz with approximately the same beamwidth as this one was also designed at Caltech and built in Germany by the Max Planck Institute for Radio Astronomy. It also achieves 40–45% aperture efficiency, according to simulations, at prime focus on the Effelsberg telescope [64].

4.7 Conclusions

Simulated and, where available, measured performance—both stand-alone and on-telescope—of five QRFH designs with nominal 10 dB beamwidths from 30 to 140 degrees have been presented. These results highlight the most appealing aspects of the horn:

1. Good beamwidth stability in E- and D- planes over 6:1 frequency range;
2. Ability to design the horn with nominal 10 dB beamwidths from 30 to 140 degrees;
3. Excellent single-ended match to 50 Ohm nominal impedance;
4. Ability to easily scale the horn for different frequency ranges;

while also bringing out some aspects that need further improvement (especially for large beamwidth horns):

1. Poor beamwidth stability in H-plane
2. Maintaining good radiation pattern performance for designs with beamwidths $>$ 110-120 degrees;
3. $>$ -10 dB peak cross-polarization in the D-plane over narrow frequency ranges.

Improving these aspects of the horn necessitates a thorough understanding of mode coupling and progression within the quad-ridge horn which is a topic of ongoing research. The aperture mode coefficients of the three of the five horns were also presented.

Part II

Compound-Semiconductor LNAs

Chapter 5

Introduction to Two State-of-the-Art HEMT Processes

The second part of the thesis focuses on room-temperature and cryogenic performance of discrete high-electron mobility transistors (HEMTs) and microwave monolithic integrated circuit (MMIC) LNAs achieving very low noise over decade bandwidths from two state-of-the-art HEMT processes: 35 nm InP pHEMT and 70 nm GaAs mHEMT, whose key features are presented in Table 5.1. The first chapter of this part of the thesis introduces the key features of the processes. The second chapter provides detailed DC, microwave, and noise characterization of discrete transistors. Finally, the LNA designs are presented in the third chapter of this part.

As alluded to in the Introduction, indium phosphide (InP) pseudomorphic HEMT (pHEMT) transistors have long been the semiconductor of choice for extremely low-noise amplifiers operating in RF, microwave and millimeter-wave bands due their superior noise and gain performance up through 150 GHz [13, 14, 15, 16, 17, 18]. On the other hand, among all semiconductors InP experiences the slowest development due to its niche market; thus, it also tends to be the most expensive.

Recent trends in radio astronomy are in the direction of increased number of elements, be it dishes or focal plane elements, simultaneously covering decade bandwidths. Such systems necessitate very large number of ultra-widebandwidth LNAs with low power consumption. Due to increasing number of receiving elements, there is renewed emphasis on cost, yield and process stability. This leads to reconsideration of GaAs which is commercially more attractive and thus, has enjoyed more investment in process development in recent years [22, 23, 24].

5.1 70 nm GaAs mHEMT

OMMIC's 70 nm GaAs mHEMT process, referred to as D007IH, employs InGaAs-InAlAs-InGaAs-InAlAs epitaxy with 52%/70% indium content on a metamorphic buffer over GaAs semi-insulating substrate as shown in Figure 5.1 [65]. The transistors are depletion mode and use double-mushroom

	NGC 100% pHEMT	NGC 75% pHEMT	OMMIC mHEMT
L_g [nm]	35	35	70
Channel	InAs	$In_{0.75}Ga_{0.25}As$	$In_{0.7}Ga_{0.3}As$
Substrate	InP	InP	GaAs
Substrate Thickness [μm]	50	50	100
f_T [GHz]	> 500	> 500	300
f_{max} [GHz]	> 500	> 500	350
max g_m [mS/mm]	2300	˜1700	2500
max I_{DS} [mA/mm]	900	N/A	600
V_{BD} [V]	2.5 (D-S)	N/A	3 (G-D)

Table 5.1: Key features, provided by the foundries, of the NGC and OMMIC HEMT processes at 300K

gates. The key features of the process are summarized in Table 5.1.

Scalable small-signal model (SSM) of the transistor as a function of bias as well as microwave models for all passive components of the process are provided by OMMIC. No temperature dependence except for ohmic loss of passive components is available in the design kit. Due to the lack of temperature dependence in the transistor model, the design of all OMMIC LNAs presented herein was performed at 300 K.

In addition to the MMIC LNAs, calibration chips were also fabricated (see Figure 5.2 for a micro photograph). The chip includes short-open-load-thru (SOLT) standards and four transistors of sizes 2f40, 2f80, 2f150, and 8f800 μm. The OMMIC LNA designs use the first three of the four sizes; discrete 2f40 and 2f150 μm devices have been characterized extensively as explained in the next chapter.

5.2 35 nm InP pHEMT

Northrop Grumman Corporation's (NGC) 35 nm InP HEMT process is still under development and has produced record-breaking results above 75 GHz [66, 17, 67, 20, 21, 68]. The active layer profile is shown in Figure 5.3 [18]. A typical, experimental run in this process includes two wafers with 75% and 100% indium mole fractions in the active InGaAs layer. The key features of both 75% and 100% devices are listed in Table 5.1.

Small-signal model of a two-finger device with 30 μm total gate periphery (2f30 μm) at $V_{DS} = 1$ V and $I_{DS} = 300$ mA/mm was provided by NGC for the 100% devices. The only temperature dependence included in the SSM is that of T_{drain} of the Pospieszalski model [69] and thermal noise

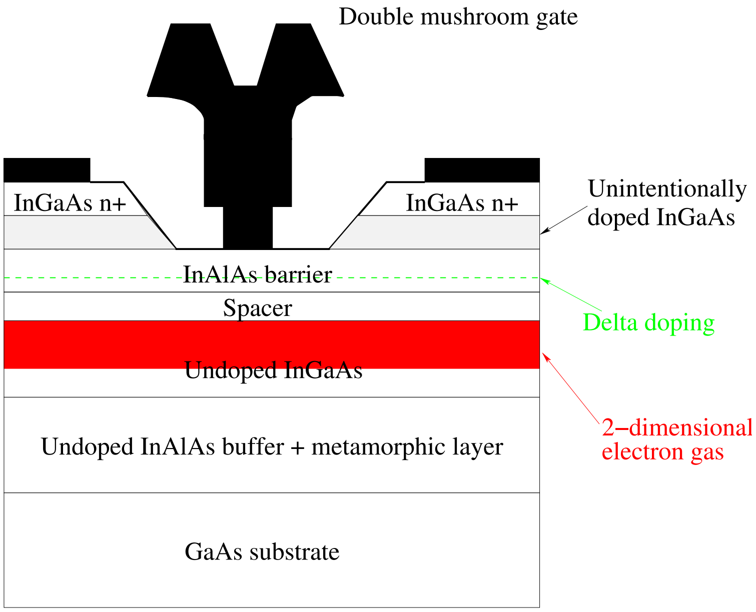

Figure 5.1: Active layer profile of OMMIC's 70 nm GaAs mHEMT

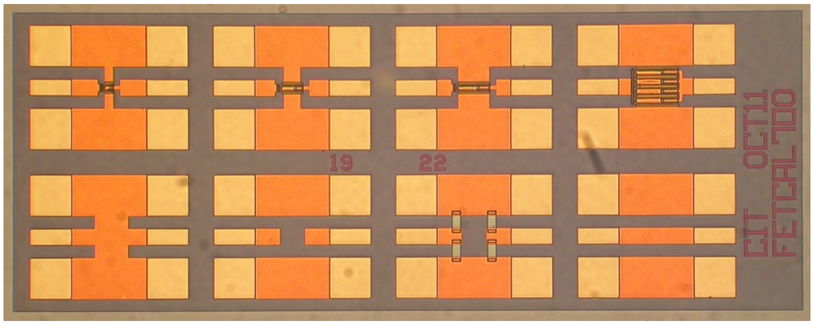

Figure 5.2: Micrograph of the OMMIC calibration chip

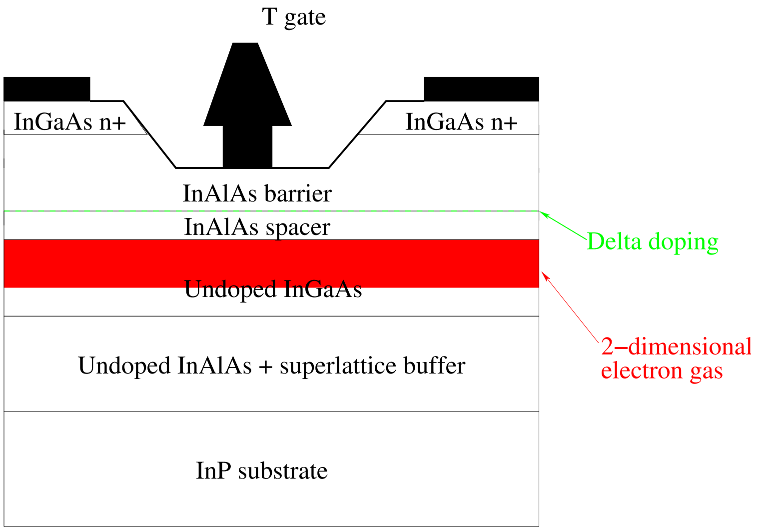

Figure 5.3: Active layer profile of NGC's 35 nm InP pHEMT

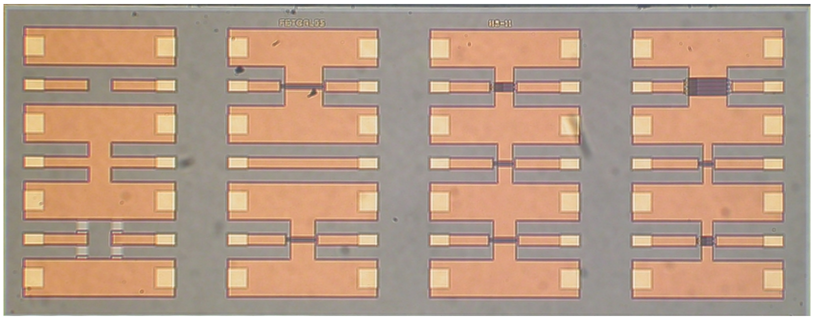

Figure 5.4: Micrograph of the NGC calibration chip

of all resistors. A scalable SSM was then generated to use in the LNA designs presented herein.

Calibration chips were fabricated on the NGC process as well and in addition to the SOLT standards, the following size transistors were included: 2f200, 2f130, 2f120, 2f80, 2f50, 4f200, 4f120, 8f800 μm. At least two of each size has been wafer-probed at room temperature; detailed measurements of discrete 2f50 and 2f200 μm devices are provided in the next chapter.

Chapter 6

Discrete HEMT Characterization

Knowledge of eight numbers, four complex and four real, are required to determine the microwave small-signal and noise performance of any two-port network at one frequency. The four complex numbers specify the current-voltage behavior of the two-port while the four real numbers are needed to completely characterize its noise performance. The determination of the former is predominantly accomplished by measuring the scattering parameters with the aid of a vector network analyzer (VNA). It is common to augment the scattering parameter measurements with DC measurements of transistor's $I-V$ characteristics.

Cryogenic measurement of a two-port's noise parameters, on the other hand, is much more difficult [70, 19]. Even at room temperature, they are measured with a dedicated test setup through lengthy tests. Therefore, the noise parameters are not explicitly measured in this work. Instead, they are inferred by using an extracted small-signal model and one 50 Ω noise measurement [71]. This approach requires a pre-determined model for the device under test. In the case of microwave transistors, Pospieszalski's FET noise model has been used widely and is employed herein [69].

6.1 Measurement Setup for DC and S-Parameters

The discrete devices investigated in this research were characterized with DC and S-parameter measurements in three stages:

1. On-chip measurements with wafer-probes at 300 K;
2. Measurements of the transistor in coaxial module at 300 K (see Figure 6.1);
3. Measurements of the transistor in coaxial module at 20 K.

While the first two data sets seem redundant, having them is very valuable in de-embedding the package effects at room temperature as well as ensuring there is no performance change when the calibration chips are diced to install the transistor in coax module. The DC measurements are

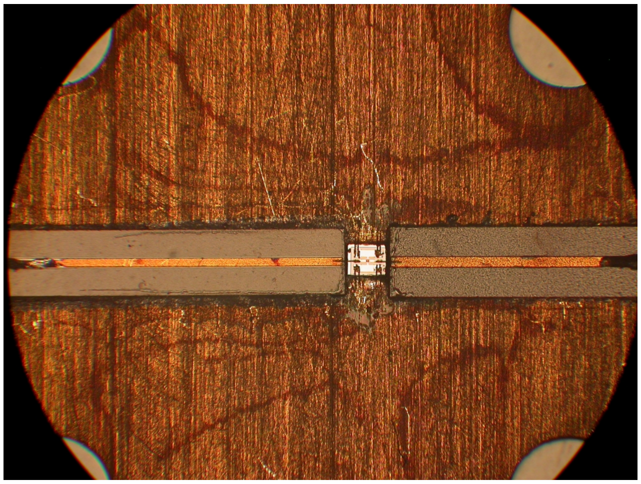

Figure 6.1: Photo of a discrete transistor in the coaxial module with K-connectors

performed with maximum 20 and 50 mV step sizes in gate and drain biases, respectively. The S-parameters are saved over a wide range of DC bias from 0.01 to 20 GHz.

Cryogenic measurements are performed with the transistor module installed in a cryostat with a copper strap to the cold head and connected to the VNA via two flexible coax cables which are not heat sunk to the cryostat cold head, as shown in top half of Figure 7.2(a) (in the red ellipse). The lack of cold straps on the flexible cables increases the physical temperature of the coaxial module; however, this increase is small and was observed to have no consequence on the measurements. Cryogenic S-parameters are de-embedded to the input of the transistor by using measurements of a short standard from the calibration chip in the same module as the transistor at 20 K.

6.2 DC Measurements

As mentioned earlier, transistors from the three processes (NGC 100%, NGC 75%, OMMIC) with varying gate widths were characterized extensively; however, only results from the largest and smallest devices are presented as they are sufficient to demonstrate the most important features. In the following, the large device means 2f200 μm for NGC and 2f150 μm for OMMIC, while the small device sizes are 2f50 μm for NGC and 2f40 μm for OMMIC.

Figure 6.2 plots drain current density as a function of drain and gate biases at room and cryogenic temperatures for the small transistor while those of the large devices are provided in Figure 6.3. Figures 6.4 and 6.5 present the extrinsic DC transconductance, namely

$$g_{m,DC} = \frac{dI_{DS}}{dV_{GS}} \tag{6.1}$$

of the small and large devices, respectively. The key observations from the room-temperature results are:

1. All devices show well-behaved and smooth response in terms of $g_{m,DC}$ and drain-source resistance r_{ds};
2. The peak $g_{m,DC}$ measured on the small transistors are 2.5, 1.8 and 1.6 S/mm for the 100%, 75%, and OMMIC devices, respectively, which are considerably different than those in Table 5.1;
3. The transconductance per unit width shows size dependence on the NGC 100% transistors. For example, the 2f50 μm device achieves peak transconductance of 2.5 S/mm whereas the 2f200 μm transistor only attains ˜ 1.6 S/mm. Tests on multiple transistors of identical sizes indicate that this is not due to device variability. The NGC 75% devices also exhibit some size dependence, but the OMMIC transistors do not.

The measurements at 20 K reveal some interesting features, namely:

1. The NGC 100% devices exhibit kinks—sudden current increase with small increase in V_{DS}—yielding large changes in output conductance;
2. The DC transconductance of the same devices is greatly enhanced with $V_{DS} > 0.4$ V and $I_{DS} < 200$ mA/mm;
3. The small OMMIC and NGC 75% transistors show very slight g_m enhancements with $V_{DS} \geq 0.8$ V and I_{DS} around 200-300 mA/mm;
4. The smaller devices on all processes display these features more prominently;
5. The drain current of the 2f40 μm OMMIC transistor begins to level out under high drain bias. A similar but more severe behavior was also observed on a different OMMIC 2f150 μm device as well as a few 100% NGC transistors. The OMMIC transistor was tested with a light-emitting diode which showed that the impact of light stimulation is quite small.

In total, eight NGC 100%, three NGC 75%, and four OMMIC transistors were DC characterized cryogenically. All of the 100% devices showed similar kinks, with the ones presented herein being among the less severe of all measured. All three 75% transistors performed at least as good as the ones shown here. One of the OMMIC devices exhibited time-varying DC characteristics, another small device showed kinks on par with the 2f200 μm 100% NGC device of this section, and the remaining two performed well.

Another FET parameter of interest in applications requiring extremely low noise is gate leakage current. It constitutes a shot noise source, therefore must be minimized [72]. It cannot be controlled by the circuit designer, but rather is a process parameter that is fairly dependent on gate passivation.

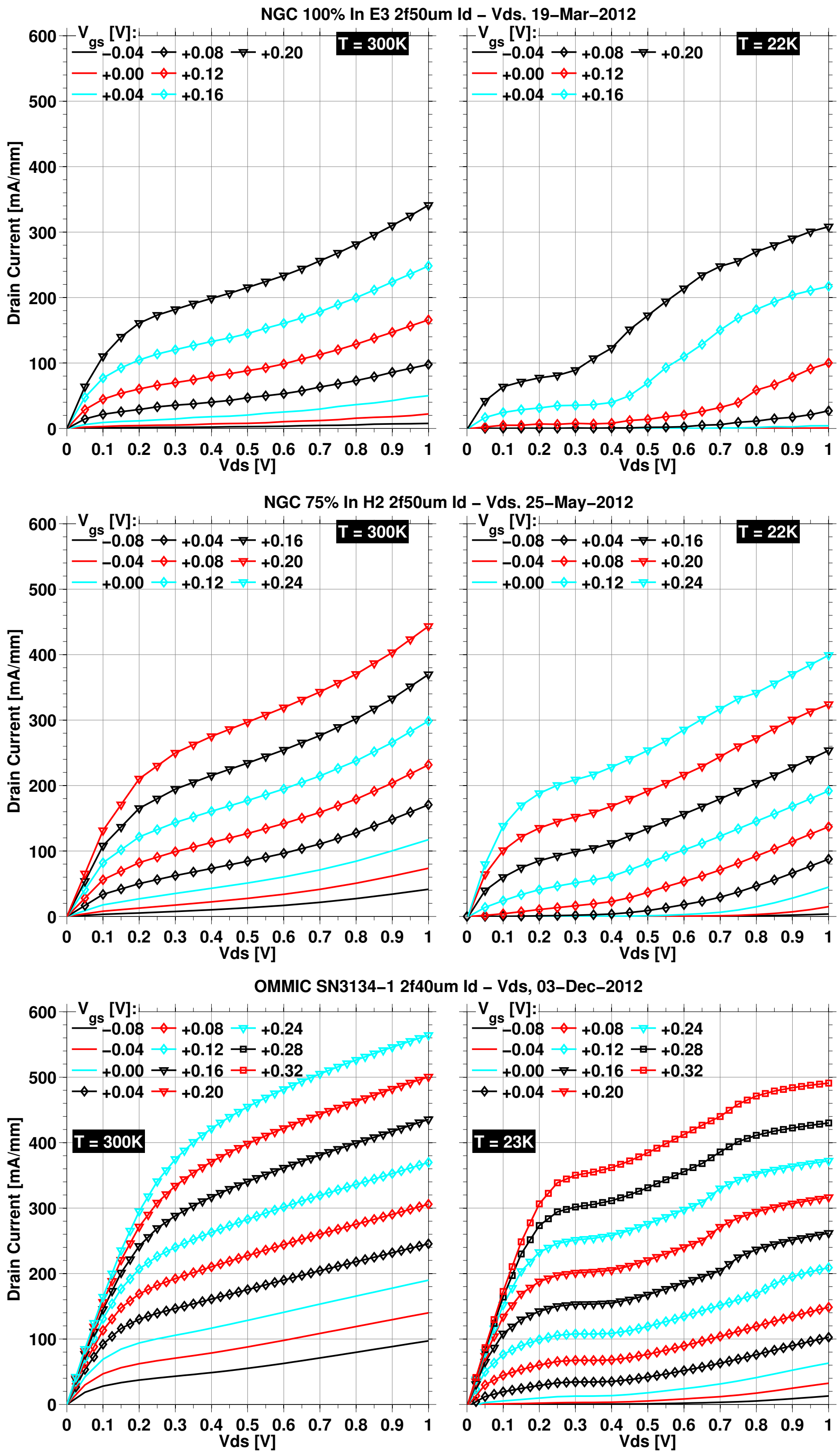

Figure 6.2: Measured $I_{DS} - V_{DS}$ of NGC 100% 2f50 μm (top), NGC 75% 2f50 μm (middle), and OMMIC 2f40 μm devices

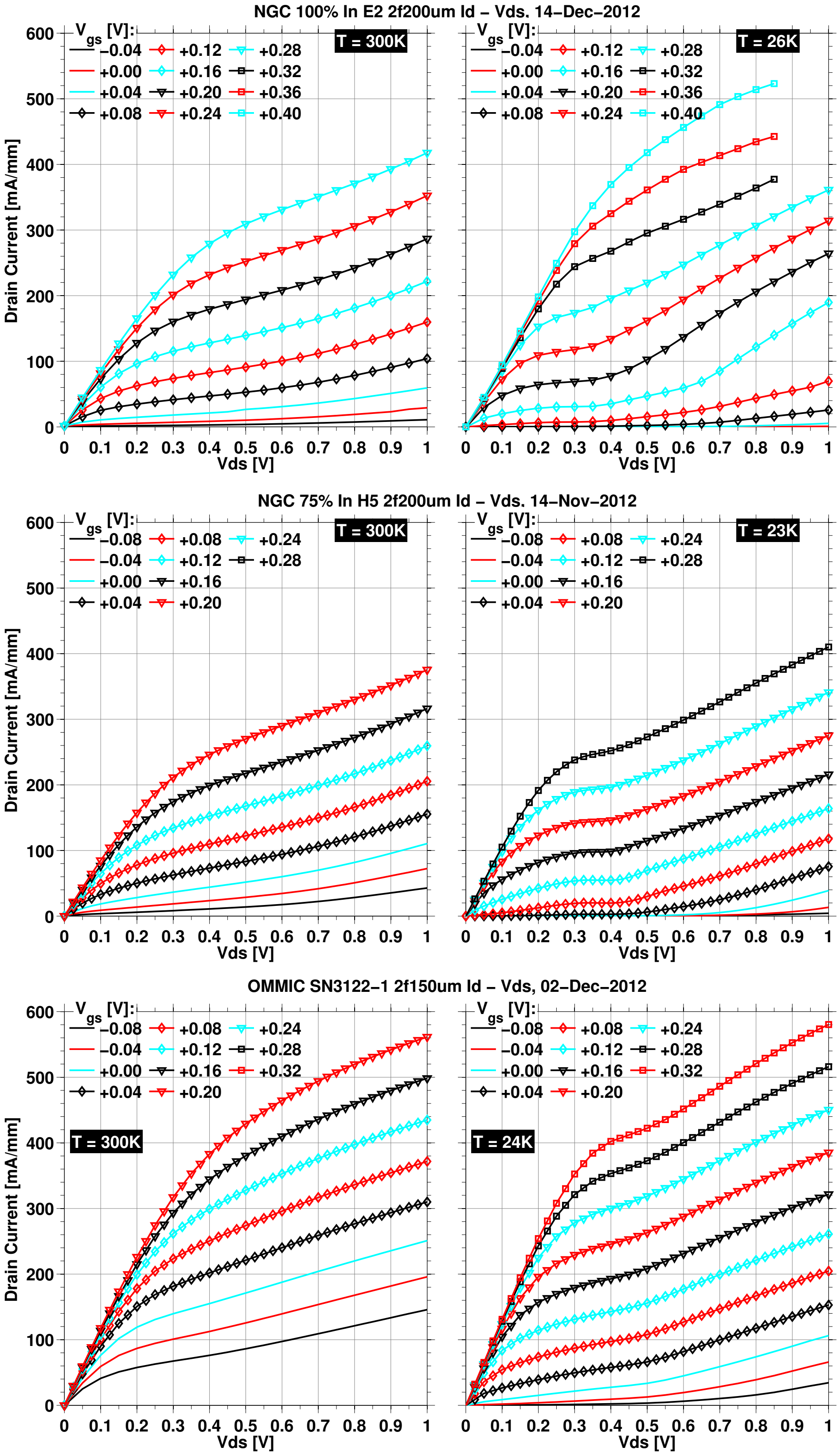
NGC 100% In E2 2f200um Id – Vds. 14–Dec–2012

NGC 75% In H5 2f200um Id – Vds. 14–Nov–2012

OMMIC SN3122–1 2f150um Id – Vds, 02–Dec–2012

Figure 6.3: Measured $I_{DS} - V_{DS}$ of NGC 100% 2f200 μm (top), NGC 75% 2f200 μm (middle), and OMMIC 2f150 μm devices

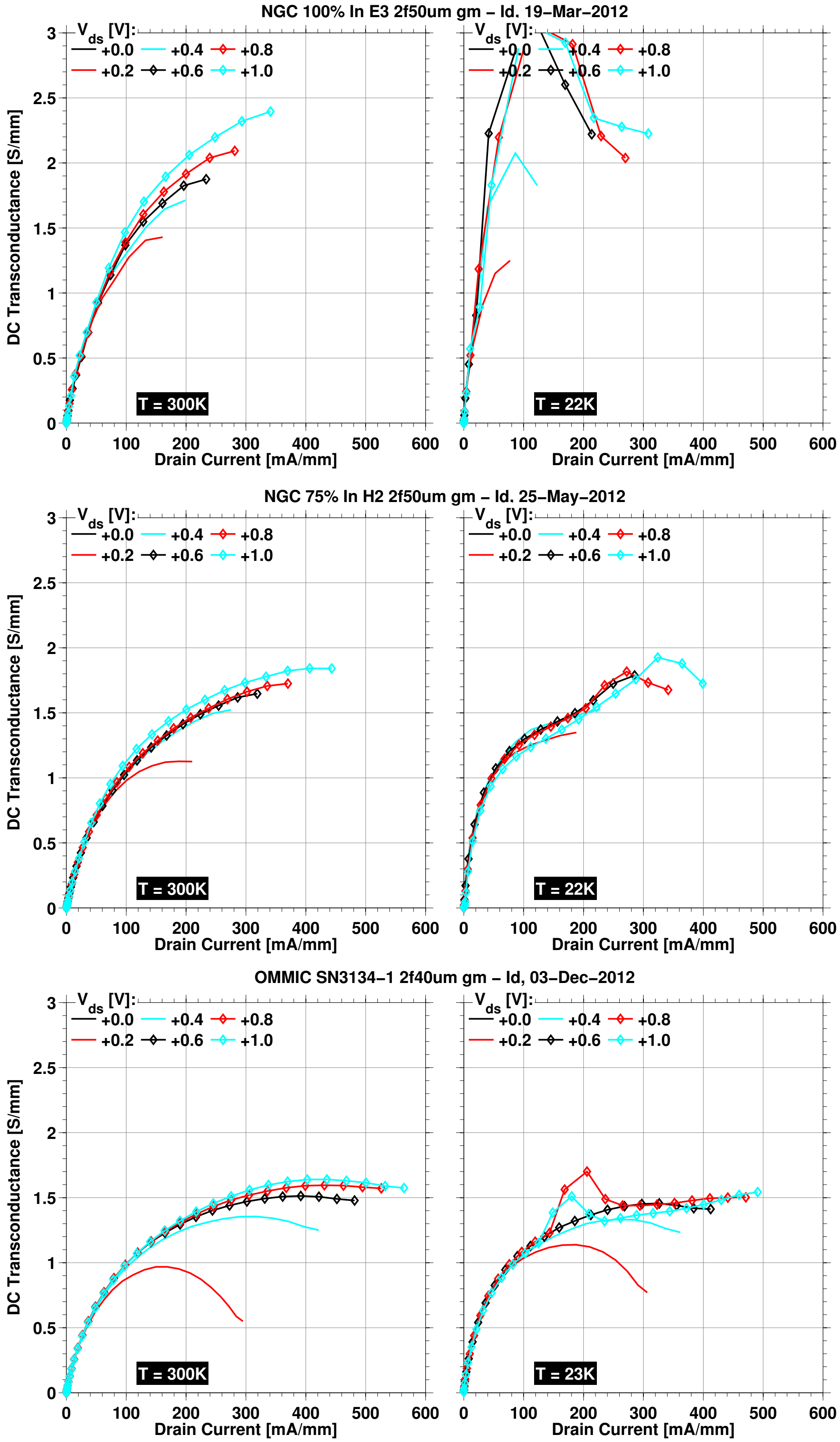

NGC 100% In E3 2f50um gm – Id. 19–Mar–2012

NGC 75% In H2 2f50um gm – Id. 25–May–2012

OMMIC SN3134–1 2f40um gm – Id, 03–Dec–2012

Figure 6.4: Measured extrinsic DC transconductance of NGC 100% 2f50 μm (top), NGC 75% 2f50 μm (middle), and OMMIC 2f40 μm devices

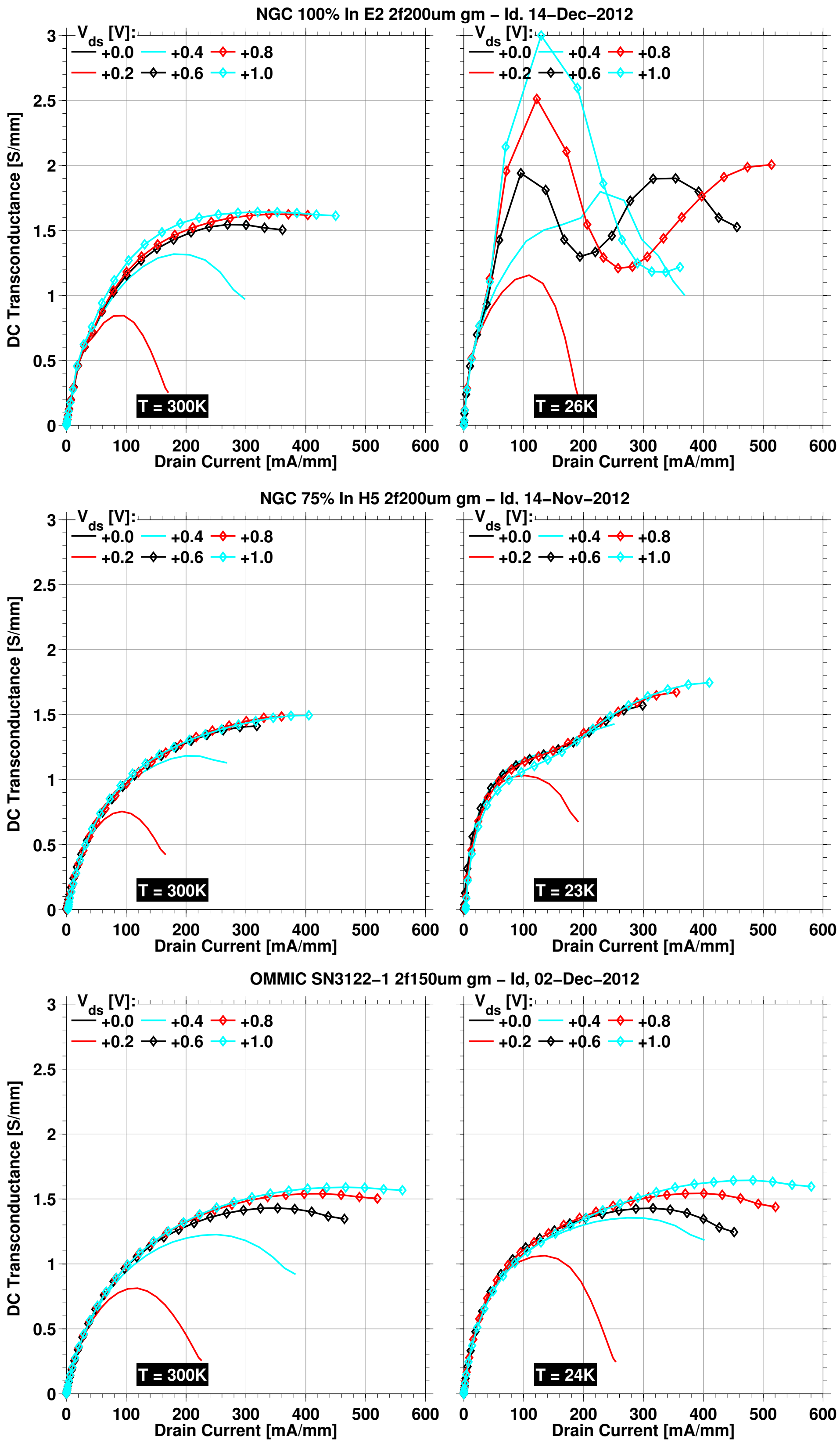

Figure 6.5: Measured extrinsic DC transconductance of NGC 100% 2f200 μm (top), NGC 75% 2f200 μm (middle), and OMMIC 2f150 μm devices

The gate leakage current of the transistors presented in this section have also been measured and the results appear in Figures 6.6 and 6.7.

All devices show significant gate leakage at room temperature. The measured leakage of the 100% devices is fairly typical among the eight we have tested; however, the small NGC 75% and OMMIC transistors shown here display above average gate leakage compared to others tested. This is attributed to chip-to-chip variability, which was observed to be significant for gate leakage. In all three processes, the large transistors are less leaky than small ones. As a reference, the increase in 50 Ω noise temperature due to 1 μA of gate leakage is approximately 0.39 K at 20 K physical temperature.

The gate leakage plots reveal another interesting feature: the bell-shaped response at high drain bias. It is visible on all devices to different extents at 300 K. It, along with total gate leakage, is much reduced cryogenically; however, it is still significant for the 100% transistor and is barely discernible on the other two. The bias range where this occurs correlates strongly with the bias range where the devices show $g_{m,DC}$ enhancement which suggests that these two symptoms are due to the same phenomenon.

Both kinks in the $I_{DS} - V_{DS}$ characteristics and bell-shaped gate leakage current have been empirically observed on HEMTs for almost three decades. The former is sometimes attributed to the so-called *kink effect* due to traps in the semiconductor [73, 74, 75], while the bell-shaped gate leakage is commonly interpreted as a symptom of *impact ionization.* Impact ionization, sometimes known as avalanche breakdown, occurs when energetic free electrons in the channel collide with semiconductor atoms in the lattice thereby generating new electron-hole pairs. The newly generated electrons are swept by the high electric field in the channel which causes *increased* I_{DS}. The corresponding holes are attracted by the relatively negative-biased gate-source region where some tunnel through the gate Schottky barrier resulting in *increased* I_{GS}. The remaining holes accumulate in the gate-source and buffer regions attracting more electrons. This positive feedback system then continues to build up. Impact ionization is exacerbated by the high indium content due to the lower energy barrier to generate new electron-hole pairs; thus, is especially more prominent on the NGC 100% transistors.

There is, however, a third interpretation that says that both phenomena are due to impact ionization [76, 77, 78, 79, 80, 81] which is the gist of the argument made herein. While the DC results of this section alone are not sufficient to demonstrate this point fully, the microwave measurements of the next section offer more clues to origins of these phenomena. In particular, Reuter and others [76, 77, 78] have shown that impact ionization also causes inductive drain impedance up to a few GHz in short-channel MOSFET, HFET, and HEMT transistors at room temperature. Such inductive output impedance is indeed observed on most of the transistors tested during this research as explained next.

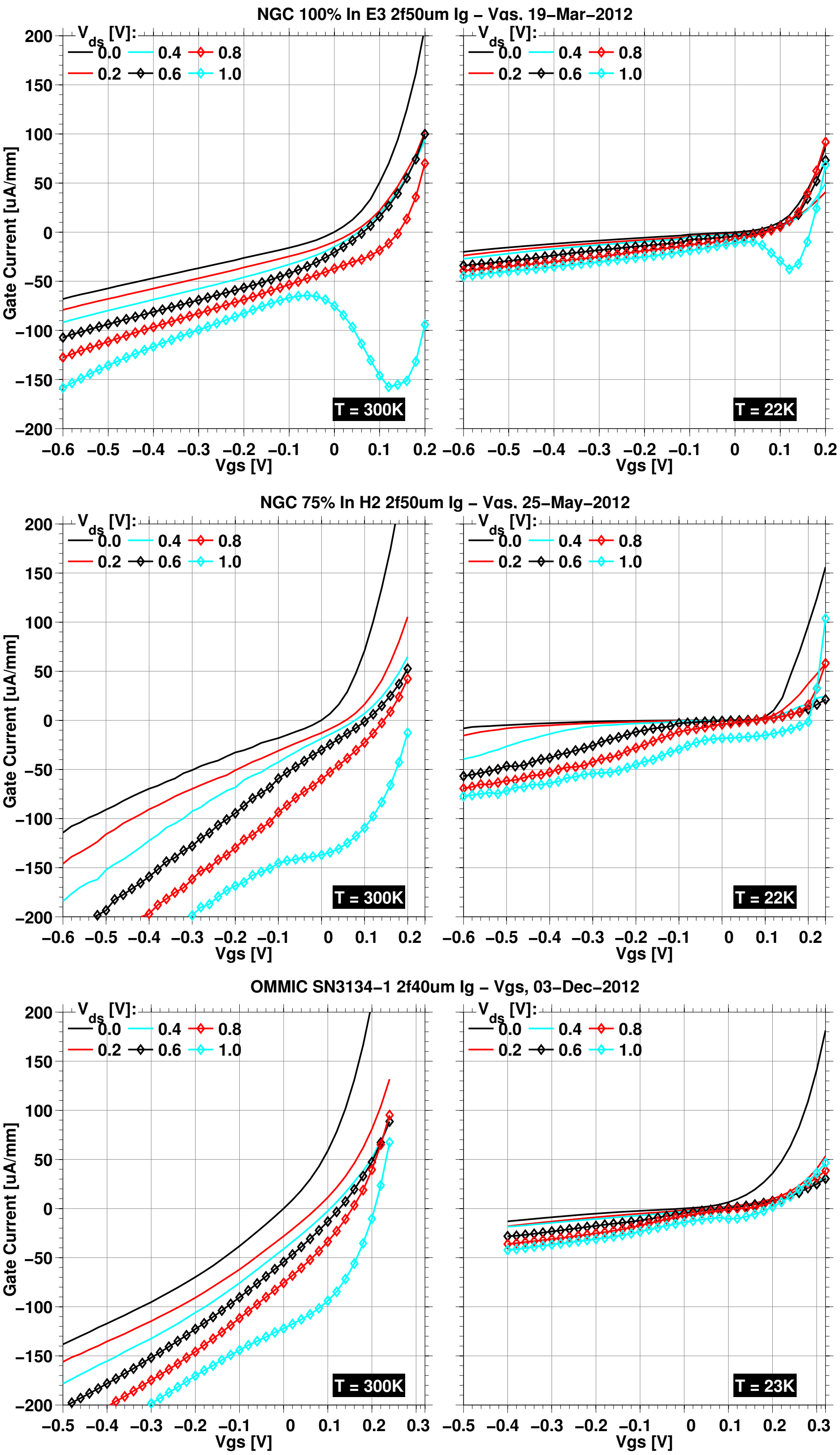

Figure 6.6: Measured $I_{GS} - V_{GS}$ of NGC 100% 2f50 μm (top), NGC 75% 2f50 μm (middle), and OMMIC 2f40 μm devices

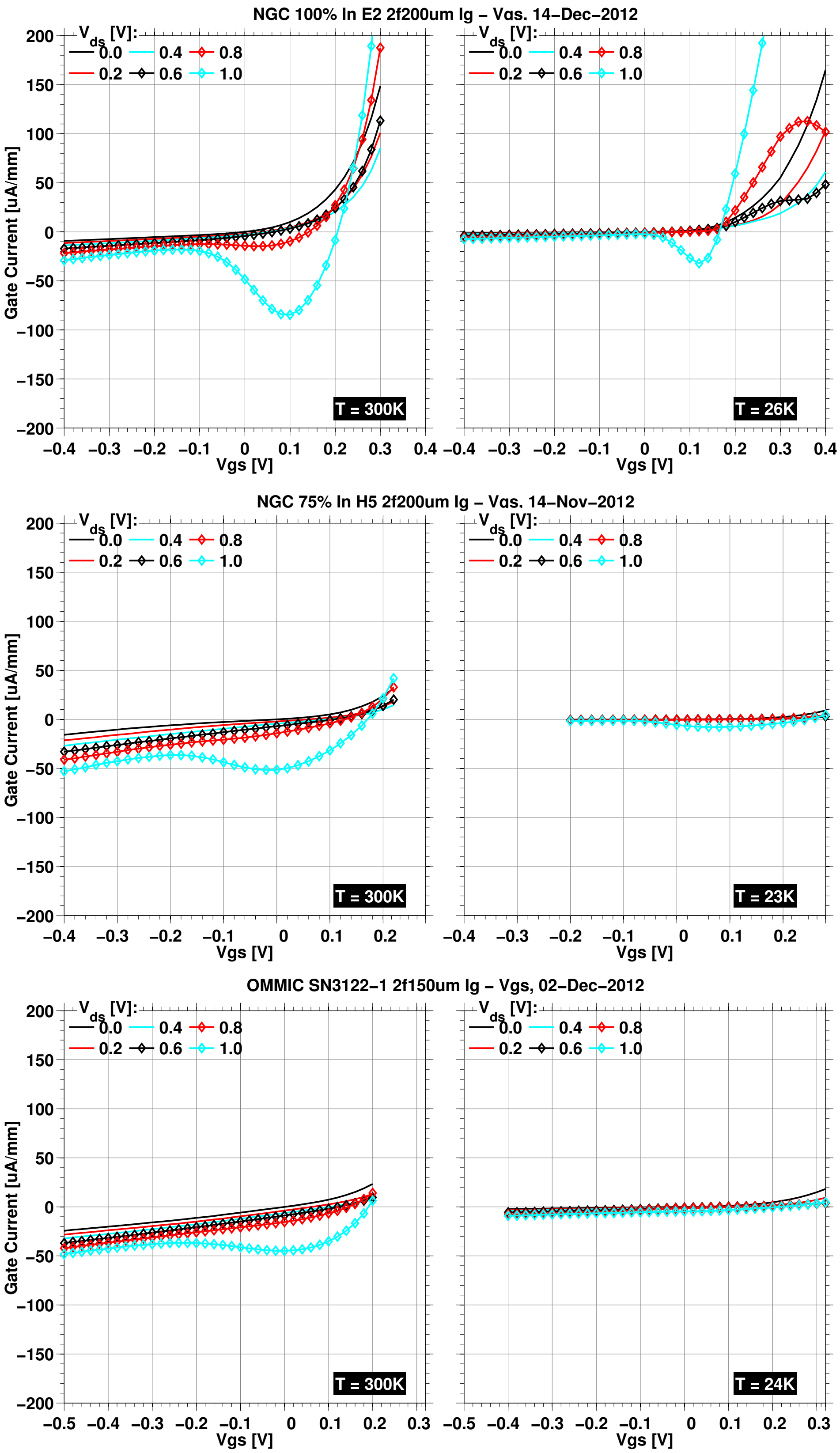

Figure 6.7: Measured $I_{GS} - V_{GS}$ of NGC 100% 2f200 μm (top), NGC 75% 2f200 μm (middle), and OMMIC 2f150 μm devices

6.3 S-Parameter Measurements

In addition to DC tests, almost all of the transistors were also characterized cryogenically by measuring their scattering parameters over wide range of DC bias. In this research, this extensive database of S-parameters is used for two purposes: 1) to evaluate effects of impact ionization on microwave performance; 2) to perform small-signal model extraction for use in transistor noise modeling as detailed in the next section. The first half of this section discusses the former.

6.3.1 Inductive drain impedance

Figure 6.8 illustrates measured, de-embedded scattering parameters of the NGC 100% 2f50 and 2f200 μm transistors up to 10 GHz at 300 and 20 K. In particular, the plots include output reflection coefficient and gain of each device under two different current bias with $V_{DS} = 0.8$ V.

It is seen that both transistors do in fact exhibit inductive output impedance at either temperature. This inductive loop, as it is seen on the Smith chart, is smaller at 300 K under low current bias, and expands considerably when the transistor is cooled or bias is increased. At 20 Kelvin physical temperature and under high bias where impact ionization is more prominent, the loop expands to the extent that negative output resistance is observed on the small transistor. Additionally, further increasing drain bias current shrinks the inductive loop which is consistent with decrease in impact ionization as gate bias is increased causing smaller gate-drain voltage drop.

All of the 100% NGC transistors measured cryogenically showed inductive output impedance in addition to the $I - V$ kinks and bell-shaped gate leakage. Moreover, the inductive loop expands outside the Smith chart at cryogenic temperature over a range of bias settings on all size transistors except the 2f200 μm presented in Figure 6.8(b). In comparison, the 75% NGC and the OMMIC transistors also displayed inductive output impedance; however, the loop was seen to span significantly smaller frequency range and exhibited much less expansion under cooling.

6.3.2 Small-Signal model extraction

Calculation of element values in HEMT small-signal models has been investigated extensively in the literature [82, 83, 84, 85, 86, 87]. The approach usually involves comparison of measurements to a small-signal model based on device physics which can take on slightly different forms depending on the application. The model used in this work appears in Figure 6.9 and is one of the most widely used for HEMTs in microwave and millimeter-wave frequencies [69]. In Figure 6.9, the components of the intrinsic FET are the bias-dependent small-signal parameters while the parasitic components (with capital subscripts) are assumed constant versus bias.

Even with an extensive collection of measurements, the problem of finding the element values usually entails solution of an overdetermined set of equations because of the large number of un-

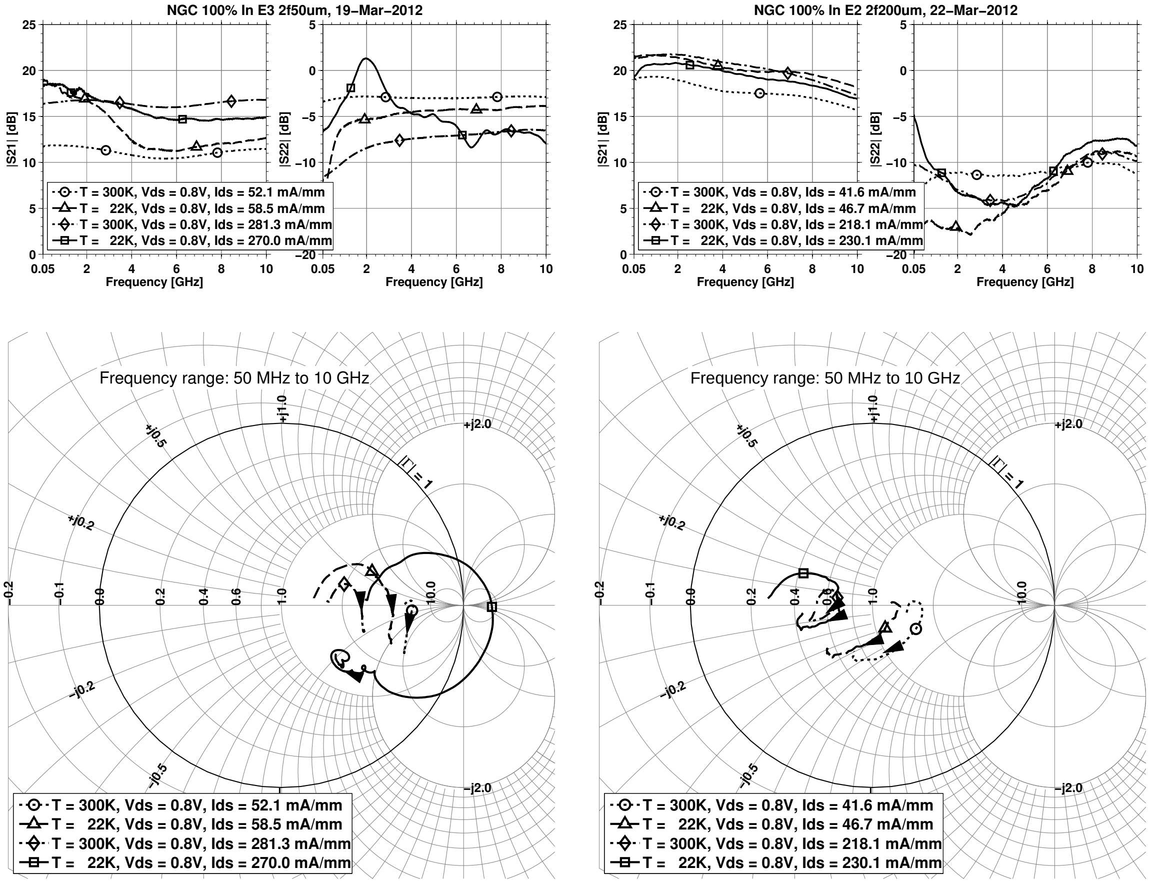

(a)

(b)

Figure 6.8: Measured, cryogenic S_{22} and S_{21} of the 2f50 and 2f200 μm NGC 100% transistors. The measurements are de-embedded to the edge of the devices which are the same devices as those presented in Section 6.2.

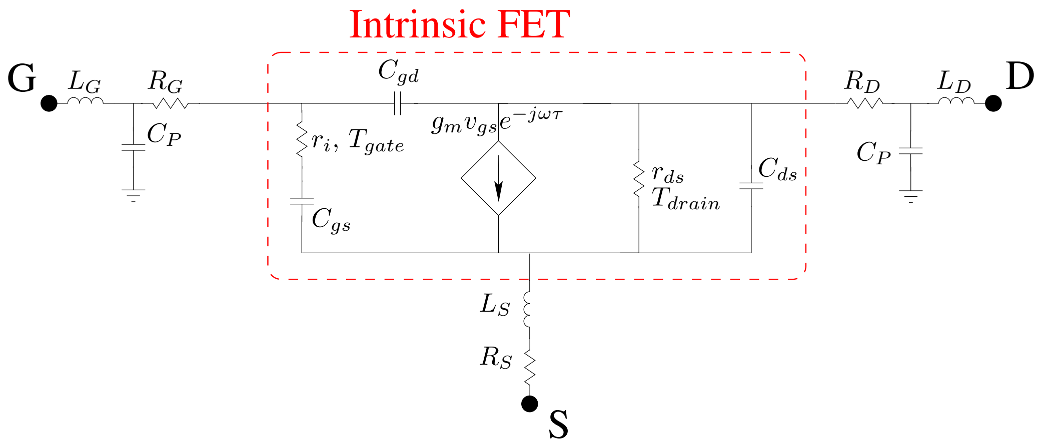

Figure 6.9: The HEMT small-signal model used in this work

knowns. Thus, the obtained values are not unique and some frequently turn out to be physically impossible (e.g., negative or extremely large/small values). Moreover, the element calculation has to be repeated for each bias point of interest. This is a formidable task and is not pursued in this research. Instead, a hybrid approach is taken that can be summarized as:

1. Determine the parasitic element values from foundry specifications and cold-FET measurements,
2. Estimate r_{ds} and g_m from measured, de-embedded low-frequency S-parameters,
3. Tweak the foundry-specified capacitor and r_i values to fit model to measurements at two or three bias points, and
4. Assume a certain bias dependence for the capacitors and r_i such that the values agree with those obtained in step 3,

where the first two steps follow the "hot-FET/cold-FET" method outlined in [85]. While this approach may not be the most robust or accurate for calculating the element values, it should be sufficiently accurate for the goals in this research: 1) evaluating microwave effects of impact ionization; 2) low-frequency noise modeling.

6.3.2.1 Parasitic resistances

The first step in the SSM extraction is determination of parasitic element values. This is accomplished via wafer-probed DC and S-parameter measurements with the gate of the transistor forward biased using a current source. The vector network analyzer is calibrated to the tip of the wafer-probes using CS-5 calibration substrate[1]. Then, the VNA ports are extended to the edge of the transistor using the short- and open-calibration standards included on the calibration chip from each process. This step is critical as lack of or incorrect port extension would yield under- or over-estimation of extrinsic elements in the FET small-signal model.

A small and a large device from each process were tested as the gate current was varied from 1 μA to 20 mA. The resulting gate voltages were recorded as well as the S-parameters for gate currents above 1 mA. Using the simplified small-signal model of the HEMT under forward-bias [85], values of the parasitic resistors and inductors can be obtained from the following equations:

$$\begin{aligned} Z_{11} &= R_G + R_S + \frac{R_{ch}}{3} + R_{dy} + j\omega\left(L_G + L_S\right) \\ Z_{12} &= R_S + \frac{R_{ch}}{2} + j\omega L_S \\ Z_{22} &= R_D + R_S + R_{ch} + j\omega\left(L_D + L_S\right) \end{aligned} \tag{6.2}$$

---

[1] GGB Industries, Florida, USA

where Z_{ij} are the impedance parameters [88]; R_{ch} is the channel resistance; R_{dy} is the dynamic resistance of the gate diode. An implicit assumption in these equations is that the measurements are performed at sufficiently low frequency such that the pad capacitance C_P can be ignored. The channel resistance is assumed to be zero which is reasonable for short gate-length devices such as the ones investigated in this work. The dynamic resistance of the diode is given by

$$R_{dy} = n\frac{kT}{qI_G} \tag{6.3}$$

where n is the diode ideality factor; k is the Boltzmann's constant; T is the ambient temperature; q is the electronic charge and I_G is the forward-bias gate current [85]. R_{dy} is either calculated using this equation if the diode ideality factor is known, or not calculated at all, because extrapolating $\Re\{Z_{11}\}$ versus $1/I_G$ to $1/I_G \to 0$ yields

$$\lim_{I_G\to\infty} \Re\{Z_{11}\} = R_G + R_S. \tag{6.4}$$

Since R_S is given by $\Re\{Z_{12}\}$, R_G and R_D are easily determined.

The second way of estimating $R_G + R_S$ is by using the DC current-voltage relationships. In particular, total resistance obtained by using Ohm's law is given as

$$\frac{V_{GS,i} - V_{GS,i-1}}{I_{G,i} - I_{G,i-1}} = R_G + R_S + \underbrace{\frac{nkT}{q}\frac{2}{(I_{G,i} + I_{G,i-1})}}_{R_{dy}} + R_{cable} \tag{6.5}$$

where $V_{GS,i}$ and $I_{G,i}$ are the ith recorded gate voltage and current, respectively, and R_{cable} is the total DC resistance in the test setup cables (easily measured by replacing device under test with a short). This method requires knowledge of the diode ideality factor. For OMMIC devices, $n = 1.67$, obtained from OMMIC's large-signal model, is used. For the NGC devices, $n = 1.5$ is assumed. R_S is obtained from the cold-FET method. The results from both techniques appear in Table 6.1 normalized to total gate periphery W_{tot}, i.e.,

$$\begin{aligned} R_G &= R_{G0}\frac{W_{tot}}{N_f^2} \\ R_S &= R_{S0}\frac{1}{W_{tot}} \\ R_D &= R_{D0}\frac{1}{W_{tot}} \end{aligned} \tag{6.6}$$

It is seen that determination of R_{G0} using the small devices is problematic which is most likely due to difficulty in obtaining a reliable gate finger resistance measurement on short finger widths. In addition, normalization in (6.6) amplifies any errors in measurement. In general, the values obtained

	Method	OMMIC		NGC 100%		NGC 75%	
		2f40	2f150	2f50	2f200	2f50	2f200
R_{G0} $[\frac{\Omega\text{-finger}^2}{\text{mm}}]$	Cold-FET	454	121	454	164	477	153
	DC	112	96	262	146	205	148
	Foundry	200/3		400/3		400/3	
	Final	80		140		140	
R_{S0} [Ω-mm]	Cold-FET	0.23	0.19	0.25	0.21	0.19	0.17
	Foundry	0.2		0.12		0.12	
	Final	0.2		0.19		0.19	
R_{D0} [Ω-mm]	Cold-FET	0.26	0.3	0.21	0.42	0.24	0.36
	Foundry	0.29		0.015		0.015	
	Final	0.29		0.3		0.3	

Table 6.1: Values of extrinsic resistors for OMMIC and NGC devices

from these analyses are fairly close to foundry-specified values also listed in the same table and the final values used in the rest of the thesis are chosen to be roughly the average of measurements and foundry specifications (ignoring the outlier measurements from small devices). The parasitic inductor values are obtained from the foundry small-signal models

$$L_{G0}\,[\text{pH-finger/mm}] = \begin{cases} 338 & \text{OMMIC} \\ 233 & \text{NGC} \end{cases}$$

$$L_{S0}\,[\text{pH/finger}] = \begin{cases} 1.6 & \text{OMMIC} \\ 1 & \text{NGC} \end{cases}$$

$$L_{D0}\,[\text{pH-finger/mm}] = \begin{cases} 398 & \text{OMMIC} \\ 87 & \text{NGC} \end{cases}$$

which are scaled as

$$L_G = L_{G0}\frac{W_{tot}}{N_f}$$
$$L_S = L_{S0}N_f$$
$$L_D = L_{D0}\frac{W_{tot}}{N_f}$$

assuming $N_f \geq 2$. Because the extracted small-signal models are primarily used for low frequencies—i.e., around 1 GHz—,these values are deemed to be sufficiently accurate.

6.3.2.2 Simplified hot-FET method: r_{ds} and g_m

Once device parasitics are known, microwave parameters of the intrinsic FET are easily obtained by transforming the de-embedded S-parameters to Z-parameters, subtracting the signature of the parasitics

$$\mathbf{Z}^{int} = \begin{bmatrix} Z_{11} - R_S - R_G - j\omega\left(L_G + L_S\right) & Z_{12} - R_S - j\omega L_S \\ Z_{21} - R_S - j\omega L_S & Z_{22} - R_S - R_D - j\omega\left(L_D + L_S\right) \end{bmatrix}, \tag{6.7}$$

and inverting $\mathbf{Z}^{int}$ to obtain the Y-parameters as the π-topology of the small-signal model naturally lends itself to admittance representation. Then, the drain-source resistance r_{ds} is given by

$$r_{ds} = \frac{1}{\Re\left\{Y_{22}\right\}} \tag{6.8}$$

and the intrinsic transconductance by

$$g_m = \sqrt{\Re\left\{Y_{21}\right\}^2 + \left(\Im\left\{Y_{21}\right\} + \omega C_{gd}\right)^2 \left[1 + \left(\omega C_{gs} r_i\right)^2\right]} \tag{6.9}$$

Explicit expressions for r_i, C_{gs}, and C_{gd} can be obtained using the results in [85] to extract values for g_m; however, this is not pursued because extraction of r_i, C_{gs}, and C_{gd} is tricky even with closed-form equations. It tends to be sensitive to noise in measurements and can yield unrealistic values.

Therefore, a different approach is followed here. Noting that the transistor is in source-degenerated common-source configuration, the closed-form expression for the intrinsic RF transconductance is found to be

$$g_m\left(S_{21}\right) = \frac{-A_v\left(R_{load} + r_{ds} + R_S\right)}{A_v r_{ds} R_S - R_{load} r_{ds}} \quad \text{with} \quad A_v \equiv \frac{10^{S_{21}/20}}{2} \tag{6.10}$$

where $R_{load} = 50\,\Omega$ and S_{21} is the measured, de-embedded gain (note that this is not the intrinsic S_{21}).

These steps are carried out in MATLAB using some specially written scripts as well as some publicly available functions for matrix manipulations[2]. The cryogenic results are presented in Figure 6.10 overlaid with those obtained from DC measurements. The drain-source conductance $g_{ds} = \frac{1}{r_{ds}}$ is plotted instead of r_{ds} as the former is more commonly used in device physics literature. It is obtained using the simplified hot-FET method and the scattering parameters between 1 and 2.5 GHz. The plots reveal couple of important observations:

NGC 100%: There is significant difference between r_{ds} and g_m obtained with the two methods.

This device, as shown above, exhibits the most severe signs of impact ionization among the

---

[2] `http://www.mathworks.com/matlabcentral/fileexchange/6080-s-parameter-toolbox-+-z-y-h-g-abcd-t`

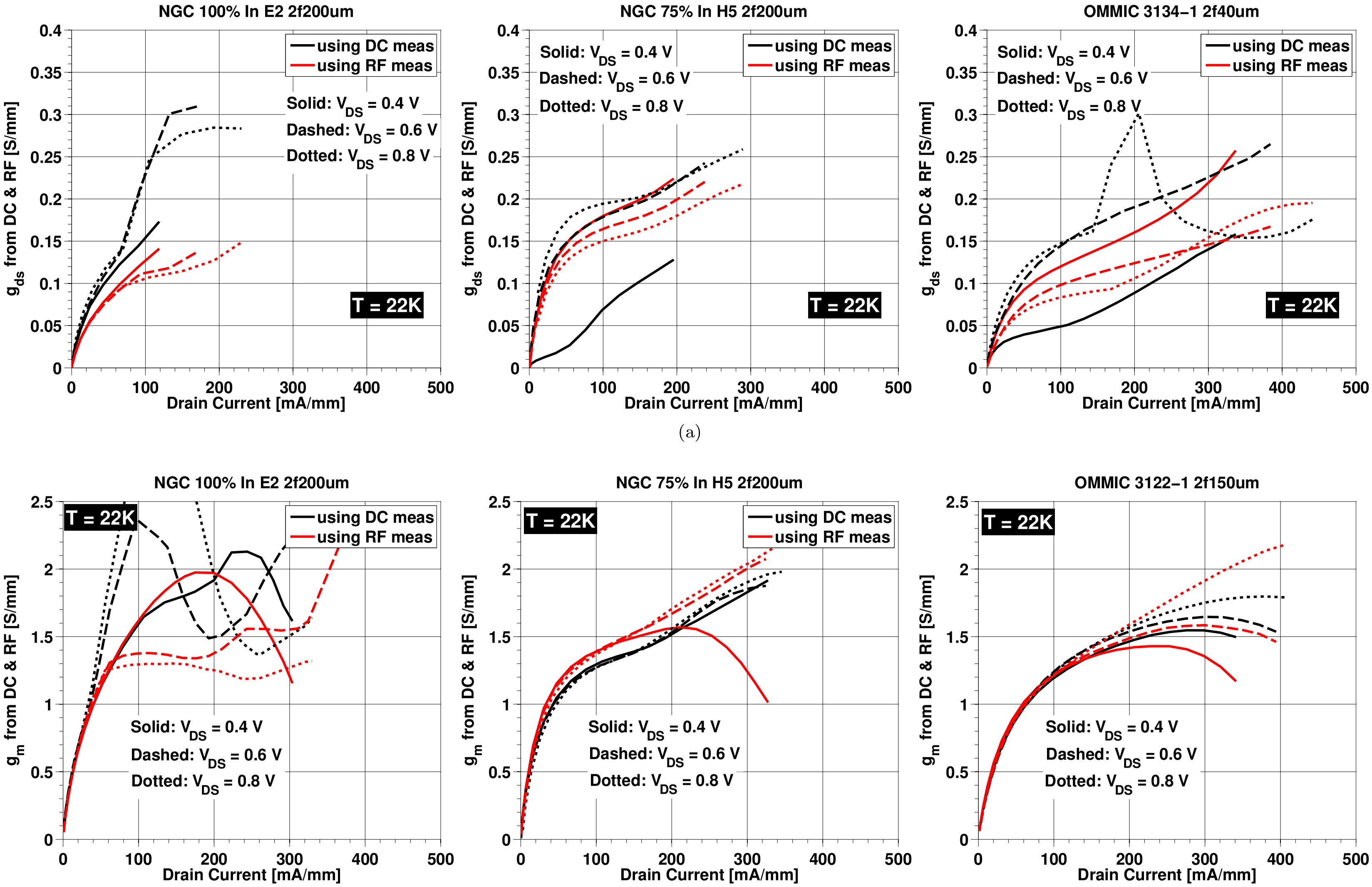

(a)

(b)

Figure 6.10: Comparison of DC and RF (a) g_{ds} and (b) g_m (intrinsic) of the NGC 100%, NGC 75% and OMMIC transistors

large transistors tested. While the RF g_m is much smoother than $g_{m,DC}$, it still shows large fluctuations, especially at $V_{DS} = 0.6$ V, and the transconductance at $V_{DS} = 0.8$ V seems to reach a plateau at very low current density. The difference in the drain-source conductance is very large except at low drain bias. That the DC and RF g_{ds} are so different is expected when traps are considered, which because of their time constant cannot respond to high-frequency signals [81]. However, these curves also suggest that traps alone are not sufficient to explain all features of the measurements.

NGC 75%: With the exception of g_{ds} at $V_{DS} = 0.4$ V, the difference between the two data sets is much smaller and g_{ds} show smoother response. The RF g_m is slightly higher, but its shape closely follows the DC curves except at $V_{DS} = 0.4$ V and $I_{DS} > 200$ mA/mm where it begins to roll off.

OMMIC: First, it should be noted that the RF g_{ds} results are measured on the small OMMIC device, because that is the only size cryogenically tested for S-parameters. Consequently, the plotted DC g_{ds} curves are also from the same transistor. The jump in g_{ds} at 200 mA/mm correlates with the $g_{m,DC}$ enhancement seen in Figure 6.4. Also, a slope change is observed on the RF g_{ds} near the same bias. There is considerable difference between RF and DC g_{ds}; however, shape of the curves at a given drain bias look fairly similar. The transconductance curves of the large OMMIC transistor look very similar for both methods.

6.3.2.3 Remaining elements of the small-signal model: Capacitors and r_i

In order to complete the small-signal model extraction, the values for the capacitors C_{gs}, C_{gd}, C_{ds} and the gate-source resistance r_i need to be computed. As alluded to earlier, the OMMIC small-signal model includes values for all of these components as a function of bias at 300 K. Therefore, for the three capacitors in the OMMIC transistor model, the values are taken directly from the foundry-specified SSM. As a check, these numbers have been verified with measurements at room temperature at a couple of bias points.

On the other hand, the NGC SSM was only provided at $V_{DS} = 1$ V and $I_{DS} = 300$ mA/mm for a 2f30 μm 100% device. Therefore, values for the three capacitors have been estimated by manually fitting measured, de-embedded S-parameters to modeled results at a handful of bias points. The bias dependence of capacitors is then assumed to be identical to that of OMMIC transistors. Because of the observed size dependence of the device parameters even after normalizing to total gate periphery, this process is carried out once for the 2f200 μm transistor and once for the 2f50 μm device.

This leaves r_i as the only unknown to determine. It is sometimes called the gate-charging resistor and is very difficult to measure accurately as it is a very small resistance in series with two resistors of approximately comparable magnitude and a very large reactance. As such, it is usually either assumed constant or obtained from model fitting to S-parameter data. The latter approach is not straightforward because the values obtained for r_i tend not to be unique and the process has to be repeated for each bias point of interest. In order to alleviate these issues, the following approach is taken to estimate r_i at room temperature:

1. Obtain an estimate by comparing wafer-probed, de-embedded S-parameter measurements to simulations at two or three bias points,
2. Restrict the range of values r_i can take by using low-frequency 50 Ω input noise temperature $T_{50,\,1\mathrm{GHz}}$ measurements (see next section) using measured values of r_{ds}, g_m , R_G, R_S and assuming r_i is an ohmic-type resistor at ambient temperature [69],
3. Further restrict possible values of r_i by restricting the temperature of r_{ds}, T_{drain}, to a reasonable, expected range, e.g., 2000–3000 K at room temperature.

While this method does not necessarily guarantee uniqueness, the resulting values should be reasonably accurate. The bias dependence of r_i is then assumed to be similar to that provided in the OMMIC small-signal model, i.e.,

$$r_i\left(I_{DS}\right) = \alpha \tanh\left(\frac{1}{100} I_{DS}\right) + 0.1 \tag{6.11}$$

where α is 0.1 for OMMIC and 0.05 for NGC and are picked by fitting predicted values to the values obtained in step 1. Units of I_{DS} and r_i are mA/mm and Ω-mm, respectively. This assumed functional form is quite similar to expected bias dependence of C_{gs} [65].

The temperature dependence of the small-signal model elements is another source of complication. For r_{ds} and g_m, the measured values are used. The capacitor values are assumed to decrease 10% from 300 to 20 Kelvin, which is somewhat conservative as others have estimated 15-20% decrease [89]. r_i is assumed unchanged. The parasitic resistor values are halved cryogenically. The values for all the small-signal model elements are provided in the next section as a function of bias and temperature.

6.4 T_{drain} Measurements

Another consequence of impact ionization has been reported to be significantly increased minimum noise figure at low frequencies [76]. In order to characterize noise performance of the NGC and OMMIC transistors and evaluate effects of impact ionization, 50 Ω input noise temperature $T_{50,\,1\mathrm{GHz}}$ was measured at room and cryogenic temperatures from which T_{drain} of the Pospieszalski model was extracted for the large devices from all processes.

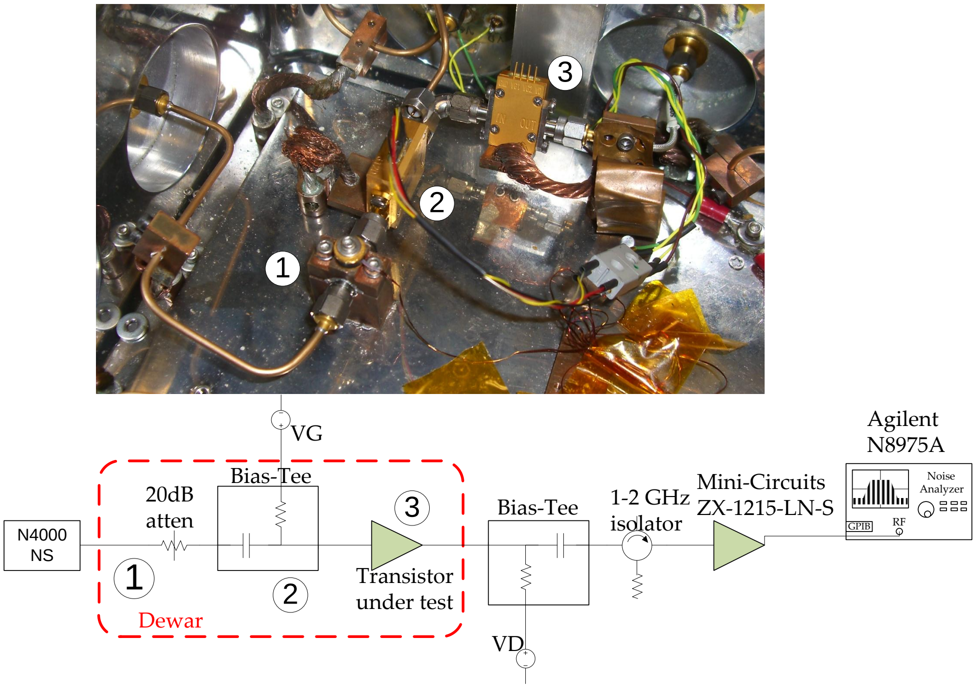

Figure 6.11: T_{drain} measurement setup block diagram.

6.4.1 Measurement setup

The single 50 Ω noise measurement required to model a two-port's noise performance could be performed cryogenically in a number of ways [90]; however, the most common approach is the cold attenuator method because of its good accuracy and relative insensitivity to uncertainty in excess noise ratio [90, 19]. This approach is used for the T_{drain} measurements.

The block diagram of the test setup used in T_{drain} measurements is displayed in Figure 6.11. The cold 20 dB attenuator is followed by a custom-built resistive bias-tee (R =50 kΩ and C =22 pF) to provide gate bias for the device under test. The bias-tee loss was measured cryogenically and taken into account in the noise measurements. The drain bias is provided through a Mini-Circuits ZX85-12G+ wideband bias-tee outside the dewar. The isolator following the bias-tee facilitates calculation of the second-stage noise contribution as a function of transistor output reflection coefficient [91, 92]. Specifically, let T_{50} and s_{21} represent the measured 50 Ω noise temperature—corrected by the noise figure analyzer (NFA)—and voltage gain of the transistor in linear units. Using the expression for output resistance of the transistor in source-degenerated common-source configuration, i.e.,

$$r_{out} = r_{ds}\left(1 + g_m R_S\right) + R_S, \tag{6.12}$$

the drain reflection coefficient is obtained

$$\Gamma_{out} = \frac{r_{out} - 50}{r_{out} + 50}. \tag{6.13}$$

The noise contribution of the back-end as a function of output reflection coefficient is found to be

$$T_{backend,corr} = \left(T_{backend} + 300\left|\Gamma_{out}\right|^2\right)\frac{1}{1 - \left|\Gamma_{out}\right|^2}. \tag{6.14}$$

where $T_{backend}$ is the noise temperature of the second stage with 50 Ω generator impedance and is measured separately. Then, the 50Ω noise temperature measurement corrected for drain reflection coefficient is

$$T_{50,\,1\mathrm{GHz}} = T_{50} - 300\frac{\left|\Gamma_{out}\right|^2}{\left|s_{21}\right|^2}. \tag{6.15}$$

The second-stage amplifier (with respectably low input noise temperature) is included to increase measurement SNR as the gain of a discrete device could be quite low depending on bias.

In the cold attenuator method, precise knowledge of the temperature of the cold attenuator's center conductor T_{atten} is necessary to achieve accurate results as any uncertainty in T_{atten} translates directly into uncertainty in measured noise temperature. The attenuator's physical temperature is measured with a thermo-couple mounted above it. However, because the attenuator is heat sunk from the outside, there is usually a temperature offset between the thermo-couple reading and the temperature of the attenuator's center conductor. This offset is determined through noise measurements of a reference amplifier calibrated at a laboratory such as NIST.

Despite being heat sunk to the cold head, the bias-tee increases the thermal resistance at the center conductor of the attenuator, thereby increasing the offset temperature by ˜1 Kelvin. As a matter of fact, an earlier version of this test setup employed the Mini-Circuits ZX85-12G+ bias-tee in the dewar as well. However, the thermal resistance of the bias-tee was so large that the attenuator offset temperature increased by more than 10 K as measured using a reference amplifier. On the other hand, the custom bias-tee has two disadvantages: 1) it has higher lowest frequency operation, e.g., 500 MHz; 2) on devices with significant gate leakage, there is significant voltage drop across the resistor in the bias-tee.

6.4.2 Theory

The T_{50} measurements are carried out at 1 GHz which is high enough to avoid $1/f$ noise corner frequency and low enough that device capacitances can be treated as open. Figure 6.12 shows the simplified, low-frequency HEMT small-signal model with the pertinent noise sources. The parasitic gate and source access resistances R_G and R_S, respectively, contribute thermal noise at the physical temperature T_{phys}. The noise contribution of drain access resistance R_D is ignored as it is after

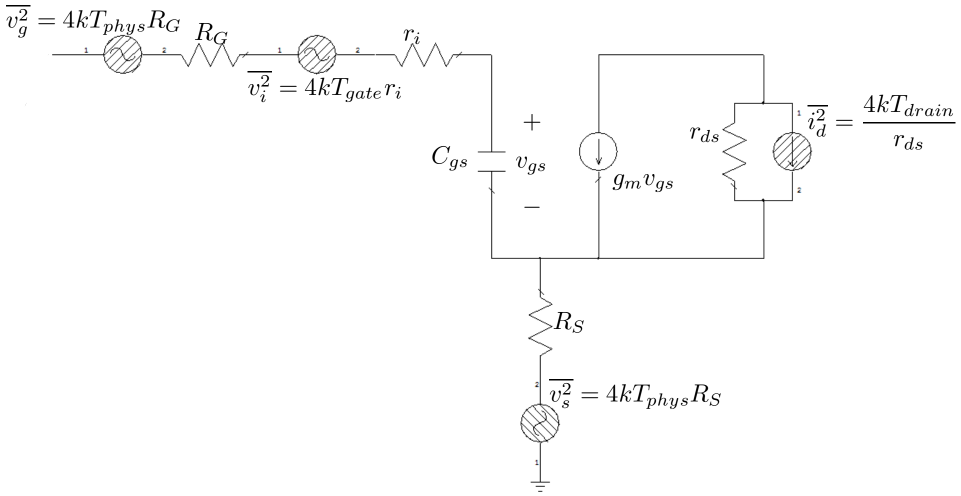

Figure 6.12: Simplified HEMT small-signal model used for T_{drain} extraction.

the gain stage. The small-signal gate-source and drain-source resistances r_i and r_{ds}, respectively, are functions of transistor bias and are assigned noise temperatures T_{gate} and T_{drain} to model the HEMT noise [69]. As mentioned previously, in this work r_i is considered as an ohmic-type resistance generating thermal noise with $T_{gate} = T_{phys}$.

Defining the total gate-source resistance as

$$R_{GS} \equiv R_G + r_i + R_S. \tag{6.16}$$

the total noise power produced at the input is easily calculated from the simplified SSM as

$$\overline{v_{in}^2} = 4kT_{phys}R_{GS} + \frac{4kT_{drain}}{r_{ds}}\frac{1}{g_m^2} \tag{6.17}$$

Then, the input noise temperature of the transistor driven with a 50 Ω source is simply

$$T_{50} = \frac{\overline{v_{in}^2}}{4k \cdot 50} \tag{6.18}$$

Consequently, T_{drain} is given by,

$$T_{drain} = \left(T_{50} - T_{phys}\frac{R_{GS}}{50}\right) g_m^2 r_{ds} 50 \tag{6.19}$$

As both T_{drain} and the small-signal model element values are known, the transistor performance including gain and noise can now be modeled. Before proceeding with the latter, a quick overview of fundamental two-port noise equations is provided. Noise temperature of a two-port at an arbitrary generator impedance $Z_{gen} = R_{gen} + jX_{gen}$ can be written as [93]

$$T_n = T_{min} + NT_0 \frac{\left|Z_{gen} - Z_{opt}\right|^2}{R_{gen} R_{opt}} \tag{6.20}$$

Here, T_{min} is the minimum noise temperature; $T_0 = 290$ K; $Z_{opt} = R_{opt} + jX_{opt}$ is the generator impedance that yields $T_n = T_{min}$; and N is a parameter invariant under lossless transformations and quantifies sensitivity of T_n with respect to generator impedance. The noise measure is given by [69]

$$M = \frac{T_n}{T_0} \frac{1}{1 - \frac{1}{G_a}}, \tag{6.21}$$

where G_a is the available gain of the two-port, from which the cascaded noise temperature T_{CAS} at an arbitrary generator impedance is easily obtained as [70]

$$T_{CAS} = T_0 M = \frac{T_n}{T_0} \frac{1}{1 - \frac{1}{G_a}} \tag{6.22}$$

which is close to T_n when the available gain of the stage is high.

Pospieszalski [69] derived closed-form expressions for all of these quantities for the intrinsic FET. They are repeated here for the sake of completeness and also because they are modified to use total gate resistance R_{GS} instead of r_i :

$$T_{min} = 2\frac{f}{f_T}\sqrt{g_{ds} R_{GS} T_{gate} T_{drain} + \left(\frac{f}{f_T}\right)^2 g_{ds}^2 R_{GS}^2 T_{drain}^2} + 2\left(\frac{f}{f_T}\right)^2 g_{ds} R_{GS} T_{drain} \tag{6.23}$$

$$NT_0 = \frac{T_{min}}{2}\left(1 + \frac{R_{GS}}{R_{opt}}\right)^{-1} \tag{6.24}$$

$$R_{opt} = \sqrt{\left(\frac{f_T}{f}\right)^2 \frac{R_{GS}}{g_{ds}} \frac{T_{gate}}{T_{drain}} + R_{GS}^2}, \qquad X_{opt} = \frac{1}{\omega C_{gs}} \tag{6.25}$$

$$f_T = \frac{g_m}{2\pi\left(C_{gs} + C_{gd}\right)} \tag{6.26}$$

where it is noted that the definition of f_T in [69] neglects C_{gd}. Available gain with arbitrary generator impedance is given as

$$\frac{1}{G_a} = \frac{1}{G_{a,max}} + \frac{g_g}{R_{gen}}\left|Z_{gen} - Z_{opt,G}\right|^2 \tag{6.27}$$

where $Z_{opt,G}$ is the generator impedance realizing maximum available gain $G_{a,max}$. The expressions for these are

$$Z_{opt,G} = R_{GS} + j\frac{1}{\omega C_{gs}} \tag{6.28}$$

$$G_{a,max} = \left(\frac{f_T}{f}\right)^2 \frac{1}{4g_{ds}R_{GS}} \tag{6.29}$$

$$g_g = \left(\frac{f}{f_T}\right)^2 g_{ds}. \tag{6.30}$$

Finally, the generator impedance minimizing the noise measure is [69]

$$Z_{opt,M} = R_{GS}\left[\sqrt{\left(\frac{T_{gate}}{T_{drain}} - 1\right)^2 + \frac{R_{opt}^2}{R_{GS}^2} - 1} - \frac{T_{gate}}{T_{drain}}\right] + j\frac{1}{\omega C_{gs}}. \tag{6.31}$$

These equations are now used along with $T_{50,\,1\mathrm{GHz}}$ measurements to model noise performance of the large transistors from each process.

6.4.3 Results

Figure 6.13 presents the measured quantities g_m, r_{ds}, and $T_{50,\,1\mathrm{GHz}}$ in addition to the derived T_{drain}. T_{CASmin} and available gain at the generator impedance that yields T_{CASmin} are plotted in Figure 6.14 at 6 and 100 GHz. Finally, calculated f_T, f_{max}, and noise current $\overline{i_d^2}$ are provided in Figure 6.15.

The most important observation from these plots is the sizable increase in all noise temperatures of all devices when V_{DS} is increased from 0.6 to 0.8 V at both temperatures. This increase is largest on the NGC 100% device which further suggests the occurrence of strong impact ionization. Moreover, this noise increase is contrary to what manufacturers' small-signal models predict. It is, however, consistent with the LNA measurements of the next chapter. There is little performance change between 0.4 and 0.6 V which suggests the devices are not very sensitive to drain bias. That is, until the onset of impact ionization when noise degrades significantly.

It is also interesting to note that the NGC 75% devices perform as well as the 100% devices noise-wise at W-band. Slightly lower available gain of these transistors, however, imply lower f_T's which would limit their use in THz applications. The OMMIC device exhibits the lowest T_{drain} over bias and temperature, and at 6 GHz exhibit performance on par with those of the NGC InP devices. As expected, it also has the lowest f_T/f_{max} values. Consequently, the OMMIC process seems to be most applicable to radio astronomy applications up to about 50 GHz.

Figure 6.16 plots T_{CASmin} and $\Re\{Z_{opt,M}\}$ versus frequency at $V_{DS} = 0.4$, 0.6, 0.8 V for 4-finger transistors from the three processes. Calculations are carried out on larger transistors at lower frequencies in order to ensure $\Re\{Z_{opt,M}\}$ is relatively closer to 50 Ω. These curves reinforce the

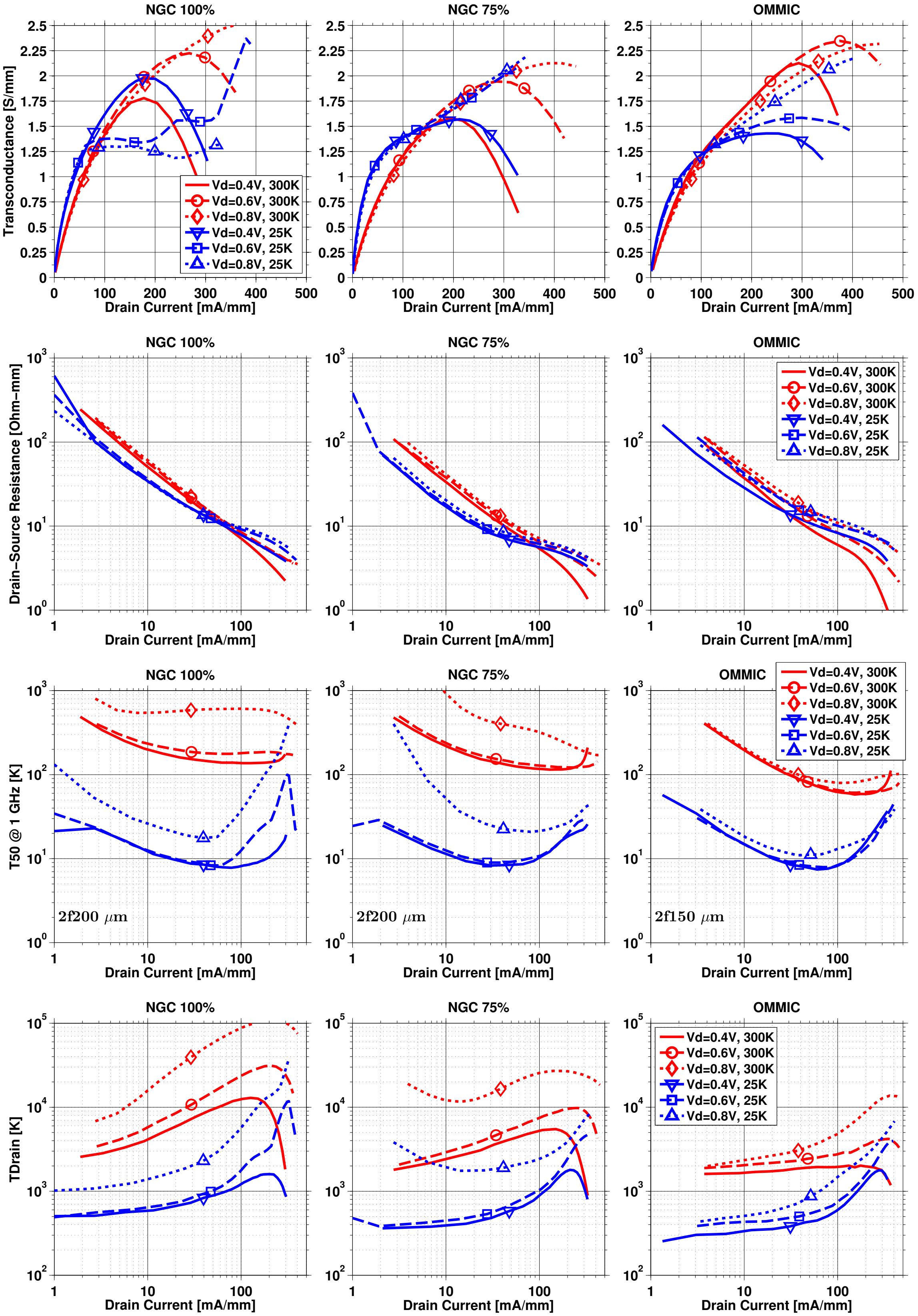

Figure 6.13: Measured g_m, r_{ds}, $T_{50,1\mathrm{GHz}}$, and derived T_{drain} of the NGC and OMMIC devices

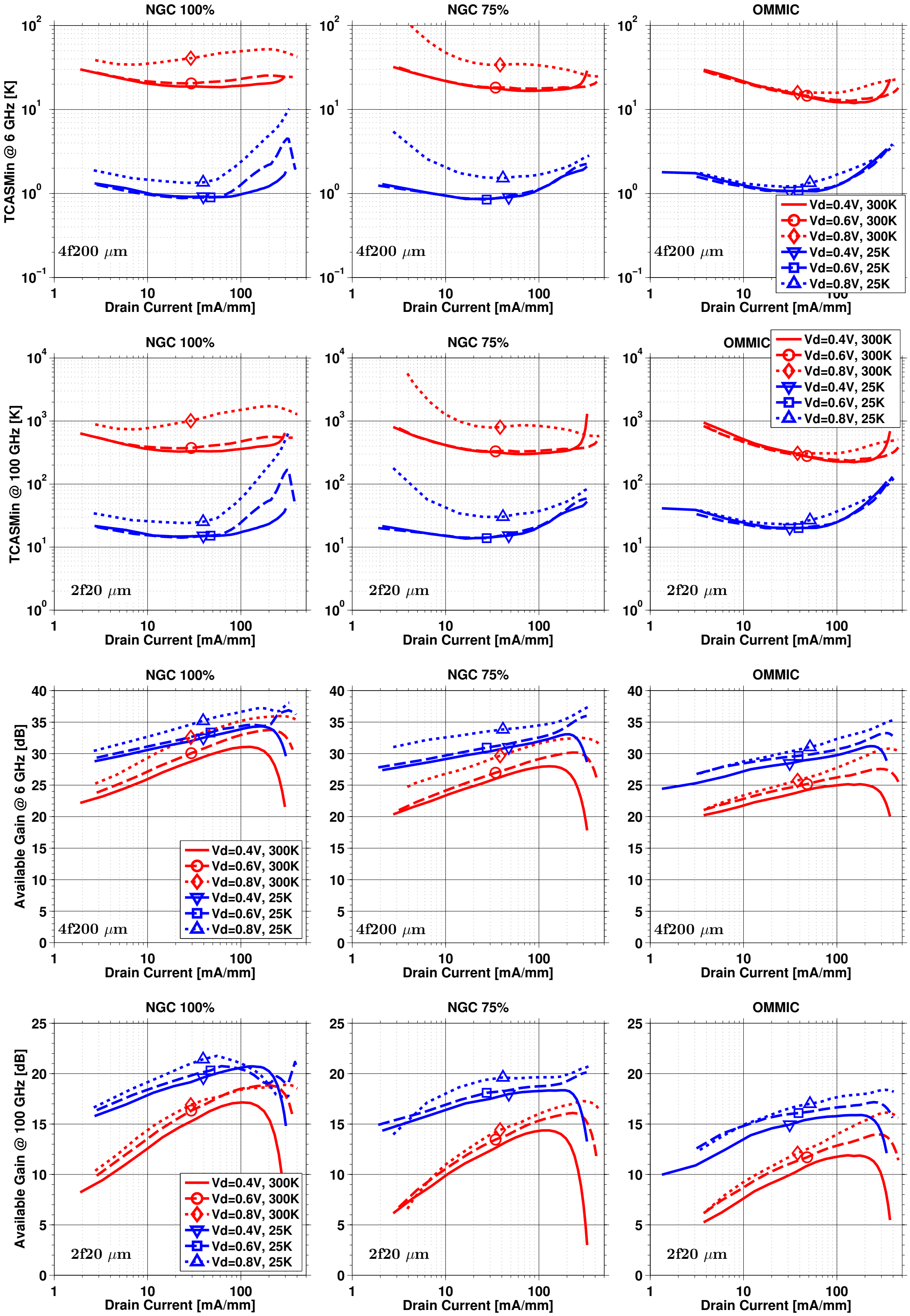

Figure 6.14: Minimum cascaded noise temperature and available gain at 6 and 100 GHz of the NGC and OMMIC transistors

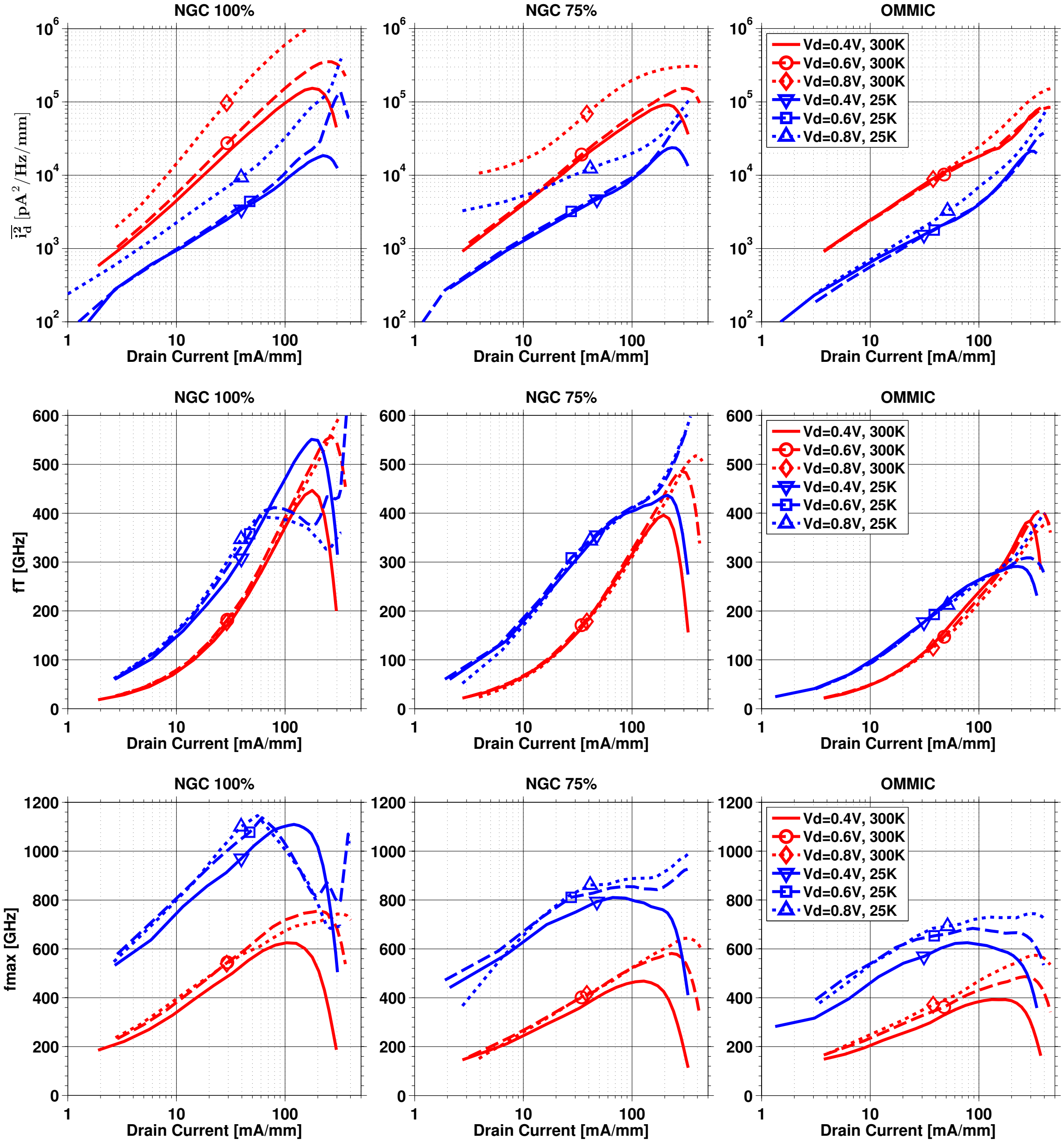

Figure 6.15: Drain noise current (normalized to gate periphery), f_T, and f_{max} of the NGC and OMMIC transistors

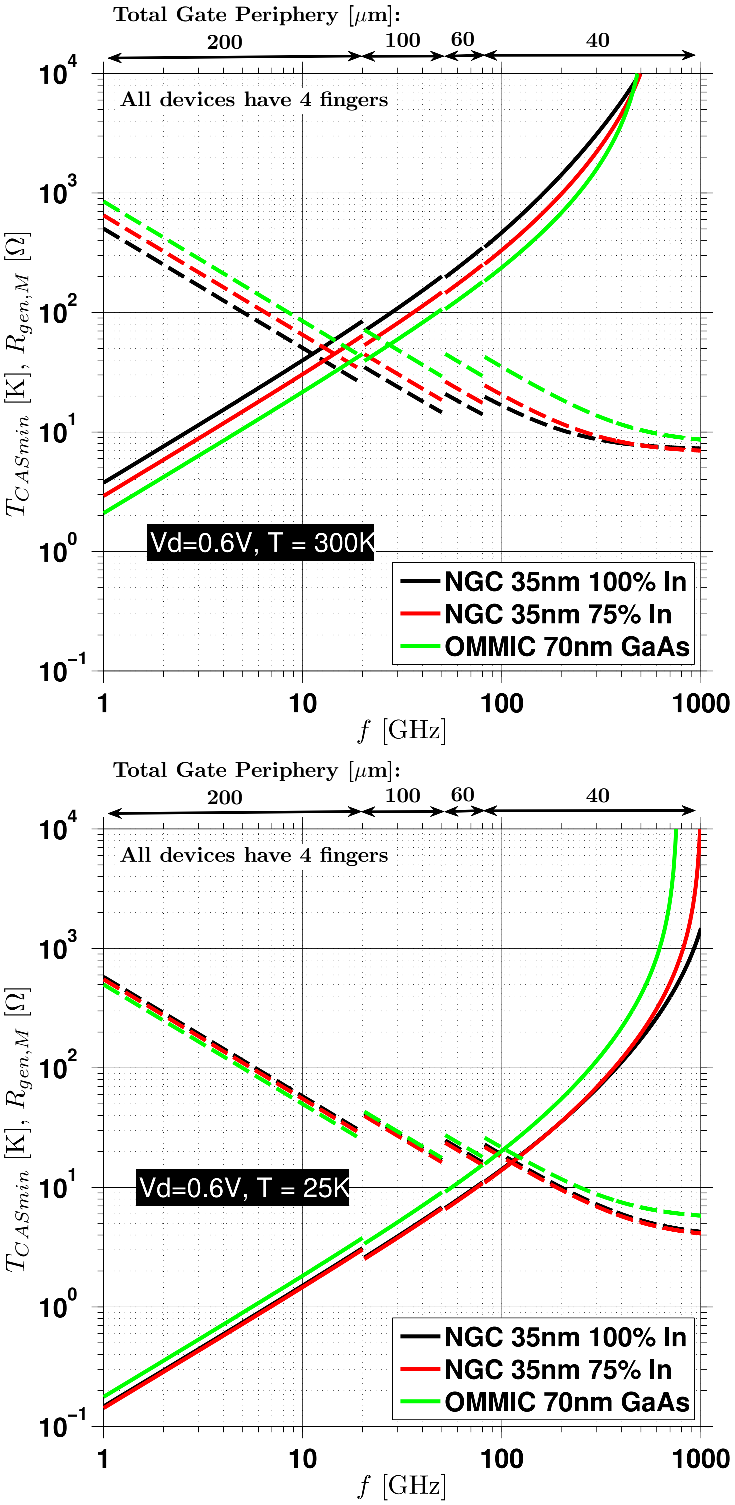

Figure 6.16: T_{CASmin} (solid) and $\Re\{Z_{gen,M}\}$ (dashed) of the three processes versus frequency at 300 K (top) and 25 K (bottom). $I_{DS} = 100$, 150 mA/mm at 300 K and $I_{DS} = 25$, 40 mA/mm at 25 K for NGC and OMMIC devices, respectively.

earlier observation regarding the suitability of the 100% NGC devices for THz applications. They also show that the OMMIC transistor is within 1–2 Kelvin of the NGC 75% transistor up to 50 GHz beyond which its noise begins to diverge slowly. $V_{DS} = 0.6$ V appears to be the optimum drain bias for $f > 250$ GHz.

The validity of T_{CASmin} predictions at $V_{DS} = 0.8$ V beyond 20 GHz is questionable. This is because the noise measurements performed at 1 GHz are affected by impact ionization; however, S-parameter measurements of previous section points to negligible effect on small-signal performance at such high frequencies which is consistent with measurements of NGC 100% LNAs at W-band [16, 94].

Tables 6.2-6.7 provide the small-signal parameters, measurements and the derived quantities at the three drain bias voltages.

6.5 Conclusions

DC, microwave, and noise performance of GaAs mHEMT and InP pHEMT transistors were presented for both room and cryogenic temperatures. Measurements indicate occurrence of impact ionization on all devices with the 100% In pHEMT devices exhibiting the most severe signs. The transistors' output characteristics exhibit kinks whose occurrence seems to be well correlated with onset of impact ionization based not only on DC tests but also cryogenic S-parameter and noise measurements. Further, the first reported measurements of T_{drain} versus bias of HEMT transistors at both temperatures were presented showing the 70 nm OMMIC GaAs process to be on par with the 35 nm NGC InP process at frequencies below 50 GHz.

A method of T_{drain} determination by 1 GHz discrete transistor measurements has been demonstrated with reasonable but questionable results for prediction of minimum cascaded noise temperature, T_{CASmin}, at 6 GHz and 100 GHz. The main limitations of the method are:

1. The accuracy of T_{drain} at 300K depends strongly on accurate values of the gate circuit resistances because their thermal noise can dominate the $T_{50,\,1\mathrm{GHz}}$ measurement. This is much less the case at cryogenic temperatures;

2. It is assumed that T_{drain} (as well as all other SSM element values) are independent of frequency. This assumption is especially questionable in the case of impact ionization. Future measurements of T_{drain} from 0.5 to 5 GHz would be interesting;

3. It should be recognized that the assignment of the drain noise to the effective temperature, T_{drain}, of r_{ds} is questionable. An assignment to a drain noise current generator, $\overline{i_d^2}$, may provide a better comparison with theory. r_{ds} is a function of $\frac{dV_{DS}}{dI_{DS}}$ while the drain noise is more likely to be a function of I_{DS};

Table 6.2: Small-signal model parameters at $V_{DS} = 0.4$ V

I_{DS} [mA/mm]		r_i [Ω]	r_{ds} [Ω]	g_m [mS]	C_{gs} [fF] 4f200	C_{gs} [fF] 2f20	C_{gd} [fF] 4f200	C_{gd} [fF] 2f20
300 K								
20	100%	0.3	142.2	86.2	55.5	7.4	51.2	4.3
	75%	0.3	93.6	75.4	55.5	7.4	51.2	4.3
	OMM	0.6	100	70.7	92.5	9.3	43.6	4.4
50	100%	0.37	64.5	178.9	65.2	8.7	50.1	4.2
	75%	0.37	44.7	154.9	65.2	8.7	50.1	4.2
	OMM	0.73	46.9	153.5	108.7	10.9	42.7	4.3
100	100%	0.44	35.8	283.4	73.1	9.8	48.6	4.1
	75%	0.44	27.1	241	73.0	9.7	48.7	4.1
	OMM	0.88	30	244.2	121.6	12.2	41.5	4.2
150	100%	0.48	24.4	345.1	78.3	10.4	47.9	4.0
	75%	0.48	19.4	296.2	78.3	10.4	47.9	4.0
	OMM	0.95	23.1	302	130.4	13.0	40.8	4.1
25 K								
20	100%	0.3	104.3	131.4	50.0	6.7	46.1	3.8
	75%	0.3	54.1	152.7	50.0	6.7	46.1	3.8
	OMM	0.6	88.2	112.2	83.3	8.3	39.3	3.9
50	100%	0.37	59.2	225.7	58.7	7.8	45.1	3.8
	75%	0.37	33.8	233.8	58.7	7.8	45.1	3.8
	OMM	0.73	54.9	185.7	97.8	9.8	38.4	3.8
100	100%	0.44	39.4	323.5	65.7	8.8	43.8	3.7
	75%	0.44	28.1	277.8	65.7	8.8	43.8	3.7
	OMM	0.88	41.4	243.4	109.6	11.0	37.3	3.7
150	100%	0.48	30.6	381.4	70.4	9.4	43.1	3.6
	75%	0.48	24.9	298.6	70.4	9.4	43.1	3.6
	OMM	0.95	35.7	270.3	116.9	11.7	36.8	3.7

Table 6.3: Small-signal model parameters at $V_{DS} = 0.6$ V

I_{DS} [mA/mm]		r_i [Ω]	r_{ds} [Ω]	g_m [mS]	C_{gs} [fF] 4f200	C_{gs} [fF] 2f20	C_{gd} [fF] 4f200	C_{gd} [fF] 2f20
300 K								
20	100%	0.3	150.8	87.0	54.8	7.3	46.5	3.9
	75%	0.3	106.7	73.9	54.8	7.3	46.5	3.9
	OMM	0.6	131.1	68.4	91.4	9.1	39.6	4.0
50	100%	0.36	71.8	182.7	68.0	9.1	44.5	3.7
	75%	0.37	51.1	153.3	68.6	9.1	44.4	3.7
	OMM	0.73	64.4	144.5	114.3	11.4	37.9	3.8
100	100%	0.44	42.4	293.5	76.7	10.2	42.7	3.6
	75%	0.44	32.5	243.1	76.7	10.2	42.7	3.6
	OMM	0.88	41.9	233.4	127.8	12.8	36.4	3.6
150	100%	0.48	32.1	367.1	83.2	11.1	41.2	3.4
	75%	0.48	25.8	304.6	83.2	11.1	41.2	3.4
	OMM	0.95	32.9	299	138.7	13.9	35.1	3.5
25 K								
20	100%	0.3	110.0	133.2	49.4	6.6	41.8	3.5
	75%	0.3	58.7	149.9	49.4	6.6	41.8	3.5
	OMM	0.6	126.0	104.2	82.3	8.2	35.6	3.6
50	100%	0.37	60.7	234.3	61.7	8.2	40.0	3.3
	75%	0.36	36.8	230.3	61.4	8.2	40.0	3.3
	OMM	0.73	67.9	181.1	102.1	10.2	34.1	3.4
100	100%	0.44	45.7	275.1	69.0	9.2	38.4	3.2
	75%	0.44	30.8	278.1	69.0	9.2	38.4	3.2
	OMM	0.88	50.6	243.8	115.1	11.5	32.7	3.3
150	100%	0.48	39.0	270.4	74.9	10.0	37.1	3.1
	75%	0.48	27.6	305.6	74.9	10.0	37.1	3.1
	OMM	0.95	44.5	276.0	124.9	12.5	31.6	3.2

Table 6.4: Small-signal model parameters at $V_{DS} = 0.8$ V

I_{DS} [mA/mm]		r_i [Ω]	r_{ds} [Ω]	g_m [mS]	C_{gs} [fF] 4f200	C_{gs} [fF] 2f20	C_{gd} [fF] 4f200	C_{gd} [fF] 2f20
300 K								
20	100%	0.3	158.6	84.3	56.2	7.5	43.5	3.6
	75%	0.3	112.4	69.5	56.1	7.5	43.5	3.6
	OMM	0.6	151.5	66.4	93.6	9.4	37.1	3.7
50	100%	0.36	71.4	173.4	69.5	9.3	41.0	3.4
	75%	0.37	54.6	145.2	69.5	9.3	41.0	3.4
	OMM	0.73	78.9	139	115.8	11.6	35.0	3.5
100	100%	0.44	40.1	280.3	79.9	10.6	38.4	3.2
	75%	0.44	35.7	230.4	79.9	10.6	38.4	3.2
	OMM	0.88	54.6	224.8	133.1	13.3	32.8	3.3
150	100%	0.48	30.3	351.4	87.0	11.6	36.3	3.0
	75%	0.48	29.6	290.2	86.8	11.6	36.3	3.0
	OMM	0.95	45.9	286.0	144.7	14.5	31.0	3.1
25 K								
20	100%	0.3	107.2	134.6	50.2	6.7	39.2	3.3
	75%	0.3	65.1	141.3	50.1	6.7	39.2	3.3
	OMM	0.6	125.5	103.7	84.3	8.4	33.4	3.3
50	100%	0.36	62.0	235.9	62.5	8.3	36.9	3.1
	75%	0.36	40.4	222.8	62.5	8.3	36.9	3.1
	OMM	0.73	75.1	179.4	104.2	10.4	31.5	3.1
100	100%	0.44	48.5	258.9	71.9	9.6	34.6	2.9
	75%	0.44	33.7	273.8	71.9	9.6	34.6	2.9
	OMM	0.88	59.1	242.1	119.8	12.0	29.5	2.9
150	100%	0.48	42.2	259.9	78.2	10.4	32.7	2.7
	75%	0.48	30.4	304.6	78.2	10.4	32.7	2.7
	OMM	0.95	51.2	282.9	130.4	13.0	27.9	2.8

Table 6.5: Measured and corrected $T_{50,1\text{GHz}}$ and derived parameters at $V_{DS} = 0.4$ V. All parameters, except those that are marked, are for 4f200 μm device size. OMMIC $R_G = R_S = 1\,\Omega$ and NGC $R_G = 1.75\Omega$, $R_S = 0.95\Omega$ at 300 K. These values are halved cryogenically.

I_{DS}		T_{50}‡	T_{drain}	i_d	T_{CASmin} [K]		$Z_{gen,M}$ [Ω]				G_{av} [dB]		f_T	f_{max}
[mA/mm]		[K]	[K]	[pA/$\sqrt{\text{Hz}}$]	6GHz	100GHz*	R 6GHz	X 6GHz	R 100GHz*	X 100GHz*	6GHz	100GHz*	[GHz]	
							300 K							
20	100%	165.2	5881	47.8	18.9	330.1	98.1	478.5	37.2	215.3	27.8	14.4	128.2	434.6
	75%	163.9	2925	41.5	18.8	339.8	98.6	478.5	36.5	215.3	24.8	11.5	112.1	309.0
	OMM	125.2	1732	30.9	17.6	371.5	91.3	286.9	42.9	172.1	22.9	9.1	82.5	254.3
50	100%	142.6	9445	89.9	18.5	331.1	102.4	407	38.9	183.1	30.0	16.4	246.8	562.6
	75%	128.6	4166	71.7	17.0	303.8	111.1	407	41.2	183.1	26.8	13.4	213.6	405.8
	OMM	78.6	1914	47.5	14.0	270.1	119.6	244.2	57.1	146.5	24.3	10.9	161.3	332.9
100	100%	137.3	12437	138.5	19.2	360.1	101.4	362.9	38.9	163.3	31.0	17.1	370.3	623.8
	75%	117.1	5232	103.2	16.7	306.5	115.7	363.6	43.2	163.6	27.9	14.3	315.2	462.0
	OMM	62.2	1949	59.9	12.2	228.1	144.1	218.1	69.7	130.9	25.0	11.8	238.1	383.8
150	100%	137.8	12674	169.2	20.1	390.9	98.2	338.9	37.9	152.5	30.9	16.8	435.3	603.2
	75%	115.2	5491	125.1	17.2	324.0	114	339	42.7	152.5	27.9	14.2	373.7	461.4
	OMM	58.2	1939	68.1	11.9	222.6	151.4	203.4	73.6	122	25.1	11.8	280.6	392.1
							25 K							
20	100%	9.7	668	18.8	0.9	14.7	92.6	531.3	36.1	239.1	31.5	18.8	217.5	862.2
	75%	9.1	429	20.9	0.9	13.8	91.9	533.3	35.7	240.0	29.9	17.2	252.1	712.8
	OMM	10.1	355	14.9	1.1	20.5	77.8	318.5	39.6	191.1	28.1	14.6	145.6	540
50	100%	8.1	888	28.8	0.9	15	98.3	452.1	38.4	203.5	32.9	19.9	346	1014.8
	75%	8.5	592	31.1	0.9	15.4	90.8	452.2	35.5	203.5	31.1	18.0	358.6	795.5
	OMM	7.8	433	20.9	1.1	20.2	86	271.3	44.7	162.8	29.0	15.5	216.8	609.5
100	100%	8.2	1216	41.3	1.0	17.2	95.2	403.6	37.7	181.6	33.9	20.6	469.9	1101.7
	75%	10.3	891	41.8	1.1	20.8	77.9	404.1	31.2	181.8	31.9	18.3	403.8	799.9
	OMM	8.2	599	28.3	1.2	24.9	80.8	242.0	43.3	145.2	29.8	15.8	263.6	618.2
150	100%	9.0	1500	52.0	1.1	20.2	86.9	377.0	34.7	169.7	34.3	20.7	534.8	1094.5
	75%	14.3	1354	54.8	1.4	29.4	62.1	376.7	25.7	169.5	32.7	18.3	418.6	773.1
	OMM	11.1	909	37.5	1.6	34.8	66.0	226.9	36.8	136.2	30.5	15.9	279.9	598.3

*: Calculated for a 2f20 μm transistor; ‡ : $T_{50,\,1\text{GHz}}$ measurements collected on NGC 2f200μm and OMMIC 2f150μm devices

Table 6.6: Measured and corrected $T_{50,1\mathrm{GHz}}$ and derived parameters at $V_{DS} = 0.6$ V. All parameters, except those that are marked, are for 4f200 μm device size. OMMIC $R_G = R_S = 1\,\Omega$ and NGC $R_G = 1.75\Omega$, $R_S = 0.95\Omega$ at 300 K. These values are halved cryogenically.

I_{DS}		T_{50}‡	T_{drain}	i_d	T_{CASmin} [K]		$Z_{gen,M}$ [Ω]				G_{av} [dB]		f_T	f_{max}
[mA/mm]		[K]	[K]	[pA/$\sqrt{\mathrm{Hz}}$]	6GHz	100GHz*	R 6GHz	X 6GHz	R 100GHz*	X 100GHz*	6GHz	100GHz*	[GHz]	
							300 K							
20	100%	199.3	8514	55.8	20.5	369.2	90.7	483.7	34.6	217.7	29.1	15.4	136.6	483.5
	75%	179.9	3672	43.6	19.1	346.3	97.2	484.2	36.1	217.9	25.7	12.3	115.8	341.0
	OMM	127.4	2177	30.3	17.1	346.9	93.8	290.4	44.8	174.2	24	10.3	83.0	292.9
50	100%	178.3	15145	107.9	21.3	408.3	89.2	390.4	34.2	175.7	31.4	17.3	258.2	619.6
	75%	142.4	5484	77.0	18.1	335.2	104.6	387.0	38.7	174.1	27.7	14.1	215.8	438.5
	OMM	80.9	2454	45.9	14.4	276	116.2	232.2	56.2	139.3	25.2	11.8	151.1	366.2
100	100%	180.1	23672	175.6	23.1	473.6	84.7	345.9	33.1	155.6	33.0	18.5	391.3	718.5
	75%	128.2	7458	112.5	17.8	336.8	109.2	346.0	40.6	155.7	29.1	15.3	324.0	520.6
	OMM	65.5	2762	60.4	13.0	241.9	135.9	207.6	66.8	124.5	26.2	12.9	226.1	430.6
150	100%	184	28874	222.8	24.6	530.9	80.6	318.7	31.9	143.4	33.5	18.8	469.4	746.2
	75%	123.4	8716	136.5	18.0	350.8	108.9	318.7	40.5	143.4	29.7	15.8	389.4	554.9
	OMM	61	3015	71.1	12.8	238	141.5	191.2	70.1	114.7	26.7	13.3	273.6	456.5
							25 K							
20	100%	10	729	19.1	0.9	14.3	95.6	538.3	36.9	242.2	32.1	19.3	231.9	930.1
	75%	10	496	21.6	0.9	14.1	91.3	539.3	35.2	242.7	30.5	17.7	260.5	762.1
	OMM	10.6	449	14.0	1.1	19.9	78.9	322.9	40.4	193.8	29.1	15.7	140.2	615.7
50	100%	8.3	1017	30.4	0.9	15.3	98.6	430.0	37.9	193.5	33.5	20.4	366.7	1089.1
	75%	9.2	693	32.3	0.9	16.3	88.3	432.3	34.1	194.5	31.6	18.4	361.2	835.1
	OMM	8.2	541	21.0	1.1	20.9	83.5	260.1	43.6	156.1	29.8	16.2	211.5	660.5
100	100%	12.5	1778	46.3	1.3	24.6	73.8	384.3	29.3	172.9	34.4	20.4	407.6	1030.2
	75%	10.8	1034	43.0	1.1	21.5	77.1	384.4	30.4	173	32.6	18.7	411.9	854.5
	OMM	8.4	751	28.6	1.3	25.3	79.5	230.7	42.9	138.4	30.7	16.6	262.5	680.8
150	100%	21.2	2682	61.6	1.8	41.4	52.7	354.1	22.1	159.4	34.5	19.6	384.2	887.5
	75%	14.1	1548	55.6	1.4	29.4	63.6	354.1	25.7	159.4	33.3	18.9	434.2	844.7
	OMM	10.4	1100	36.9	1.6	33.7	67.1	212.5	37.5	127.5	31.4	16.8	280.7	670.2

*: Calculated for a 2f20 μm transistor; ‡ : $T_{50,\,1\mathrm{GHz}}$ measurements collected on NGC 2f200μm and OMMIC 2f150μm devices

Table 6.7: Measured and corrected $T_{50,1\text{GHz}}$ and derived parameters at $V_{DS} = 0.8$ V. All parameters, except those that are marked, are for 4f200 μm device size. OMMIC $R_G = R_S = 1\,\Omega$ and NGC $R_G = 1.75\Omega$, $R_S = 0.95\Omega$ at 300 K. These values are halved cryogenically.

I_{DS}		T_{50}‡	T_{drain}	i_d	T_{CASmin} [K]		$Z_{gen,M}$ [Ω]				G_{av} [dB]		f_T	f_{max}
[mA/mm]		[K]	[K]	[pA/$\sqrt{\text{Hz}}$]	6GHz	100GHz*	R 6GHz	X 6GHz	R 100GHz*	X 100GHz*	6GHz	100GHz*	[GHz]	
							300 K							
20	100%	569	29132	100.7	38.6	916.3	49.6	472.3	21.8	212.5	31.5	16.1	134.4	487.6
	75%	505.5	12260	77.6	36.1	848.2	52.9	472.6	22.5	212.7	28.1	12.9	110.9	338.5
	OMM	137.1	2661	31.1	17.9	365.2	89.5	283.4	43.3	170	24.6	10.8	80.9	308.5
50	100%	602.3	58178	212.1	45.1	1236	43.9	382.8	20.6	172.2	33.8	17.6	249.1	595.5
	75%	383.3	19136	139.1	34.5	832.7	56.4	381.9	23.8	171.8	30.2	14.8	209	440.6
	OMM	91.7	3423	48.9	15.9	307.3	106.1	229.1	52.3	137.4	26.3	12.6	146.7	394.4
100	100%	608.9	87979	347.9	49.4	1507	41.3	332.2	20.4	149.5	35.2	18.4	377	673.7
	75%	320.0	25552	198.7	33.5	836.8	59.3	332.2	25.1	149.5	31.6	16.0	309.9	522.6
	OMM	79.7	4820	69.8	15.8	306.9	112.3	199.3	56.8	119.6	27.8	14.0	215.7	469.3
150	100%	600.2	102863	432.7	51.5	1664.6	40.2	305.0	20.4	137.3	35.7	18.6	453.7	700.8
	75%	268.6	27051	224.8	31.5	781.4	63.8	305.6	26.4	137.5	32.1	16.6	374.9	571.5
	OMM	81.2	6696	89.7	17.1	341.8	106.3	183.4	54.9	110.0	28.8	14.8	259.1	510.4
							25 K							
20	100%	20.9	1713	29.7	1.4	24.5	63.1	530.1	25.0	238.6	33.9	20.3	238.6	940.3
	75%	31.2	1762	38.7	1.6	32.1	49.0	531.2	20.0	239.1	33.2	19.0	250.6	770.4
	OMM	13.3	580	16	1.2	23.6	69.2	315.1	35.8	189.1	29.7	15.9	139.9	613.7
50	100%	18	2710	49.1	1.4	27.6	62.9	425.2	25.0	191.4	35.7	21.6	376.9	1130
	75%	22	1991	52.2	1.6	31.8	53.7	425.6	21.7	191.5	33.9	19.6	356.1	862.8
	OMM	11.1	858	25.1	1.3	26.5	69.5	254.7	37.1	152.8	31.0	17.0	210.2	691.8
100	100%	37.8	5743	80.8	2.4	60.0	40.6	369.3	17.8	166.2	36.6	21.0	387.0	1008
	75%	21.3	2430	63.1	1.7	37.2	52.2	369.1	21.6	166.1	34.5	19.6	409.3	887.8
	OMM	13.1	1479	37.2	1.7	36.8	60.2	221.5	33.8	132.9	32.3	17.7	258.1	723.6
150	100%	73.5	10132	115.1	3.6	118.1	27.5	339.4	14.2	152.7	37.2	20.1	373.1	897.4
	75%	23.8	3056	74.5	1.9	45.1	47.7	339.3	20.2	152.7	35.0	19.7	437.2	891.3
	OMM	15.3	2070	47.3	2.0	46.8	53.1	203.5	31.1	122.1	33.0	17.9	284.6	728.3

*: Calculated for a 2f20 μm transistor; ‡ : $T_{50,\,1\text{GHz}}$ measurements collected on NGC 2f200μm and OMMIC 2f150μm devices

4. Much attention must be paid to the accuracy of the 1 GHz noise measurements. Factors such as calibration accuracy of the noise source, losses in DC bias tees, extrinsic vs intrinsic g_m, and correction for post-amplifier noise in the presence of a mismatched output of the test transistor must be considered;

5. Gate leakage current, which constitutes a shot noise source, is neglected in this development. While total gate leakage is easily obtained from $I-V$ measurements, what is needed is the individual components of gate leakage, i.e., $I_G = I_{GS} + I_{GD}$ from which the shot noise source can be modeled using $\overline{i_g^2} = 2q\left(|I_{GS}| + |I_{GD}|\right)$. Inclusion of this noise source would lower predicted T_{drain} measurements presented herein.

Chapter 7

Wideband, Cryogenic, Very-Low Noise Amplifiers

This chapter discusses design and measurements of two wideband LNAs designed on both the NGC and OMMIC processes. The first LNA is designed to cover 1–20 GHz with < 10 K noise temperature and > 30 dB gain cryogenically, and the second design covers 8–50 GHz. These designs were fabricated on both the 100% and 75% In NGC processes.

All of the MMIC LNAs employ common-source stages. Large devices with inductive source degeneration are used in first stages of the amplifiers to improve match and bring real part of optimum noise impedance, R_{opt}, close to 50 Ohm. Thus, the first stage tends to be the bandwidth-limiting stage and in order to compensate, inductive peaking is used to enhance high-frequency gain. Subsequent stages employ smaller transistors with shunt and/or series inductive peaking to achieve flat gain over the bandwidth. Furthermore, two-finger devices were used on all stages of all designs in order to avoid potential instability sometimes observed on devices with more fingers (assuming same total gate periphery) [95].

Because the transistor characterization results of the previous chapter were not available during design phase of the LNAs presented herein, they were designed using foundry small-signal models. In the case of NGC, the SSM was provided at a single bias point as mentioned previously and this model was used for LNA design. The OMMIC SSM is applicable at 300 K only, therefore the OMMIC LNAs were designed for room temperature.

7.1 Measurement Setups

7.1.1 Wafer-probed S-Parameters at 300 K

At least half of the MMICs fabricated in each foundry were first tested at room temperature using wafer-probes for S-parameters up to 50 GHz at a range of bias values. The bias values were selected to be fairly conservative as the goal of the tests were to confirm functionality rather than performance.

Figure 7.1: Photograph of the test setup for wafer-probed S-parameter measurements at 300 K. The bias is provided using three Keithley KE2400 DC supplies, one of which is not shown in the photo.

The test station employs Picoprobe's 67A-GSG-120 coplanar probes with 120 μm pitch. Calibration is performed using the GGB Industries' CS-5 calibration substrates with the appropriate calibration coefficients loaded onto the Agilent PNA. The calibration is checked periodically during tests to ensure there is no drift. A photo of the test setup is presented in Figure 7.1.

7.1.2 Cryogenic noise

Block diagrams of the cold attenuator and hot/cold load test setups used in LNA noise measurements are provided in Figure 7.2(a) and (b), respectively. The cold attenuator method is used for measurements up to 18 GHz. The input and output stainless steel coaxial cables are heat sunk to the 77 K stage. The test setup is regularly calibrated against a reference amplifier and the uncertainty in noise temperature measurements is ±1 Kelvin.

Despite its significantly higher measurement duration, the hot/cold load setup is preferred for 50 GHz LNA measurements, because poor input return loss of the LNAs coupled with low ENR from the noise source above 30–35 GHz with the 10 dB cold attenuator produced unreliable results. The output of the device under test (DUT) is down-converted with a variable local oscillator (LO), which is provided by a 67 GHz Anritsu synthesizer and controlled by the noise figure analyzer (NFA), producing a fixed IF frequency of 50 MHz. The test setup works up to 50 GHz; however, uncertainty in measurements grows rapidly above 43 GHz due to gains of the post-amplifier and LO driver amplifier rolling off. The uncertainty up to 40 GHz is estimated to be ±2 Kelvin.

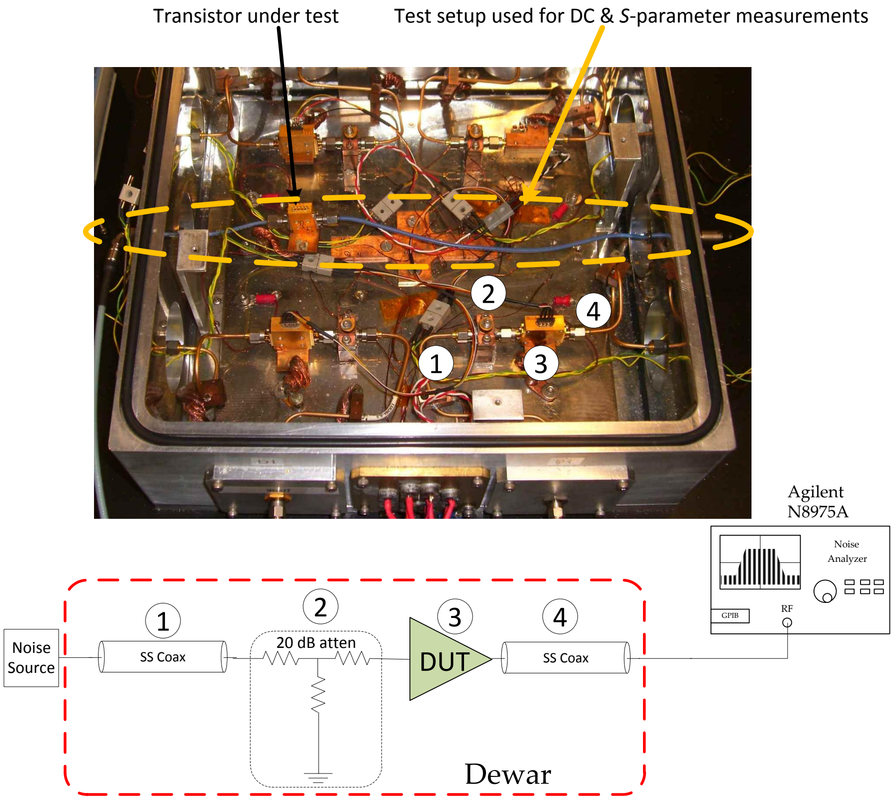

(a)

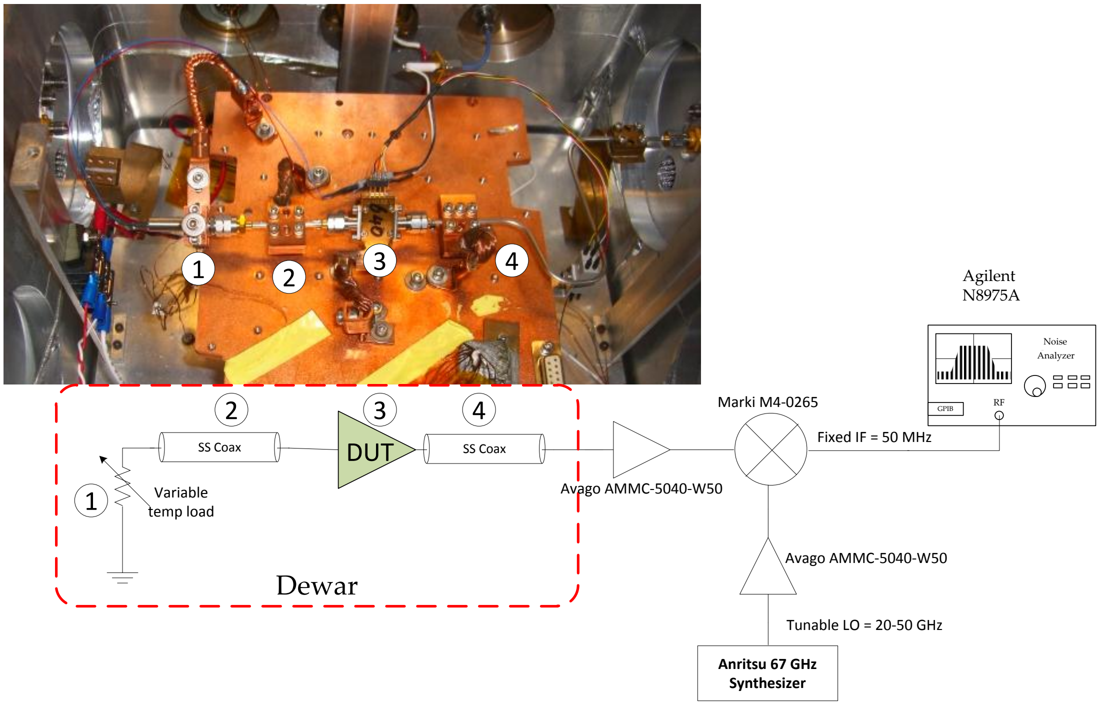

(b)

Figure 7.2: Block diagrams of the (a) cold attenuator, (b) hot/cold load test setups used for LNA noise temperature measurements

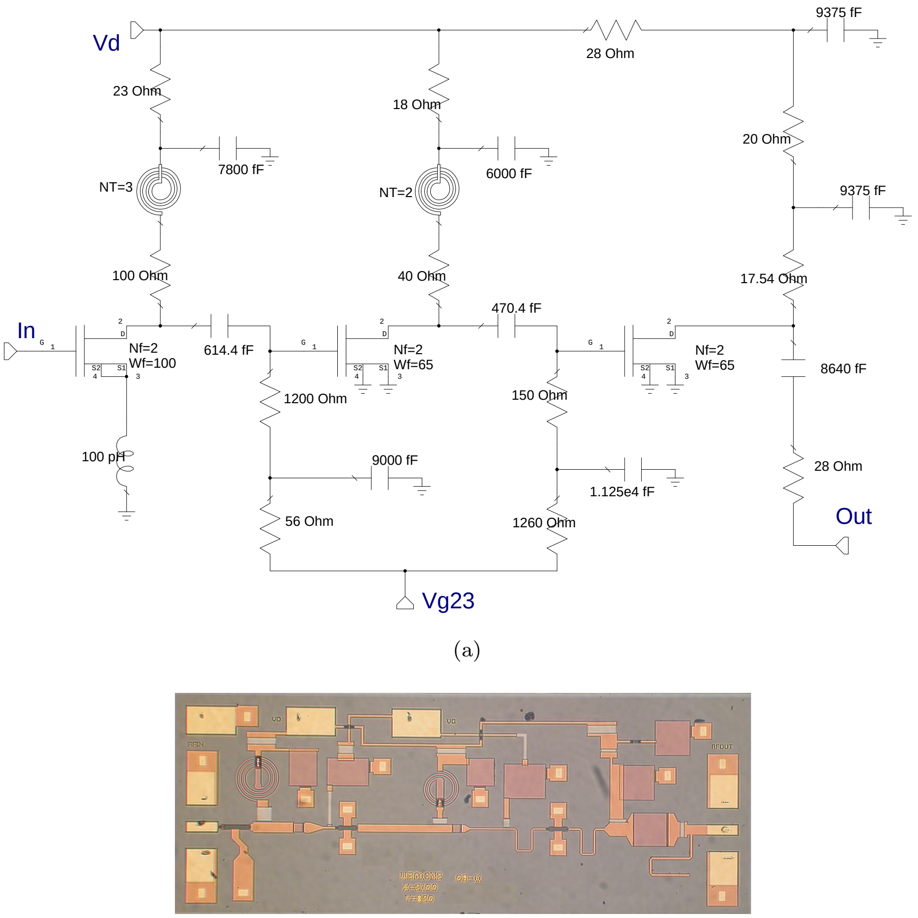

(a)

(b)

Figure 7.3: (a) Schematic, and (b) chip micrograph of the 1–20 GHz NGC LNA. In the schematic, Nf is number of fingers and Wf is finger length in micrometers of the transistor

7.2 NGC 1–20 GHz LNA

The NGC 1–20 GHz LNA consists of three stages with the following device sizes from input to output: 2f200, 2f130, and 2f130 μm. Figure 7.3 displays the schematic and chip micrograph of the LNA.

The wafer-probed S-parameters of MMICs from both the 100% and 75% In wafers appear in Figure 7.4. For the 100% In MMICs, two sets of curves with different bias conditions are presented. In the first case (left half of Figure 7.4(a)), the 100% In MMICs are biased at $V_{DS} = 1.2$ V, $I_{DS} = 20$ mA with gate biases chosen such that all three stages of the MMIC have approximately 0.7 V drain-source voltage drop on the transistor. This is also what was done for the 75% MMICs in part (b). This corresponds to about 20 mA/mm current density in the first stage, which is very low for room-temperature operation. In the right half of part (a), the MMICs are biased at higher drain voltage and current which is closer to the bias of the original SSM.

A large gain slope is observed on LNAs from either process at low bias. The reason for this is

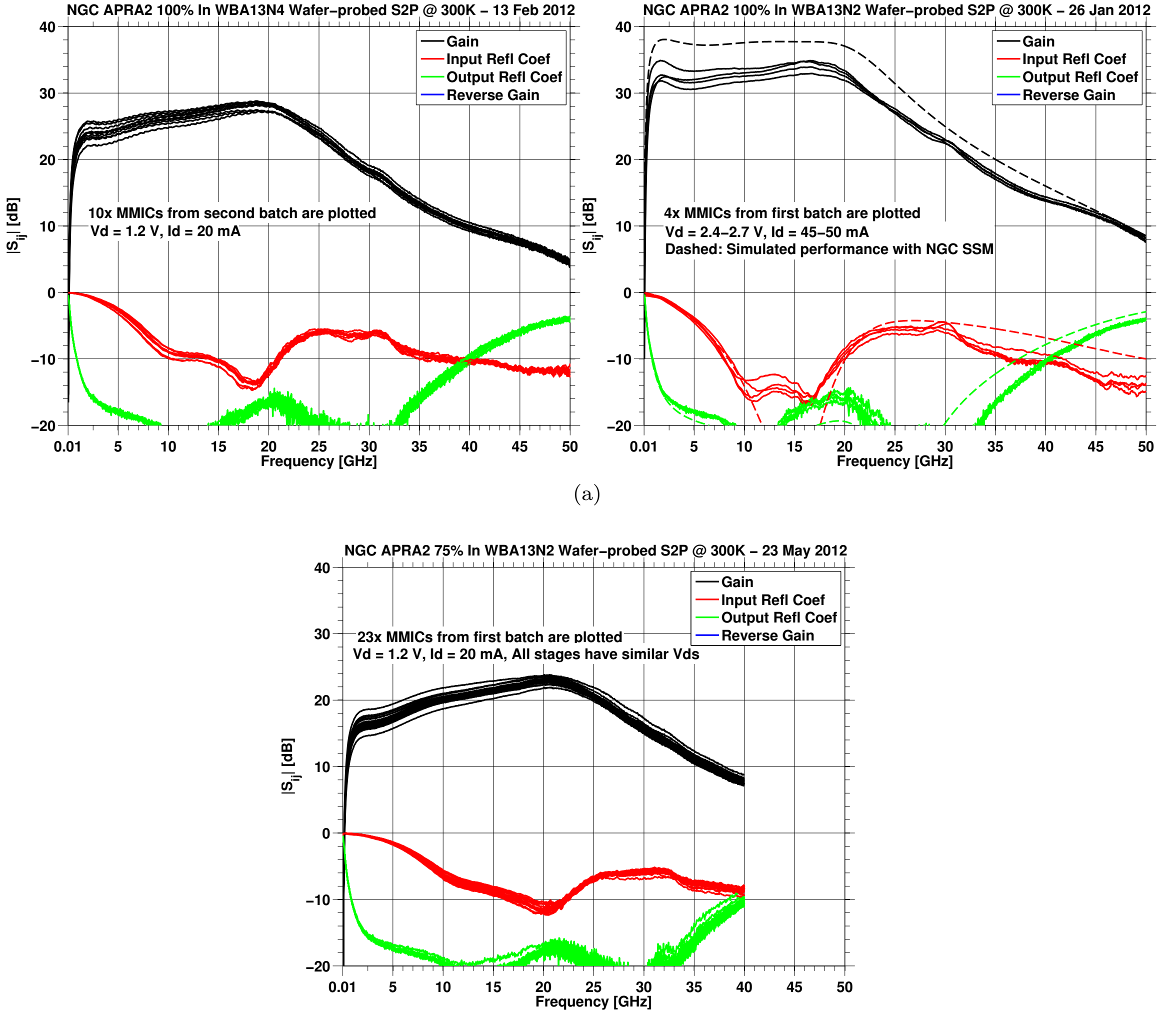

(a)

(b)

Figure 7.4: Wafer-probed S-parameters of NGC 1–20 GHz LNAs from (a) 100% and (b) 75% In wafers. In part (a), two sets of curves are shown with different bias conditions. The simulated performance of the MMIC using NGC 100% In SSM is plotted using dashed lines biased at $V_{DS} = 1$ V and I_{DS} =300 mA/mm (i.e., ∼ 140 mA total MMIC drain current). Chips from the first and second batches are from the same wafer and are identical.

three fold:

1. The first stage has the biggest transistor and thus, has the highest gain at low frequencies and when it is biased at such low current density, the low-frequency gain suffers due to the fact that the gain of the stage is a function of the gate-to-drain capacitor C_{gd} in addition to the transconductance. The reason the first-stage bias was so low is due to a design error in selecting appropriate resistor values for the drain resistors of each stage. In particular, the first stage has the highest resistor value on the drain. This error has somewhat smaller impact in packaged LNA results, because the on-chip drain bias line was cut and two separate drain voltages were provided to the chip;
2. Series inductive peaking used in between second and third stages to increase the gain bandwidth to 20 GHz. This causes a bias-dependent gain peak at the upper end of the frequency band and exacerbates the gain slope;
3. Difference in the foundry-specified SSM and the observed discrete device characteristics.

Another observation from these plots is the lower gain of the 75% In devices by about 5-8 dB when biased similarly to the 100% MMICs. This is in agreement with the discrete device measurements of the previous section where it was observed that the 75% In g_m was roughly 20% lower. When biased at higher drain voltage and current, the 100% MMICs display fairly good input and output match despite the limitations in small-signal modeling. There is still a sizable gain slope and the "average" gain is lower than that predicted by the SSM which also agrees with the difference in measured g_m and that predicted by the small-signal model.

A wafer-probed MMIC is then installed in a coaxial package as shown in Figure 7.5. The input matching network has not been optimized and is a 70 Ω transmission line on a 15-mil-thick Duroid 6002 printed circuit board (PCB) followed by a section of 50 Ω microstrip on 15-mil-thick alumina board. The first-stage gate bias is brought in via a 5 kΩ resistor. The off-chip bypassing is accomplished by three 47pF Skyworks single-layer capacitors next to the chip in addition to 0.01 μF surface-mount capacitors on the DC board. The input AC coupling capacitor is a Skyworks 22pF single-layer capacitor. The on-chip drain bias line on the MMIC is cut and two drain bias voltages are provided. In particular, the first-stage drain bias is connected to the drain power supply directly with some bypassing. The drain bias of the second and third stages, however, have a series 50 Ω resistor (appears right above the three bypass capacitors next to the chip in Figure 7.5) in order to reduce the intrinsic drain voltage on these transistors when the MMIC is biased to optimize first-stage performance.

The measured and simulated scattering parameters and input noise temperature of the LNA at 22 K physical temperature are provided in Figure 7.6 along with the measured noise and gain of the 75% In MMIC in green. The simulations are performed by modifying g_m and g_{ds} of the

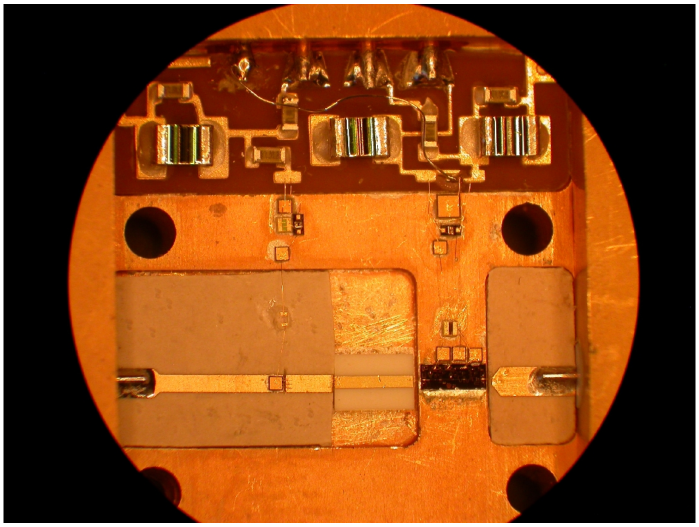

Figure 7.5: Photograph of the NGC 100% In 1–20 GHz LNA

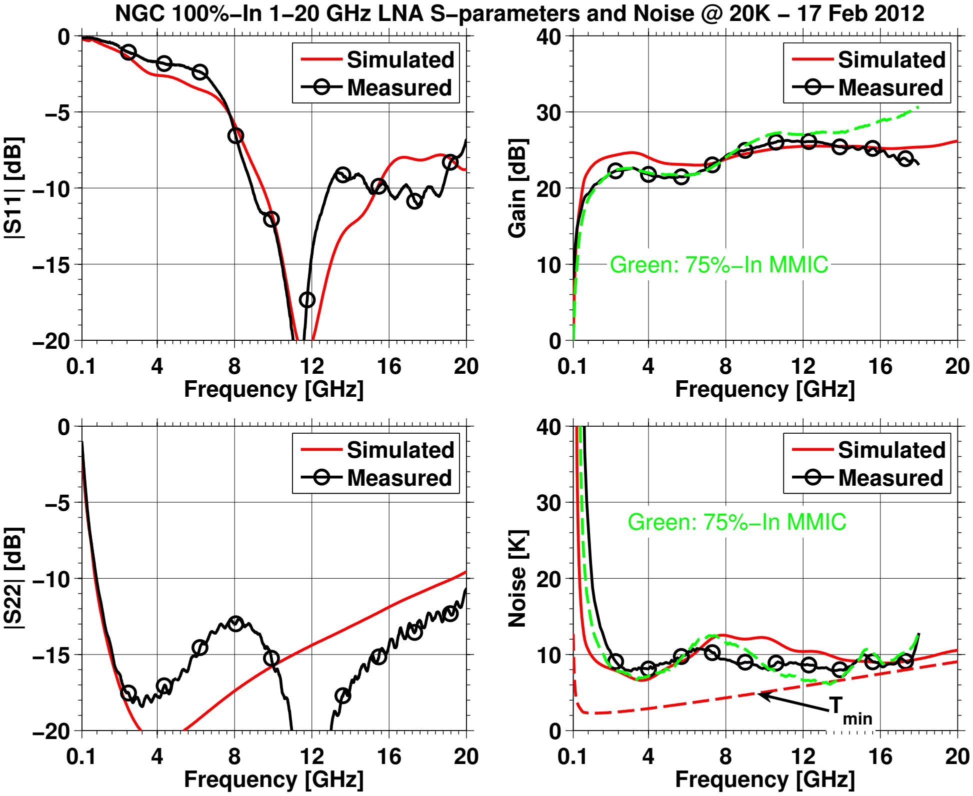

Figure 7.6: Comparison of simulated (red) and measured (black) performance of the 1–20 GHz LNA on NGC's 100% In 35 nm process at 22 Kelvin physical temperature. The supply voltage is 1.2 V with total drain current of 12.6 mA. Simulations include the input matching network. The green dashed gain and noise curves are measured results of the 75% 1–20 GHz LNA.

SSM per discrete HEMT measurements of the previous chapter at the measured bias for each stage. The agreement between the modeled and measured S-parameters is quite good considering the aforementioned limitations. The input return loss is poor below 7 GHz and is approximately 10 dB or higher from 10 to 18 GHz. Comparison of Figures 7.4 and 7.6 reveals that the primary reason for the poor input return loss is the matching network. It has not been optimized at all and was pieced together using available parts in the laboratory. The output return loss is higher than 10 dB over the entire frequency band.

The measured noise is ≤ 10 K from 2 to 17 GHz and compares well with the simulations which also use the results of the T_{drain} measurements from the previous chapter. It is seen that the minimum noise temperature of the MMIC is notably higher than that of a single transistor. One of the reasons for this is the inclusion of a shot noise source between gate and drain of the first-stage device whose power spectral density is taken to be proportional to total gate current instead of sum of absolute values of I_{GD} and I_{GS} because these were not measured. Due to the high R_{opt}, this noise source degrades T_{min} by approximately 1 Kelvin for 0.5 μA gate leakage on the 100% devices. The increased T_{min} may also be due to the fact that the MMIC was not measured at the optimum noise bias; however, the effect of this is thought to be quite small given the fairly flat T_{min} versus bias performance demonstrated in Chapter 6. Furthermore, the T_{min} value calculated in the previous chapter is for a four-finger device versus the two-finger transistors on the MMIC. Nevertheless, the measured noise approaches T_{min} at the upper end of the band.

Four 100% and one 75% MMICs were tested cryogenically. All of the 100% LNAs suffered from low-frequency oscillations and the results presented herein are from the only 100% LNA measurement that yielded respectable noise over the desired frequency range without stability issues. The oscillations, which were not observed on the 75% MMIC, mainly occurred below 1 GHz and exhibited strong dependence on bias of the second and third stages. Many tests have been performed to pinpoint the source of the instability such as measuring the same MMIC in different coaxial packages, trying many different off-chip bypass arrangements including different capacitor values, different resistor values in between capacitors to prevent resonance, etc. Moreover, it was noted that the MMICs oscillated even with the first stage pinched off. All of these empirical observations combined with the fact that 75% MMIC could not be made to oscillate suggest impact ionization, especially the strong inductive behavior of the drain impedance, as the source of the instability. In fact, understanding these results was one of the motivations for the discrete HEMT characterization of the previous chapter.

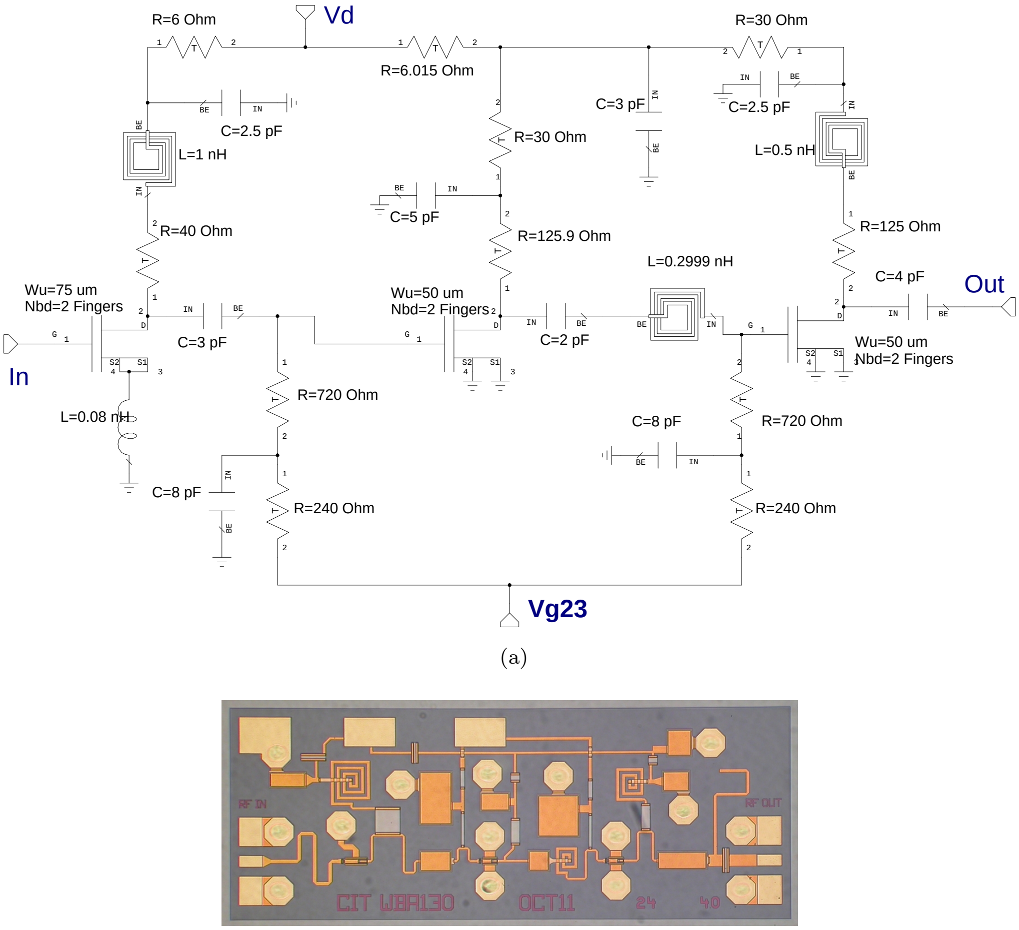

(a)

(b)

Figure 7.7: (a) Schematic, and (b) chip micrograph of the 1–20 GHz OMMIC LNA. In the schematic, Nbd is number of fingers and Wu is finger length in micrometers of the transistor.

7.3 OMMIC 1–20 GHz LNA

This LNA was designed primarily for cryogenic use but the design utilizes the OMMIC design kit SSM values intended for 300K. Fortunately, good results were obtained at both 300K and 20K temperatures. The amplifier consists of three common-source stages with 2f150, 2f100 and 2f100 μm transistors. The schematic and chip micrograph appear in Figure 7.7.

Figure 7.8 plots the wafer-probed S-parameter measurements of the first eight MMICs biased identically which, due to small threshold voltage variations, yields slightly different drain currents. It is seen that there is excellent uniformity in performance at 300 K. Furthermore, at this conservative bias the chips have > 30 dB gain up to 25 GHz as opposed to the design target of 20 GHz. The input impedance is poor but matchable to 50 Ω beyond 10 GHz. The output return loss is decent, but worse than the simulated performance of > 10 dB.

One of the wafer-probed MMICs, serial number 2416, is installed in a coaxial package as shown

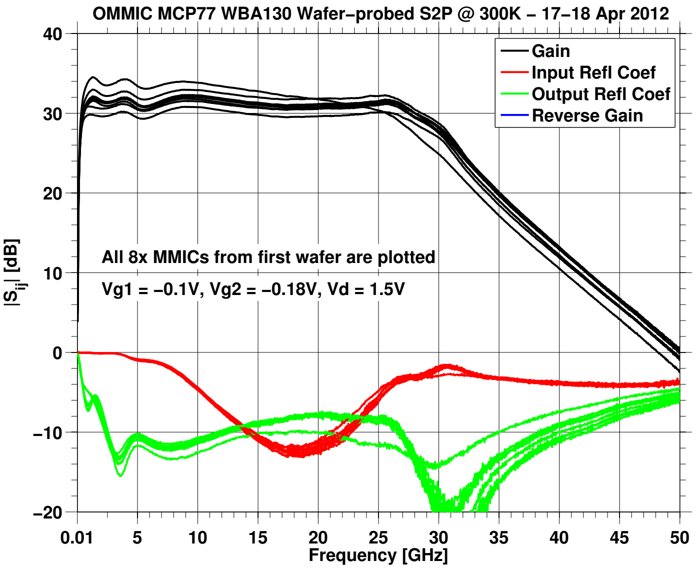

Figure 7.8: Wafer-probed S-parameters of eight OMMIC 1–20 GHz LNAs. The MMICs are biased at identical gate and drain voltages with $I_{DS} = 20 - 25$ mA.

in Figure 7.9. The input matching network has not been optimized and is a simple, 9.5 mm-long, 70 Ω transmission line on a 15-mil-thick Duroid 6002 PCB. It is made by stitching together parts of existing PCBs in the lab. The first-stage gate bias is brought in via a 10 kΩ resistor. The off-chip bypassing is accomplished by 68pF Skyworks single-layer capacitors next to the chip in addition to 0.01 μF surface-mount capacitors on the DC board. The input AC coupling capacitor is a Skyworks 22 pF single-layer capacitor. The measured best input noise temperature and the corresponding S-parameters at room temperature are plotted in Figure 7.10 at the optimum noise bias along with the simulated performance. The simulations are performed at the measurement bias using the discrete device measurements presented previously. The agreement between the two data sets is excellent.

The measured gain is approximately 38 dB and the gain flatness is very good. The measured input match is slightly worse than the simulations which is likely due to small parasitic effects in the SMA connector, the input matching network and the single-layer AC coupling capacitor at the MMIC input. The input return loss needs improvement across the entire frequency range. However, it is worth pointing out that the input return loss of the MMIC alone is better than this performance, and the degradation is mainly due to the input matching network which is not matching the input but bringing the input impedance closer to Z_{opt} of the MMIC. The output match is better than 10 dB from 1.5 to 16 GHz. The input noise temperature at 300 K is impressive, $<$ 80 K (noise figure $<$ 1.06 dB) up to 16 GHz.

Similar to the NGC 1–20 GHz LNA, the simulated MMIC minimum noise temperature deviates from that of the transistor. While the gate leakage of the OMMIC devices are much lower than that of NGC 100% In devices, it still contributes non-negligible noise due to 300 Kelvin ambient

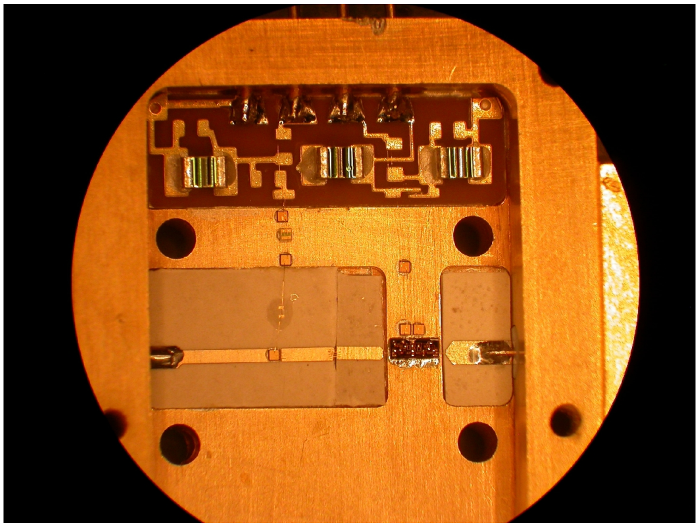

Figure 7.9: Photograph of the OMMIC 1–20 GHz LNA

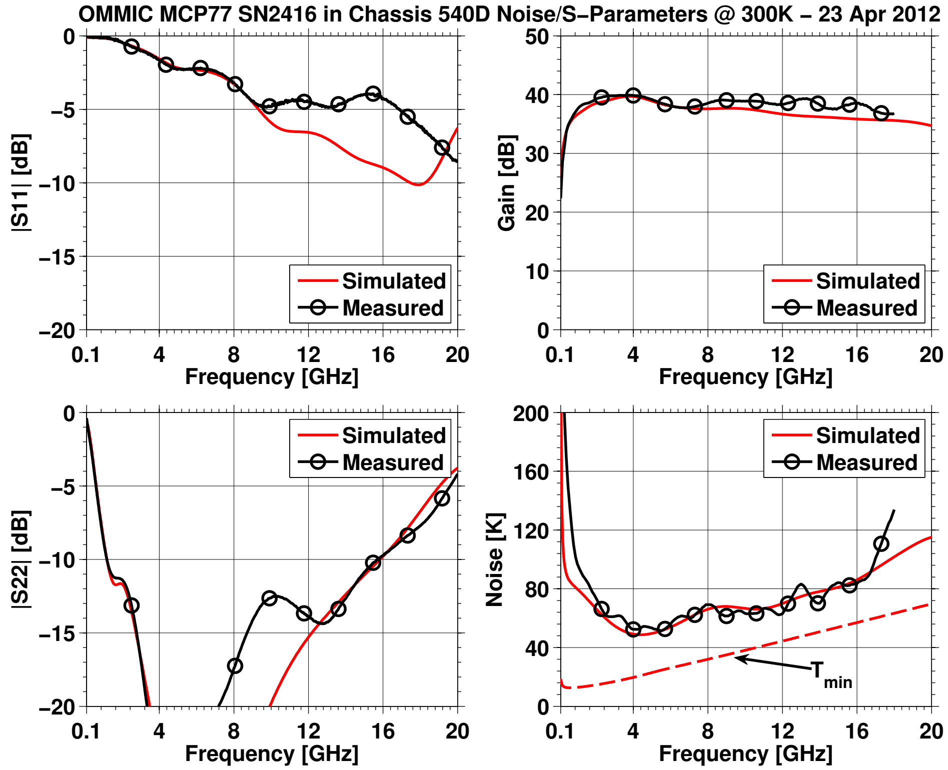

Figure 7.10: Comparison of simulated and measured performance of the 1–20 GHz LNA on OMMIC's D007IH process at 300 Kelvin physical temperature. Agreement between the two data sets is excellent with the exception of a constant gain offset versus frequency. The supply voltage is 2 V with total drain current of 38 mA. Simulations include the input matching network.

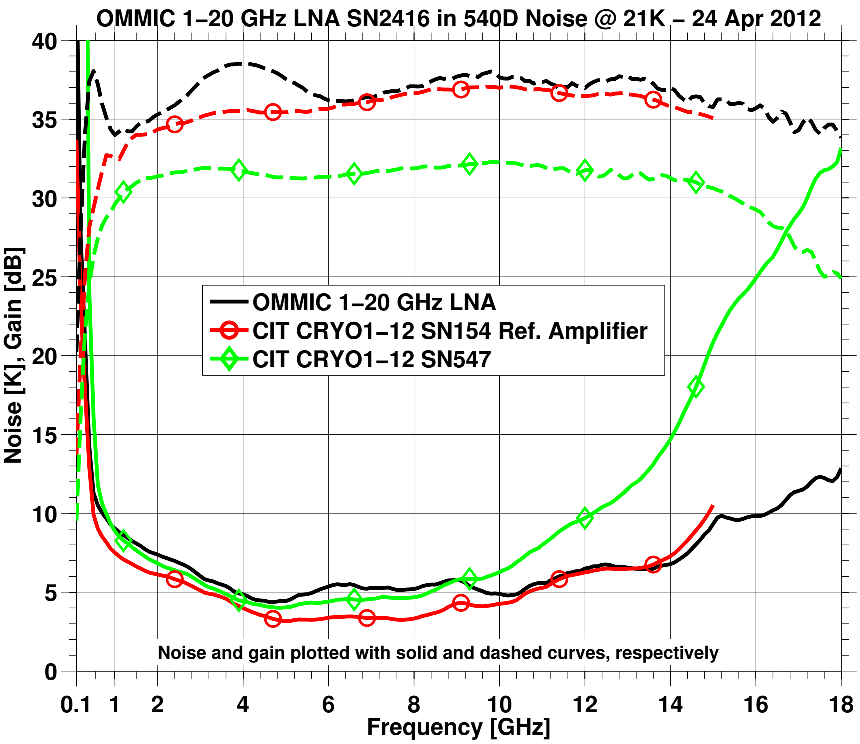

Figure 7.11: Measured input noise temperature and gain of the OMMIC 1–20 GHz LNA at 21 Kelvin physical temperature showing excellent performance over more than two decades of bandwidth (i.e., 0.7 to 16 GHz). The supply voltage is 1 V with total drain current of 16 mA. Also plotted is the performance of a typical and the best 1–12 GHz 130 nm InP LNAs both developed at Caltech.

temperature, e.g., from 5 to 13 K at 1 GHz and 23 to 26 K at 6 GHz due to 1.4 μA gate leakage current. Another reason for the difference is loss preceding the transistor which is very small, but contributes significant noise at 300 K. Another point the T_{min} curve underlines is the sub-optimal input matching network design at the upper end of the frequency band.

The cryogenic input noise temperature and gain of this LNA appear in Figure 7.11 along with those of a typical and the best (reference) 1–12 GHz LNAs developed at Caltech. This LNA achieves $<$ 10 K noise from 0.7 to 16 GHz and 12 K at 18 GHz with measured noise on the order of 5 K from 4 to 10 GHz. In comparison with the typical 130 nm, InP-based, 1–12 GHz LNA, the OMMIC LNA provides much improved noise above 9 GHz. Overall, it works as well as the best InP-based amplifier while its biggest disadvantage is the poor input match as shown in Figure 7.12, which is addressed in the next design iteration (see Section 7.6).

LNAs consuming very low DC power are of interest to THz astronomy where they serve as IF amplifiers following SIS or HEB mixers operating at or below 4 K ambient temperature. In such an application, reducing power consumption decreases the total heat load on the cooler and enables collocation of the LNA and the mixer. The OMMIC 1–20 GHz LNA exhibits $<$ 10 K from 2 to 14 GHz at 3 mW DC power consumption, as shown in Fig. 7.13. While not shown here for brevity,

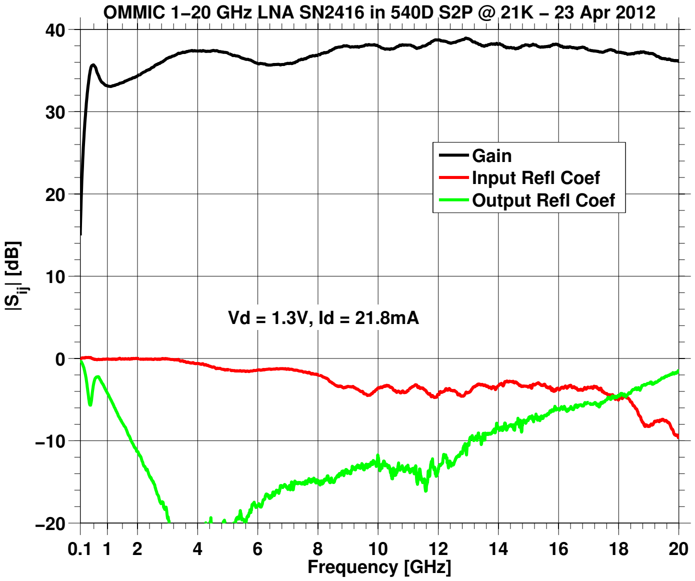

Figure 7.12: Measured cryogenic scattering parameters of the 1–20 GHz OMMIC LNA. The bias is slightly different than that of the noise measurements; however, the performance difference was observed to be very small.

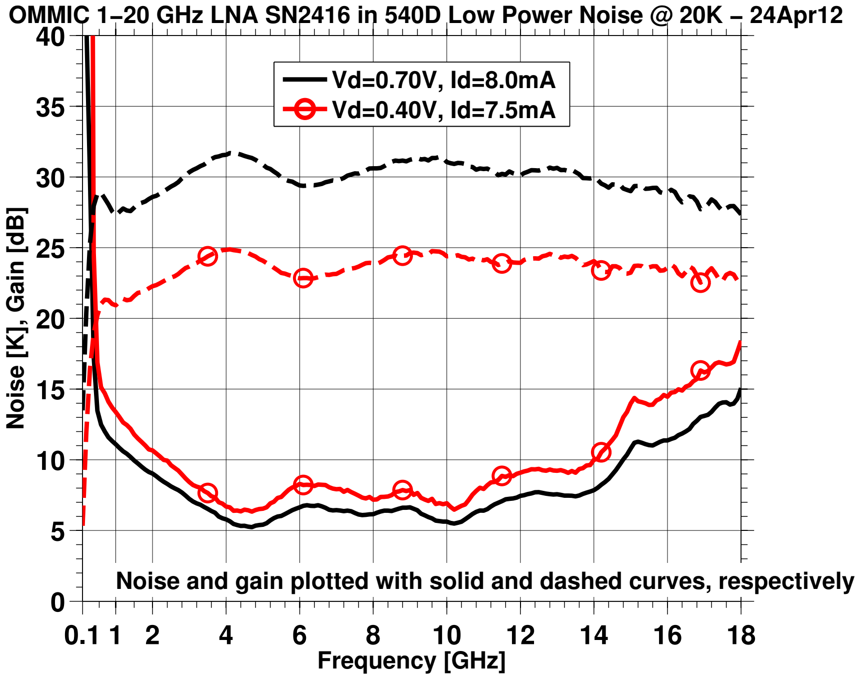

Figure 7.13: Measured cryogenic noise and gain of the 1–20 GHz OMMIC LNA under low-power operation

it achieves > 15 dB power gain and ~ 20 K input noise temperature at 8 GHz with less than 1 mW power consumption from 0.25 V drain supply. As such, it is a very attractive candidate for IF amplifiers in following superconducting mixers, especially if the LNA is collocated with the mixer such that impact of poor input match is minimized.

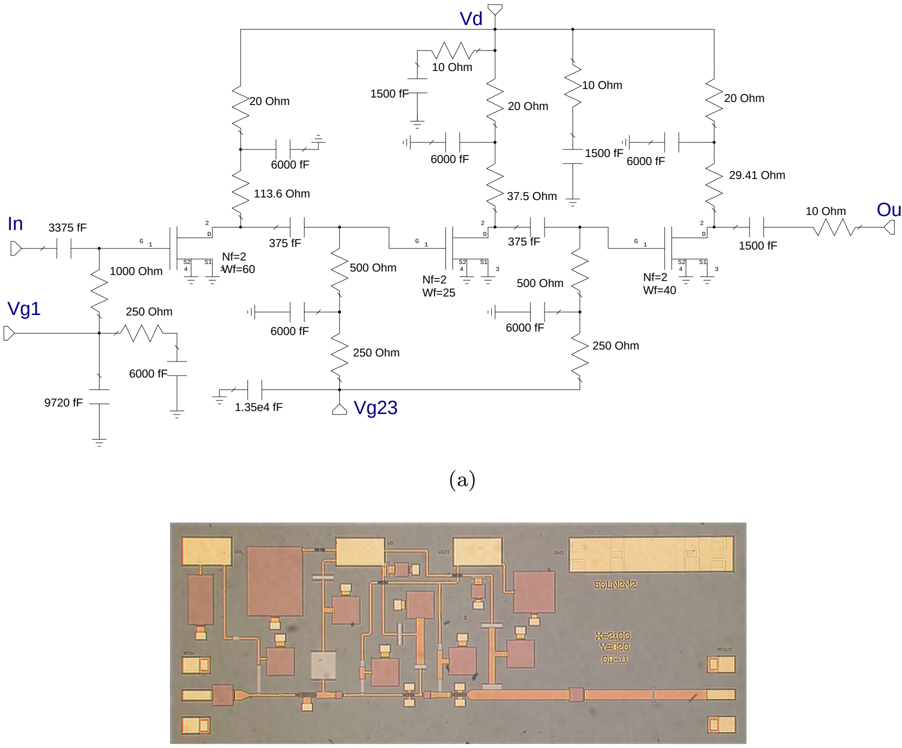

(a)

(b)

Figure 7.14: (a) Schematic, and (b) chip micrograph of the 8–50 GHz NGC LNA

7.4 NGC 8–50 GHz LNA

The 8–50 GHz LNA comprises three stages with 2f120, 2f50 and 2f80 μm transistors. Unlike the lower frequency LNAs, the first-stage gate bias is on chip. A chip micrograph and the LNA schematic are provided in Figure 7.14.

The wafer-probed, room-temperature scattering parameters appear in Figure 7.15 for two bias conditions. Similar to the 1–20 GHz NGC LNAs, the MMICs exhibit more gain variability with frequency in comparison with the simulations and significant gain slope under low bias which is again due in part to error in drain resistor value. Unlike the low-frequency LNAs, however, the input and output match of the MMICs operated near the NGC SSM bias are notably worse than simulations. Results from 75% In MMICs are not included due to very limited testing performed on those chips.

A V-band chassis was designed to test the 50 GHz MMICs in a coaxial package. It uses Anritsu V-band glass beads and sliding contacts to make solid electrical connection with the 5-mil-thick, 50 Ω alumina boards at the input and the output. Similar to the other LNAs presented above, the off-chip bypass capacitors are 47 pF Skyworks single-layer capacitors. While this MMIC also suffers from the design error regarding the drain resistor values, the on-chip drain line is not cut and one common drain voltage is used. It is reasonable to expect some improvement in the results presented

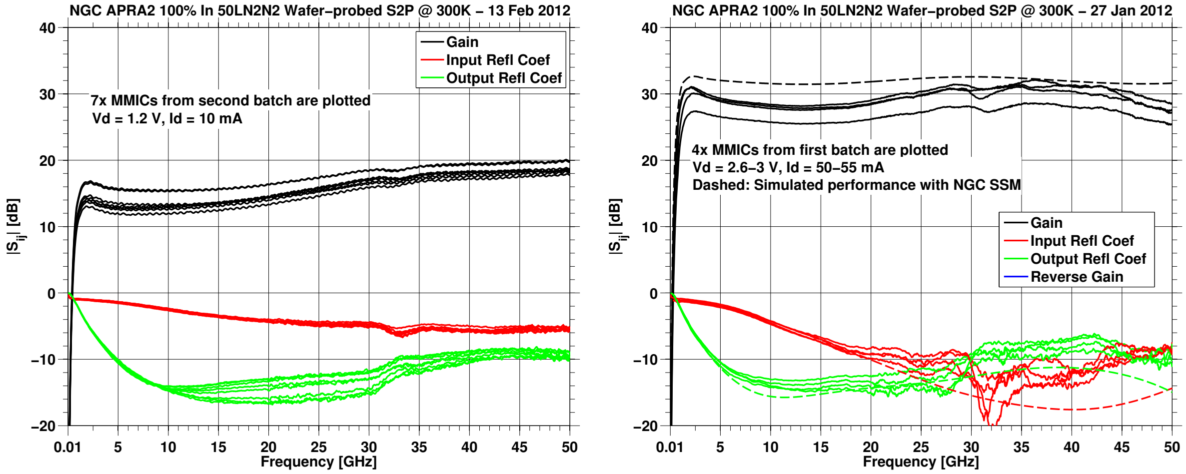

(a) (b)

Figure 7.15: Wafer-probed S-parameters of NGC 100% In 8–50 GHz LNAs with total drain current of approximately (a) 10 mA at 1.2 V, and (b) 50 mA at 2.8 V. Chips from the first and second batches are from the same wafer and are identical.

in this section if the drain lines were to be separated between first and subsequent stages.

The measured and simulated scattering parameters and input noise temperature are provided in Figure 7.17, where the simulations incorporate the measured g_m, g_{ds}, and T_{drain} in the small-signal model. The only caveat is that T_{drain} values from measurements were reduced manually because otherwise the simulated noise was considerably higher than measured noise throughout the band. This manual adjustment is in line with the earlier observation that impact ionization increases T_{drain}, but this should mostly be at low frequencies, i.e., $<$ 10 GHz and the noise performance at higher frequencies should not be affected as severely. Nevertheless, the manually adjusted T_{drain} values are still obtained from measurements, but at a bias point prior to onset of impact ionization.

The agreement between predictions and measurements is mediocre for input and output return loss. This is primarily due to inadequate modeling of the V-band glass-bead and sliding contact attachment to the 50 Ω alumina traces. Nonetheless, the simulations are fairly close to the “mean” level of measurements for most of the frequency band. The measured gain is, as expected, low and exhibits considerable slope.

The simulated and measured noise performance are somewhat different, especially above 20 GHz due in part to inadequate modeling of the MMIC packaging. In spite of that, the measured noise temperature is still $\leq$ 20 K from 6 to 40 GHz at 30 mW power consumption and is reasonably close to simulated minimum noise temperature T_{min} above 20 GHz. Also plotted in the same figure is the input noise temperature of another MMIC (green dashed) which exhibits better performance, i.e., $T_n \sim T_{min}$ throughout the upper half of the frequency range. This improvement is due to two factors:

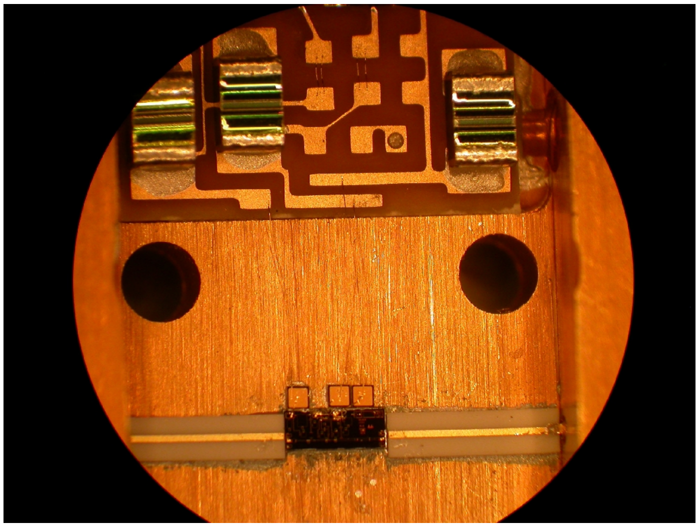

Figure 7.16: Photograph of the NGC 100% In 8–50 GHz LNA

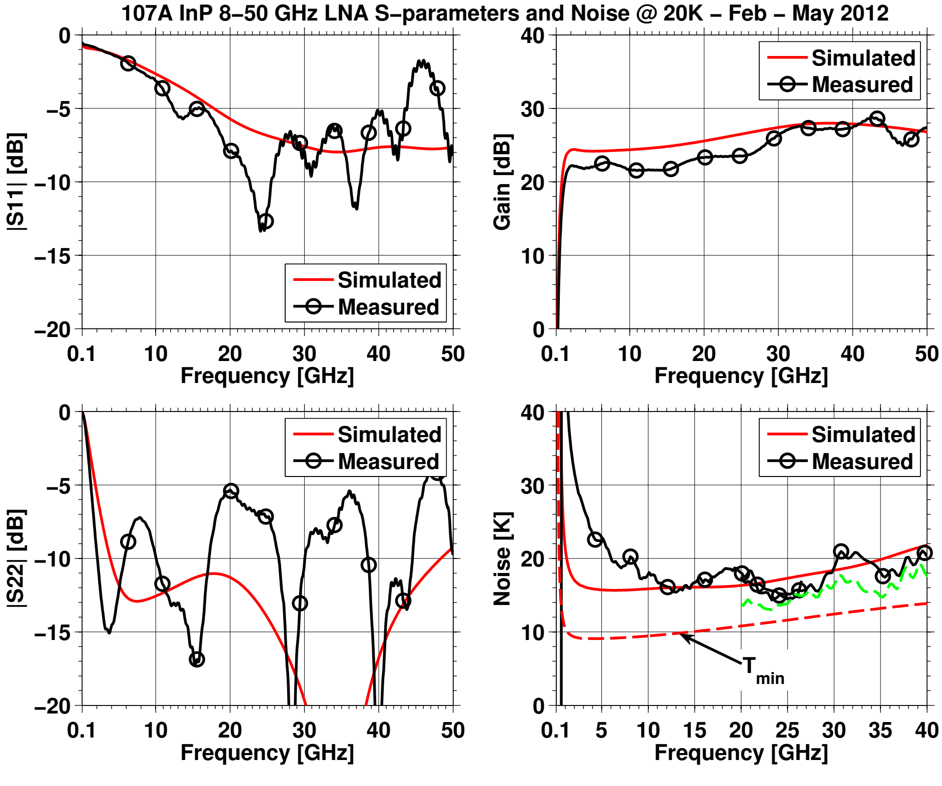

Figure 7.17: Comparison of simulated (red) and measured (black) performance of the 8–50 GHz LNA on NGC's 100% In 35 nm process at 22 Kelvin physical temperature. The supply voltage is 1.3 V with total drain current of 23.6 mA. Also plotted in green dashed is measured noise of another 8–50 GHz 100% In MMIC.

1. Improvements to the test setup: A few months after the initial MMIC was tested, an attenuator was incorporated following the DUT outside the dewar and the post-amplifier bias was adjusted. Prior to these changes, the second MMIC performed almost identical to the one plotted in black;
2. Packaging: Some time after the tests, it was noticed that the V-band sliding contacts were not epoxied as instructed by Anritsu;

The first MMIC could not be tested after these changes, because it was re-used elsewhere. However, it is reasonable to conjecture that the test setup and the sliding contact attachment may have had a signature on the results. The as-measured noise performance of this amplifier is somewhat higher than the existing cryogenic LNAs, but may possibly be closer to the state of the art once more careful and reliable tests are performed. In addition, this LNA spans much wider frequency range than the currently available ones, most of which usually only cover a waveguide band, e.g., 26–40 GHz.

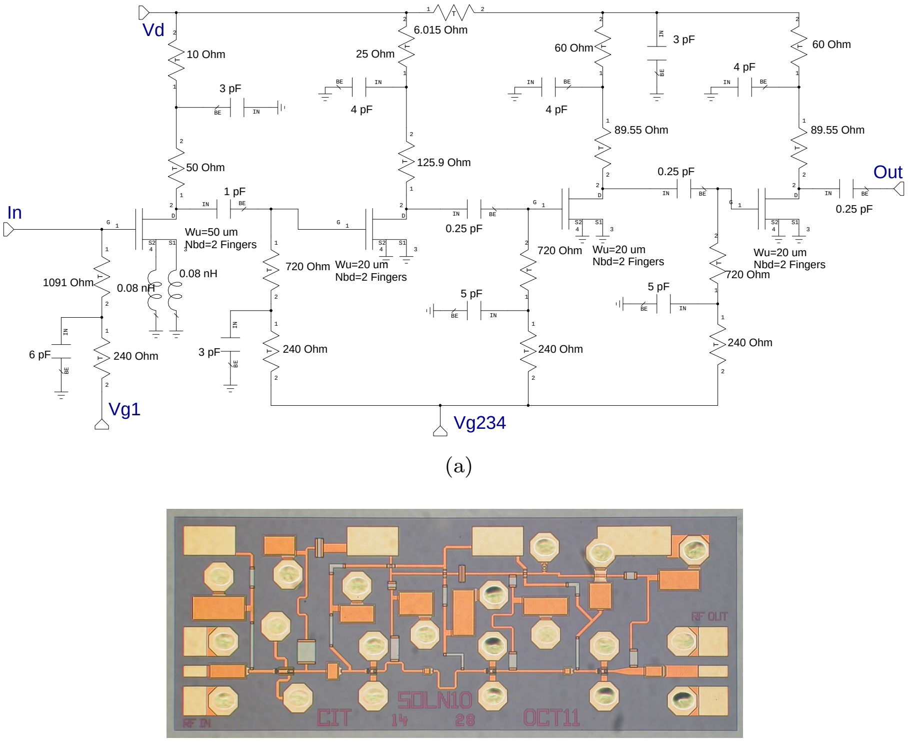

(a)

(b)

Figure 7.18: (a) Schematic and (b) chip micrograph of the 8–50 GHz OMMIC LNA

7.5 OMMIC 8–50 GHz LNA

The final LNA presented is the 8–50 GHz OMMIC design, which, unlike the other designs, is a four-stage amplifier. The first stage consists of a 2f100 μm device followed by three stages employing 2f40 μm transistors. The first-stage gate bias is once again on chip. The circuit schematic and a chip micrograph appear in Figure 7.18.

The first nine MMICs were wafer-probed at 300 K and their S-parameters are displayed in Figure 7.19 along with the expected performance per simulations. The most important observation is the large gain slope. The gain peaks around 50 GHz and the peak location in frequency exhibits strong bias dependence. The input and output return loss both approach 0 dB near the gain peak. Moreover, both deviate considerably from simulations as the gain slope starts to dominate the frequency response. This suggests that these are all due to the same phenomenon which is thought to be due to feedback from the output of the fourth stage to that of the second stage. The only way a similar effect could be reproduced in simulations was by tweaking the resonance frequency of the bypass capacitors on the second-stage drain and the drain bias line such that their response becomes inductive at lower frequency than the OMMIC SSM predicts.

The MMIC is installed in the same V-band package as the NGC 50 GHz LNA. The gate DC bias lines have series resistors to prevent possible resonance with the surface-mount capacitors.

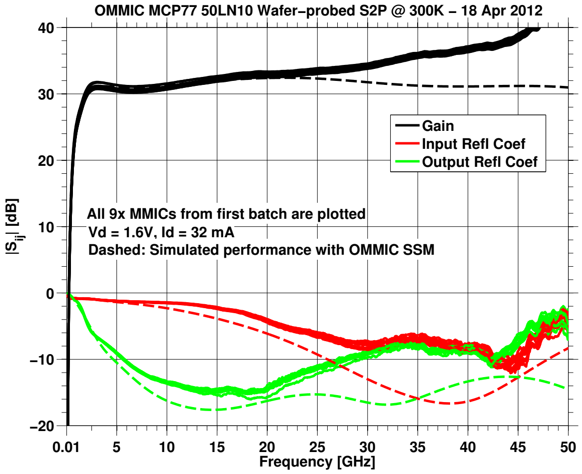

Figure 7.19: Wafer-probed S-parameters of nine OMMIC 8–50 GHz LNAs biased with total drain current of 32 mA at 1.6 V. Simulated performance is plotted using dashed curves.

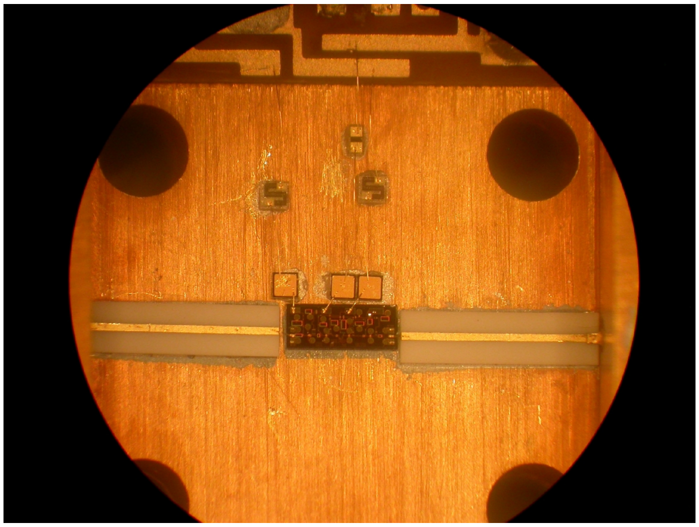

Figure 7.20: Photograph of the OMMIC 8–50 GHz LNA

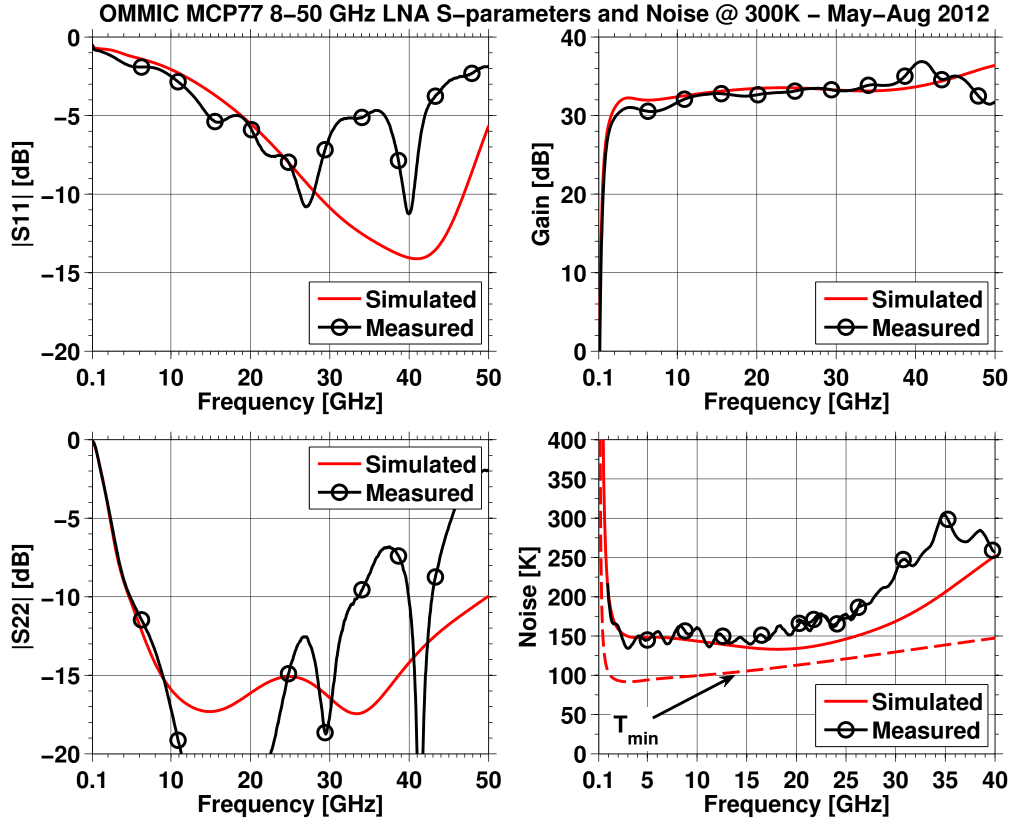

Figure 7.21: Comparison of simulated (red) and measured (black) performance of the OMMIC 8–50 GHz LNA at room temperature. The supply voltage is 1.85 V with total drain current of 35 mA.

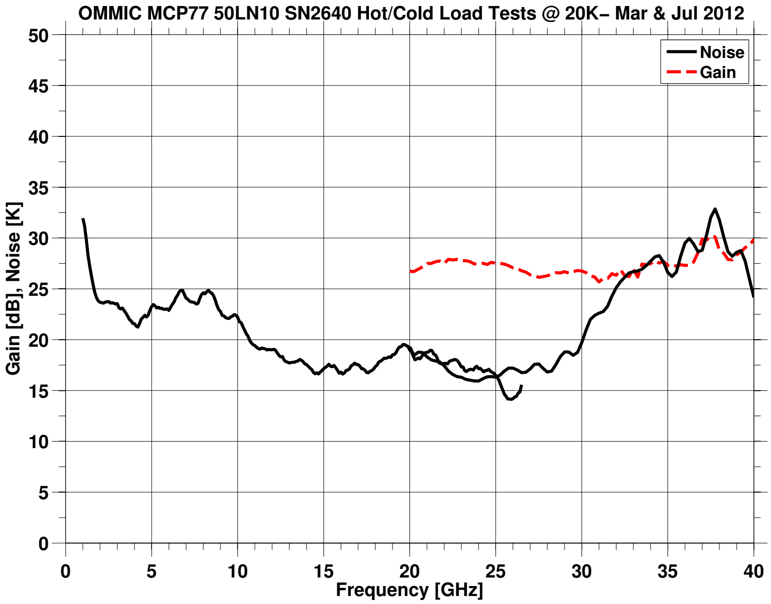

Figure 7.22: Measured input noise temperature (black solid) and gain (red dashed) of the OMMIC 8–50 GHz LNA at 21 Kelvin physical temperature. The supply voltage is 1 V with total drain current of 11 mA. Cryogenic gain was not measured between 1 and 20 GHz.

Also included is a series 10 Ω resistor on the drain bias line for the same purpose. The measured performance at room temperature is compared to simulations in Figure 7.21. The agreement between the data sets is quite reasonable, especially up to 30 GHz. The room-temperature noise performance is poor compared to other published results [24]; however, this LNA covers a much wider frequency range, nearly a decade bandwidth. The degradation in noise above 30 GHz is also thought to be related to the feedback mechanism mentioned above.

Finally, Figure 7.22 presents cryogenic noise and gain of the LNA which was measured after the 50 GHz noise test set was upgraded (see Section 7.4). The noise is 5-10 K higher than the NGC 50 GHz LNA and the gain is somewhat lower. The latter is related to the DC bias which is quite low. It was selected to minimize 40 GHz noise by measuring the noise temperature of the MMIC using the hot/cold load method at a single frequency (the same approach was used for the NGC 50 GHz LNA). Overall, the performance is respectable given the DC power consumption; however, it needs improvement to be useful in radio astronomy.

7.6 Revised Designs

As alluded to earlier, revised designs are submitted to both foundries. The revisions were primarily made based on the discrete device characterization results of the prior chapter with the exception of the T_{drain} results which were not available at the time.

In particular, the revised NGC 1–20 GHz LNA was targeted for the 75% In wafer whereas the revised 8–50 GHz LNA is intended for the 100% In wafer. Number of changes were kept to a minimum to reduce uncertainty as much as possible with the primary improvements being:

1. the drain resistor design error was fixed on both LNAs which will enable operation in wider range of DC bias;
2. all stages are designed to operate with low intrinsic drain-source voltage, e.g., ˜ 0.4–0.5 V;
3. $>$ 30 dB gain with much less slope;
4. improved input and output return loss at the target DC bias point;
5. drain bias lines of the first and subsequent stages are separated on chip to reduce potential feedback. The MMICs are still designed to operate off of a single drain supply; however, the two on-chip drain lines are intended to be tied together after RF bypassing.

Only the OMMIC 1–20 GHz LNA is revised for the second iteration and it is split into two designs: 1) 1-18 GHz LNA; 2) 1–12 GHz LNA. For both, the primary goal was to improve input return loss while maintaining, or if possible improving, all other performance metrics. The revisions, again based on discrete transistor measurements, were a bit more "radical" on these designs and include:

1. all stages are designed to operate with low intrinsic drain-source voltage, e.g., ˜ 0.4–0.5 V;
2. transistors with four or more fingers are employed instead of two-finger devices only;
3. drain bias lines of the first and subsequent stages are separated like the new NGC MMICs;
4. better than 10 dB input return loss for $f > 5$ GHz and much better output return loss on both designs;
5. 1–12 GHz LNA employs feedback for the first time in published HEMT LNA literature and also employs large first- and second-stage devices. This increases power consumption but helps reduce low-frequency noise in addition to bringing R_{opt} closer to 50 Ω.

7.7 Cryogenic Performance of Coupling Capacitors

The 1–20 GHz LNAs presented herein do not have on-chip gate bias for the first stage. Consequently, the packaged amplifiers employ off-chip, single-layer AC coupling capacitors which must be resonance-free over the entire bandwidth of the MMICs and low loss to ensure impact on input noise temperature and S-parameters of the LNA is minimal. In order to quantify the impact of coupling capacitors on measured noise of amplifiers, cryogenic microwave performance of five capacitors, four single-layer and one surface-mount, are evaluated. In particular, effective noise contribution of each capacitor is calculated using cryogenic scattering parameter measurements. The five capacitors tested to date are:

1. Dielectric Labs Milli-Cap 82 pF multi-layer, size 50 mil by 20 mil;
2. Presidio Components 4 pF, size 12 mil by 12 mil;
3. Presidio Components 10 pF, size 15 mil by 15 mil;
4. Skyworks 10 pF, 9 mil by 12 mil;
5. Skyworks 22 pF, 15 mil by 18 mil.

Each capacitor is mounted, in series configuration, in a V-band package (same as the one used for 50 GHz LNAs) with 50 Ω input and output alumina microstrip lines. The packaged capacitor is characterized by measuring its S-parameters up to 50 GHz both at room and cryogenic temperatures. The packaging effects on the measurements are mostly de-embedded via measurements of a thru package. The cryogenic measurements were performed at 77 K by dipping the packaged capacitor in liquid nitrogen (Figure 7.23). In the following, the capacitor performance is assumed unchanged from 77 to 22 K.

Let the effective loss of the capacitor be defined as the reciprocal of its available gain with $R_{gen} = 50\,\Omega$, i.e.,

$$L_{eff} \equiv \frac{1 - |s_{22}|^2}{|s_{21}|^2}, \tag{7.1}$$

then, input noise temperature of the capacitor followed by the MMIC LNA is given simply by the Friis' formula for noise [88]

$$T_n = T_{cap} + L_{eff} T_{LNA} \tag{7.2}$$

where T_{LNA} is the noise temperature of the LNA, and the noise temperature of the capacitor T_{cap}—a lossy, passive two port—is obtained using Bosma's theorem [96]

$$T_{cap} = T_{phys} \frac{1 - |s_{22}|^2 - |s_{21}|^2}{|s_{21}|^2} = T_{phys}\left(L_{eff} - 1\right). \tag{7.3}$$

Figure 7.23: Measurement setup for cryogenic capacitor tests

T_{phys} is the physical temperature of the capacitor, namely 300 or 22 K. Then, the effective noise contribution due to ohmic losses in the capacitor is defined as

$$\Delta T \equiv T_n - T_{LNA} = \left(T_{phys} + T_{LNA}\right)\left(L_{eff} - 1\right). \tag{7.4}$$

Here, s_{21} represents the de-embedded transmission coefficient while no de-embedding is performed on s_{22}.

Figure 7.24 presents the calculated noise contribution of the five capacitors. For these plots, T_{LNA} is assumed to be 55 and 5 Kelvin at room and cryogenic temperatures, respectively. The effect of the capacitor reactance is negligible above 1 GHz for values > 10 pF. The ripples in response around 12 and 18 GHz are remnants of package effects after de-embedding. From the noise contribution perspective, the two Skyworks capacitors perform the best. However, their performance starts to degrade above 12 GHz with the 10 pF capacitor exhibiting slightly wider bandwidth. Presidio 4 pF capacitor achieves even wider bandwidth without any resonances; however, its noise contribution is significantly higher thereby limiting its use for extremely low-noise applications. Dielectric Labs 82 pF Milli-Cap is an SMT single-layer capacitor with the data sheet indicating resonance-free and low-loss operation up to 40 GHz. The measurements reveal significantly different performance; however, it is possible that there are artifacts due to mounting of the SMT capacitor in the coaxial package (e.g. capacitor is installed on 4-mil-wide microstrip trace) which could explain some of the unexpected performance degradation.

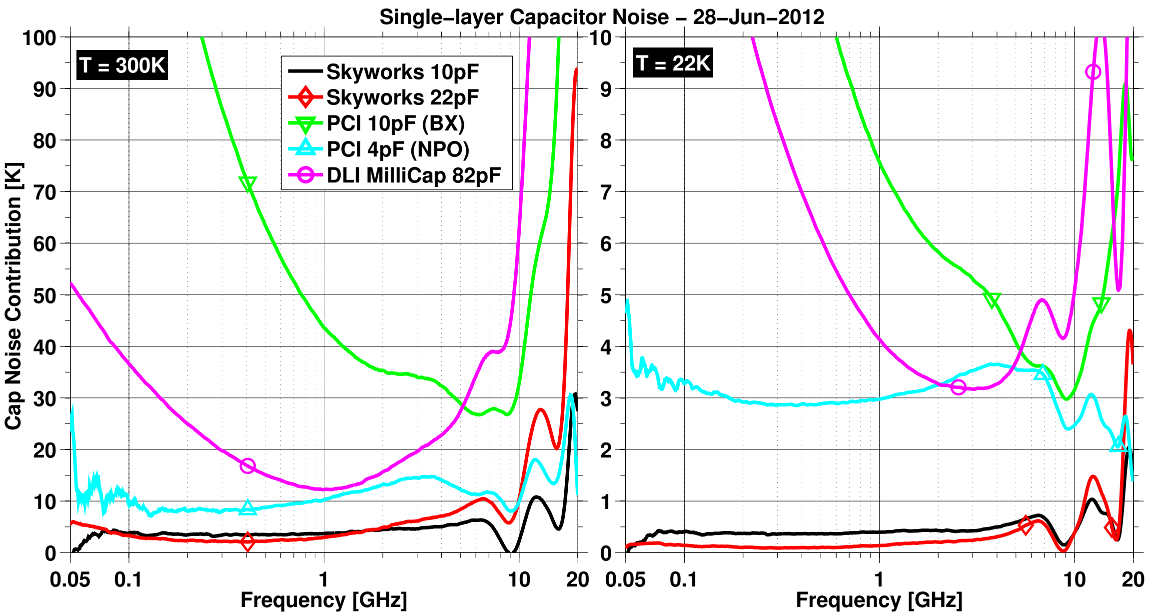

Figure 7.24: Effective noise contribution due to ohmic loss of five microwave capacitors at 300 and 22 K

7.8 Conclusions

In this chapter, the measurements of 1–20 and 8–50 GHz LNAs on Northrop Grumman Corporation's 35 nm InP and OMMIC's 70 nm GaAs processes have been discussed at length. The results have been extensively compared to simulated performance using discrete HEMT results of the previous chapter, and in general, the agreement was observed to be very good.

Of the LNAs presented, three stand out by improving the state of the art in noise and bandwidth of cryogenic LNAs:

1. the OMMIC 1–20 GHz LNA achieved ≤ 10 K from 0.7 to 16 GHz and ~ 5 K over half of that band with approximately 15 mW DC power consumption. Furthermore, it performs very well under ultra-low-power operation with ≤ 10 K noise temperature from 2 to 14 GHz at 3 mW;
2. the low-frequency InP LNA measured ≤ 10 K from 2 to 17 GHz, but exhibited large gain slope due mostly to limited SSM availability and design error in drain resistor values;
3. the NGC 8–50 GHz LNA achieves < 20 K noise from 6 to 40 GHz which is only slightly higher than state-of-the-art Ka-band amplifiers in the literature, but covers a much wider frequency band.

All LNAs exhibit poor input return loss which is addressed in the next design iteration in addition to correcting the large gain slopes observed on NGC LNAs.

The results of this chapter highlight the trade-off between low-frequency noise temperature and bandwidth of ultra-wideband LNAs. In particular, improving the former requires large first-stage devices with R_{opt} values closer to 50 Ω in addition to significant inductive source degeneration. However, both degrade high-frequency noise and gain of the LNAs. On the other hand, small devices in the first stage not only move R_{opt} away from 50 Ω, but also makes the input impedance of the LNA very difficult to match. This further complicates the LNA design as the amount of matching one can do is very limited to begin with in ultra-wideband applications.

Bibliography

[1] P. Demorest, "A pulsar timing array for gravitational wave detection," presented at the Building on New Worlds, New Horizons: New Science from Sub-millimeter to Meter Wavelengths, Mar. 2011.

[2] A. Niell, A. Whitney, B. Petrachenko, W. Schluter, N. Vandenberg, H. Hase, Y. Koyama, C. Ma, H. Schuh, and G. Tuccari. VLBI2010: Current and future requirements for geodetic VLBI systems. IVS Memorandum 2006-008v01. [Online]. Available: ftp://ivscc.gsfc.nasa.gov/pub/memos/ivs-2006-008v01.pdf

[3] B. Petrachenko. VLBI2010 frequency considerations. IVS Memorandum 2008-015v01. [Online]. Available: ftp://ivscc.gsfc.nasa.gov/pub/memos/ivs-2008-015v01.pdf

[4] J. D. Kraus, *Radio Astronomy*, 2nd ed. Powell, OH: Cygnus-Quasar Books, 1986, ch. 8-3 Source Spectra.

[5] G. E. Jones, "Instrumentation for wide bandwidth radio astronomy," Ph.D. dissertation, California Institute of Technology, Pasadena, CA, Jun. 2010. [Online]. Available: http://resolver.caltech.edu/CaltechTHESIS:10122009-094525715

[6] P. J. Hall, Ed., *The SKA: An Engineering Perspective.* The Netherlands: Springer, 2005.

[7] US SKA Consortium, "The square kilometer array preliminary strawman design large N - small D," SKA Memo 18, Jul. 2002.

[8] J. Yang, M. Pantaleev, P.-S. Kildal, Y. Karandikar, L. Helldner, N. Wadefalk, and C. Beaudoin, "Cryogenic 2-13 GHz Eleven feed for reflector antennas in future wideband radio telescopes," *IEEE Trans. Antennas Propag.*, vol. 59, no. 6, pp. 1918–1934, Jun. 2011.

[9] G. Engargiola and W. J. Welch, "Log-periodic antenna," U.S. Patent 6 677 913, Jan. 13, 2004.

[10] R. S. Gawande and R. F. Bradley, "Characterization of the active, inverted, conical sinuous antenna," in *XXIX General Assembly of URSI*, Chicago, IL, Aug. 2008.

[11] C. A. Balanis, *Antenna Theory: Analysis and Design*, 3rd ed. New Jersey: Wiley, 2005.

[12] S. Weinreb, “Low-noise cooled GASFET amplifiers,” *IEEE Trans. Microw. Theory Tech.*, vol. MTT-28, no. 10, Oct. 1980.

[13] J. D. Pandian, L. Baker, G. Cortes, P. F. Goldsmith, A. A. Deshpande, R. Ganesan, J. Hagen, L. Locke, N. Wadefalk, and S. Weinreb, “Low-noise 6-8 ghz receiver,” *IEEE Microwave Magazine*, vol. 7, no. 6, Dec. 2006.

[14] J. Schleeh, G. Alestig, J. Halonen, A. Malmros, B. Nilsson, P. Nilsson, J. Starski, N. Wadefalk, H. Zirath, and J. Grahn, “Ultralow-power cryogenic InP HEMT with miunimum noise temperature of 1 K at 6 GHz,” *IEEE Electron Device Lett.*, vol. 33, no. 5, May 2012.

[15] D.-W. Tu, S. W. Duncan, A. Eskandarian, B. Golja, B. C. Kane, S. P. Svensson, S. Weinreb, and N. E. Byer, “High gain monolithic W-band low noise amplifiers based on pseudomorphic high electron mobility transistors,” *IEEE Trans. Microw. Theory Tech.*, vol. 42, no. 12, Dec. 1994.

[16] M. Varonen, R. Reeves, P. Kangalashti, L. Samoska, A. Akgiray, K. Cleary, R. Gawande, A. Fung, T. Gaier, S. Weinreb, A. C. S. Readhead, C. Lawrence, S. Sarkozy, and R. Lai, “A 75-116 GHz LNA with 23-K noise temperature at 108 GHz,” in *submitted to 2013 IEEE International Microwave Symposium*, Seattle, WA, Jun. 2013.

[17] L. Samoska, M. Varonen, R. Reeves, K. Cleary, R. Gawande, P. Kangalashti, T. Gaier, R. Lai, and S. Sarkozy, “W-band cryogenic InP MMIC LNAs with noise below 30K,” in *2012 IEEE MTT-S International Microwave Symposium Digest*, Jun. 2012.

[18] H. Wang, G. I. Ng, R. Lai, Y. Hwang, D. C. W. Lo, R. Dia, A. Freudenthal, and T. Block, “Fully passivated W-band InAlAs/InGaAs/InP monolithic low noise amplifiers,” in *IEE Proceedings Microwaves, Antennas and Propagation*, vol. 143, no. 5, Oct. 1996.

[19] D. S. Russell, “Technology advances for radio astronomy,” Ph.D. dissertation, California Institute of Technology, Pasadena, CA, Jun. 2013. [Online]. Available: http://resolver.caltech.edu/CaltechTHESIS:11262012-212534634

[20] W. R. Deal, K. Leong, V. Radisic, S. Sarkozy, B. Gorospe, J. Lee, P. Liu, W. Yoshida, J. Zhou, M. Lange, R. Lai, and X. B. Mei, “Low noise amplification at 0.67 THz using 30 nm InP HEMTs,” *IEEE Microw. Wireless Compon. Lett.*, vol. 21, no. 7, Jul. 2011.

[21] W. R. Deal, X. B. Mei, V. Radisic, K. Leong, S. Sarkozy, B. Gorospe, J. Lee, P. Liu, W. Yoshida, J. Zhou, M. Lange, J. Uyeda, and R. Lai, “Demonstration of a 0.48 THz amplifier module using InP HEMT transistors,” *IEEE Microw. Wireless Compon. Lett.*, vol. 20, no. 5, May 2010.

[22] A. Tessmann, M. Kuri, M. Riessle, H. Massler, M. Zink, W. Reinert, W. Bronner, and A. Leuther, “A compact W-band dual-channel receiver module,” in *2006 IEEE MTT-S International Microwave Symposium Digest*, Jun. 2006.

[23] C. Schwörer, A. Tessmann, A. Leuther, H. Massler, W. Reinert, and M. Schlechtweg, “Low-noise W-band amplifiers for radiometer applications using a 70nm metamorphic HEMT technology,” in *European Gallium Arsenide and other Compound Semiconductors Application Symposium*, Oct. 2003.

[24] W. Ciccognani, E. Limiti, P. Longhi, and M. Renvoise, “MMIC LNAs for radioastronomy applications using advanced industrial 70 nm metamorphic technology,” *IEEE J. Solid-State Circuits*, vol. 45, no. 10, Oct. 2010.

[25] R. C. Johnson and H. Jasik, *Antenna Engineering Handbook*, 2nd ed. New York: McGraw-Hill, 1984.

[26] S. Ramo, J. R. Whinnery, and T. V. Duzer, *Fields and Waves in Communication Electronics*, 3rd ed. John Wiley & Sons, 1994.

[27] D.-W. Duan and Y. Rahmat-Samii, “A generalized three-parameter aperture distribution for antenna applications,” *IEEE Trans. Antennas Propag.*, vol. 40, no. 6, pp. 697–713, Jun. 1992.

[28] A. C. Ludwig, “Antenna feed efficiency,” Jet Propulsion Laboratory/NASA, Pasadena, CA, USA, Space Programs Summary 37-26, vol. IV, Apr. 1964.

[29] ——, “Radiation pattern synthesis for circular aperture horn antennas,” *IEEE Trans. Antennas Propag.*, vol. AP-14, no. 4, pp. 434–440, Jul. 1966.

[30] P.-S. Kildal, *Foundations of Antennas A Unified Approach.* Lund, Sweden: Studentlitteratur, 2000.

[31] R. E. Collin, “Aperture efficiency for parabolodial reflectors,” *IEEE Trans. Antennas Propag.*, vol. AP-32, Sep. 1984.

[32] P.-S. Kildal, “Factorization of the feed efficiency of paraboloids and cassegrain antennas,” *IEEE Trans. Antennas Propag.*, vol. AP-33, Aug. 1985.

[33] A. C. Ludwig, “The definition of cross polarization,” *IEEE Trans. Antennas Propag.*, vol. 21, Jan. 1973.

[34] H. M. Pickett, J. C. Hardy, and J. Farhoomand, “Characterisation of a dual-mode horn for submillimetre wavelengths,” *IEEE Trans. Microw. Theory Tech.*, vol. 32, no. 8, Aug. 1984.

[35] P. D. Potter, “A new horn antenna with suppressed sidelobes and equal beamwidths,” *Microwave Journal*, vol. VI, no. 6, Jun. 1963.

[36] S. B. Cohn, “Properties of ridged wave guide,” *Proceedings of the IRE*, vol. 35, Aug. 1947.

[37] N. Marcuvitz, Ed., *Waveguide Handbook*, ser. MIT Radiation Laboratory. Lexington, MA: Boston Technical, 1964, vol. 10.

[38] S. Hopfer, “The design of ridged waveguides,” *IRE Trans. Microw. Theory Tech.*, vol. 3, Oct. 1955.

[39] J. P. Montgomery, “On the complete eigenvalue solution of ridged waveguide,” *IEEE Trans. Microw. Theory Tech.*, vol. MTT-19, Jun. 1971.

[40] M. H. Chen, G. N. Tsandoulas, and F. G. Willwerth, “Modal characteristics of quadruple-ridged circular and square waveguides (short papers),” *IEEE Trans. Microw. Theory Tech.*, vol. 22, Aug. 1974.

[41] W. Sun and C. A. Balanis, “MFIE analysis and design of ridged waveguides,” *IEEE Trans. Microw. Theory Tech.*, vol. 41, pp. 1965–1971, Nov. 1993.

[42] ——, “Analysis and design of quadruple-ridged waveguides,” *IEEE Trans. Microw. Theory Tech.*, vol. 42, pp. 2201–2207, Dec. 1994.

[43] G. M. Coutts, “Octave bandwidth orthomode transducers for the expanded very large array,” *IEEE Trans. Antennas Propag.*, vol. 59, no. 6, pp. 1910–1917, Jun. 2011.

[44] C. Granet and G. L. James, “The quad-ridged omt: The effects of fin shape on performance,” CSIRO, Australia, Tech. Rep. RPP 3879, Oct. 1996.

[45] R. J. Bauerle, R. Schrimpf, E. Gyorko, and J. Henderson, “The use of a dielectric lens to improve the efficiency of a dual-polarized quad-ridge horn from 5 to 15 GHz,” *IEEE Trans. Antennas Propag.*, vol. 57, no. 6, pp. 1822–1825, Jun. 2009.

[46] S. A. Soroka, “A physically compact quad ridge horn design,” in *1986 Antennas and Propagation Society International Symposium*, Jun. 1986.

[47] M. Gilbert, K. Higgins, and L. Romero, “Quad-ridge horn utilizing resistive films to reduce sidelobes,” in *2007 IEEE Antennas and Propagation Society International Symposium*, Jun. 2007.

[48] CST Microwave Studio 2011. Darmstadt, Germany: CST AG, 2011.

[49] C. Granet, “Profile options for feed horn design,” in *2000 Asia-Pacific Microwave Conference*, Sydney, NSW, Australia, Dec. 2000.

[50] J. Shin and D. H. Schaubert, “A parameter study of stripline-fed Vivaldi notch-antenna arrays,” *IEEE Trans. Antennas Propag.*, vol. 47, no. 5, May 1999.

[51] S. Silver, Ed., *Microwave Antenna Theory and Design*, ser. MIT Radiation Laboratory. London, UK: Peter Peregrinus, 1984, vol. 12.

[52] Y. Rahmat-Samii, “Chapter 15 - reflector antennas,” in *Antenna Handbook*, Y. T. Lo and S. W. Lee, Eds. New York: Van Nostrand Reinhold, 1988.

[53] MATLAB version 7.10.0. Natick, MA: The Mathworks, Inc., 2010.

[54] J. L. Doane, *Infrared and Millimeter Waves.* Orlando, FL, USA: Academic Press, 1985, vol. 13 Millimeter-wave Components and Techniques Part IV, ch. 5.

[55] W. A. Imbriale, S. Weinreb, G. Jones, H. Mani, and A. Akgiray, “The design and performance of a wideband radio telescope for the GAVRT program,” *IEEE Trans. Antennas Propag.*, vol. 59, Jun. 2011.

[56] W. A. Imbriale, “Radio frequency optics design of the 12-meter antenna for the array-based deep space network,” Jet Propulsion Laboratory/NASA, Pasadena, CA, USA, IPN Progress Report 42-160, Feb. 2005.

[57] J. W. M. Baars, P. G. Mezger, and H. Wendker, “The spectra of the strongest non-thermal radio sources in the centimeter-wavelength range,” *Astrophysical Journal*, vol. 142, Feb. 1965.

[58] ——, “The absolute spectrum of Cas A; an accurate flux density scale and a set of secondary calibrators,” *Astronomy and Astrophysics*, vol. 61, no. 1, Oct. 1977.

[59] M. Ott, A. Witzel, A. Quirrenbach, T. P. Krichbaum, K. J. Standke, C. J. Schalinski, and C. A. Hummel, “An updated list of radio flux density calibrators,” *Astronomy and Astrophysics*, vol. 284, no. 1, Apr. 1994.

[60] G. C. Medellin, “Antenna noise temperature calculation,” SKA Memo 95, Jul. 2007.

[61] H. Hase, R. Dassing, T. Klügel, G. Kronschnabl, A. Neidhardt, P. Lauber, R. Kilger, and K. Pausch, “Twin Telescope Wettzell - a VLBI2010 project,” presented at the IVS VLBI2010 Workshop on Future Radio Frequencies and Feeds, Wettzell, Germany. [Online]. Available: http://www.fs.wettzell.de/veranstaltungen/vlbi/frff2009/Part8/ttwvlbi2010e.pdf

[62] W. Imbriale, “Faster antenna noise temperature calculations using a novel approximation technique,” in *Int. Symp. on Ant. and Prop. and CNC-USNC/URSI Radio Science Meeting*, Toronto, ON, Jul. 2010, pp. 1–4.

[63] MIT Haystack Observatory Westford radio telescope. [Online]. Available: http://www.haystack.mit.edu/obs/westford/technical.Wes.html

[64] R. Keller, C. Kasemann, S. Weinreb, A. Akgiray, U. Bach, P. Freire, K. Grypstra, R. Karuppusamy, M. Kramer, P. Müller, F. Schäfer, and B. Winkel, “An ultra broad band radiometer receiver for the Effelsberg 100m telescope,” Advances in Radio Science, 2013.

[65] OMMIC, “D007ih small-signal model,” Dec. 2010.

[66] R. Lai, X. Mei, W. Deal, W. Yoshida, Y. Kim, P. Liu, J. Lee, J. Uyeda, V. Radisic, M. Lange, T. Gaier, L. Samoska, and A. Fung, “Sub 50 nm InP HEMT device with Fmax greater than 1 THz,” in *2007 IEEE International Electron Devices Meeting*, Dec. 2007.

[67] P. Kangalashti, D. Pukala, T. Gaier, W. Deal, X. Mei, and R. Lai, “Low noise amplifier for 180 GHz frequency band,” in *2008 IEEE MTT-S International Microwave Symposium Digest*, Jun. 2008.

[68] L. Samoska, A. Fung, D. Pukala, P. Kangalashti, R. Lai, S. Sarkozy, X. Mei, and G. Boll, “On-wafer measurements of S-MMIC amplifiers from 400-500 GHz,” in *2011 IEEE MTT-S International Microwave Symposium Digest*, Jun. 2011.

[69] M. W. Pospieszalski, “Modeling of noise parameters of MESFETs and MODFETs and their frequency and temperature dependence,” *IEEE Trans. Microw. Theory Tech.*, vol. 37, no. 9, 1989.

[70] J. C. Bardin, “Silicon-germanium heterojunction bipolar transistors for extremely low-noise applications,” Ph.D. dissertation, California Institute of Technology, Pasadena, CA, Jun. 2009. [Online]. Available: http://resolver.caltech.edu/CaltechETD:etd-06092009-113849

[71] G. Dambrine, H. Happy, F. Danneville, and A. Cappy, “A new method for on wafer noise measurement,” *IEEE Trans. Microw. Theory Tech.*, vol. 41, no. 3, Mar. 1993.

[72] W. A. Strifler, B. T. Pugh, and R. D. Remba, “Shot noise in GaAs metal semiconductor field effect transistors with high gate leakage current,” *Solid-State Electronics*, vol. 37, no. 10, Sep. 1989.

[73] J. B. Kuang, P. J. Tasker, G. W. Wang, Y. K. Chen, L. F. Eastman, O. A. Aina, H. Hier, and A. Fathimulla, “Kink effect in submicrometer-gate MBE-grown InAlAs/InGaAs/InAlAs heterojunction MESFET’s,” *IEEE Electron Device Lett.*, vol. 9, no. 12, Dec. 1988.

[74] B. Georgescu, A. Souifi, G. Post, and G. Guillot, “A slow-trap model for the kink effect on InAlAs/InP HFET,” presented at the International Conference on Indium Phosphide and Related Materials, May 1997.

[75] J. L. C. de Diego, “Cryogenic technology in the microwave engineering: Application to MIC and MMIC very low noise amplifier design,” Ph.D. dissertation, Universidad de Cantabria, Santander, Spain, May 2010. [Online]. Available: http://www.tdx.cat/handle/10803/10674

[76] R. Reuter, M. Agethen, U. Auer, S. van Waasen, D. Peters, W. Brockerhoff, and F.-J. Tegude, “Investigation and modeling of impact ionization with regard to the RF and noise behavior of HFET,” *IEEE Trans. Microw. Theory Tech.*, vol. 45, no. 6, Jun. 1997.

[77] M. Isler and K. Schünemann, “Impact-ionization effects on the high-frequency behavior of HFETs,” *IEEE Trans. Microw. Theory Tech.*, vol. 52, no. 3, Mar. 2003.

[78] C.-I. Lee, W.-C. Lin, and Y.-T. Lin, “Modeling inductive behavior of MOSFET scattering parameter s_{22} in the breakdown regime,” *IEEE Trans. Microw. Theory Tech.*, vol. 60, no. 3, Mar. 2012.

[79] R. T. Webster, S. Wu, and A. Anwar, “Impact ionization in InAlAs/InGaAs/InAlAs HEMT’s,” *IEEE Electron Device Lett.*, vol. 21, no. 5, May 2000.

[80] M. H. Somerville, J. A. del Alamo, and W. Hoke, “Direct correlation between impact ionization and the kink effect in InAlAs/InGaAs HEMT’s,” *IEEE Electron Device Lett.*, vol. 17, no. 10, Oct. 1996.

[81] M. H. Somerville, A. Ernst, and J. A. del Alamo, “A physical model for the kink effect in InAlAs/InGaAs HEMT’s,” *IEEE Trans. Electron Devices*, vol. 47, no. 5, May 2000.

[82] W. Curtice, “A MESFET model for use in the design of GaAs integrated circuit,” *IEEE Trans. Microw. Theory Tech.*, vol. 28, no. 5, May 1980.

[83] D. Widiger, K. Hess, and J. J. Coleman, “Two-dimensional numerical analysis of the high electron mobility transistor,” *IEEE Electron Device Lett.*, vol. 5, no. 7, Jul. 1984.

[84] A. Materka and T. Kacprzak, “Computer calculation of large-signal GaAs FET amplifier characteristics,” *IEEE Trans. Microw. Theory Tech.*, vol. 33, no. 2, Feb. 1985.

[85] G. Dambrine, A. Cappy, F. Heliodore, and E. Playez, “A new method for determining the FET small-signal equivalent circuit,” *IEEE Trans. Microw. Theory Tech.*, vol. 36, no. 7, 1988.

[86] I. Angelov, H. Zirath, and N. Rosman, “Computer calculation of large-signal GaAs FET amplifier characteristics,” *IEEE Trans. Microw. Theory Tech.*, vol. 40, no. 12, Dec. 1992.

[87] J. Mateos, T. Gonzalez, D. Pardo, V. Hoel, and A. Cappy, “Monte Carlo simulator for the design optimization of low-noise HEMTs,” *IEEE Trans. Electron Devices*, vol. 47, no. 10, Oct. 2000.

[88] D. M. Pozar, *Microwave Engineering*, 2nd ed. USA: John Wiley and Sons, Inc., 1998.

[89] T. Gaier, P. Kangalashti, and L. Samoska, private communication, 2012.

[90] J. E. Fernandez, "A noise-temperature measurement system using a cryogenic attenuator," Jet Propulsion Laboratory/NASA, Pasadena, CA, USA, TPO Progress Report 42-135, Nov. 1998.

[91] M. W. Pospieszalski, "On the noise parameters of isolator and receiver with isolator at the input," *IEEE Trans. Microw. Theory Tech.*, vol. MTT-34, no. 4, Apr. 1986.

[92] ——, "Correction to "On the noise parameters of isolator and receiver with isolator at the input"," *IEEE Trans. Microw. Theory Tech.*, vol. MTT-34, no. 6, Jun. 1986.

[93] J. Lange, "Noise characterization of linear twoports in terms of invariant parameters," *IEEE J. Solid-State Circuits*, vol. SC-2, no. 2, Jun. 1967.

[94] R. Reeves, private communication, 2013.

[95] J. Schleeh, private communication, 2013.

[96] H. Bosma, "On the theory of linear noisy systems," Ph.D. dissertation, Technical University of Eindhoven, Holland, 1967. [Online]. Available: http://alexandria.tue.nl/extra3/proefschrift/PRF1A/7706673.pdf

Appendix A

Geometries of the Example Quad-Ridged Horns

Ridge Profile		Horn Profile	
x	y	x	y
122.81	12.18	122.81	0
122.81	0	122.81	29.18
27.71	0	125.43	211.29
27.71	12.18	132.37	393.39
2.9	12.18	143.92	575.5
2.9	29.18	160.25	757.6
5.27	194.02	180.71	939.71
11.69	358.86	205.83	1121.81
22.14	523.69	235.04	1303.92
36.57	688.53	268.09	1486.02
55.56	853.36	305.37	1668.13
78.38	1018.2	346.01	1850.23
104.92	1183.04	390.13	2032.34
135.08	1347.87	437.48	2214.44
169.28	1512.71	487.5	2396.55
206.8	1677.55	540.37	2578.65
247.46	1842.38	595.42	2760.76
291.11	2007.22	652.41	2942.86
328.26	2139.09	711.17	3124.97
367.15	2270.96	771.16	3307.07
407.67	2402.83	832.18	3489.17
449.68	2534.69	893.83	3671.28
493.07	2666.56	951.33	3853.38
537.7	2798.43	967.97	3894.83
583.45	2930.3	990.97	3931.99
630.16	3062.17	1019.18	3963.01
677.72	3194.04	1051.17	3986.32
725.96	3325.91	1085.35	4000.76
774.76	3457.78	1120	4005.6
823.96	3589.65	1153.38	4000.61
873.41	3721.52		
918.08	3853.38		
951.33	3853.38		
893.83	3671.28		
832.18	3489.17		
771.16	3307.07		
711.17	3124.97		
652.41	2942.86		
595.42	2760.76		
540.37	2578.65		
487.5	2396.55		
437.48	2214.44		
390.13	2032.34		
346.01	1850.23		
305.37	1668.13		
268.09	1486.02		
235.04	1303.92		
205.83	1121.81		
180.71	939.71		
160.25	757.6		
143.92	575.5		
132.37	393.39		
125.43	211.29		
122.81	29.18		
122.81	12.18		

Table A.1: $x-y$ coordinates of the ridge and horn profiles of the very high gain QRFH for $f_{lo} = 0.5$ GHz. Dimensions are in millimeters.

Ridge Profile		Horn Profile	
x	y	x	y
77.22	7.71	77.22	0.00
77.22	0.00	77.22	18.41
16.79	0.00	77.65	65.63
16.79	7.71	79.52	112.85
2.71	7.71	83.32	160.07
2.71	18.41	89.39	207.28
2.94	42.02	98.02	254.50
3.73	65.63	109.44	301.72
5.16	89.24	123.86	348.93
7.25	112.85	141.48	396.15
10.05	136.46	162.48	443.37
13.58	160.07	187.00	490.59
17.85	183.67	215.22	537.80
22.88	207.28	247.27	585.02
28.69	230.89	283.29	632.24
35.30	254.50	323.40	679.45
42.71	278.11	345.03	703.06
50.94	301.72	355.00	712.71
60.00	325.33	365.70	720.75
69.90	348.93	376.59	726.78
80.64	372.54	387.12	730.50
92.24	396.15	396.77	731.71
104.71	419.76	405.05	730.37
118.04	443.37	411.55	726.53
132.26	466.98		
147.37	490.59		
163.36	514.19		
180.26	537.80		
198.07	561.41		
216.79	585.02		
236.43	608.63		
256.99	632.24		
278.49	655.85		
300.92	679.45		
324.28	703.06		
336.14	703.06		
345.03	703.06		
323.40	679.45		
283.29	632.24		
247.27	585.02		
215.22	537.80		
187.00	490.59		
162.48	443.37		
141.48	396.15		
123.86	348.93		
109.44	301.72		
98.02	254.50		
89.39	207.28		
83.32	160.07		
79.52	112.85		
77.65	65.63		
77.22	18.41		
77.22	7.71		

Table A.2: $x-y$ coordinates of the ridge and horn profiles of the high-gain QRFH for $f_{lo} = 0.7$ GHz. Dimensions are in millimeters.

Ridge Profile		Horn Profile	
x	y	x	y
28.05	7.04	28.05	0.00
28.05	0.00	28.05	11.50
11.37	0.00	28.61	21.97
11.37	7.04	29.32	32.44
0.65	7.04	30.21	42.91
0.65	11.50	31.32	53.38
1.06	16.74	32.73	63.85
1.51	21.97	34.50	74.32
2.02	27.21	36.72	84.79
2.59	32.44	39.52	95.26
3.22	37.68	43.04	105.73
3.93	42.91	47.46	116.20
4.72	48.15	53.03	126.67
5.61	53.38	60.02	137.14
6.59	58.62	68.82	147.60
7.70	63.85	79.89	158.07
8.94	69.09	86.45	163.31
10.32	74.32	88.10	164.34
11.86	79.55	89.94	164.99
13.59	84.79	91.88	165.21
15.51	90.02	93.81	164.99
17.67	95.26	95.65	164.35
20.08	100.49	97.30	163.31
22.77	105.73	98.68	161.93
25.78	110.96		
29.14	116.20		
32.90	121.43		
37.10	126.67		
41.80	131.90		
47.05	137.14		
52.92	142.37		
59.47	147.60		
66.80	152.84		
74.99	158.07		
84.15	163.31		
86.45	163.31		
79.89	158.07		
68.82	147.60		
60.02	137.14		
53.03	126.67		
47.46	116.20		
43.04	105.73		
39.52	95.26		
36.72	84.79		
34.50	74.32		
32.73	63.85		
31.32	53.38		
30.21	42.91		
29.32	32.44		
28.61	21.97		
28.05	11.50		
28.05	7.04		

Table A.3: $x-y$ coordinates of the ridge and horn profiles of the medium-gain QRFH for $f_{lo} = 2$ GHz. Dimensions are in millimeters.

Ridge Profile		Horn Profile	
x	y	x	y
17.84	4.75	17.84	0.00
17.84	0.00	17.84	7.89
6.93	0.00	17.84	13.61
6.93	4.75	17.86	19.33
0.53	4.75	17.93	25.05
0.53	7.89	18.09	30.77
1.03	16.91	18.35	36.49
1.53	25.93	18.79	42.21
2.03	34.95	19.42	47.93
2.53	43.97	20.27	53.65
3.04	53.00	21.45	59.37
3.66	62.02	22.94	65.09
4.69	71.04	24.82	70.81
5.54	75.25	27.15	76.53
6.82	79.46	29.93	82.25
8.68	83.67	33.31	87.97
11.30	87.88	37.26	93.69
14.82	92.09	41.84	99.41
19.31	96.30	47.18	105.13
24.74	100.51	53.24	110.85
30.93	104.72	60.17	116.57
37.55	108.93	67.99	122.29
44.12	113.14	76.68	128.01
50.11	117.35	80.91	130.41
54.95	121.56	85.23	132.23
58.17	125.77	89.42	133.38
64.59	131.63	93.26	133.80
72.64	134.89	96.57	133.46
81.33	135.14	99.18	132.40
87.82	132.94	100.95	130.65
85.23	132.23		
80.91	130.41		
76.68	128.01		
67.99	122.29		
60.17	116.57		
53.24	110.85		
47.18	105.13		
41.84	99.41		
37.26	93.69		
33.31	87.97		
29.93	82.25		
27.15	76.53		
24.82	70.81		
22.94	65.09		
21.45	59.37		
20.27	53.65		
19.42	47.93		
18.79	42.21		
18.35	36.49		
18.09	30.77		
17.93	25.05		
17.86	19.33		
17.84	13.61		
17.84	7.89		
17.84	4.75		

Table A.4: $x - y$ coordinates of the ridge and horn profiles of the low-gain QRFH for $f_{lo} = 2.3$ GHz. Dimensions are in millimeters.

Ridge Profile		Horn Profile	
x	y	x	y
16.67	4.86	16.67	0.00
16.67	0.00	16.67	7.61
6.51	0.00	16.69	14.86
6.51	4.86	16.73	22.11
0.58	4.86	16.78	29.35
0.58	7.61	16.88	36.60
0.74	11.11	17.04	43.85
0.90	14.61	17.30	51.09
1.06	18.11	17.74	58.34
1.22	21.61	18.46	65.59
1.38	25.11	19.65	72.83
1.54	28.60	21.62	80.08
1.70	32.10	24.88	87.33
1.86	35.60	30.27	94.57
2.02	39.10	39.19	101.82
2.18	42.60	53.97	109.06
2.34	46.10	64.66	112.69
2.50	49.59	67.15	113.36
2.66	53.09	69.63	113.69
2.83	56.59	71.96	113.66
3.00	60.09	74.03	113.27
3.20	63.59	75.73	112.54
3.42	67.09	76.99	111.51
3.69	70.58	77.73	110.23
4.06	74.08		
4.57	77.58		
5.33	81.08		
6.48	84.58		
8.23	88.07		
10.89	91.57		
14.94	95.07		
21.00	98.57		
30.01	102.07		
43.21	105.57		
47.92	106.43		
45.65	105.44		
34.17	98.19		
27.23	90.95		
23.04	83.70		
20.51	76.46		
18.98	69.21		
18.05	61.96		
17.49	54.72		
17.15	47.47		
16.95	40.22		
16.83	32.98		
16.75	25.73		
16.71	18.48		
16.68	11.24		
16.67	4.86		

Table A.5: $x - y$ coordinates of the ridge and horn profiles of the very low gain QRFH for $f_{lo} = 2.3$ GHz. Dimensions are in millimeters.

Appendix B

Sample MATLAB Codes for QRFH Design

```
% prepCST.m
% Main interface to write QRFH geometry defined in MATLAB to CST
%
% The inputs are the geometric parameters listed in "Prmtrs" variable
% The program then generates the ridge & horn profiles using four
% custom functions: genProfile.m, genRidgeProfile.m, genHornProfile.m, and
% mergeProfiles_new.m
%
% If the user elects to upload geometry to CST by setting "writeCST" equal
% to one, the program writes the parameters to CST as well as to a text
% file.
%
% If the user elects to run the EM simulation by setting "doSave" equal
% to one, the program runs the simulation engine and once complete:
% 1) downloads the S—parameters and far—fields to MATLAB; 2) writes the
% results to disk using the functions: CST_saveFF.m and CST_saveSpar.m;
% 3) plots the results for user evaluation using the function plotCSTRun.m

clear

prj_path = 'D:\CST';
prj_fname = 'qrfh.cst';

% PARAMETER SETUP %
p_name = {
    'rpInd'          , 'hpInd'           ,...
    'rp_ai'          , 'hp_ai'           ,...
    'rp_ao'          , 'hp_ao'           ,...
    'rp_L'           , 'hp_L'            ,...
```

```
    'rp_R'          , 'hp_R'            ,...
    'rp_p'          , 'hp_p'            ,...
    'rp_A'          , 'hp_A'            ,...
    'rp_g'          , 'hp_g'            ,...
    'alpha'         , 'curv_rad'        ,...
    'fin_depth'     , 'fin_thick'       ,...
    'fin_width'     , 'gap_w'           ,...
    'leg_width'     , 'fin_angle'       ,...
    'p1_h'          , 'p2_h'            ,...
    'tip_w'         , 'trans_L'         ,...
    'max_fin_t'     , 'aper_ang'        ,...
    'aper_Rx'       , 'aper_Rz'         ,...
    'donut_Ri'      , 'donut_L'         ,...
    'donut_offset'  , 'scaleFctr'       };

halfAng = 50; % Half—subtended angle

Prmtrs = [
    9               ; 9                 ;...
    NaN             ; NaN               ;...
    83.5            ; 85.8              ;...
    151.8           ; 151.8             ;...
    21.255e—3       ; 21.898e—3         ;...
    1               ; 1                 ;...
    1               ; 1                 ;...
    1               ; 1                 ;...
    45              ; —25               ;...
    7.04            ; NaN               ;...
    10.72           ; 1.3               ;...
    16.68           ; 0                 ;...
    0.914           ; 1                 ;...
    0.514           ; 4.466             ;...
    3               ; 0                 ;...
    8.7             ; 8.7               ;...
    0.7             ; 2                 ;...
    0               ; 1                 ];

writeCST = 0;
doSave = 1;

%% PERFORM SCALING PER THE VALUE OF "scaleFctr"
Prmtrs(3) = 0;
Prmtrs(4) = Prmtrs(21) + Prmtrs(23);
Prmtrs(20) = Prmtrs(29);

```

```
scaleFctr = Prmtrs(36);
Prmtrs([3:8, 18:23, 25:29, 31:32, 34:35]) = ...
    Prmtrs([3:8, 18:23, 25:29, 31:32, 34:35]) / scaleFctr;
Prmtrs([9:10]) = Prmtrs([9:10]) * scaleFctr;

%% GENERATE PROFILES
ridgePrf = genProfile(Prmtrs(1), Prmtrs(3:2:15), 0);
ridgePrf = genRidgeProfile(ridgePrf, Prmtrs(28), Prmtrs(19), ...
    Prmtrs(21), Prmtrs(23), Prmtrs(18));

hornPrf = genProfile(Prmtrs(2), Prmtrs(4:2:16), 0);
hornPrf = genHornProfile(hornPrf, Prmtrs(31), Prmtrs(32), ...
    Prmtrs(28), Prmtrs(19), Prmtrs(4));

[prf, hornPrf] = mergeProfiles_new(ridgePrf, hornPrf);

if isempty(prf)
    error('Horn and fin do not intersect!');
end

%% SOME MISC STUFF
p_name = [p_name, 'xmax', 'ymax', 'zmax'];
Prmtrs = [Prmtrs; ...
          max(hornPrf(:,1)); max(hornPrf(:,1)); max(hornPrf(:,2))];
Prmtrs(Prmtrs == 0) = 1e-3;

%% ARE WE WRITING GEOM TO CST?
if writeCST

    time = datestr(now,30); time(end-1:end) = [] %%% TIME STAMP
    fid = fopen([prj_path '\' prj_fname(1:end-4), ...
        '_Parameters_' time '.txt'],'wt');
    prf_fname = [prj_path '\' prj_fname(1:end-4) '_' time];

    cst = actxserver('CSTSTUDIO.application');
    mws = invoke(cst, 'OpenFile',[prj_path '\' prj_fname]);
    solver = invoke(mws,'Solver');

    %%% WRITE GEOM PARAMETERS TO CST AND TXT FILE %%%
    rx_lbl = strtrim( cellstr( [num2str([1:length(prf)]')] ) );
    rx_lbl = cellfun(@(x) ['rx',x], rx_lbl, 'UniformOutput',false);
    ry_lbl = strtrim( cellstr( [num2str([1:length(prf)]')] ) );
    ry_lbl = cellfun(@(x) ['ry',x], ry_lbl, 'UniformOutput',false);

    hx_lbl = strtrim( cellstr( [num2str([1:length(hornPrf)]')] ) );
```

```
    hx_lbl = cellfun(@(x) ['hx',x], hx_lbl, 'UniformOutput',false);
    hy_lbl = strtrim( cellstr( [num2str([1:length(prf)]')] ) );
    hy_lbl = cellfun(@(x) ['hy',x], hy_lbl, 'UniformOutput',false);

    CST_writePar( mws, p_name, Prmtrs, fid);
    CST_writePar( mws, rx_lbl, prf(:,1), fid);
    CST_writePar( mws, ry_lbl, prf(:,2), fid);
    CST_writePar( mws, hx_lbl, hornPrf(:,1), fid);
    CST_writePar( mws, hy_lbl, hornPrf(:,2), fid);

    invoke( mws, 'RebuildForParametricChange' );
    fclose(fid);

    invoke(solver, 'HardwareAcceleration','True');

    %%% RUN SOLVER %%%
    if doSave
        solvOut = invoke(solver, 'Start');
        fname_SPar = [prj_path '\' prj_fname(1:end-4) '_' time];
        CST_saveFF(mws, [1 15], prj_path, prj_fname, time);
        CST_saveSPar(mws, fname_SPar);

        plotCSTRun(prj_path, prj_fname(1:end-4), time, halfAng);
        invoke( mws, 'Save');
        invoke( mws, 'Quit');
    end
end
```

```
function prf = genProfile(prfInd, in)

if prfInd <1 || prfInd > 13
    error('Profile index must be an integer between 1-12');
end

ai = in(1);     % radius at bottom
ao = in(2);     % radius at aperture
L = in(3);      % taper length

R = in(4);

p = in(5);      % power p
A = in(6);      % A
g = in(7);      % Gamma

len = 30;

z = linspace(0,L,len)';

% Linear
all(:,1) = ai + (ao - ai) * z/L;


% Sinusoid
all(:,2) = ai + (ao-ai)*( (1-A).*z/L + A.*sin(pi/2*z/L).^p );


% Tangential
all(:,3) = ai + (ao-ai)*( (1-A).*z/L + A.*tan(pi/4*z/L).^p );


% x^p
all(:,4) = ai + (ao-ai)*( (1-A).*z/L + A.*(z/L).^p );


% Exp
all(:,5) = ai*exp(log(ao/ai)*z/L);


%Hyperbolic
all(:,6) = sqrt(ai^2 + z.^2 * (ao^2 - ai^2)/L/L);


```

```
% Polynomial
all(:,7) = ai*(1-A) + (ao-ai) * (1-A).*(z/L) + ...
    A.*(ai + (p+1)*(ao-ai)*(1-p*z/(p+1)/L).*(z/L).^p);

% Asymmetric sine-squared
L1 = L/(1+g); L2 = g*L1;
ind = find(z<=L1); ind = ind(end);

all(:,8) = ai + 2*(ao-ai)/(1+g) *...
    [sin(pi/4*z(1:ind)/L1).^2;...
     g*sin(pi/4/L2 * (z(ind+1:end)+L2-L1)).^2 + (1-g)/2];


% original exponential
x2 = ao;
x1 = ai;
z1 = 0;
z2 = L;
c1 = (x2-x1) ./ ( exp(R.*z2) - exp(R.*z1) );
c2 = ( x1*exp(R.*z2) - x2*exp(R.*z1) ) ./ ...
        ( exp(R.*z2) - exp(R.*z1) );

x = c1 .* exp(R.*z) + c2;
all(:,9) = x;


% original elliptical
a = max([ao,L]); % semi-major axis
b = min([ao,L]); % semi-minor axis
dp = 0;

if ao > L,
    phi = 0;
    theta = linspace(-pi, -3*pi/2, len)';
else
    phi = pi/2;
    theta = flipud(linspace(0+dp, pi/2, len)');
end

xe = ao + a * cos(theta) * cos(phi) - b * sin(theta) * sin(phi);
ze = a * cos(theta) * sin(phi) + b * sin(theta) * cos(phi);


% original exponential modified to include linear portion
x2 = ao;
```

```
x1 = ai;
z1 = 0;
z2 = L;
c1 = (x2-x1) ./ ( exp(R.*z2) - exp(R.*z1) );
c2 = ( x1*exp(R.*z2) - x2*exp(R.*z1) ) ./ ...
        ( exp(R.*z2) - exp(R.*z1) );

all(:,11) = ai*(1-A) + (ao-ai) * (1-A).*(z/L) + A.*(c1 .* exp(R.*z) + c2);

% super quadric
a = ao - ai;
b = L;

phi = linspace(-pi,-3*pi/2, len)';

xs = a * sign(cos(phi)) .* abs(cos(phi)).^(1/p);
zs = b * sign(sin(phi)) .* abs(sin(phi)).^(1/p);

xs = xs - xs(1) + ai;
zs = zs - zs(1);

xs = A .* xs + (1-A) .* ( ai + (ao-ai) * (zs/L) );


% output
if prfInd ~= 10 && prfInd ~= 12
    prf = [all(:,prfInd), z];
elseif prfInd == 10
    prf = [xe, ze];
elseif prfInd == 12
    prf = [xs, zs];
end
```

```
function CST_writePar(mws, p_name, p_val, fid)

for ii = 1:length(p_val)
    invoke( mws, 'StoreParameter', p_name{ii}, num2str( p_val(ii),'%10.6f' ) );
    if ~isempty(fid)
        fprintf(fid, '%s\n', [p_name{ii} ' ' num2str(p_val(ii),'%10.6f')]);
    end
end
```